

SCIENTIFIC & TECHNICAL REPORT 2024

IMPRINT

Full report title CSEM Scientific and Technical Report 2024

Editor and publisher CSEM SA
info@csem.ch
T +41 32 720 5111

Publication Yearly frequency
Printed and digital editions



Cover page design Contreforme
www.contreforme.ch

Printing Imprimerie Baillod SA, Bevaix (Switzerland)

PREFACE

Dear Reader,

Forty years ago, the world was on the cusp of a technological revolution. Personal computers were just beginning to make their way into homes, mobile phones were a rarity, and the internet was a blossoming concept. Today, technology is seamlessly integrated into every aspect of our lives, opening up endless possibilities.

In 1984, in this rapidly changing landscape, CSEM was founded to address the challenges faced by the Swiss watch industry. Over the four subsequent decades, we have grown far beyond our initial mission. Today, our goal is to develop technologies that not only benefit the Swiss economy, but also address the challenges faced by humanity and the environment.

We develop and transfer disruptive technologies to make a significant impact in three key areas: precision manufacturing, digitalization, and sustainable energy solutions. But realizing such ambitions would be unthinkable without the support of leading academic players and industrial partners. They help us ensure the latest scientific advances are translated into practical applications, benefiting society.

Looking ahead, we envision technology serving people and the planet, fostering a brighter future for all. We look forward to the next 40 years of growth, collaboration, and technological advances with our dedicated staff, research network, industrial partners, stakeholders, and everyone who has been part of this incredible journey. Thank you for your invaluable contributions.

Alexandre Pauchard

CEO, CSEM SA

CONTENTS

PREFACE	1	MedPhab – Photonics Solutions at Pilot Scale for Accelerated Medical Device Development	40
MULTIDISCIPLINARY INTEGRATED PROJECTS—MIPS	7	Revolutionizing Precision Health through Multi-modal and Knowledge-driven AI	41
COSETE – Cooperative Sensors for Electrical Impedance Tomography	9	Smart Labware for Organoid Positioning	42
REVISIMO – Contactless Monitoring of Beat-to-beat Heart Rate and other Vital Parameters via Cameras	10	AirLiwell – Organoid Production and Culturing at the Air-Liquid Interface	43
ORCA2 – Organoid Dissociation for Single Cell Analysis	11	Bioreactors – Inline Sterility Test and Nutrient Multi-sensing Module	44
FLORES – Frog Escapement: Design Update	12	Optical Sensor System for Monitoring Cardiac Tissue Contractility in a Multi-well Plate	45
PRECIZE2 – Predictive Quality Towards Zero-defect Manufacturing in 3D Printing	13	Compact, Safe, and Automated Air Samplers for Collection of Viral Aerosols	46
LEVIATAN – Leveraging Open-source AI for Embedded Software Development	14	Towards Miniaturized, Eco-responsible, and Multi-sensing Platforms for Point-of-care	47
ENFRED – Life Cycle Analysis for Green and Sustainable Electronics: An Extended Model for IoT	15	Microfluidic PIC Integration for Aquaculture	48
SUMON2 – Hybrid Sustainable Bio-monitoring Test Strips with Dedicated Ultra-low-power ICs	16	MIRLA – Mid-infrared Liquids Analytics Platform	49
BEAST – Embedded Medical Secure Platform: Securing Data from the SoC up to the Cloud	17	Digital Lateral Flow and Electronics	50
PRECISION MANUFACTURING	19	DIGITAL DIPSTICK Revolutionizing Urine Sensing at the Point-of-care	51
Stiffness Engineering of Silicon-based Flexure Mechanisms using Residual Stress	20	New LiDAR and Oxygen Sensor for Cultural Heritage Site Protection	52
MEMS Magnetic Gradiometer	21	Configurable Slit Mask Unit for the MIRMOs Instrument	53
A MEMS Gas Chromatograph and its Fluidic Connections	22	TRACTOR – Thruster Pointing Mechanism with Novel Electroactive Polymer Actuator	54
Ultra-sensitive Photonics-MEMS Accelerometers for Next-generation Seismic Sensor	23	Next-generation Astrocombs, from Near-infrared to Ultra-violet F _{ceo} Detection on GaN PIC Platform	55
Developing the Mechanical Watches of Tomorrow using Advanced Silicon Microfabrication	24		56
A Novel Scintillator Detector for Online High-resolution Beam Profiling	25	DIGITALIZATION TECHNOLOGIES	57
Novel Dental Clear Aligner with Integrated Microfluidic Channels for Precise, High-efficiency Antibacterial and Fluoride Delivery	26	Evaluation of Ultra-wideband and Bluetooth® Technologies for Low-power and Precise Localization	58
High-resolution Lithography-based Manufacturing of Metals and Ceramics	27	A 22 nm, 6-9 GHz ADPLL for UWB Ranging and Communication Applications	59
Additive Manufacturing of Functionally Graded Composite of Shape Memory Alloy and Titanium	28	22nm, <10nW, Switched Capacitance or Resistance-based Always-on Circuits for IoT	60
3D Printed Pipe Segments with Built-in Heating and Temperature Sensing Capabilities	29	Feasibility Study for a Dense Analog Asynchronous Spiking Neural Network in a 22 nm Process with On-chip Synaptic Time Dependent Plasticity Unsupervised Learning	61
Additively Manufactured Flexible Pivots tested in Cryogenic Conditions	30	High-mmWave FMCW Radar with Antennas-in-package aided by Machine Learning	62
Efficient Anticorrosion Layer for Aluminum Current Collectors in Li-ion Batteries	31	60-GHz FMCW Radar Platform Demonstrator for Presence Detection Applications	63
Development of a Versatile Platform for Electrochemical Multi-sensing Evaluation	32	Beyond-ML – Accelerating Non-ML Tasks with CSEM EdgeML System-on-Chip	64
Sensor Components for Health Monitoring of Newborns and Pregnant Women	33	Minimizing Power Consumption in Speech Processing using MRAM-based Duty Cycling and Weight Storage	65
Antibacterial Sol-gel Coatings, a Kinetics Study	34	Monolayer-thick GaN/AlN Quantum Well Anodes and Far-UVC Field Emission Device	66
Standardized TFLN Photonic Integrated Circuits Platform	35	A Pre-industrial Two Photons High-performance Optical Atomic Clocks	67
Efficient Light Coupling to Thin-film Lithium Niobate on Insulator Photonic Integrated Circuits	36	SAND – Stochastic Approach for Feature Selection	68
Electro-optical Modulators in a Thin-film Lithium Niobate Foundry Process	37	Efficient and Privacy-preserving Smart Edge for Hierarchical Vision Systems	69
Surface Acoustic Wave Actuator on Thin-film Lithium Niobate for Acousto-optic Modulator	38	Constrained Zero-shot Neural Architecture Search on Small Classification Dataset	70
Mastering of Advanced-shape Microlens Arrays at Wafer Scale	39	Contactless Water Quality Monitoring for Wastewater Treatment Plants	71
		Advances in Sustainable Electronics: Innovations in Circular Design, Degradable Components, and Eco-efficiency	72

Biodegradable Chipless Sensor Tags for Sustainable Smart Packaging in Logistics	73	SUSTAINABLE ENERGY	103
Functionalization of Helmet with Electromagnetic Stimulation and Near-infrared Spectroscopic Measurement	74	High-efficiency Perovskite-on-Silicon Tandem Solar Cells Developments	104
Ultra-low-cost Near-field Wireless Power Transfer across Neighborhoods of Tiles	75	Developing Copper Metallization for Sustainable Production of TOPCon Cells	105
A 24-GHz 4-Element Multi-beam Wireless Energy Harvesting Array with Class-F Rectifiers Achieving 51.5 PCE	76	Perovskite Thin Films for Energy Harvesting and Sensing for IoT	106
IoT Fleet Key Management with built-in Post Compromise Recovery	77	PV Modules Reliability Testing Platform	107
Extending End-to-end Data Encryption & Sharing Technology with Microledger Audit Trails	78	New Enhancements of CSEM's Internal LCA Tool for Photovoltaic Systems	108
Detecting Heap Memory Bugs with Emulation Fuzzing Testbench	79	Tunnel IBC HJT Cell Technology Integrated in Modules	109
Low-energy Implementation of ECDSA using Hardware Acceleration	80	Solar-powered Balloons: Crossing the Atlantic with the Force of the Winds	110
Multi-sensor Embedded AI Platform for the Acoustic Weather Station Aurora	81	SolarTiles to Cover any Surface from Complex to Heritage Protected Roofs	111
Time-of-flight Based Gesture Recognition for Touch-free Wearables	82	Solar-powered Van around Switzerland	112
A Framework for AI-based Side-channel Attacks Featuring a New AI Method	83	Vehicle Integrated Photovoltaics (VIPV)	113
Wireless TDMA-based Protocol for Long-term Periodic Monitoring of Batteries	84	Integrating Satellite Imagery and Spatiotemporal Graph Neural Networks for Enhanced Day-ahead Solar Irradiance Forecasting	114
Showcasing the CSEM Bluetooth Low Energy Stack at UnPlugFest	85	Unsupervised Anomaly Detection for Commercial Refrigeration Systems using Language Models	115
μ 169 – A Cutting-edge Ultra-low-power OS with Robustness and Security Capabilities	86	Detection of Crack Patterns to Increase the Yield of Solar Module Production	116
AMC® – Additive Membrane Care	87	Feasibility and Control of Low-temperature District Heating Network with Distributed Sources	117
Path Planning Optimization in Deposition-based Additive Manufacturing	88	Towards PFAS-free Aqueous Production of Cathodes for Greener Li-ion Batteries	118
Optimal Coverage Path Planning in Robotic Wood Floor Grinding	89	Smart Battery Management System with Embedded Electrochemical Impedance Spectroscopy	119
Instantaneous 360° 3D Scanner of Human Body Parts for Orthopedics Applications	90	Multi-chemistry Validation of CSEM's 'EIS2MOD' Model for State of Charge Estimation	120
Self-supervised Numerical Pre-training for Symbolic Regression	91	ANNEXES	121
Self-supervised Foundation Models in Holographic Imaging	92	Publications	121
Simplifying Collaborative Robot Programming and Smart Vision Integration for Flexible Lab Automation	93	Proceedings	125
Optimizing Bin Picking with 2D Vision – A Cost-effective Approach for Robotic Automation	94	Conferences and Workshops	130
Visard-HE – Visard for Headless and Embedded Applications	95	Research Projects	130
Monaural Electroencephalogram towards Brain-controlled Hearing Aids	96	Innosuisse – Swiss Innovation Agency	132
Dry Electrodes with an Active Guard to Improve Bioimpedance Measurement Accuracy	97	European Commission Projects	136
Electrode Localization through Impedance Measurements	98	European Space Agency, Swiss Space Office, and Swiss Space Center Projects	141
SwissFever – Cloud-based Platform Enabling Real-time Fever Alerts for Children Undergoing Chemotherapy	99	Industrial Property	142
Continuous Non-invasive Measurement of Core Vital Signs on the Hospital Ward	100	Collaboration with Research Institutes and Universities	142
Cuffless Blood Pressure Monitoring: Precision is Maintained four Months after Calibration	101	Teaching	147
Unobtrusive Long-term Sleep Staging using Photoplethysmography-based Wearables	102	Theses	148
		Commissions and Committees	150
		Prizes and Awards	152

CSEM SA

In 2024, we celebrated 40 years of pioneering innovation and technology transfer. We continue to focus on our three research priorities: Digital Technologies, Precision Manufacturing, and Sustainable Energy. They are essential to environmental, economic, and social well-being. By fostering collaboration and knowledge exchange within the scientific community, CSEM plays a vital role in advancing renewable energy, healthcare innovations, digitalization of manufacturing, precision engineering, and sustainable practices.

CSEM's **Digital Technologies** program centers on ultra-low-power (ULP) ASICs, data-driven solutions, and advanced applications in healthcare and industry. Recognized as a leader in ULP ASIC design, CSEM crafts custom hardware that significantly reduces power consumption while delivering real-time insights with minimal latency. The program integrates software and hardware to transform digital data into actionable insights, supporting sectors such as IoT, aerospace, and energy. In digital health, CSEM develops ISO-13485 certified solutions that enhance patient monitoring and drive behavioral changes. The Industry 4.0 focus area optimizes manufacturing processes through predictive analytics and automation. Additionally, CSEM's IoT and vision systems provide secure, intelligent platforms for real-time data collection. Finally, the program explores quantum technologies, revolutionizing measurement capabilities across various fields. Together, these initiatives position CSEM as a key player in shaping a sustainable and connected future.

CSEM's **Precision Manufacturing** program is committed to advancing innovative manufacturing solutions across various sectors. This research priority excels in Additive Manufacturing (AM), enabling the creation of highly precise and customizable 3D components through hybrid technologies. CSEM also specializes in Functional Surfaces, utilizing nano-structuration and surface modification to enhance the properties of materials for applications in sensing, aerospace, and energy. The MEMS focus area develops cutting-edge microfabrication processes, offering tailored devices and foundry services. Photonics leverages expertise in optics and integrated circuits to revolutionize sectors such as healthcare and communication. Additionally, the program includes Scientific Instruments that provide high-precision solutions for space and terrestrial applications. Finally, Tools for Life Sciences bridge engineering and biology, creating impactful solutions for personalized medicine and diagnostics. Together, these initiatives position CSEM as a leader in precision manufacturing, driving technological advancements for a sustainable future.

CSEM's **Sustainable Energy** program focuses on advancing renewable energy technologies and promoting sustainable practices to address global energy challenges. With a focus on integrating innovative solutions, the program emphasizes the development of efficient photovoltaic systems, energy management strategies, and cutting-edge battery technologies. CSEM is committed to enhancing energy efficiency and reducing carbon footprints across various sectors, including transportation, healthcare, and industrial applications. The program also explores the potential of digitalization in energy management, ensuring that renewable sources are effectively utilized. By collaborating with industry partners and leveraging advanced technologies, CSEM is driving the transition to a sustainable energy future, positioning itself as a leader in the field, and contributing to global efforts in combating climate change.

MULTIDISCIPLINARY INTEGRATED PROJECTS—MIPS

Harry Heinzelmann

Multidisciplinary Integrated Projects (MIPs) play a crucial role in advancing CSEM's research initiatives. This program enhances collaboration across our three key research priorities: Precision Manufacturing, Digital Technologies, and Sustainable Energy. Each year, CSEM invests significant resources into these projects, boosting its capacity to create innovative solutions.

MIPs are regularly launched to ensure the program remains dynamic and responsive to emerging market demands. Each initiative focuses on developing high-maturity technology bricks with substantial market potential, typically within a one-year timeframe.

A brief overview of the MIP 2024 program is provided here, and for more detailed insights into the projects, please refer to the subsequent pages.

COSETE – Cooperative Sensors for Electrical Impedance Tomography

The COSETE MIP project develops cooperative sensors for Electrical Impedance Tomography (EIT), enabling long-term cardiopulmonary monitoring and future applications like non-invasive continuous glucose monitoring (NICGM). CSEM's miniature ASIC-based sensors, arranged in a two-wire parallel bus, allow for high integration in wearable devices. A 25-sensor EIT belt prototype is in development to map thoracic impedance, aiding in pulmonary artery pressure (PAP) monitoring. Key challenges include achieving high-resolution imaging while maintaining ultra-low-power low-noise electronics. To mitigate signal interference, an optimized design and a third-wire alternative are explored. A test chip and prototypes are set for early 2025, advancing next-gen medical wearables.

REVISIMO – Contactless Monitoring of Beat-to-beat Heart Rate and Other Vital Parameters via Cameras

The REVISIMO MIP project develops a contactless monitoring solution that uses consumer-grade cameras to extract remote photoplethysmography (rPPG) signals, enabling beat-to-beat heart rate and other vital sign measurements contactless. A deep learning model reconstructs rPPG signals from facial videos, which are processed with CSEM's clinically validated PPG algorithms. A study with 101 volunteers confirmed feasibility under controlled conditions, even with motion. However, rPPG signal quality remains lower than contact-based PPG, affecting accuracy in high-motion scenarios. Future work will focus on real-world validation, adapting the system for smartphone or webcam use, and expanding to cardiac arrhythmia monitoring and telemedicine applications.

ORCA2 – Organoid Dissociation for Single Cell Analysis

The ORCA2 MIP project enhances single-cell analysis by developing efficient organoid dissociation technologies with minimal cell loss and seamless integration into microfluidic-based single-cell analysis. The project introduces Smart Labware, combining mechanical and enzymatic dissociation to ensure high cell recovery and viability in a user-independent, standardized process. A low-dead-volume microfluidic interface enables precise single-cell encapsulation in droplets for

downstream analysis. Additionally, a portable fluorescence reader facilitates single-cell quantification and sorting. ORCA2's innovations improve reliability and scalability in organoid-based drug discovery, disease modeling, and personalized medicine, supporting the growing adoption of organoid models in the pharmaceutical industry.

FLORES – Frog Escapement: Design Update

The FLORES MIP project advances mechanical watchmaking by refining the frog escapement, a FlexMEMS-based innovation designed for high-precision chronometry (1s/day). As a pioneer in silicon microfabrication CSEM leverages frictionless flexure blades to eliminate lubrication and wear, ensuring long-term reliability. Initial prototypes confirmed the escapement's functionality but revealed insufficient amplitude for optimal performance. To address this, CSEM optimized the escapement layout to reduce frictional resting phases and improved component positioning to enhance energy transmission efficiency. The redesigned components are currently in production, with validation pending. If successful, this innovation will offer watchmakers a high-performance escapement that merges traditional craftsmanship with cutting-edge microfabrication.

PRECIZE2 – Predictive Quality Towards Zero-defect Manufacturing in 3D printing

The PRECIZE2 MIP project enhances additive manufacturing quality control by integrating in-situ process monitoring with machine learning (ML) for laser powder bed fusion. Using optical thermotomography (OT) and melt pool monitoring (MPM), the tool identifies defects and deviations in real time, reducing reliance on costly post-production testing. The project developed an ML model trained on channel clogging detection and fatigue blade defects, correlating OT data with physical compliance. A user applet was created for fast OT and MPM data processing. Future developments aim to expand thermographic resolution, improving 2D spatial defect detection, advancing zero-defect manufacturing, and optimizing industrial 3D printing reliability.

LEVIATAN – Leveraging Open-source AI for Embedded Software Development

The LEVIATAN MIP project develops a large language model (LLM) agentic solution for embedded software development, ensuring privacy through self-hosted, open-source models. It introduces EmbeddedEval, a benchmark dataset for embedded code challenges, and an automated pipeline for generating, compiling, testing, and refining embedded firmware. Using retrieval-augmented generation (RAG), the system extracts relevant datasheet information to enhance code accuracy and efficiency. The project also benchmarks its performance against existing solutions using a Pass@k-inspired scoring system. By integrating autonomous agents that iterate on code, LEVIATAN improves developer productivity, code reliability, and resource efficiency, paving the way for AI-driven embedded software development in secure environments.

ENFRED – Life Cycle Analysis for Green and Sustainable Electronics: An Extended Model for IoT

The MIP project extends Life Cycle Assessment (LCA) methodologies to evaluate the environmental impact of IoT devices, guiding the transition toward sustainable electronics. CSEM adapted and improved the Pirson model, analyzing commercial products and an in-house smart biologic test strip to assess carbon footprints. Results highlighted the dominance of IC chips and PCBs in emissions and demonstrated the potential for footprint reduction in CSEM's test strip. The methodology was extended to include use and end-of-life phases, enabling informed sustainability decisions. The project produced a user-friendly LCA model, helping industry partners identify feasible, low-impact alternatives to support the ecodesign of greener IoT devices.

SUMON2 – Hybrid sustainable bio-monitoring test strips with dedicated ultra-low-power ICs

The MIP project advances sustainable bio-monitoring test strips by integrating printed sensors, NFC coils, and ultra-low-power ICs onto a single substrate. This approach enables self-contained, disposable sensors that provide quantitative results without bulky external readers. Using screen-printed enzymatic glucose sensors, an NFC coil for wireless power and data transmission, and a commercial off-the-shelf analog front-end IC, the demonstrator validates the feasibility of fully disposable printed electronics. Successful aerosol-jet printed interconnects confirm compatibility with miniaturized ICs, paving the way for future multi-analyte sensing with custom ASICs.

BEAST – Embedded Medical Secure Platform: Securing Data from the SoC up to the Cloud

The BEAST MIP project develops an end-to-end secure communication platform for medical IoT devices, ensuring confidentiality and integrity from sensor nodes to the cloud. Based on the Nordic nRF5340 chip, it implements a custom transport layer over BLE and a security protocol with mutual authentication, using cryptographic verification and Public Key Infrastructure (PKI). BEAST eliminates the need for cumbersome BLE pairing and protects medical data exchanges from unauthorized access. A proof-of-concept demonstrator successfully validated secure transmission of heart rate data using Zephyr RTOS and Trusted-Firmware-M. This scalable solution enhances secure medical data acquisition, transmission, and processing, supporting future privacy-focused healthcare applications.

COSETE – Cooperative Sensors for Electrical Impedance Tomography

A. Fivaz, B. Sporrer, O. Chételat, D. Besse

CSEM's cooperative sensors (CS) are designed to equip medical devices for long-term patient monitoring and everyday use. They are miniature sensors capable of electrographic imaging and electrical impedance tomography (EIT). Arranged in a two-wire parallel bus configuration, they achieve an outstanding level of integration in wearables requiring multiple electrodes. The present article reports the ongoing implementation of the bioimpedance electronics front-end which, in conjunction with biopotential measurement developed in previous activities, should enable regional cardiopulmonary function using EIT such as the pulmonary artery pressure (PAP), a method patented by CSEM. In the future the device will be extended to provide electrical impedance spectroscopy (EIS), a feature that is required for non-invasive continuous glucose monitoring (NiCGM) which is an upcoming methodology already patented by CSEM.

Monitoring PAP or NiCGM requires EIT imaging with multiple sensors, and the belt prototype shown in Figure 1, currently under development, provides for this purpose 25 sensors placed around the thorax.

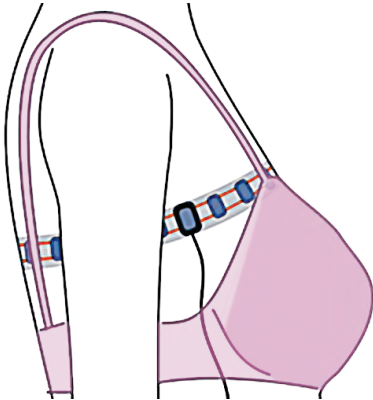


Figure 1: EIT belt prototype in development.

The sensors are composed of an application-specific integrated circuit (ASIC) with just a few surrounding components and a housing. They will look like the cooperative sensor for biopotential measurement developed previously and shown in Figure 2. The ASIC is packaged in a prototyping case and currently requires a size of $7 \times 7 \text{ mm}^2$. Further size optimizations are possible.



Figure 2: Sensor board prototype for biopotentials (similar formfactor for EIT sensor in development).

The measurement of impedance is achieved by multiple sensors working in tandem. Two sensors inject alternating currents i with equal amplitude, but opposite phase, into the body. The resulting voltages are then measured by all other sensors providing enough information to compute an EIT image, i.e., an impedance map of a cross-section of the thorax. The technical challenge is to resolve the resistance on the injection path within $\rho = 5 \text{ m}\Omega$ (rms) in a 2 Hz bandwidth. From the following equation, where N is the number of stimulation patterns and ν the electronic noise of the acquisition chain:

$$\rho = 2\sqrt{N} \frac{\nu}{i}$$

the only ways to reduce ρ without relying only on the reduction of the noise ν of the acquisition chain are to limit the number of patterns N , which in turn reduces the resolution of the imaging, and to use the highest possible injection current i , which is however limited by the voltage range provided by the current source i and the dry electrode/skin impedance. With a value of $i = 100 \mu\text{A}$ (rms), a target specification of $\rho = 5 \text{ m}\Omega$ (rms) and $N = 25$ patterns, as a typical example, this requires a noise floor for the acquisition chain of only $\nu = 50 \frac{\text{nV}}{\sqrt{\text{Hz}}}$ (comparable to the noise floor of a single $100 \text{ k}\Omega$ resistor). This is a challenging noise specification for ultra-low power microelectronics. Moreover, the stringent noise limit also applies to any distortion and perturbation picked up by the circuit, e.g., through coupling from other blocks within the ASIC.

Since each sensor has a single electrode, the electrode potential acquisition is obtained against a reference voltage. In a 2-wire CS system the only available reference is the system ground wire (see Figure 3), which also serves as the return path for all powering and signals currents, for all sensors in the system. Over the finite impedance of the bus this leads to the occurrence of interference signals. In this work, the design is optimized to maximize the rejection of out-of-band perturbations by providing strong filtering before any chopping or sampling operation is conducted. In scenarios where this is not expected to lead to sufficient suppression (e.g., when powering frequency and EIT signal frequency are too close to each other) an alternative approach is obtained with the same ASIC but with one additional wire (in blue in Figure 3) so the current return and potential reference functions are implemented by two separate wires. This mitigation measure avoids the possibility of wire crosstalk in the system.

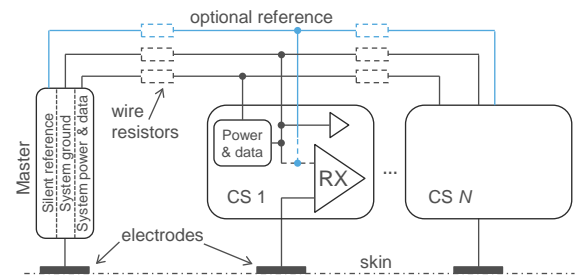


Figure 3: CS implementation showing the optional use of a third wire (in blue) to mitigate the risk of crosstalk.

A test chip will be produced in early 2025 and belt prototypes will be manufactured and tested later in the year.

REVISIMO – Contactless Monitoring of Beat-to-beat Heart Rate and other Vital Parameters via Cameras

F. Braun, G. Bonnier, C. Aguet, J. Van Zaen, M. Dia, R. Vuagniaux, P. Stadelmann, C. Gimkiewicz, M. Frosio, V. Springmann, S. Saeedi, N. Maamari, D. Ferrario, M. Lemay

With the advent of smartwatches and other wearables, the continuous optical monitoring of vital signs using photoplethysmography (PPG) has become broadly available. At CSEM, we have developed an advanced solution that adapts this capability to consumer grade cameras, removing the need for dedicated wearable devices. Our approach integrates a specialized deep learning model to extract remote PPG (rPPG) signals from camera videos. These rPPG signals are then processed with CSEM's clinically validated PPG algorithms for the continuous estimation of various vital signs. We successfully showed the feasibility for remotely monitoring beat-to-beat heart rate via cameras under controlled conditions, including scenarios with motion. If validated in real-life settings and specific patient populations, this solution has the potential to enable convenient and widespread telemonitoring through commonly available cameras, increasing accessibility for personal health monitoring.

Contactless monitoring of vital signs via cameras has been studied for several years^[1], with much of the focus on monitoring the breathing rate and heart rate, as these parameters are the easiest to measure reliably in a contactless manner. Consequently, most medically certified solutions available on the market are limited to monitoring heart rate and breathing rate.

The aim of the present work was to investigate the potential of expanding the contactless monitoring via cameras by reconstructing the remote photoplethysmography (rPPG) signals and evaluating their feasibility for more advanced measurements, such as beat-to-beat heart rate estimation.

A total of 101 volunteers participated in a protocol that involved simultaneous acquisition of facial videos and biosignals, including ECG and upper arm PPG. During the protocol, the participants were exposed to controlled artificial illumination and underwent different short (2-3 minutes) controlled scenarios in standing and sitting positions (including orchestrated breathing, head movements and leg extension) as well as a 10-minute free working scenario sitting in front of a computer and performing usual office work. This study was approved by the local ethics committee (CER-VD Project-ID 2023-00324).

A pretrained YOLO-based deep learning algorithm was used to detect and extract the faces from the video data along with some facial landmarks needed for motion tracking. A spatiotemporal autoencoder-based 3D convolutional neural network (CNN) was then trained on the preprocessed and windowed facial videos. The 3D CNN is designed to predict the rPPG from a given sequence of frames by leveraging both spatial and temporal information simultaneously.

Out of the 101 subjects, 10 had to be rejected due to technical issues. The remaining 91 subjects were separated in 86 for model training and 5 for testing.

The resulting rPPG signals were then processed with CSEM's algorithms for optical monitoring, which were originally developed for contact-based PPG and have been extensively validated in previous studies^[2]. To evaluate the beat-to-beat heart rate measurement, reference heartbeats were extracted from the ECG and compared to heartbeats from both contact-based PPG and rPPG. Beat-to-beat detection performance was evaluated by classifying the number of correctly detected heartbeats (F1 score) and the mean absolute error (MAE) of subsequent heartbeats, i.e., the inter-beat-intervals.

Table 1 shows the heartbeat detection performance comparing contact-based PPG to contactless rPPG for different scenarios. Even for scenarios with high motion ("Head Movements") most of the heartbeats are correctly detected (i.e., high F1 score). However, the higher the motion, the higher the error (MAE) for the contactless rPPG approach. Even for very controlled scenarios with low motion ("Breathing") the MAE of rPPG remains more than three times higher than for PPG. This can be explained by rPPG signals showing lower signal quality (both in terms of signal-to-noise ratio as well as frequency content) than contact-based PPG signals.

Table 1: Heartbeat detection performance for remote (rPPG) and contact-based PPG (PPG) as median [1st and 3rd quartiles].

	Scenario	F1 Score (%)	MAE (ms)
rPPG	Breathing	99.4 [99.2, 99.6]	15.7 [12.8, 20.8]
	Leg Extension	99.7 [99.6, 99.8]	14.7 [12.6, 16.7]
	Head Movements	98.8 [95.9, 99.6]	25.0 [19.1, 38.7]
	Free Working	99.3 [99.2, 99.4]	27.9 [24.9, 30.7]
PPG	Breathing	99.5 [99.3, 99.6]	4.1 [3.3, 6.6]
	Leg Extension	99.8 [99.7, 99.8]	4.0 [2.6, 5.3]
	Head Movements	99.5 [97.0, 99.6]	3.6 [3.3, 17.4]
	Free Working	99.7 [99.5, 99.8]	5.8 [5.3, 7.1]

Nevertheless, the current performance remains promising for estimating vital parameters beyond beat-to-beat heart rate such as breathing rate, heart rate variability or the detection of cardiac arrhythmia^[2]. Estimating blood pressure from rPPG remains particularly challenging and requires further investigation and adaptation to improve accuracy and reliability.

This approach shows significant potential but is currently limited in two areas. First, the recordings were performed in a very controlled environment and future work should explore more challenging scenarios, such as varying illumination and recordings via smartphones or webcams. Second, the study population should be extended to include the target population, such as patients with cardiac arrhythmia, in real-world settings like their home environment for telemonitoring.

In summary, we successfully showed the contactless monitoring of beat-to-beat heart rate via cameras under controlled conditions, including scenarios with motion. Further validation in real-life settings and specific patient populations is required to confirm its broader applicability.

^[1] Wang, W., & Wang, X. (Eds.). (2021). Contactless vital signs monitoring. Academic Press.

^[2] Lemay, M., et al. (2021). Applications of optical cardiovascular monitoring. In Wearable Sensors (pp. 487-517). Academic Press.

ORCA2 – Organoid Dissociation for Single Cell Analysis

C. Bichsel, S. Heub, F. Boudoire, L. Chen, M. Blache, C. Loussert-Fonta, P. Rottmann, P. Cristofolini, J. Zhou, C. Fonta, E. Aeby, C. Obrist, D. Di Stadio, M. Garzuel, P. Odermatt, S. Graf, F. Kurth, G. Weder

As organoid and microtissue models gain importance in drug development, the need for precise single cell analysis becomes crucial. ORCA2 aims to enhance single cell data quality by developing modules for organoid dissociation with minimal cell loss and seamless integration to single cell analysis tools. The technologies developed in ORCA2 can be integrated in any organoid analysis workflow, from drug testing to disease modeling.

Organoid models recapitulate some of the organ complexity and are increasingly used in drug screening, disease modeling, regenerative medicine and tissue banking. The FDA modernization act 2.0 in 2022^[1] has accelerated this development in the pharma sector, as organoid model systems are now allowed in the drug approval process. Nevertheless, the organoid complexity also brings about challenges, such as sample heterogeneity. Single-cell profiling is a powerful tool for capturing and quantifying cellular heterogeneity. However, current methods for dissociating individual organoids and integrating single-cell analysis still lack efficiency. The objective of ORCA2 project is to develop a comprehensive workflow from single organoid dissociation to single cell analysis, coupled with single cell analysis, while ensuring minimal cell loss (Figure 1).

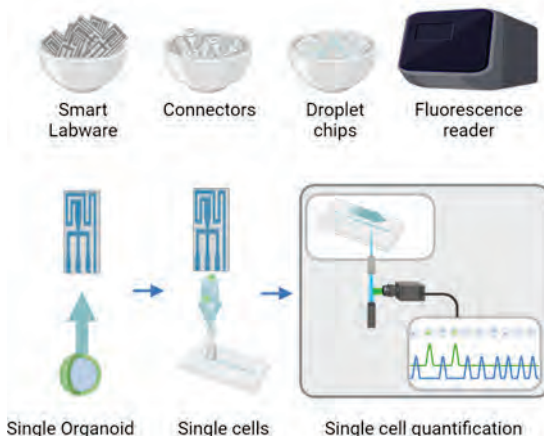


Figure 1: Illustration of the ORCA2 technologies (top row) and proposed workflow (lower row).

A smart labware for organoid dissociation technology addresses the unmet need for efficient single-organoid dissociation with high cell recovery. It combines mechanical forces and enzymatic action in a unique format for the efficient dissociation of small to medium organoids (100 to 500 µm), typically collected from a 96-well culture plate (< 300 µl per sample). Compared to manual, non-standardized dissociation by multiple manual pipette mixing and centrifugation steps, the Smart labware aims for a simple, one-step user-independent process, leading to high cell recovery and viability (Figure 2). The Smart labware can be actuated using an existing laboratory equipment. The final sample format and quality are compatible with downstream single-cell analysis, particularly single-cell encapsulation.

After dissociating the organoid with the smart labware, the resulting single cells must be encapsulated in a microfluidic chip for analysis. To address this, a custom pressurizable low-dead-volume interface between the Smart labware and chip was developed (Figure 2). This is achieved using droplet generator microfluidic chips, where water droplets form within a continuous oil phase. To ensure uniform droplet size and ideally one cell per droplet, stable and controlled flow rates at the water and oil inlets are essential. However, conventional large reservoirs are unsuitable for the small sample size resulting from dissociation. The initial design was created via additive manufacturing with a biocompatible polymer, and an adapted version for scalable production via injection-molding is being developed.

A newly developed portable fluorescence reader offers a compact, user-friendly, and cost-effective solution for seamless single-cell analysis. (Figure 2). The basic configuration consists of a blue and green laser, with the option of two more lasers and the respective PMTs for fluorescent signal detection. Commercial and custom-made software allow for fluorescence analysis and quantification on the single cell level. Notably, the fluorescence reader can be adapted to sort single droplets based on their fluorescent characteristics to address specific cells of interest for further downstream processes.

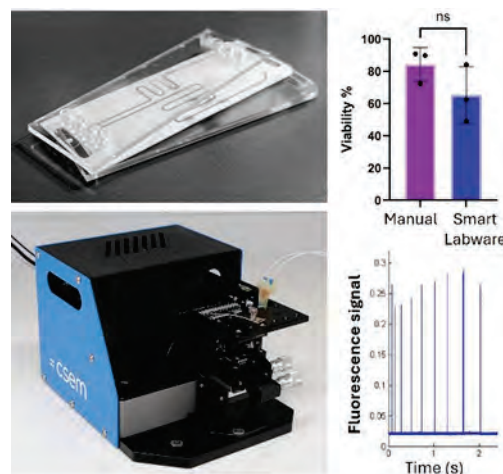


Figure 2: Smart labware prototype and cell viability measurement after dissociation (top); Connector-reservoirs on a microfluidic chip on the fluorescence reader, and fluorescence traces of labeled cells (bottom).

Reliable cell dissociation and single cell analysis with minimal handling and high repeatability are commercially valuable in biotech and pharma. ORCA2 technologies can enhance organoid use in drug discovery, diagnostics, and personalized medicine, boosting the value of organoid models.

[1] S.5002 - 117th Congress (2021-2022): FDA Modernization Act 2.0 | Congress.gov | Library of Congress

FLORES – Frog Escapement: Design Update

F. Barrot, G. Musy, O. Laesser •, Y. Petremand, R. Winiger •, L. Giriens, E. Dominé

Leveraging its combined expertise in micro-fabrication techniques and in the design of precision mechanisms guided by flexure blades in lieu of classical bearings, a frictionless guiding approach requiring no lubrication, CSEM has been a pioneer in proposing to the Watch Industry the so called "FlexMEMS approach" for the design and production of novel high-end oscillators and escapements. This year, CSEM presents a design update of the Frog Escapement to cope with the low amplitude observed on the first prototypes.

In an era where digitization and microelectronics are permeating our daily lives, altering our habits and the objects we use, traditional watchmaking continues to stand out. This sector successfully resists this wave of modernization by maintaining its expertise in very small-scale and high-precision mechanics. Watchmakers perpetuate ancestral techniques while integrating innovations, proving that traditional craftsmanship can coexist with modern technological advancements.

For over 20 years, silicon has been used in watchmaking for the manufacture of extremely precise micromechanical parts. Thanks to the precision of etching offered by the DRIE (Deep Reactive Ion Etching) process, it is possible to produce various types of delicate components such as balance springs, escape wheels, and silicon anchors. This approach allows for the mass production of parts with micrometric precision.

CSEM has played a crucial role in the introduction of silicon in mechanical watchmaking^[1] and continues to conduct research in this field. The goal is to enable the design and production of watch mechanisms that would be impossible to achieve at the scale of a watch without the combined use of the DRIE process and silicon.



Figure 1: The frog escapement (paired with a CR3 oscillator).

For several years, CSEM has designed, produced, and tested various watch escapements and oscillators based on the combined use of silicon and flexible guides^{[2][3][4]}. These flexible guides, used by CSEM for decades in the design of highly precise mechanisms in the space and astrophysics industries, are an ingenious combination of flexible blades arranged to work together to precisely guide a movement throughout their deflection.

The absence of friction, unlike conventional guides (pivots or bearings), eliminates the need for oils and greases, ensuring

movement without wear. This feature, combined with the absence of plastic deformation and mechanical hysteresis inherent to silicon, allows for alternating movements with highly reliable and repeatable behavior over time. These advancements pave the way for innovative watch mechanisms that combine precision and durability without the drawbacks of traditional guiding systems.

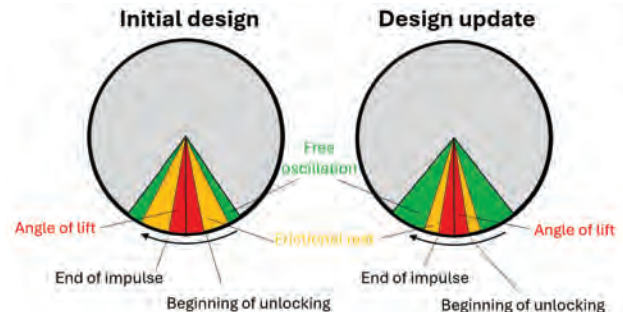


Figure 2: Design update of the frog escapement.

The latest escapement proposed by CSEM, named the "frog escapement"^[5] due to the shape of its anchor, aims for very high chronometric precision (1s/day). The initial prototypes demonstrated that the concept was functional, but the amplitudes achieved, for a given power and torque range, were not sufficient to meet the targeted performance. Additional tests were conducted to better characterize the existing prototypes and identify the causes of the observed lack of amplitude.

Two improvement paths were identified, leading to a detailed redesign of the escapement. The escapement layout was optimized by reducing the frictional resting phase, as illustrated in Figure 2. Furthermore, special care was taken in the design of the components to ensure precise positioning between the anchor, the escape wheel, and the balance wheel. It was found that, in addition to modifying the layout, minimizing the errors in the center distance and reference points was crucial to ensure good operating amplitudes.

The designed components are currently in production at the time of writing this article. Therefore, the redesign of the frog escapement has not yet been experimentally validated, but if the established model is realistic, the results should meet our expectations. This would allow us to offer watchmakers a novel innovation aimed at high performance, combining tradition and advanced technology.

• External key contributors: "Olivier Laesser" and "Winiger Horloger".

^[1] A. Perret, Le silicium comme matériau dans la fabrication de pièces mécaniques, SSC, 2001.

^[2] F. Barrot, *et al.*, Flexure based oscillators for mechanical watches, *CSEM Scientific and Technical Report* (2018), 19

^[3] G. Musy, *et al.*, Les technologies de micro-fabrication et de l'aérospatiale au service de l'innovation horlogère, SSC 2021.

^[4] F. Barrot, *et al.*, A novel Constant Force Escapement, *CSEM Scientific and Technical Report* (2021), 14.

^[5] F. Barrot, *et al.*, A novel Escapement for FlexMEMS-based watch oscillators, *CSEM Scientific and Technical Report* (2022), 14

PRECIZE2 – Predictive Quality Towards Zero-defect Manufacturing in 3D Printing

E. Poli, J. Montesinos, I. Sideris, B. Platerrier, J. Poccard, F. Crivelli, V. Pejchal

In-situ process monitoring and quality evaluation represents the next vital step in enhancing reliability of additive manufacturing processes. PRECIZE2 focusses on developing a defect and non-compliance detection tool for laser powder bed fusion (LPBF) additive manufacturing, utilizing optical thermotomography and machine learning.

Additive manufacturing enables the rapid prototyping and manufacturing of complex parts, reducing material needs and design iterations. However, part compliance and quality are more difficult to control, and the resulting defects can reduce the life and function of the manufactured parts. Non-destructive testing provides a costly solution to quality control and is conducted once the part is already printed. To reduce manufacturing and quality control time, in-situ monitoring sensors are integrated in laser powder bed fusion machines.

The monitoring of each additive manufactured part layer generates a vast amount of data, that requires time consuming processing. Therefore, it is of interest to use automated analysis to evaluate defects and process deviation when monitoring prints. Optical Tomography (OT) is based on using a sCMOS-based camera to measure the light emitted from the hot laser interaction zone in a layer-by-layer fashion. Additionally, Melt Pool Monitoring (MPM) is performed using a photodiode measuring light emissions from the melt pool and geometrical information of the laser position is obtained for each layer of the process.

The geometrical information is used for the determination of the area of interest (i.e. part or feature within a part), and thermographic OT information is then extracted from this area. Physical part compliance is verified and compared with the extracted OT signals, to train a machine learning (ML) model in evaluating the compliance and acceptable signal deviation from nominal parts. To this effect, 2 types of parts have been used: channels and fatigue blades.

Squares with channels of different diameters were printed, to detect the clogging of channels and train the model to automatically identify a clogged channel. This application is of special interest for channels in complex features within parts that are difficult to access. Figure 1 shows the algorithm at work, with detected channels labelled red for unclogged and blue for clogged, using the OT data to compare the contrast in intensity between the channel and the part. The intensity is taken from the green line in the X-Y plane.

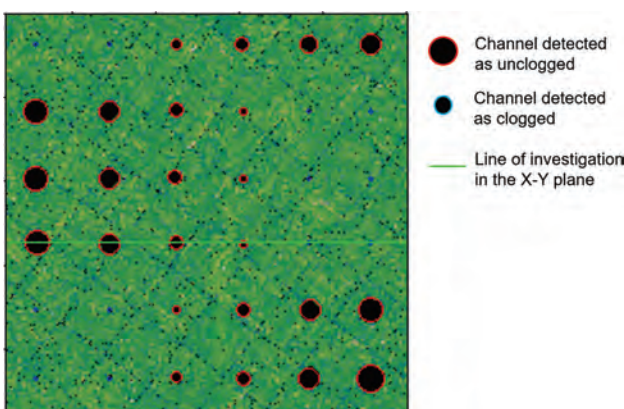


Figure 1: LPBF process MPM XY cross-section and channels detection. Green line represents Z cross-section shown in Figure 2.

The results of extracting the intensity along the line of investigation are plotted per layer (Figure 2-left) and on average for all layers (Figure 2-right). The resulting image and data provide an insight into the clogging of channels. The dip in intensity corresponds to location of the channels - however, to determine whether they are clogged, a threshold is necessary - as partially clogged channels will also display a dip in intensity. To set this threshold and train the ML algorithm, physical inspection is conducted, and results are reported for the correction. A user applet was developed to improve fast processing of OT and MPM images and intensity extraction over a 1D line on the x-y axis for all layers.

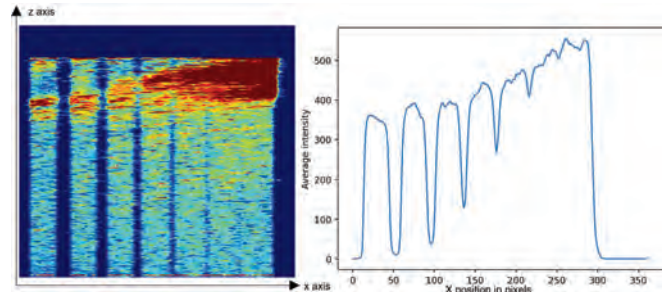


Figure 2: (left) LPBF OT intensity map Z cross-section with detected channels. (right) Aggregate OT intensity along the X-axis.

The second type of parts, the lattice fatigue blades, have been printed with and without defects to study the impact of defects on fatigue life and correlate it with OT data. The blades were subjected to bending at 10 Hz, 66 MPa to failure or max. 120 000 cycles.

The defects were generated by damaging the recoater, spattering, poor powder compaction, and inclusion of holes in the CAD file. All defects reduced fatigue life significantly, even when, upon visual inspection, the blades appeared nominal. The OT and MPM signals were extracted and the information along all layers was extracted for a 1D line (Figure 3).

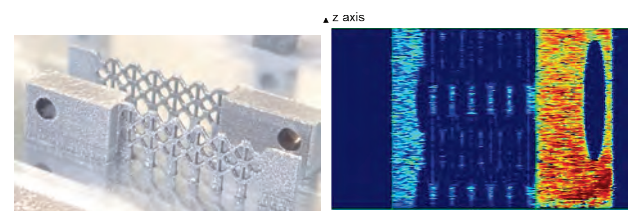


Figure 3: Lattice blades and OT results in Z axis.

For non-nominal parts to appear nominal, defects must remain of limited size, which greatly impedes on their detection. Future work will therefore focus on extending the spatially resolved thermotomography capabilities, by narrowing further the area of interest, and extending the signal to a 2D area on the x-y plane of the buildplate, rather than a 1D line for all layers.

LEVIATAN – Leveraging Open-source AI for Embedded Software Development

C. Aguet, R. Berguerand, J. Beysens, D. Hoover, J. Lahera Perez, R. Safai-Naeeni, A. Rubio

This project aims to implement a large language model (LLM) agentic solution tailored for embedded code development. By utilizing open-source, self-hosted models, it ensures the use of confidential data without privacy concerns. Additionally, an automatic pipeline has been developed to facilitate the computation of metrics, assessing the performance of the solution and enabling its benchmarking with other solutions on the market. Ultimately, this project improves embedded software development engineers' productivity by focusing their effort on the most meaningful tasks.

Dedicated models and tools, such as GitHub Copilot^[1] or Codestral^[2], have already been developed for large language model (LLM) code generation. However, these tools are primarily designed for high-level programming and may not meet the specific challenges of embedded programming, including hardware dependencies, low-power consumption, and low-memory footprint. This project addresses this aspect by implementing an agentic solution on top of existing LLMs to enhance embedded software generation. By integrating autonomous agents, the solution enables to independently perform tasks, make decisions, take actions, and interact with their environment without constant human intervention. Similar to HumanEval, a benchmark dataset for assessing LLMs coding skills, the first phase of this project aimed to create a comparable dataset of embedded software challenges, named EmbeddedEval. These challenges involved writing drivers (e.g., UART, Timer, GPIO) typically found in microcontrollers and specifically targeted two families of microprocessors frequently used at CSEM: Nordic nRF52 and STM32. An autonomous pipeline was then created to automate code development tasks. It processes challenge descriptions, which include function definitions specifying input parameters and intended functionality. The prompt is enhanced with common information, such as format, coding language (C, C++), and platform requirements.

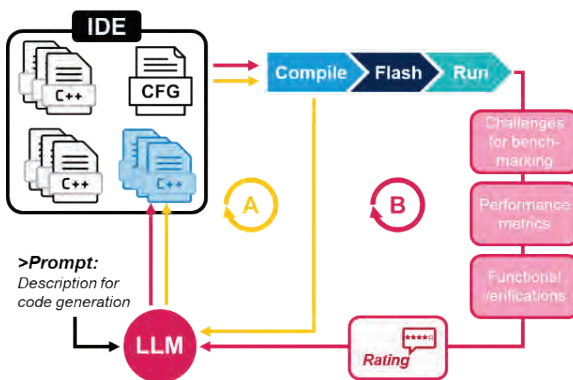


Figure 1: Automated pipeline.

To generate structured data from LLM outputs, the Pydantic^[3] library is utilized. This allows relevant data retrieval (such as the code or the number of errors) to be directly used in subsequent steps of the pipeline without the need for manual parsing. After generating the code, it is inserted into a template project for compilation. If compilation fails, the LLM parses the output to list the errors and suggest corrections; then attempts to fix them. This process is repeated until the code compiles successfully or a defined threshold is reached, marking the pipeline as failed.

[1] GitHub Copilot: <https://github.com/features/copilot>

[2] Codestral: <https://mistral.ai/fr/news/codestral/>

[3] Pydantic: <https://docs.pydantic.dev/latest/>

[4] Unstructured.io: <https://unstructured.io/>

If the firmware is successfully generated, it is automatically flashed onto a test board. Dedicated unit tests verify the code for correctness, with results retrieved via a serial interface. If tests fail, the output is used to regenerate the code. To enhance code generation, retrieval-augmented generation (RAG) is employed. In the first phase, semi-structured data (such as PDFs) are parsed to extract and separate the text and tables present in the documents. An LLM is then used to generate summaries for each part, facilitating better indexing and retrieval process. These summaries are processed to generate embeddings, which are stored in a database. During the pipeline's code generation phase, the RAG vector base is queried to retrieve relevant information from datasheets, which is then added to the prompt.

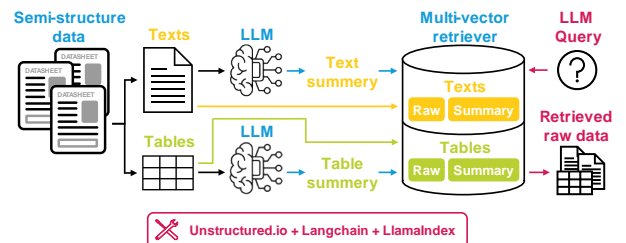


Figure 2: Retrieval-augmented generation (RAG) workflow^{[4] [5]}.

To ensure privacy when using confidential data, LLMs are hosted on a local server, preventing external companies from accessing queries. The Ollama^[6] tool is used on this server to host open-source models. As a final step of this still ongoing project, the agentic solution will be benchmarked against existing solutions. A scoring formula inspired by Pass@k^[7] was designed, considering the number of iterations needed by the agent and the quality of the generated code in terms of runtime latency and memory consumption.

In conclusion, LEVIATAN has laid the groundwork for advancing embedded code generation by leveraging the capabilities of LLMs. This development enabled the creation of the EmbeddedEval dataset, an evaluation framework designed to benchmark embedded code generation solutions through specific challenges. We have developed an agent capable of iterating and refining its own code outputs, utilizing a combination of tools and RAG modules, supported by relevant datasheets. The pipeline covers the full process, from code generation to compilation, flashing, testing, and rating of final outputs. Looking ahead, we envision further enhancements in the agent's autonomy, and we see opportunities for a more seamless deployment of these solutions in a hosted environment.

[5] Langchain: <https://www.langchain.com/>

[6] Ollama: <https://ollama.com/>

[7] M. Chen, et al., arXiv preprint arXiv:2107.03374 (2021).

ENFRED – Life Cycle Analysis for Green and Sustainable Electronics: An Extended Model for IoT

C. Hennemann, A. Barrou, I. Marozau, C. Rupf, M. Monroe, P. Nussbaum, C. Ballif

Increasingly stringent regulations drive the demand of key technologies for sustainable electronics. The Life Cycle Assessment (LCA) model allows for the evaluation of the environmental impact of manufactured goods, including electronic components and devices. CSEM uses this model to assess alternative architectures, manufacturing processes, and materials towards more sustainable electronics.

Beyond the inherent social and environmental benefits, proactively adopting sustainable solutions in an increasingly regulated landscape offers a strategic advantage to the industry. Notably, the transition to sustainable products is now central to the strategies of most CSEM customers. Key partners are already collaborating with CSEM to explore alternative solutions that reduce the environmental footprint of their products. However, identifying suitable technological alternatives can be challenging and often requires expertise beyond that of individual market players.

In this context, CSEM aims to stand at the forefront of agile and tailored Life Cycle Assessment (LCA) studies. Prior to this project, the approach has already been successfully applied to photovoltaics (PV) [1] and Printed Circuit Boards (PCBs). Also, within the EU project i-EDGE, the LCA methodology was successfully applied to MEMS silicon switches for memory and computing applications, as well as packaged components and demonstrator systems based on these nano-switches.

The developed LCA model for green electronics is an adaptation and extension of the Pirson [2] model, specifically tailored to assess the carbon footprint of Internet of Things (IoT) devices. This improved model incorporates additional parameters and methodologies to better evaluate the environmental impacts and sustainability of IoT technologies throughout their entire lifecycle (from production to end-of-life).

First, two representative products and a third smart connected biologic test strip (in-house development) were chosen (Figure 1) and evaluated using the Pirson model (Figure 2).



Figure 1: Commercial products (top) and CSEM test strip (bottom).

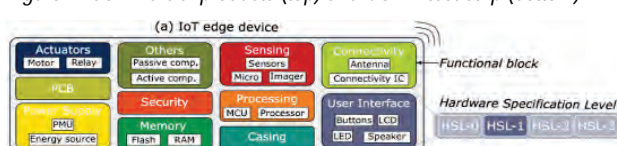


Figure 2: Pirson IoT edge device functional blocks.

[1] A. Barrou, Life Cycle Analysis of Heterojunction Solar Cells - From Raw Materials to Final Devices, MsC thesis, EPFL (2022)

Both commercial products were dismantled to get the precise size and weight of all components. Then Pirson methodology was applied with correcting factors, leading to a precise estimation of the carbon footprint of each device. The results (Figure 3) show the dominance of the processing (IC chips) and Printed Circuit Board (PCBs). Furthermore, it demonstrated the potential of carbon footprint reduction of CSEM test strip compared to commercially available tests.

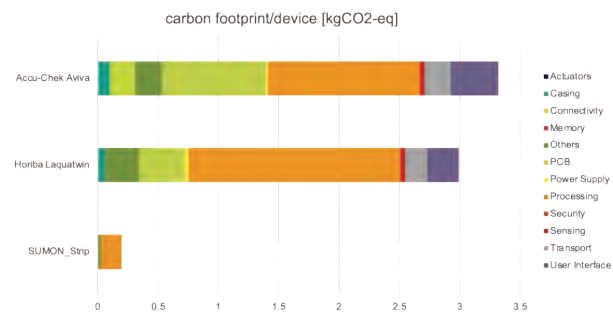


Figure 3: Carbon footprint of selected IoT devices using adapted Pirson methodology.

In a second time, the Pirson methodology was extended to include the use and end-of-life phases of IoT devices. Different use case scenarios were developed to match the diversity potential applications. Up-to-date data were collected from both the literature and use case owners, covering resources inputs, energy consumption, lifetime and end-of-life strategies (disposal, burning, recycling). This step was essential to produce reliable results and make informed decisions about the product's sustainability.

Finally, recommendations for viable alternative materials and processing methods were proposed. These alternatives were then incorporated into the LCA model to assess their potential benefits across the entire product life. Thanks to CSEM's understanding of the technologies being analyzed and industrial connections, the technological feasibility (TRL) and performance of each option were evaluated.

Overall, combining CSEM's pre-existing LCA and electronics expertise lead to the development of a user-friendly LCA model to assess the carbon footprint of IoT devices as well as potential mitigation alternatives. By identifying the TRL, performance, and environmental impact of alternatives, this model can be used to guide the ecodesign of new IoT edge devices and promote greener electronics.

[2] T. Pirson, Environmental perspectives and limits for the Internet of Things in the Anthropocene: going beyond systematic Life-Cycle Assessment, PhD Thesis, UCLouvain (2023)

SUMON2 – Hybrid Sustainable Bio-monitoring Test Strips with Dedicated Ultra-low-power ICs

M. Monroe, J. Disser, G. Bouilly, A. Sukumaran, A. Zandara, C. Hennemann, P. Nussbaum

Multiple functional sub-components were integrated onto a single sustainable substrate, including printed sensors and coils, and a dedicated CoS AFE for electro-chemical sensing. This demonstrator is a major milestone towards sustainable devices made of printed electronics and integrated ICs, to allow for multi-analyte sensing.

Monitoring of biochemical analytes is a growing trend for which many products are already on the market: disease detection, food pathogens detection, body fluids monitoring for sport or health, etc. Most of these sensors are and will remain short-lived and involve coupling a disposable sensor to a costly and bulky reader device performing the analysis. CSEM addresses this by integrating the sensor management and connectivity on the same miniaturized, expandable, and sustainable sensor substrate. Instead of addressing multiple pieces of miniaturized equipment, the user would just have to take another same test strip from the bottle and dispose of it after use. This scenario applies for sensing in biofluids (e.g.: saliva, urine, perfusion bags), where the device is activated at the start of use and discarded after operations.

The disposable sensor and reusable reader combination is an attractive business model for many applications (e.g.: chronic diseases, therapy monitoring) but not sustainable for applications that don't require repeated monitoring (e.g.: infectious diseases, pregnancy) or in extreme remote conditions. For such cases, the opportunity of offering disposable sensors providing quantitative results would be a game changer. After the success of SUMON2's building block demonstrator, the next step towards this goal is to integrate the various components needed for the test strip onto a single substrate using printed electronics technologies and sustainable materials.

The architecture of the proposed test strip is shown in Figure 1. A brief description of each component is given below.

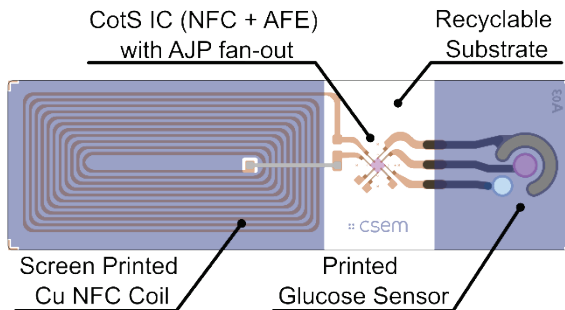


Figure 1: Architecture of SUMON2 prototype showing the integration of printed NFC coil and glucose sensor components with a CoS IC.

Sensor: The miniaturized enzymatic glucose sensors for saliva testing are screen-printed on a polymer film (Figure 2), including custom electrodes. The sensors were prototyped, characterized, and quality controlled by means of calibration curve in artificial saliva and subjected to interferences testing and lifetime storage stability testing.

NFC Coil: The test strip involves an NFC coil tailored to function without the need for an additional tuning capacitor. Test coils were modelled, fabricated, then characterized. The design was

then iteratively adjusted to converge on a coil architecture that was both fabricable with printing technologies and would have suitable resistance and inductance to function at the targeted frequency of 13.56 MHz. Empirical results from coil measurement were found to match well with the model values. Figure 3 shows the realized test coil, with comparison of simulated design and printed device.

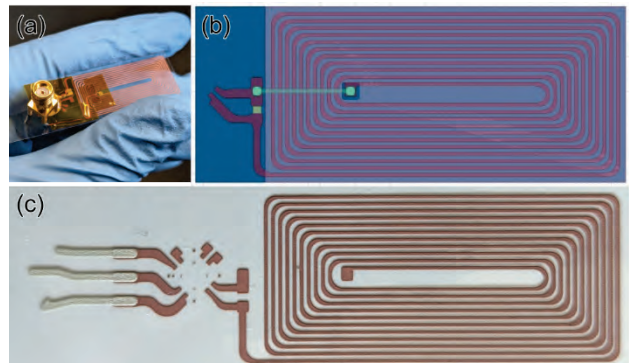


Figure 3: Screen-printed copper NFC coil for the test strip, including (a) as tested, (b) as modelled, and (c) as printed.

System-on-Chip: Ultimately, the test strip will consist in a System on Chip (SoC) containing an analog front-end, a wireless transceiver, a power management unit and a microcontroller. While this multi-analyte SoC is being developed internally, the present iteration utilizes an off-the-shelf solution (SiliconCraft4341), able to measure a single analyte, to allow for investigating the integration of the bare die IC onto the substrate. Feasibility studies have confirmed that this is possible with aerosol-jet printed fanouts, and similar studies are underway for making this connection using flip-chip technologies. Figure 4 shows images of the aerosol-jet printed fanouts connecting the off-the-shelf chip to screen-printed copper interconnects.

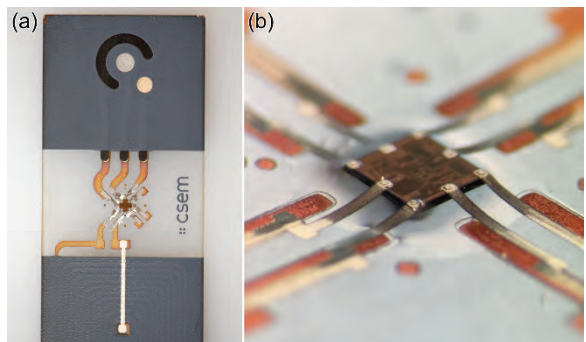


Figure 4: Integration of the SiC4341 IC with a screen-printed copper fanout via aerosol-jet printing, as seen from (a) a top-down view and (b) an oblique angle.

The excellent results and encouraging yield validate the approach and constitute a great milestone towards the objective of fully disposable devices made of printed electronics and electronic components. Following this success, the design will be expanded to include multi-sensing capabilities utilizing the CSEM custom designed ASIC.

BEAST – Embedded Medical Secure Platform: Securing Data from the SoC up to the Cloud

M. I. Ben Salah, D. Vizár, J.-M. Koller, A. Dherse, P. Liechti, J.-N. Pfeuti, D. Hoover, A. Farnier

There's more and more medical IoT devices exchanging personal data with many stakeholders over unsecure networks and storage, which creates security and confidentiality issues. We propose a solution providing easy to use end to end security and confidentiality from the sensor node up to the cloud, based on COTS hardware components.

CSEM developed an end-to-end secure, yet practical and easy to deploy, communication and data exchange platform codenamed *BEAST* based on the Nordic nRF5340 chip, taking advantage of CSEM know-how on security and on PPG (Photoplethysmography) acquisition & processing. This platform suits particularly well the requirements of applications acquiring and exchanging sensitive data, e.g. personal information in medical and healthcare applications

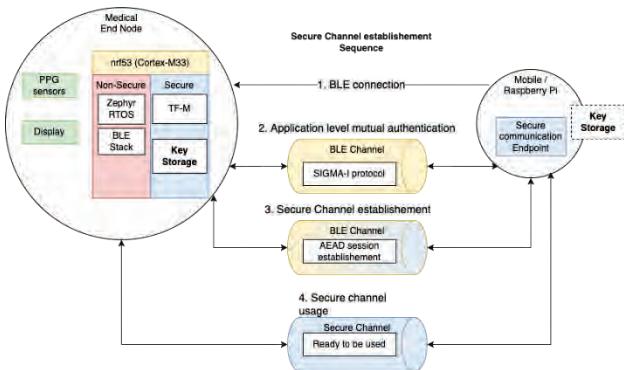


Figure 1: Secure end to end Channel establishment.

BLE wireless communication typically imposes a cumbersome pairing procedure, which is impractical in an application handling sensitive data with a large number of everchanging stakeholders (e.g. patients in a hospital), in particular because of the time it takes to launch and ensure that the BLE pairing code is correct. Security is required at two levels of the application, to ensure the transfer of sensitive data only to a trusted infrastructure (from device to the cloud, through gateways) and to prevent a third-party application could eavesdrop and intercept sensitive data when using mobile applications to retrieve medical data.

The CSEM BEAST secure IoT platform addresses these issues by implementing a custom transport layer over Bluetooth Low Energy (BLE) and a security protocol and key management architecture with their implementation on all stakeholder endpoints, typically made of the End Nodes running Zephyr, with Trusted-Firmware-M (TF-M), and the Gateways running Linux, with Python on a Raspberry Pi 5.

It automatically secures the connection, based on device trust, obtained through cryptographic verification and establishes a secure channel based on SIGMA-R protocol. This guarantees the mutual authentication where both devices ensure that they interact with an authorized device. Furthermore, the Authenticated Encryption Authenticated Decryption (AEAD) session establishment ensures that whatever payload is transmitted is cryptographically validated and authenticated at the decryption. Once the AEAD session is established, the secure channel can be used for transmitting the sensitive payload.

The BEAST transport layer allows to transmit payload over BLE and takes care of framing/splitting of data, retransmission and missing data notification. It also indicates the status either for an

error during the reception or during the security processing. The gateway/infrastructure can also transmit data to the end node, through a 'command' endpoint.

The security architecture is based on a mutual authentication protocol based on a four rounds version of SIGMA-R with a minimal subset of persistent keys and a device certificate, for minimal overhead when it comes to deployment. A successful mutual authentication allows the gateway & the device to communicate securely. The second element of the security architecture is a digital certificate PKI hierarchy, made of a root certificate (CertR), a device certificate (CertEN), a gateway certificate (CertGW) and a cloud certificate (CertCL). These certificates allow each party to identify that they're under the same certificate authority and to trust each other using the beforementioned security protocol.

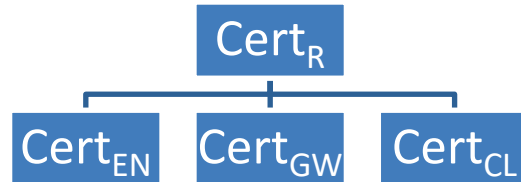


Figure 2: BEAST Public key Infrastructure (PKI) Hierarchy.

A proof-of-concept system demonstrator, based on nRF5340 and a Zephyr compatible PPG library for the medical end node and a Raspberry Pi 5 for the gateway, has been realized and successfully evaluated, demonstrating secure channel establishment and transmission of medical heartrate data in a secure manner and showcasing it through a visualization. The BEAST end node runs the Zephyr RTOS, on which the PPG acquisition operates together with the processing library integrated to the Zephyr DeviceTree. The Zephyr BLE stack provides wireless connectivity. Finally, the BEAST security library, based on the Trusted-Firmware-M, implements the security protocol, the key management and the secure storage of the device certificates. By using TF-M, this solution is portable to any TF-M compliant MCUs. On the gateway side, the implementation of the secure node is based on Linux using BlueZ for the BLE part and the BEAST security endpoint application is a python-based solution (for the cryptography and the BLE interface) and web technologies for the visualization (javascript + MQTT).

In conjunction to the demonstrator 2 reference documents are available: (i) BEAST security specification & (ii) BEAST software architecture document. The BEAST demonstrator can form the basis for many deployments involving the data acquisition, transmission, sharing and processing of sensitive data.

PRECISION MANUFACTURING

Michel Despont

The Precision Manufacturing program at CSEM is designed to address the evolving challenges faced by Switzerland's manufacturing sector, particularly in the context of digitalization and sustainability. As the industry seeks to maintain its reputation for quality, the program focuses on integrating resource-efficient materials and processes while minimizing environmental impact. Key initiatives include developing advanced microsystems, smart labware for 3D cell processing, and innovative MEMS technologies. By leveraging recent advancements in AI and fostering local manufacturing networks, CSEM aims to enhance the competitiveness of Swiss SMEs. Ultimately, the program strives to deliver impactful research that meets societal needs and supports technology transfer to the industry, ensuring a sustainable future for precision manufacturing in Switzerland.

To achieve these ambitious goals, the program is structured around six key focus areas, each addressing specific technological advancements and industry needs.

TECHNOLOGY-BASED AREAS

CSEM's **MEMS** focus area offers a versatile micro-fabrication platform tailored to specialty applications requiring high precision. This area is crucial to integrating MEMS technologies into various sectors, including photonics, scientific instrumentation, and life sciences. CSEM leverages its extensive experience and state-of-the-art infrastructure to provide small and medium enterprises (SMEs) access to advanced manufacturing capabilities that would otherwise be unattainable due to high entry barriers. The focus area supports the entire valorization chain, from development to small-scale production, ensuring compliance with ISO9001 quality standards. By fostering collaboration across different focus areas, CSEM enhances the capabilities and applications of MEMS technologies, driving innovation in precision manufacturing.

The **Additive Manufacturing (AM)** focus area is dedicated to advancing AM technologies in order to achieve high precision and functionality in manufacturing. It emphasizes the use of high-performance materials and innovative design techniques, such as topology optimization, to create complex components that integrate multiple functions. CSEM targets key markets, including aerospace, watchmaking, and MedTech, facilitating the production of intricate parts that are challenging to manufacture using traditional methods. The focus area also prioritizes the development of standardized design guidelines and process parameters to ensure quality and reliability across various AM systems. By developing and offering a unique portfolio of advanced technology solution with advanced data analysis, CSEM aims to reinforce the competitive edge of the Swiss precision industry.

The **Functional Surfaces** focus area emphasizes the engineering of surfaces and interfaces to enhance components and devices performance across various applications. CSEM aims to unlock the potential of new materials by developing expertise in surface structuring and modification. This is achieved through a deep understanding of atomic and molecular interfacial phenomena. This area addresses challenges in scaling up processes for industrial applications, targeting sectors

such as watchmaking, energy harvesting, and medical technologies. Key initiatives include creating multi-functional surface treatments that improve protective and optical properties, particularly for components exposed to harsh environments, and developing new sensing layers and components with improved sensitivity, selectivity, and reliability in order to address the demand for multi-sensing detectors. Additionally, CSEM integrates sustainability into its processes, focusing on eco-friendly alternatives. The goal is to provide partners with innovative solutions that enhance product functionality while promoting environmental responsibility.

SYSTEM-BASED AREAS

CSEM's **Photonics** focus area specializes in the development of innovative optical elements and systems, leveraging micro and nano-optics, integrated photonic circuits (PICs), and high-performance laser sources. This area addresses the diverse needs of the Swiss industry by enhancing the performance and efficiency of optical technologies. Key initiatives include the development of laser sources for industrial applications, AI-enhanced multispectral image sensors, wafer-scale processes of integrated optics, and the offer of advanced solutions and prototyping of intricate thin-film lithium niobate PIC designs. CSEM aims to miniaturize photonic components while extending their wavelength range to support emerging applications in sensing, imaging, and quantum technologies.

The **Tools for Life Sciences** focus area integrates hardware engineering, biology, and artificial intelligence to develop advanced technologies for drug testing, diagnostics, and regenerative medicine. This area addresses significant challenges in the life sciences sector, particularly in enhancing the quality of patient care. CSEM develops and provides essential tools and devices for the handling and monitoring of body fluids and cells. By leveraging expertise in microfluidics, MEMS, surface functionalization and structuration, and artificial intelligence, CSEM supports industry innovation and the development of new products that improve reproducibility and usability in biomedical research. Collaborations with other focus areas further enhance the capabilities of life sciences tools, ensuring they meet the evolving demands of the healthcare sector.

The **Scientific Instrumentation** focus area is dedicated to developing advanced systems that meet the growing demands for precision and functionality across various domains, including space, astrophysics, metrology, and industrial instrumentation. This expertise encompasses three key application-oriented topics: high-precision mechanisms, flexMEMS (an expertise built on MEMS technologies and flexure-based mechanisms), and Lidar technologies. It emphasizes the design and testing of miniature and hybrid systems. CSEM partners with leading organizations, such as ESA and CERN, to create innovative solutions that enhance measurement accuracy and operational efficiency. By integrating cutting-edge manufacturing techniques and fostering collaboration with other focus areas, CSEM aims to drive significant advancements in scientific instrumentation, contributing to the future of precision manufacturing.

Stiffness Engineering of Silicon-based Flexure Mechanisms using Residual Stress

L. Tissot-Daguette • Y. Petremand, F. Cosandier • Q. Gubler • S. Henein • M. Despont

CSEM and Instant-Lab at EPFL, led by Professor S. Henein, are collaborating on the development of silicon mechanisms with flexible guides using a method to modify their stiffness through the growth or deposition of stressed layers. The effectiveness of this approach in reducing the bending stiffness of double-clamped (overconstrained) beams has been demonstrated using thermally grown oxide layers under compressive stress. Mechanisms with low stiffness, zero stiffness, negative stiffness, or controlled buckling have been demonstrated. Such concept could help to manufacture low stiffness compliant mechanisms for application in MEMS and Mechanical Watches.

Residual stresses in micro mechanisms can be advantageously used to permanently preload flexures, thereby modifying their deflection and stiffness. This can be achieved by conformally coating said flexures with another material.

The uniform coating of a double-clamped beam with another material will produce stress that tends to extend or compress the beam, thereby reducing or increasing its stiffness. In a practical implementation compatible with wafer level fabrication, the double clamping is achieved by encasing the beam in a frame with a large cross-section that is hence more rigid and less subject to deformation. A coating producing compressive stress (e.g. thermally grown silicon oxide) will tend to extend the beam, reducing its stiffness and ultimately causing it to buckle if the stress is large enough (Figure 1). On the other hand, applying a coating with tensile stress (e.g. silicon nitride produced by low pressure chemical vapor deposition) will stiffen the beam^[1].

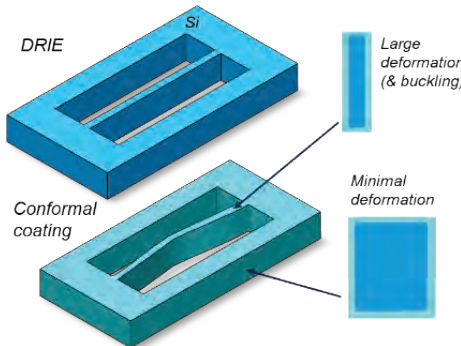


Figure 1: Fabrication process and cross section at the beam level (small silicon cross section and large deformation) and at the frame level (large cross section and small deformation).

Applying a coating with compressive stress uniquely reduces the stiffness and resonance frequency of micro mechanisms in one degree of freedom, while maintaining structural stiffness in the other degrees of freedom. The concept has been demonstrated on a translation stage, which was designed by EPFL, fabricated by CSEM, and characterized by EPFL (Figure 2). The fabrication was done by Deep Reactive Ion Etching (DRIE) on a 380 μm thick wafer with a compliant beam width of 20 μm . To introduce a compressive stress, a 3 μm thick thermal oxide was grown.

The design includes a novel amplification structure based on a chevron configuration (preloading mechanism) coupled with a buckling mechanism that produces a preload on the translation

^[1] EPFL, INSTANT-LAB – IGM – STI – EPFL, Switzerland

^[1] CH718081B1 "Élément Elastique pour un Système Micromécanique"

^[2] EP24199124.9 "Flexure based mechanism with reduced stiffness"

stage, which is guided with a pair of parallel beams (guiding mechanisms)^{[2],[3]}.

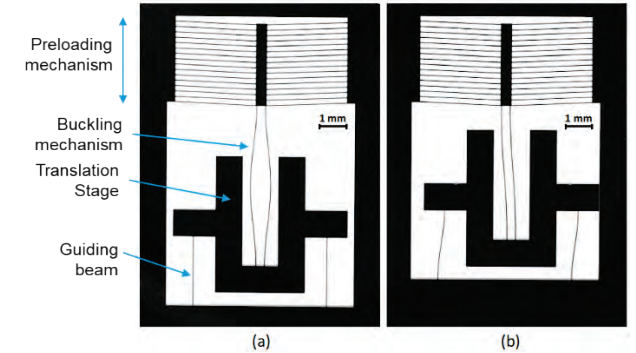


Figure 2: Photographs (top view) of translation table mechanisms having (a) a near-zero positive stiffness (buckling beam length = 6 mm) and (b) a negative stiffness (buckling beam length = 5 mm).

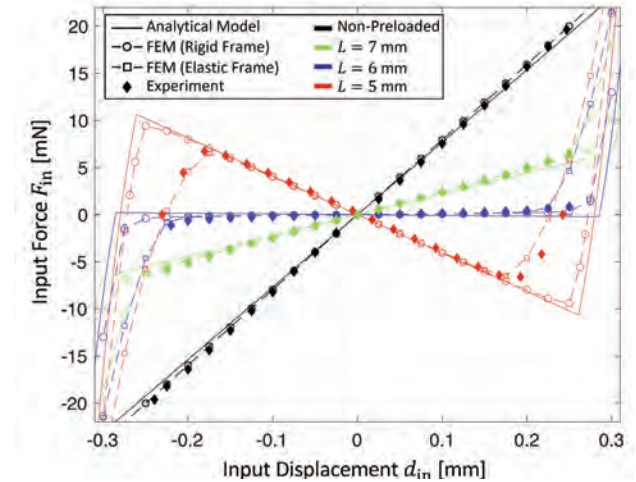


Figure 3: Force-displacement characteristics of the translation stage for different buckling beam lengths in comparison to the non-preloaded stage.

As shown in Figure 3, the measurements match well with the developed models. Depending on the length of the buckling beam L , stiffness reduction, near-zero stiffness, or negative stiffness can be achieved with a noticeable good linearity over a large displacement span. This method can be effectively used to develop highly sensitive physical sensors, such as accelerometers and gyroscopes, with low stiffness and low resonance frequency that are resilient to gravity and shocks as required in inertial MEMS and in mechanical watch regulators.

^[3] L. Tissot-Daguette, et. al., Residual Stress Chevron Preloading Amplifier for Large-Stroke Stiffness Reduction of Silicon Flexure Mechanisms, J. Microelectromech. Syst., submitted

MEMS Magnetic Gradiometer

A. Hoogerwerf, D. Bayat, G. Spinola Durante, Y. Petremand, M. Despont, E. Gasparin • M. Tormen • G. Close •

High-sensitivity magnetometers often measure the gradient (spatial variation) of a magnetic field, as these measurements are not affected by stray uniform fields, such as the Earth's magnetic field. We have developed a magnetic gradiometer based on a miniature permanent magnet fixed to a MEMS accelerometer structure. The MEMS sensor has a noise level below 4 nT/mm/√Hz, making it suitable for non-contact current measurements.

A multitude of magnetic sensors exists for various magnetic field strengths and application^[1]. For low magnetic field measurements, magnetic gradiometers are used to measure the spatial variations of magnetic fields, as they are not affected by the Earth's uniform magnetic field of around 60 mT. However, there are very few miniaturized gradiometers that directly measure the magnetic field gradient.

In collaboration with Melexis, CSEM has developed a MEMS-based direct magnetic gradiometer that can sense magnetic field gradients below the mT/mm level. The concept is based on the fact that a magnetic field gradient exerts a linear force on a permanent magnet, whereas a magnetic field exerts a torque. If the movement of the permanent magnet is restricted to linear movements, it will only respond to a magnetic field gradient.

The permanent magnet has a non-negligible mass, causing it to move in response to accelerations as well. This undesired sensitivity is mitigated by a mass-balance scheme that incorporates an identic, non-magnetic counter mass into the sensor. This arrangement measures the difference in displacement between the permanent magnet and the non-magnetic mass. The displacement difference is not sensitive to accelerations, as they affect both masses equally. A magnetic field gradient, on the other hand, exerts a force only on the permanent magnet, creating a differential displacement. The resulting magnetic gradiometer is depicted in Figure 1.

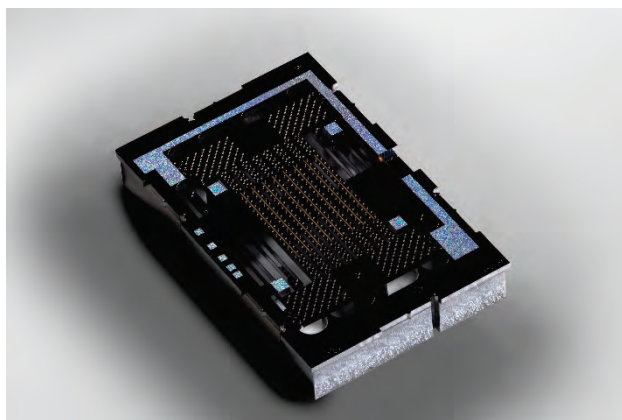


Figure 1: Picture of the MEMS-based magnetic gradiometer.

The gradiometer has been characterized for its magnetic performance and acceleration sensitivity^[2]. Figure 2 shows the

linearity of the sensor capacitance change with respect to the magnetic field gradient. The response is linear until the end-of-travel parasitic capacitances increase the response.

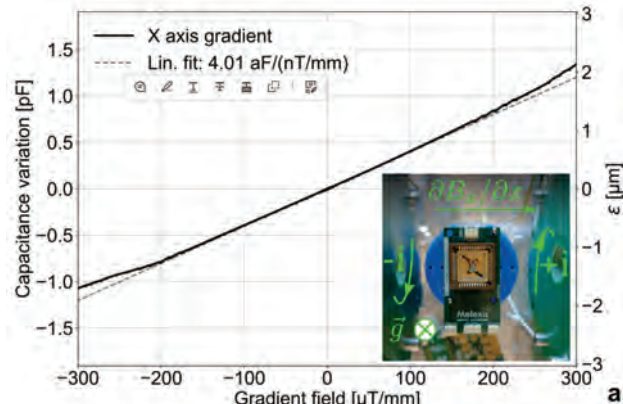


Figure 2: Sensor capacitance variation as function magnetic field gradient.

The sensor was rotated in the gravitational field and the response is shown in Figure 3. The effect of gravitation is +/- 2% full scale. Without the mass balance, the effect of gravitation would have been more than +/- 200% full scale.

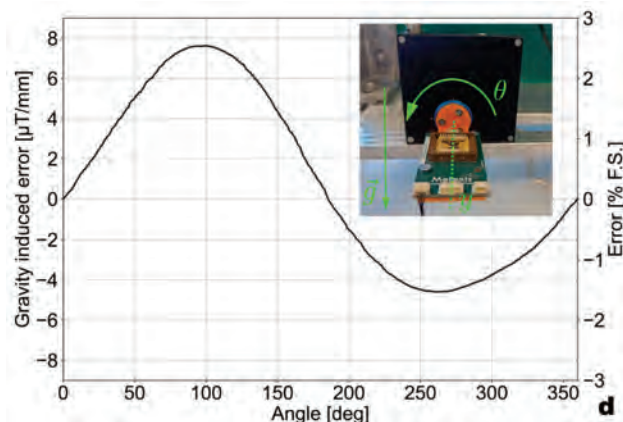


Figure 3: Typical measured magnetic gradient error due to gravitation as a function of rotation angle.

The magnetic gradiometer has been used to measure the current in a busbar running above the sensor. A full-scale response was obtained with a current ranging from - 30 A to + 30 A.

• Melexis Technologies S.A, CH-2022 Bévaix

^[1] B. Brajon, E. Gasparin, G. Close, A Benchmark of Integrated Magnetometers and Magnetic Gradiometers, IEEE Access, vol. 11, pp. 115635–115643, 2023.

^[2] E. Gasparin, et. al., An Integrated MEMS Magnetic Gradiometer Rejecting Vibrations and Stray Fields, Proc. ESSERC 2024, <https://www.techrxiv.org/doi/full/10.36227/techrxiv.172547675.54945155/v1>

A MEMS Gas Chromatograph and its Fluidic Connections

A. Hoogerwerf, G. Spinola Durante

We present MEMS components of a gas chromatograph with fluidic connections that can withstand operating temperatures of up to 300°C of the MEMS components. The components that have been developed are a pre-concentrator, different types of columns, and a Thermal Conductivity Detector. The developments will enable future hand-held gas chromatography systems.

Since the first published paper [1] on MEMS Gas Chromatography (GC) columns, much work has been done on making complete GC systems using MEMS technology. Much progress has been published on many aspects of MEMS GC systems. However, very little effort has been placed on making reliable fluidic connections to the MEMS system. Almost all MEMS GC components use a glass capillary that is inserted sideways into the silicon chip and that is held in place and sealed leak tight with epoxy around it. Such a simple sealing will have high leak rates of helium which is generally used as a carrier gas in GC systems. Moreover, the seals cannot withstand operating temperatures much higher than 150°C due to the deterioration of the epoxy.

CSEM has developed fluidic connections for MEMS components that are compatible with operating temperatures of up to 300°C and that connect to standard GC glass capillaries using standard SilFlow® nuts and ferrules [2]. The connections are made out of gold-plated Invar whose coefficient of thermal expansion is close to that of silicon.

Two GC components that have been made are columns and Thermal Conductivity Detectors (TCDs). It turns out that it is best to bond the TCDs directly to the columns, as depicted in Figure 1. The larger columns can then be bonded to the Invar connection piece (not shown in Figure 1).

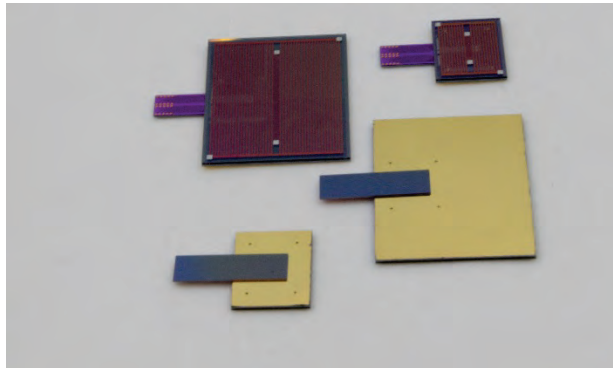


Figure 1: Picture of two different sizes of columns (big) with bonded TCDs (small), from frontside and backside. The Invar connection block (not shown) will connect to the 4 small inlets.

The third GC component that has been fabricated is a pre-concentrator. The pre-concentrator is a cavity filled with an absorbent material that absorbs volatiles from the air over a long duration of time. The gas flow through the pre-concentrator is then led through the column. The pre-concentrator is rapidly heated, so that the absorbed volatiles are rapidly desorbed and enter the column together, where they can be separated based on their chemical composition. A rapid heating and desorption process is paramount for the effective chemical analysis. A

Comsol Multiphysics® study has therefore been carried out to optimize the layout of the pre-concentrator heater and dimension the isolators around it. The model takes into account the gas flow through the porous absorber material and the heat conduction from the heater to the absorber material. The result of the optimization is that 64% of the pre-concentrator volume reaches a temperature in the range of 265°C - 285°C in 2.5 s, while 2% reaches a temperature of over 300°C that can deteriorate the absorber material. The simulated temperature versus volume distribution is shown in Figure 2.

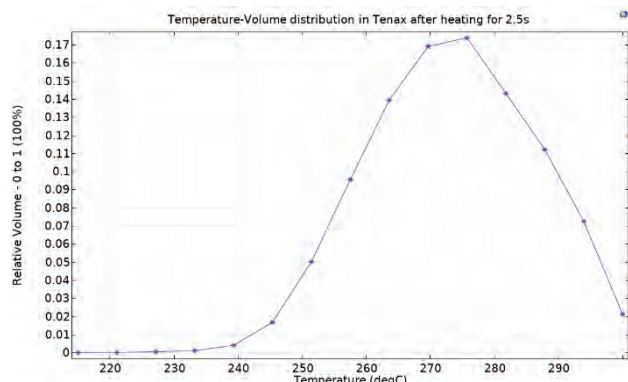


Figure 2: The simulated temperature-volume distribution in the pre-concentrator.

The pre-concentrator based on the simulation results is shown in Figure 3. The gap between the pre-concentrator and the connection block is there to minimize the heat loss from the pre-concentrator to the Invar.



Figure 3: The pre-concentrator with the Invar connection block.

This work has been supported under ESA Contract No. 4000139571/22/NL/KML.

[1] S. C. Terry, J. H. Jerman, J. B. Angell, A gas chromatographic air analyzer fabricated on a silicon wafer, IEEE Trans.Electron. Dev., vol. ED-26, no. 12, Dec. 1979

[2] <https://www.trajanscimed.com/collections/silflow>

Ultra-sensitive Photonics-MEMS Accelerometers for Next-generation Seismic Sensor

F. Ebrahimi, A. Manzoor, D. Bayat, Y. Petremand, H. Sattari, A. Hoogerwerf, G. Spinola Durante, A. H. Ghadimi, M. Despont

Seismic sensors are highly effective, adaptable, and cost-efficient tools utilized across various applications that demand particular frequency responses and sensitivities. In this SNF-funded project, CSEM collaborates with the Swiss Seismic Institute at ETHZ to design and field-test a new generation of optomechanical accelerometers and seismic sensors, achieving nano-g level sensitivity and ultra-high bandwidth.

Deploying compact, calibrated, passive sensor arrays with wide bandwidth and high sensitivity is essential for seismology. To this aim, we present a new vacuum-packaged Photonics-MEMS accelerometer with the targets of $< 100 \text{ ng}/\sqrt{\text{Hz}}$ sensitivity, a frequency range of 1 kHz to 50 kHz, > 140 dB dynamic range, and 20 dB off-axis rejection. The design features a high-quality factor (Q) resonator with optimized mass distribution which is supported by highly stressed silicon nitride beams for enhanced bandwidth, sensitivity, and directionality. Vibration detection is enabled by an integrated Mach-Zehnder Interferometer (MZI).

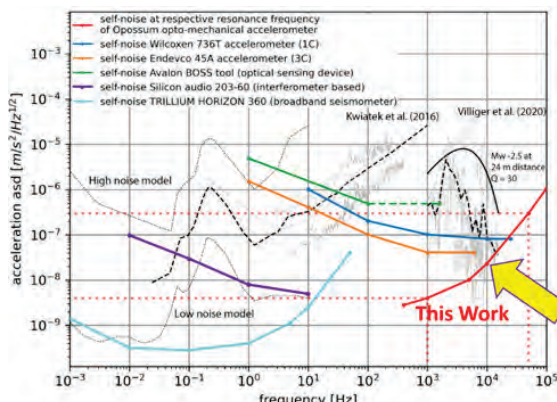


Figure 1: Comparing the target self-noise and frequency range of our sensor (based on our simulations) with state of the art^[7].

To meet the objectives, the sensor design underwent optimization to align with fabrication compatibility and target specs. Three resonators at 1 kHz, 10 kHz, and 50 kHz were designed and simulated to meet bandwidth, noise, and directionality requirements, while remaining fabrication-compatible (Figure 2).

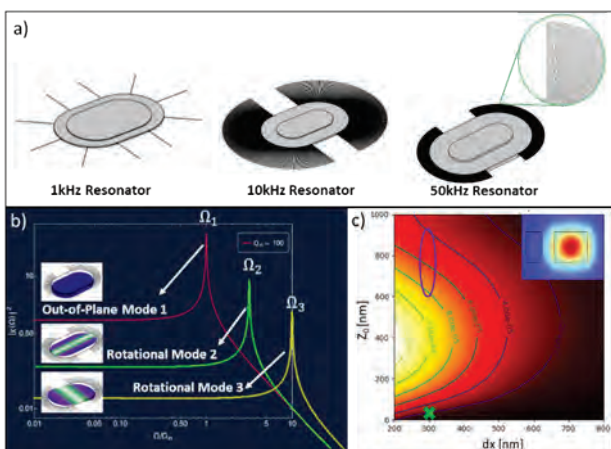


Figure 2: a) FEM simulation of resonators with 1, 10, 50 kHz having between 10 and hundreds of pre-stressed tethers; b) frequency separation in higher modes; c) D_{eff}/Z_0 heat map.

The high Q factor is achieved with a set of hundreds of pre-stressed (~1 GPa) silicon nitride nano-beams, while a central silicon block supplies enough mass for target sensitivity. The movement of the resonator mass is restricted in other directions by design, enhancing directionality. The first device generation is shown in Figure 3.

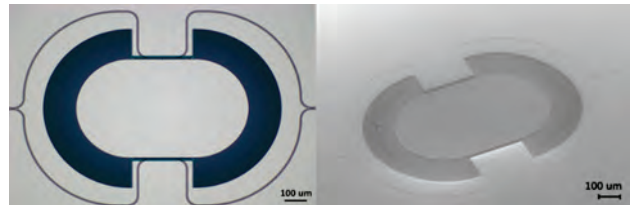


Figure 3: First generation of a Photonics-MEMS seismic sensor.

Optical interaction with the test mass occurs via evanescent coupling to SiN waveguides, which are monolithically fabricated on the same wafer for efficient, strong opto-mechanical coupling. Light is coupled in and out of the chip through optical fibers connected to the optical interrogator.

Initial characterization of the 50 kHz sensors under low pressure vacuum using a laser doppler vibrometer (Figure 4) illustrate that the sensor performance is well in line with the simulations. A sharp low-noise peak at 52 kHz appears with a Q of 7'000 at $5 \cdot 10^{-2}$ mbar. These initial measurements are highly promising and confirm the strong performance predicted by our analytical and numerical analysis.

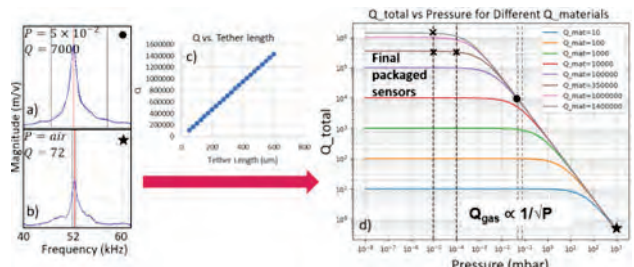


Figure 4: Characterization at (a) $5 \cdot 10^{-2}$ mbar and (b) in air; c) Q vs. tether length; d) Q_{total} vs. pressure for different resonating materials.

This research is as part of the project "40B2-0_194746 Ultra-sensitive Photonic Accelerometers for Next-generation Seismic Sensor Networks (OPOSSUM)" and received funding from BRIDGE, a collaborative program of the Swiss National Science Foundation (SNF) and the Swiss Innovation Agency (Innosuisse).

^[1] F. Ebrahimi, et al., Ultra-Sensitive, High-Bandwidth Photonics-MEMS Seismic Sensor, IEEE MEMS, 2024, in press.

Developing the Mechanical Watches of Tomorrow using Advanced Silicon Microfabrication

D. Bayat, A. Hoogerwerf, Y. Petermand, C. Alleb  , F. Cardot, M. Despont

The METEORE project focuses on creating advanced mechanical watch components using silicon microfabrication techniques, creating tiny mechanical worlds that come to life at the push of a button. The initial progress is showcasing the innovative design and its aesthetic enhancements, including complicated geometries based on compliant mechanisms and showcasing different colors achieved via microfabrication. Future developments will continue refining these processes to improve product reliability and market readiness.

Traditional Swiss mechanical watchmaking has predominantly relied on intricate assemblies of cogs, wheels, and pinions for over 500 years. The METEORE project aims to revolutionize this field by introducing compliant mechanisms made from silicon that combine the dial and hands of a watch, allowing for more compact, reliable, and aesthetically pleasing designs. This endeavor will be accomplished by the design showcased in Figure 1. Figure 1a shows the general design of the compliant mechanism that consists of several linear elements that can be pushed up (red arrow) by the rotating mechanism of the watch. This linear motion is then transformed into a rotational motion that brings several separate pieces of the mechanism together, revealing the numbers, as shown in Figure 1b.

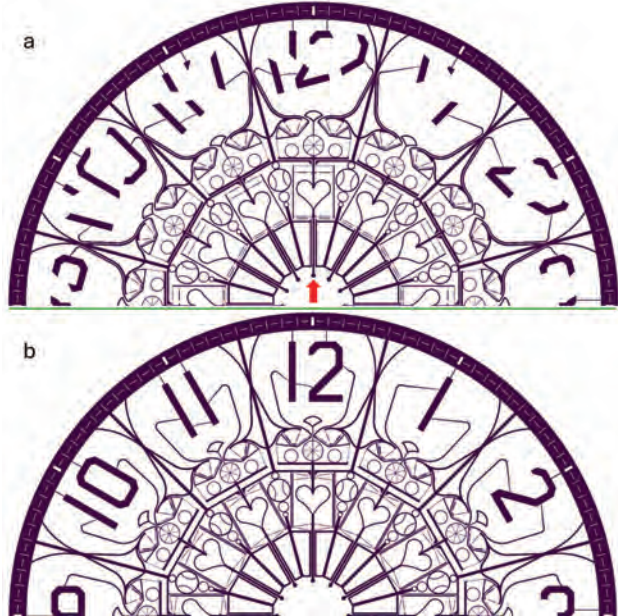


Figure 1: The open dial (a). The red arrow shows where the force is applied. The closed state (b) revealing the numbers.

Several challenges must be overcome in the project to integrate decorative elements with functional robustness, such as fatigue and shock resistance. The project aims to bring silicon-based mechanisms from a Technology Readiness Level (TRL) of 6-7 to 8-9, making them market-ready.

During the first year, METEORE achieved progress in developing new processes to modify silicon surfaces, enabling color customization through the deposition of silicon nitride layers of different thicknesses. These processes allow for a range of colors without compromising the structural integrity of the parts. The team proposed a modified fabrication process that separates the rough, aesthetic elements from the mechanically sensitive parts through thermal oxidation, to address concerns about shock resistance. This approach improves the resilience of components, particularly flexure springs, essential for maintaining device performance under stress.

Figure 2 illustrates a silicon wafer featuring a pyramidal etch pattern, as depicted in the top right corner of the figure, with a silicon nitride deposition, which gives a satin-blue coloration to the surface that imparts a diffuse, homogeneous appearance, maintaining consistent color perception regardless of the viewing angle. Silicon nitride deposition thickness can give rise to a variation of different colors.

Another key achievement, illustrated in Figure 3, includes the successful deposition of silicon nitride as well as the application of gold coatings to specific components via shadow masks on the fabricated dials.

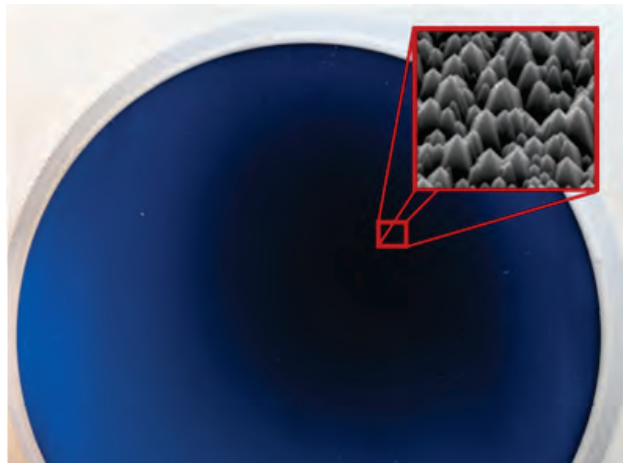


Figure 2: Silicon wafer with a pyramidal etch pattern and a thin layer of silicon nitride deposited on top of it, resulting in a satin-blue colour.



Figure 3: Gold coating via shadow masks, and the dials were coated with silicon nitride or gold.

Upcoming phases will focus on refining the process to enhance durability and maintain aesthetic quality. Additionally, further testing will optimize the designs, ensuring they meet high-performance standards in fatigue and shock performance.

Acknowledgments: This project is funded by Innosuisse, under contract 105.241 IP-ENG.

A Novel Scintillator Detector for Online High-resolution Beam Profiling

V. Leccese, B. Truc • M. Caldara •

A novel beam profiler is introduced for precise, high-resolution monitoring in proton therapy, addressing critical limitations of current diagnostic systems. With microfabricated scintillating channels, the device achieves a spatial resolution of $\sim 50 \mu\text{m}$ and a profiling rate up to 3.8 kHz. This compact, plug-and-play profiler supports advanced treatments such as FLASH therapy, enhancing treatment accuracy and safety.

Effective beam monitoring is essential for proton accelerators, from commissioning to operation, ensuring optimal performance and safety through accurate diagnostics¹. Current beam profiling solutions fail to meet the high spatial resolution, fast time response, and high frame rate requirements necessary for characterizing the intense, short pulses required for FLASH therapy.

Organic scintillators are widely used in monitoring high-energy particle beams across various applications². However, existing scintillating screens and fiber arrays are hindered by slow acquisition rates and complex fabrication processes. To overcome these limitations, we propose a novel beam transverse profiler that leverages microfabrication technology. This approach streamlines fabrication while addressing the critical challenges of current systems. Our innovative technology offers high-performance, compact, plug-and-play solutions, potentially compatible with the demanding requirements of FLASH therapy.

Methods

The detector features a sensitive area composed of scintillating channels, each $100 \mu\text{m}$ wide, arranged in an array. This array is created by microstructuring a silicon wafer, which is then filled with a commercially available moldable scintillating resin. The channels at the end of the array are coupled with a custom-made readout system that includes a photodetector array and a microcontroller. This design provides high spatial resolution ($\sim 50 \mu\text{m}$) and supports a profile monitoring rate of up to 3.8 kHz, with an adjustable integration time ranging from 4.5 μs to 1.4 s.

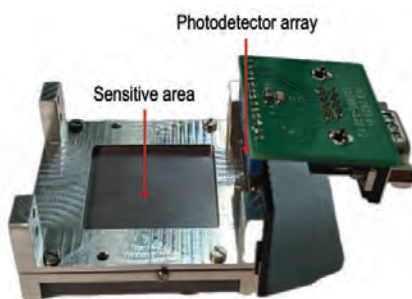


Figure 1: Picture of the detector, comprising a metallic frame supporting both the sensitive area and the photodetection system.

Results

The device was tested on a proton beamline at CNAO (Italy) with beam energies ranging from 70 MeV to 230 MeV. The obtained profiles match the ones of the reference detector, an ionization chamber (IC), for low energies (Figure 2), while showing a broadening for high energies (Figure 3) due to possible different factors, e.g., secondary particles detected by the photodetectors and the air gap featured between the channels end and the photodetectors.

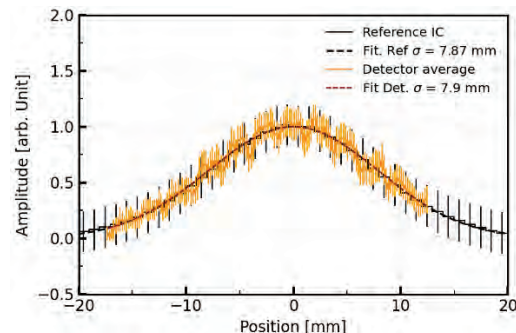


Figure 2: Comparison between the beam profilers measured with our detector and the IC. The beam energy was set at 74 MeV.

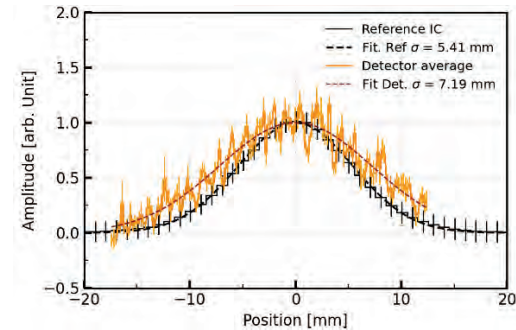


Figure 3: Comparison between the beam profilers measured with our detector and the IC. The beam energy was set at 226 MeV.

Conclusions

Although further optimization is required, the novel beam profiler shows promising results for high-energy particle monitoring, particularly in proton therapy, breaking ground for a new line of high spatial and temporal resolution detectors essential for accurate beam profiling and FLASH therapy.

- EPFL, IPhys-LUMES, Lausanne 1015 CH, Switzerland
- [1] M. Gasior, *et al.*, Introduction to Beam Instrumentation and Diagnostics, Proceedings of the CAS-CERN Accelerator School: Advanced Accelerator Physics, Norway, edited by W. Herr, CERN-(2014) 2014-009.

- [2] S. Tavernier, Detectors Based on Scintillation, in Experimental Techniques in Nuclear and Particle Physics (2009) Springer, Berlin, Heidelberg.

Novel Dental Clear Aligner with Integrated Microfluidic Channels for Precise, High-efficiency Antibacterial and Fluoride Delivery

N. Kalentics, F. Boudoire, E. C. Poli, C. Cattin

Clear dental aligners, a popular alternative to metal braces, have driven significant market growth. However, they pose oral health challenges due to restricted saliva and oxygen flow. CSEM's innovative directly 3D-printed aligners with integrated microfluidic channels release beneficial liquids like fluoride and antibacterial agents, addressing these issues and improving oral health during the aligner wear period.

Clear dental aligners offer a subtle, removable, and transparent alternative to conventional metal braces. In recent years, orthodontic treatments with dental aligners have become increasingly popular which has led to an exceptional growth of the global clear aligners market, estimated at 6.29 billion USD in 2022 and expected to surpass around 46.3 billion USD by 2030, expanding at a compound annual growth rate of 28.3% during the forecast period 2022 to 2030^[1].

While these aligners have significantly impacted the dental industry, they come with certain challenges. Aligners are worn approximately 22 hours a day and cover the full surface of the teeth. Therefore, they restrict the access of saliva and oxygen to the teeth and periodontal tissues, which causes significant bacterial buildup on the surface of the teeth and leads to plaque biofilms creation^[2], white spot lesions^[3], and caries formation as well as gingival/periodontal issues^[4]. These problems could be overcome by maintaining the oral flora in a stable manner in terms of its acidity, by reducing the microbial presence through the slow release of antibacterial and fluoride-containing liquids intraorally. Introduction of a slow-release fluoride device would further improve the enamel surface through remineralization and would leave a tooth surface with improved strength.

A patented solution developed at CSEM proposes a novel generation of directly 3D-printed aligners with integrated microfluidic channels (Figure 1a). These microchannels act as reservoirs and are prefilled with beneficial liquids such as fluoride and antibacterial fluid, which are slowly released over the 10 days course that the aligner is worn (Figure 1b).

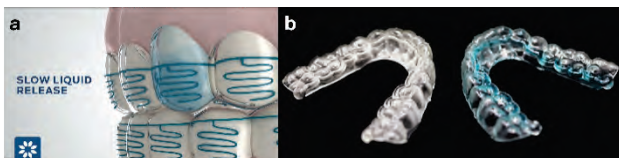


Figure 1: a) A schematic of the Active Aligner with integrated microfluidic channels, and b) the 3D printed Active Aligner. The colored liquid was used for better visualization.

With this proposed solution for the novel generation of directly 3D printed dental aligners, not only is an Active Aligner with added value created, but the manufacturing process also becomes significantly shorter. This results in a more efficient and cost-effective production flow, as shown in Figure 2. Following the initial intraoral scan and treatment planning using

commercially available software, the step for 3D printing aligner models (negatives) is bypassed, moving directly to manufacturing of aligners. The process proceeds with aligner design and the use of CE and FDA certified resins to 3D print aligners with integrated microfluidic channels based on in-house developed and optimized processing parameters. The aligners are then post-processed in a similar step as required for conventional aligners. Since the aligners are 3D printed, there is no need for thermoforming, cutting, or polishing steps. In the final step, the micro-channels of the aligners are prefilled with antibacterial fluid and fluoride.

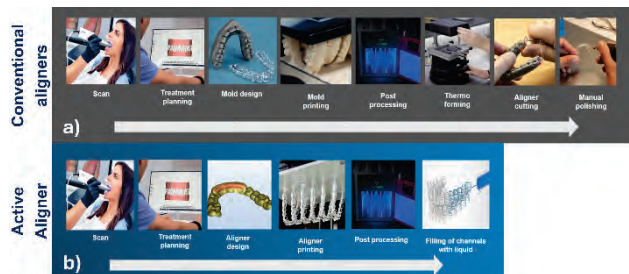


Figure 2: a) Workflow for a conventional aligner, and b) workflow of the novel directly 3D printed Active Aligner with integrated channels.

Throughout this project, the following processes will be undertaken:

- Optimization of the microchannel design and 3D printing processes.
- Investigation of different beneficial liquids and their release dynamics.
- Evaluation of mechanical properties, geometrical accuracy, and cytotoxicity of aligners.
- Performing in vitro studies on the impact of our Active Aligners on bacterial plaque accumulation and white spot lesions compared with conventional aligners.

The development of directly 3D-printed dental aligners with integrated microfluidic channels represents a significant advancement in orthodontic treatment by addressing oral health challenges and enhancing production efficiency and cost-effectiveness.

This project is in partnership with the University of Bern and is funded by Innosuisse. CSEM thanks them for their support.

[1] Clear Aligners Market Size to Hit USD 46.3 Billion By 2030. Accessed: Dec. 01, 2023. [Online]. Available: <https://www.precedenceresearch.com/clear-aligners-market>

[2] M. Rouzi, X. Zhang, Q. Jiang, H. Long, W. Lai, X. Li, Impact of Clear Aligners on Oral Health and Oral Microbiome During Orthodontic Treatment., Int. Dent. J. 73.5 (2023) 603.

[3] S. Bisht, A. K. Khera, P. Raghav, White spot lesions during orthodontic clear aligner therapy: A scoping review, J. Orthod. Sci. 11.1 (2022) 9.

[4] M. Moshiri, J. E. Eckhart, P. Mcshane, D. S. German, Consequences of Poor Oral Hygiene During Clear Aligner Therapy, JCO 8.47 (2013) 494.

High-resolution Lithography-based Manufacturing of Metals and Ceramics

F. Boudoire, D. Di Studio, D. Sinayuc, M. Despont, C. Cattin, V. Pejchal

CSEM is pioneering high-resolution additive manufacturing by advancing lithography-based manufacturing for metals and ceramics. By achieving fine resolution and precision, our technology allows for the fabrication of complex geometries that are challenging or impossible to produce through conventional manufacturing methods. These capabilities open new business opportunities across industries requiring high-strength, wear-resistant, and thermally or electrically conductive components. Applications in jewelry and watchmaking benefit from our ability to fabricate stainless steel and titanium parts with intricate designs and polished finishes, meeting both aesthetic and mechanical demands.

CSEM is at the forefront of additive manufacturing, driving innovations in high-resolution fabrication across various materials and industries. By achieving exceptionally fine resolutions, we harness the design flexibility of additive manufacturing to enable breakthroughs that are otherwise unattainable with traditional production methods.

Building on our expertise and state-of-the-art infrastructure in high-resolution UV stereolithography, we have developed advanced capabilities for fabricating polymer-based microscale structures with outstanding precision, minimal surface roughness, and high throughput. UV stereolithography, which uses UV light to solidify liquid resins layer by layer, provides the accuracy and speed necessary for sophisticated micro-manufacturing applications. However, this technique is generally constrained to thermoset polymers.

Expanding beyond polymer-based applications, CSEM is pioneering methods for microscale manufacturing of metal and ceramic components through polymer templating. In this lithography-based approach, UV stereolithography shapes polymers into intricate structures that serve as scaffolds embedded with metal or ceramic particles. Following post-processing steps—debinding of the polymer and particle sintering—the polymer scaffold is converted into metal or ceramic parts. This process enables the creation of complex geometries in materials that are challenging to manufacture at such small scales.

In Figure 1, we demonstrate the design intricacy achievable with our technology through high-fidelity test specimens fabricated in metal (316L stainless steel), ceramic (alumina), and polymer (acrylate). The metal and ceramic polymer-templated parts exhibit comparable resolution, surface quality, and structural complexity to their polymer counterpart, highlighting the versatility and precision of our approach across diverse materials.

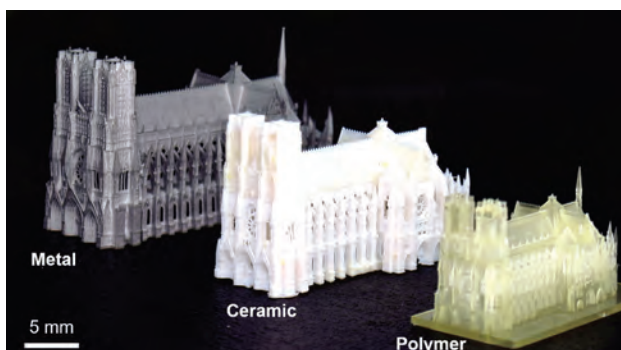


Figure 1: High resolution showcase for different materials; Notre-Dame de Reims Cathedral, 1:6000 scale.

By adapting UV stereolithography to accommodate new material categories, we are extending the possibilities of microscale additive manufacturing to materials with enhanced properties, such as high strength, wear resistance, and improved thermal and electrical conductivity.

Our first targeted industry is jewelry and watchmaking where lithography-based metal manufacturing can satisfy the required mechanical properties and aesthetics. For this application we are working with two materials: stainless steel and titanium. In Figure 2, we showcase a chain bracelet in stainless steel. For this material we can achieve a mirror surface finish thanks to in-house electropolishing.

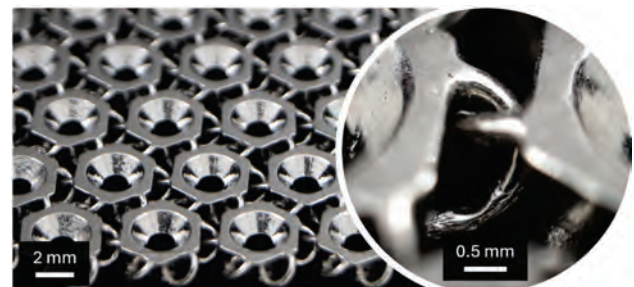


Figure 2: Design flexibility and polishing showcase; interlocked chainmail in stainless steel with electropolished surface ($S_a = 400 \text{ nm}$).

We are also working with titanium, which has an exceptional strength-to-weight ratio, offering high durability while remaining lightweight. Our manufacturing method allows us to produce for example fine decorative designs (Figure 3) overcoming the challenges associated with machining such details.



Figure 3: Titanium watch case with a decorative Voronoi lattice structure.

In conclusion, CSEM's advancements in high-resolution additive manufacturing are unlocking new possibilities for fabricating complex metal and ceramic parts. By adapting UV stereolithography and polymer templating for these materials, we demonstrate a versatile, precise approach that combines design flexibility with robust mechanical performance.

Looking ahead, our developments will focus on advancing further the quality of the materials in our current portfolio (density, resolution, polishing). We are also developing process for new materials such as copper and aluminum to achieve high conductivity, addressing specific needs in wireless communication technologies.

Additive Manufacturing of Functionally Graded Composite of Shape Memory Alloy and Titanium

V. Pejchal, R. Ramezani

Functionally Graded Materials (FGMs) produced by Laser Powder Bed Fusion (LPBF) represent a cutting-edge advancement in additive manufacturing. LPBF allows for the precise control of material composition and microstructure, enabling the creation of components with tailored properties that vary gradually across their volume. This capability is particularly beneficial for applications requiring a combination of different material characteristics. More recently, the integration of AM with shape memory materials has given rise to the pioneering field of 4D printing. Although shape memory materials offer unique functionalities not achievable with conventional metals, they are generally more expensive, less strong, and denser than lightweight structural metals such as titanium. This work demonstrates the combination of the functionality of the shape memory alloy Nitinol with the structural strength and lightness of a titanium alloy into a single functionally graded composite.

In the present work we developed LPBF process for combining NiTi and Ti6Al4V to leverage the unique shape memory properties of NiTi with the high strength and lightweight characteristics of Ti6Al4V, creating a functionally graded material (FGM) that offers both enhanced functionality and structural integrity. Combining NiTi and Ti6Al4V directly without an interlayer is challenging due to the formation of brittle intermetallic compounds, particularly Ti_2Ni , in the fusion zone. These brittle phases significantly weaken the interface, making it prone to cracking and failure under stress. The differences in thermophysical properties between NiTi and Ti6Al4V also contribute to high residual stresses and segregation issues during the fusion process [1]. To address the challenges of direct fusion, we have developed an LPBF process that incorporates a carefully selected interlayer metal to mitigate the formation of brittle intermetallic compounds and ensure a robust, high-performance interface.

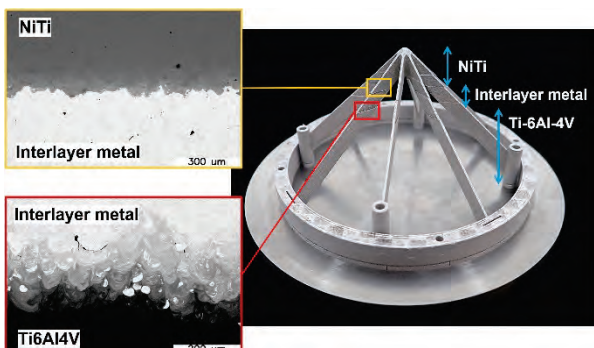


Figure 1: SEM micrographs of two interfaces in the LPBF manufactured FGM flexural pivot demonstrator.

Commercially available LPBF grade powder feedstock of NiTi, Ti6Al4V and the selected metal interlayer was procured. Manufacturing was performed in-house using TruPrint 1000 (Trumpf GmbH) LPBF machine. The LPBF process parameters were first optimized for manufacturing the selected metal interlayer on top of the Ti6Al4V substrate, and subsequently for depositing NiTi on top of the metal interlayer. In-depth microstructural investigation of the resulting interface helped in the selection of optimum parameters. The optimized parameters were used to manufacture monolithic FGM material coupons with two distinct interfaces as shown in Figure 1. The microstructural observations showed no signs of microcracking at the two interfaces and overall high density of parts exceeding 99.5%. In all experiments, the interlayer thickness was kept above 1 mm.

[1] Teshome, F.B., et al., J. Mater. Eng. Perform. 31, 9777–9790 (2022). <https://doi.org/10.1007/s11665-022-07064-0>

Mechanical characterization of the novel FGM in as-build condition is summarized in Figure 2. The shape memory recovery, tested in a three-point bending, demonstrated comparable results to LPBF-manufactured NiTi, achieving up to 8% recoverable shape memory strain after an 11% applied flexural strain upon heating above the A_f temperature. The mechanical strength of the FGM in its as-built condition reached an ultimate tensile strength (UTS) of 350 MPa, with improved elongation at failure compared to LPBF-manufactured NiTi.

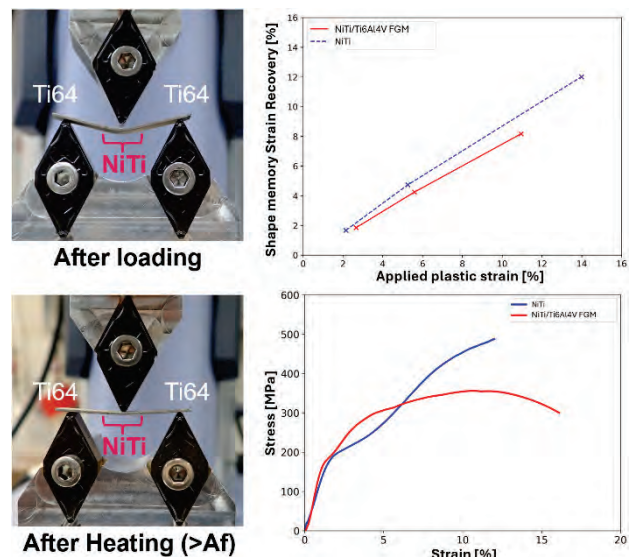


Figure 2: Summary of mechanical characterization in three-point bending of LPBF-manufactured shape memory FGM and its performance in comparison with LPBF-manufactured NiTi.

Finally, a flexural pivot demonstrator was manufactured, as shown in Figure 2. The original design [2], was adapted to accommodate the developed LPBF process, enabling the gradual build of various materials along the Z axis. Consequently, the manufactured demonstrator features (i) a central hub and the initial length of flexural arms radiating from the hub made of shape memory NiTi, and (ii) the remaining length of the arms and the structural ring made of Ti6Al4V. In conclusion, the novel FGM shows significant potential for developing innovative devices and actuators that combine the shape memory effect of NiTi with the structural strength of Ti6Al4V for highly demanding applications. To the best of the authors' knowledge, this is the first study in the literature to demonstrate a shape memory NiTi and Ti6Al4V FGM using LPBF.

[2] Manzoor, A., et al., Proceedings of the Euro PM2023 Congress, (2023). <https://doi.org/10.59499/EP235763857>

3D Printed Pipe Segments with Built-in Heating and Temperature Sensing Capabilities

H. Saoudan, L. Kiener, L. Salamin, J. Rouvinet, D. Novo, N. Blondiaux, M. Crenna, S. Khan, C. Marro •, F. Montredon •, P. Houy •, S. Eyrignoux ••, C. Manoli *, P. Petagna *

In the framework of the EU project AHEAD led by CSEM, a pipe segment including 3D Printed built-in heating and temperature sensing elements was co-developed by CSEM (design, sensor Aerosol Jet Printing), LISI Aerospace Additive Manufacturing (metallic additive manufacturing) and Thales Alenia Space France (end-user requirement specifications, co-design, and validation testing). Thanks to a built-in electrical connector and precisely machined terminations, this one-part plug and play component offers heating power up to 60W and temperature measurement from -65 to +85°C, without the need for integrating any additional component.

Spacecraft thermal regulation is crucial to ensure survival, optimum operation and lifetime of onboard systems and components by preventing overheating or freezing. To ensure the best control and subsequent performances, thermal management systems such as fluidic ones require temperature sensors and heating elements (see Figure 1) to be integrated at strategic locations. Nowadays, the mechanical and electrical integration of those Commercial Off-The-Shelf (COTS) elements involves constraints that limit efficiency, a problem which is not limited to this specific use-case.



Figure 1: State-of-the-art COTS temperature sensor and linear flexible heater integrated using adhesive bonding process.

To answer those limitations, CSEM, LISI and Thales co-developed a pipe segment including 3D Printed built-in heating and temperature sensing capability. The new design (see Figure 3) brings key advantages compared to the state-of-the-art solution.

- Single-part architecture, simplifying assembly
- No adhesive bonding, i.e. no risk of delamination
- Power transfer all around the tube, improving performance

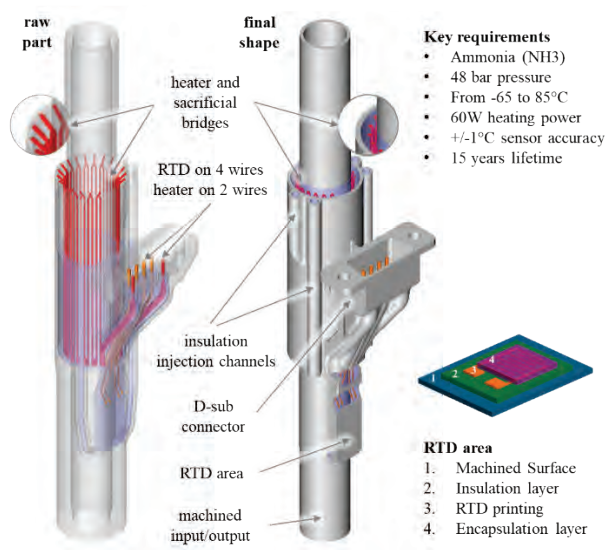


Figure 3: Functionalized pipe segment design description.



Figure 2: Prototype functional testing and CT scan.

In total, 16 prototypes were manufactured, inspected and tested. No notable non-conformances were detected during initial functional tests, excepted for one prototype where the heater was found in short-circuit with the structure. CT scans were performed to double-check deviations between the design and the prototypes, and to check the presence of internal defects such as cracks or voids in the resin and short-circuits between the wires and the structure. No problematic deviation was detected.

Among all sensors, the resistance at 0°C was found measured between 589Ω and 923 Ω, whereas 1kΩ was targeted. The accuracy of the best sensor was found ±1.6 °C and ±5.3 °C for the worst one, whereas the targeted accuracy was ±1 °C. Those results are rather disappointing, knowing that the sensors produced at sample level were showing significantly better accuracy. In-depth investigations would be required to understand the root cause(s).

The prototypes successfully passed leak, proof pressure, thermo-elastic, thermal lifetime, vibration and heating performance tests at system level, demonstrating the exceptional robustness of the 3D-printed heating element. Beyond the aforementioned advantages, the integration of a built-in heating element enables the creation of complex curvature shapes that are very difficult to achieve with state-of-the-art solutions. The benefits of Design for Additive Manufacturing (AM) can be further leveraged, for instance, by incorporating heat exchange or insulation design features. Moreover, much higher temperatures (exceeding 1000°C) can be envisioned through the use of cast ceramic as an insulation material instead of epoxy resins. Finally, the built-in heater eliminates the dependency on external heating element suppliers, providing greater flexibility to optimize and customize product design at reasonable costs and with minimal impact on lead time. Additional applications for this heater technology are currently under study.

* Thales Alenia Space
•• LISI Aerospace Additive Manufacturing

* CERN

Additively Manufactured Flexible Pivots tested in Cryogenic Conditions

L. Kiener, G. Lang, H. Saudan, L. Salamin, P. Spanoudakis

Flexible pivots made by metal additive manufacturing were developed, manufactured and tested under extreme cryogenic conditions. Thanks to this novel production technology, the final parameters have been tuned according to customer specifications and produced within three weeks, including the final machining to cope with conventional high-precision dimensions for interfaces.

The Centre Spatial de Liège (CSL), in Belgium is developing a new mechanism based on the Space Infrared Telescope for Cosmology and Astrophysics (SPICA) mission requirements. The Mode Selector Mechanism (Figure 1) moves a flip mirror that picks either a low or high-resolution beam and directs it into the instrument light path. This mechanism must ensure an accurate and reliable positioning of the flip mirror in two fixed and stable (unpowered) positions in a temperature range from 4 to 300K. The mirror is mounted between two flexure pivots providing a small angular displacement (+5/-2°) with a low spring torque of 4mNm/deg.

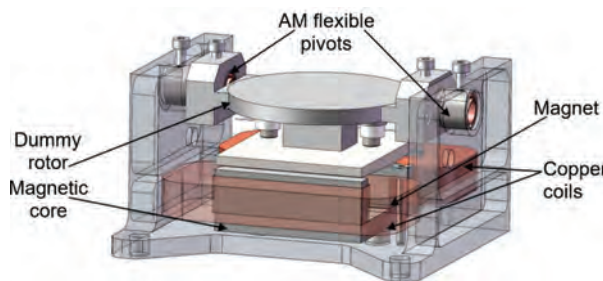


Figure 1: Mode Selector Mechanism (MSM).

Based on CSEM background in design and manufacture of precise Additive Manufacturing (AM) metallic flexible parts, the optimization of the flexure geometry was performed to cope with the specifications. To benefit at most from the AM possibilities, the pivot design integrates Interlocked Lattice Flexure (ILF) blades (Figure 2). This allows to increase the performances compared to commercial off-the-shelf products. The design integrates special features to ease the machining, which is performed to ensure precise tolerances at the interfaces (i.e. external diameter, length and concentricity).



Figure 2: AM ILF flexible pivot after machining.

The fatigue limit at room temperature of the pivots was validated early in the project on representative flexure blades with an infinite lifetime bending stress of 230 MPa and 450 MPa for 1e4 cycles. Surface finish processes using a chemical treatment were also evaluated to improve the cleanliness of these AM parts.

In total 12 flexible pivots were 3D printed in 316L stainless steel with a blade thickness of 210 µm and delivered to CSL for integration and testing in the mechanism. The ILF pivots were characterized at room temperature and ambient pressure both at CSEM and CSL to set a reference point, then cooled down to cryogenic temperature (4.2 K) with liquid helium (LHe).

The AM ILF pivots were tested in cryogenic conditions down to 4.2 K without performance degradation. The rotational stiffness of some ILF pivots was slightly higher than the requirement due to variations in flexure thickness and roughness. Nevertheless, the average rotational stiffness measurement was only 10% higher than the predicted simulation results.

Table 1: Flexible pivot rotational stiffness measurements.

Rotational stiffness	[mNm/deg]
Measurement at room T and pressure	4.0
Measurement at room T under vacuum	4.4
CSL measurement at 77 K	4.7
CSL measurement at 4.2 K	4.6
CSL measurement at room T after LHe	4.4

The evolution of the Young's modulus as a function of temperature is consistent with 316L material properties:

- increase by 7% from 300 to 77 K
- decrease by ~0.6% from 77 to 4.2 K

Two AM ILF pivots were integrated in the Mode Selector Mechanism (Figure 3) by CSL to verify the functionalities. The mechanism was actuated and successfully tested at room temperature, then under cryogenic conditions down to 4.2 K.

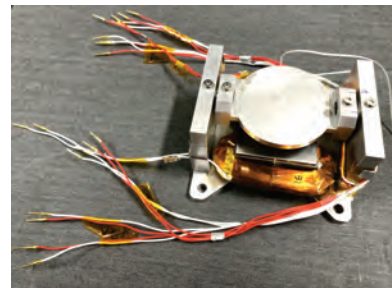


Figure 3: Mode Selector Mechanism equipped with ILF pivots (Courtesy CSL).

The AM interlocked lattice flexible pivots were successfully designed, printed and tested according to customer requirements. Functional AM pivots were obtained in four weeks including machining and cleaning, which confirms the possibility of fast production and the ability to have multiple iterations in case of design change.

This project demonstrates that flexible pivots – and more generally any kind of compliant mechanism - can be designed, optimized and produced by metallic additive manufacturing. The main advantages are the design freedom, the possibility to finely tune the characteristics according to a specific need and the fast production time. A wide range of alloys is available, including stainless steels, Titanium, Invar, Inconel and Aluminium.

The project partner is Centre Spatial de Liège (CSL), Belgium. CSEM thanks them for their support.

Efficient Anticorrosion Layer for Aluminum Current Collectors in Li-ion Batteries

J. Gay, A. Jaffrè

The interface between the aluminum current collector and cathode materials is crucial for ensuring long-term cyclability of Li-ion batteries. This interface is primarily degraded through corrosion of the aluminum current collector. Fast degradation of the aluminum current collector is observed when cycling at high voltages or when using corrosive electrolytes. This study presents the development of a hybrid protective and conductive coating on aluminum ensuring efficient corrosion protection of aluminum against LiFSI-based electrolyte up to 5.0 V vs Li+/Li. Investigation of coated aluminum in half-cell configurations with high-voltage cathode LMNO demonstrated a stable capacity after 100 cycles at 1C, whereas cells made with bare aluminum could not be cycled under such high voltage conditions.

Ensuring stable interfaces in Li-ion batteries is key for long-term cyclability. Regarding the interface between the aluminum current collector (Al CC) and the cathode materials, its degradation is mainly due to corrosion of the Al CC. Up to ~ 3.8 V, corrosion of Al is prevented by its native oxide layer of Al_2O_3 ^[1]. However, this latter can deteriorate when batteries are operated at higher voltages (e.g. 5.0 V) or in the presence of aggressive electrolytes (e.g. LiFSI salt). To mitigate corrosion of the aluminum CC, several strategies have been explored, including electrolyte engineering (e.g. salt conc.), incorporation of inhibitors, and coating the Al CC. When coating the Al CC, the deposited layer must fulfill the following criteria: (1) prevent corrosion, (2) maintain electron conductivity, and (3) establish stable interfaces with other battery materials.

In this study, a hybrid coating (HC) was deposited on Al CC to prevent corrosion while preserving electron conductivity. The coating formulation is adapted to bar coating and spray coating deposition methods. The corrosion resistance of uncoated Al and HC Al was firstly investigated in LiFSI-based electrolyte. Corrosion resistance tests were performed with six cycles of cyclic voltammetry between 2.5 and 5.0 V in 1M LiFSI in EC:DMC 1:1 (vol.)^[2]. The corroded area was then investigated using optical microscopy and quantified with image analysis. The corroded areas are reported in Figure 1 for uncoated and HC aluminum. It can be observed that unprotected Al is corroded to ~ 6% of area while HC Al is close to 0% area. This indicates sufficient corrosion protection thanks to the HC.

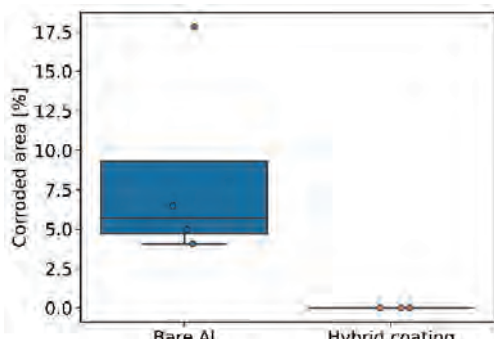


Figure 1: Percentage of corroded area of uncoated Al and HC Al after cyclic voltammetry tests in LiFSI-based electrolyte.

Battery cycling was then performed in half-cell configuration with lithium nickel manganese oxide (LMNO) cathode, coated on bare

Al CC and HC Al CC, against Li (electrolyte: LP71 + 10% FEC). Coin cells made with bare Al could not be cycled up to 4.9 V vs Li+/Li, probably due to a lack of protection of the bare Al CC. In comparison, cells made with HC Al could cycle for at least 100 cycles at 1C while maintaining a capacity retention above 90% (Figure 2).

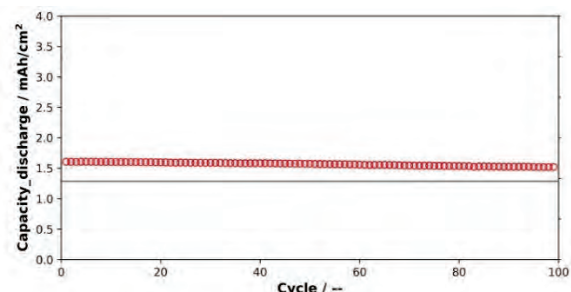


Figure 2: Electrochemical evaluation in half-cells configuration with LMNO, coated on HC Al CC, against Li.

The charge transfer resistance of such cells was also investigated by performing electrochemical impedance spectroscopy (EIS) before and after cycling, as shown in Figure 3. It can be observed that the charge transfer resistance decreases after 100 cycles at 1C, indicating the formation of a stable interface between the HC and the cathode materials upon cycling.

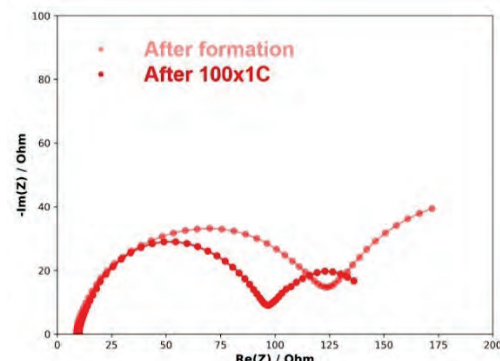


Figure 3: EIS data before and after cycling (LMNO vs Li).

Future works will focus on long-term cells evaluation up to 5000 cycles. Different electrolyte compositions will also be studied (LiTFSI salts). This work was funded in the frame of the SOLiD project (EU) under grant agreement number 101069505.

[1] Gabryelczyk, A., Ivanov, S., Bund, A., Lota, G., Corrosion of aluminium current collector in lithium-ion batteries: A review. *J Energy Storage* 43, (2021).

[2] Bizot, C. et al., Aluminum current collector for high voltage Li-ion battery. Part II: Benefit of the En' Safe® primed current collector technology. *Electrochim commun* 126, (2021).

Development of a Versatile Platform for Electrochemical Multi-sensing Evaluation

P. Clément, A. Beard, S. Khan, X. Lefèvre, P.-F. Rüedi, G. Bergonzi

Within the scope of internal (MIRA, EXBIDI) and European (ECLIPSE, AGRARSENSE) projects focused on developing electrochemical (bio)sensors for health and water monitoring, the need for a common sensing platform was identified allowing reliable characterization of different sensing layers. A user-friendly platform, with reliable electrical contacts and multi-sensing capability has been developed.

The development of electrochemical sensors involves multiple technological bricks, including a sensing layer. When focusing on the sensing layer development, commercially available screen-printed substrates are usually utilized. However, these substrates are often unsuitable for sensing layer requiring high electrode surface quality, as additives used in their fabrication can cause surface contamination and reduce charge transfer. Therefore, when developing a sensing layer, it is crucial to have a reliable substrate to minimize associated risks of failure.

To achieve this goal, we combined microfabrication and additive manufacturing techniques with electronic integration, to build a robust sensing platform. We selected silicon as the substrate with sputtered metal electrodes, chosen for its high purity and reproducibility across devices. Additionally, the electrode design can be adjusted to suit specific applications, allowing changes not feasible with commercial substrates.

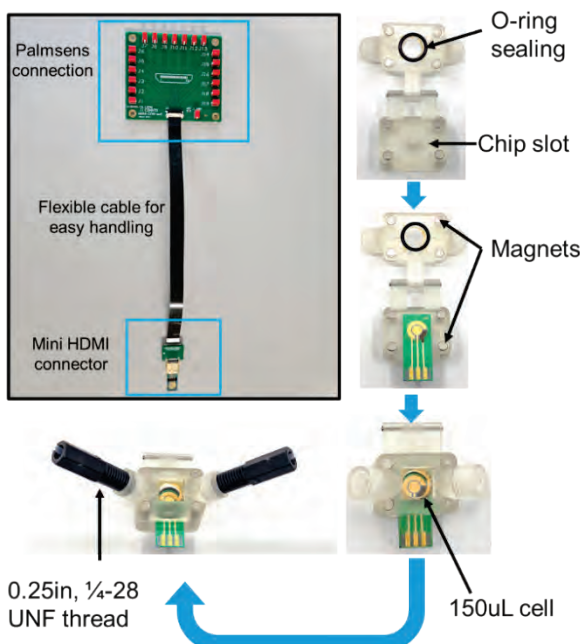


Figure 1: Different elements of the sensing platform.

To integrate a reference electrode (RE) on the silicon chip, Ag/AgCl ink was printed onto Ag electrodes using aerosol jet printing. For good electrical connectivity, we opted against wire bonding and chose a plug-and-play solution instead as it is cost efficient and user-friendly. Commercially available 20 output channels mini-HDMI connector was selected for its slot dimensions that are compatible with the thickness of a silicon wafer. A flexible cable connects the chip to a PCB, enabling further electrical characterization with measurement equipment. Additionally, a cartridge was designed and fabricated using stereolithography (SLA) 3D printing to transport the analyte to the silicon chip through a fluidic channel or well. The cartridge consists of a bottom section with a slot for chip insertion and a top section with an o-ring seal and fluidic channel. These two parts are securely closed using permanent neodymium magnets. The fluidic cell includes an opening with a glass window, sealed

with polyurethane to allow optical measurements. The cartridge is also compatible with standard microfluidic connectors with 1/4-28 (0.25 in) threads.

A series of electrochemical tests were conducted to demonstrate the efficiency of the newly developed setup and to verify the quality and suitability of the designed clean room electrodes. The outstanding reproducibility and reversibility of these samples was confirmed by measurements in electrolytes as shown in Figure 2.

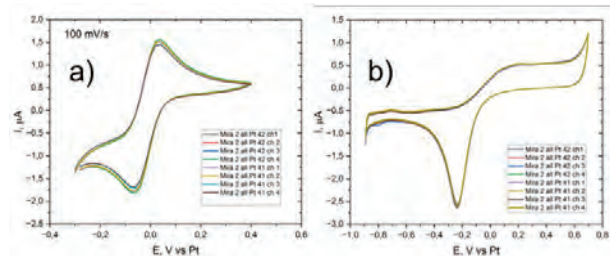


Figure 2: Pt working electrode test in $[Fe(CN)_6]^{4-}/[Fe(CN)_6]^{3-}$, CVs @100mV/s (a) and CV in 50mM H_2SO_4 (b).

This platform has been used for the detection of carbamazepine (CBZ), an active compound found in commonly used drug and highly durable in the environment, particularly in wastewater. Aptamers are a class of short single-stranded nucleic acids that can selectively interact with their target rivalling those of antibodies. An electrochemical aptasensor was developed where a conformational change is induced by CBZ target binding within the aptamer structure, which subsequently alters electron transfer between a redox tag appended at a distance and the surface of an electrode. The aptamer was modified with a thiol group on the 5'-end for immobilization on the gold sensing electrode and a methylene blue (MB) tag on the 3'-end for readout. For the sensor characterization, CBZ was diluted in PBS buffer ($pH=7.4$) at different concentrations and square-wave voltammetry (SWV) was recorded when the signal was stabilized. In Figure 3, an increase of CBZ concentration is correlated with a decrease of the current.

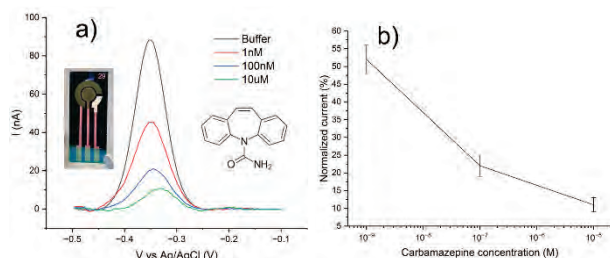


Figure 3: SWV of the aptasensor (a) with its corresponding calibration curve (b).

To conclude, a reliable sensing platform was developed and will support future studies on sensing layers. The authors would like to acknowledge financial support from the European Union (grants number 101046787 and 101095835) and CSEM.

Sensor Components for Health Monitoring of Newborns and Pregnant Women

S. Khan, X. Bulliard, N. Bonzon, C. Aguet, G. Dudnik, R. Pugin

Sensing components are developed for applications to health monitoring of pregnant women and newborns. One of the focus points is the manufacturing of novel dry electrodes for electrocardiograms (ECG) using novel ink compositions and processing techniques for deposition, such as AerosolJet Printing (AJP). Printing on different substrates, polymeric and fabrics, are also considered, and the different configurations were tested with the aim of applying them to the monitoring of vital parameters of pregnant women. In another use case, the focus is put one the manufacturing of new oxygen-sensitive patch that could be applied to the skin of newborns. Coupled to a read-out system, this transcutaneous oxygen monitoring is seen as a complementary technique to photoplethysmogram (PPG).

Dry electrodes are particularly adapted to long-term monitoring of health parameters, which is one of the targets of NewLife project. They would complement gel electrodes that are commonly used nowadays for short-term parameter reading. In this project, AerosolJet Printing has been used to manufacture dry electrodes for ECG monitoring using different nanoparticles based colloidal inks. For testing the impact of substrates, PEN (polyethylene naphthalate) and textile (with polyurethane adhered) were used to determine the best matching materials and process protocol. The current designs are inspired by existing geometries of electrodes for a test setup developed at CSEM, and the goal is to replicate the same dimensions and shape for AJP printing. In this study, three different metal nanoparticles-based materials are printed to evaluate the electrical performance, impedance matching and most importantly the conformability as well as biocompatibility of the electrode with human skin. The materials are silver (Ag), silver/silver chloride (Ag/AgCl), gold (Au), Carbon (C) and copper (Cu). Three different circular geometries are printed i.e. 10, 15, and 20 mm diameter. Electrodes are connected via a printed interconnection line (1 mm wide and 20 mm long), linked to a circular pad of 6 mm diameter on the other end. This is finally connected to the testing system via a snap button connector attached to the 6 mm diameter pad. To protect contact with the skin, the interconnection line is encapsulated with a thin epoxy layer, printed also via AJP. Fig 1. shows pictures of the printed electrodes with snap buttons connectors.

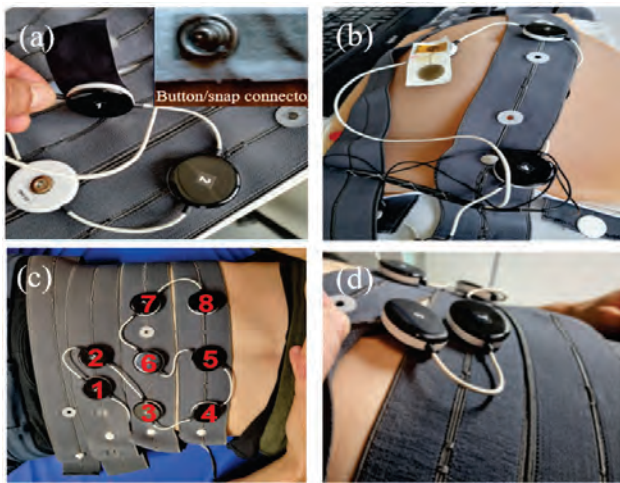


Figure 1: Test set-up: (a) Snap-button connection, (b). After connecting to the system and attached to skin, (c) All electrodes placement, (d). configuration with the stretching belt.

The test setup (comprised of ELAINE system) is used to test the dry electrodes in real time on human subjects (results shown in Figure 2). A total of eight electrodes are used in such configuration to cover the maximum surface area on the belly. From the initial assessment, silver based dry electrodes results are very promising (compared to standard gel-based electrodes)

and have relatively better response than the other AJP printed electrodes materials. These results have been validated for two patients so far, and more data is being generated now using silver electrodes.

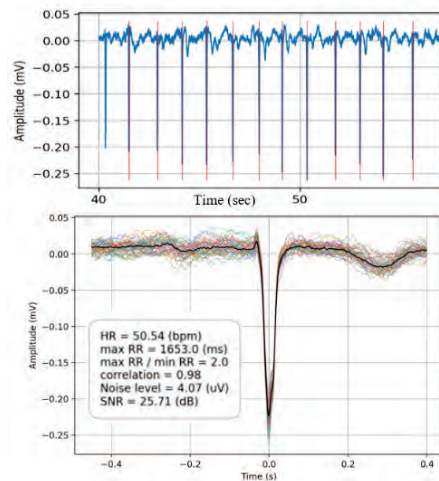


Figure 2: Signal response of the dry electrodes printed by AJP.

Regarding transcutaneous monitoring, the focus is put on the integration and interrogation of the oxygen-sensitive patch for transcutaneous monitoring. An illustration of a first geometry is given in Figure 3. The patch is placed on a silicon membrane (medical grade) for placement on the skin. This membrane is also an encapsulation layer to avoid perturbation by oxygen from ambient air. Additional tests should be needed to assess for the biocompatibility of the patch, and a semi-permeable biocompatible membrane can be added between the skin and the oxygen sensitive patch.

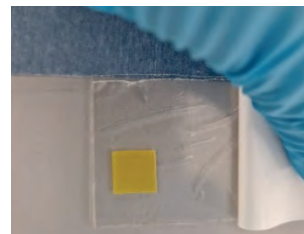


Figure 3: Oxygen-sensitive patch that can be applied to the skin.

In summary a series of different components are currently developed for novel sensing components. All these elements, coupled with other sensors developed by different partners in the project would lead to an increase in the comfort of newborns or pregnant women during long-term health monitoring. After final integration of all sensing elements, the common interrogation of multiple sensors will be the next step of the project.

This project has received funding from the Chips JU under grant No 101095792 and from the Swiss State Secretariat for Education, Research and Innovation (SERI)

Antibacterial Sol-gel Coatings, a Kinetics Study

X. Bulliard, M. Crenna, A. Finelli, X. Lefèvre, J. Gay, R. Pugin, J. F. Laithier •, C. Storrer •, T. Zwingelstein ••, V. Humblot •, A. Figarol ••, A. Marguier ••, F. Chérioux ••

Silver ions are added to sol-gel coatings to give antibacterial properties to the treated surface. The release of ions is followed kinetically with the aim of finding a window, for which the coating has antibacterial properties without being cytotoxic for human cells. This is achieved through the selection of a starting concentration of silver nitrate that is added to the sol-gel solution before coating. Despite not being thermodynamically directed, the antibacterial/cytotoxic effect is kinetically controlled. This approach would therefore be adapted to the treatment of parts or devices, for which antibacterial properties by contact killing is required.

Coatings based on sol-gel chemistry can be functionalized by adding a chemical species into the bulk material or at the surface. In the bulk, different approaches can be selected for having antibacterial properties. For instance, it is possible to mix silver salt with the sol-gel solution before coating or silver salt can be reduced to form finely dispersed Ag^0 colloids inside the coatings afterwards. Alternatively, silver Ag^0 nanoparticles can be directly mixed with the sol-gel solution before coating.

In this study, the approach based on the addition of salt was selected as it did not significantly modify the original properties of the sol-gel, typically its transparency.^[1] For the preparation of the coatings, a solution comprising sol-gel silane precursors, ethanol and acidified water was prepared. AgNO_3 salt was added to this solution in concentration ranging from 0.5 to 2.5 wt% and finally the solution was deposited on a glass substrate by dip coating. The thickness of the coating was controlled by adjusting the withdrawing rate of the substrate from the sol-gel solution.

To evaluate the bactericidal effect of the sol-gel coatings loaded with AgNO_3 , contact killing assays were performed on Petri dishes previously inoculated with 50 μL of *Escherichia coli* bacteria at 106CFU/mL, as shown in Figure 1. Bactericidal efficiency was observed for both coatings loaded respectively with 0.5 and 2.5 wt% of AgNO_3 , characterized by the absence of bacteria under the antibacterial coating. As control, the test was repeated with a bare sol-gel coating, without AgNO_3 , and no bactericidal effect was observed.

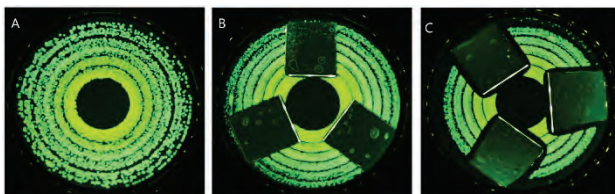


Figure 1: Contact killing experiment against *E. coli* bacteria culture: (a) growth control, (b) sol-gel 0.5 wt% AgNO_3 , (c) sol-gel 2.5 wt% AgNO_3 .

To assess for the cytotoxicity of the sol-gel coatings, the viability of human fibroblast cells was evaluated after exposure to the coatings at the two initial concentrations in AgNO_3 . After 24 hours exposure (Figure 2), all conditions led to a necrosis of cells, highlighting the difficulty to find a long-term thermodynamic range, for which the coating would be antibacterial without being cytotoxic.

A detailed evaluation of Ag^+ cations release as a function of time in liquid media was then carried to find a time span, during which the bacteria are killed without inducing fibroblast cells necrosis.

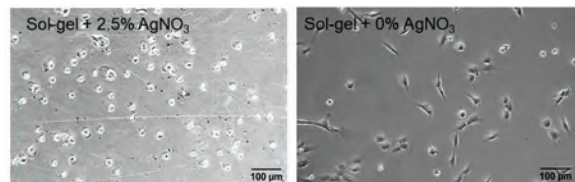


Figure 2: Cytotoxicity tests – microscopic observation of the fibroblast cells after 24 hours exposure to the sol-gel coatings: without AgNO_3 (right) and with 2.5 wt% AgNO_3 (left).

In these experiments, the cells and bacteria were exposed to the minimum inhibition concentration of bacteria (MIC and MIC/2). As expected, the bacteria viability dropped significantly in a very short time, while the cell response kinetics was slower. The results are illustrated in Figure 3. A decrease to 70% of viability was observed after 20.6 min for cells and 2.7 min for bacteria exposed to 2.5 mg/L Ag^+ cations (MIC concentration). The arrow in Figure 3 represents the time window, during which bactericidal protection would be achieved while maintaining the biocompatibility of the sol-gel.

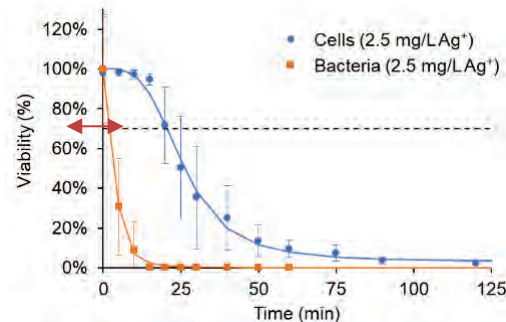


Figure 3: Kinetics of the viability decrease after exposure of bacteria (orange line) and cells (blue line) to the MIC concentration. The arrow represents the time for bacterial killing without cytotoxicity.

To summarize, silver salt incorporation into a sol-gel coating can be used to generate bactericidal effect by contact killing without altering biocompatibility. These effects are however time dependent. A way to further tune the kinetics would be to change the curing of the sol-gel coating, that directly impacts its density and directs the release of silver ions to the environment.

METEOR project is supported by the Interreg France-Suisse 2014-2020 program and has benefited from the European Regional Development Fund (FEDER), and on the Swiss side from federal and cantonal grants (Neuchâtel, Vaud). All authors thank them for their support.

• Coloral SA, Cressier, Switzerland
•• FEMTO-ST, Besançon, France

[1] T. Zwingelstein, et al., ACS Omega 2024, 9, 23, 24574–24583

Standardized TFLN Photonic Integrated Circuits Platform

H. Sattari, I. Prieto, H. Zarebidaki, J. Leo, G. Choong, M. Orvietani, F. Arefi, A. D. Torre, A. Mettraux, D. Herle, F. Dubois, Y. Petremand, M. Palmieri, O. Dubochet, M. Despont

We present a thin-film lithium niobate (TFLN) on insulator photonic integrated circuits (PICs) platform based on a 150 mm wafer-scale manufacturing technology. The platform comprises a library of standardized building blocks, so-called process design kit (PDK). Low loss waveguides and fast electro optical (EO) modulators are reliably manufactured in a well-defined foundry process addressing the demands from telecom to quantum applications.

Thin-film lithium niobate (TFLN) is a promising material for photonic integrated circuits (PICs), especially in the data-telecommunication industry. With high optical nonlinearity, a wide transparency window, piezoelectricity, and strong optical power handling, TFLN supports scalable solutions and advanced functionalities. It allows faster light modulation with lower power consumption compared to other PIC technologies. Recent advances in thin-film substrates and micromachining have led to significant milestones, including high-speed, low $V\pi$ EO modulators, frequency combs, and wavelength conversion. The challenge for industrial adoption is to achieve reliable, high-yield fabrication, paving the way for dedicated TFLN PIC foundries. TFLN PICs are moving towards process design kits (PDKs), offering tested building blocks and design rules similar to those in the semiconductor and silicon photonics industries. CSEM has established an open-access TFLN PIC foundry with a validated PDK and wafer-scale fabrication, enabling the integration of passive and active components—a significant step in integrated photonics.

Our fabrication process uses commercially available thin-film lithium niobate wafers with a technology stack comprising multiple waveguide layers, metal layers, and VIA structures. We produce passive components such as low-loss waveguides, grating couplers, multimode interference couplers, and directional couplers. The multiple waveguide layers facilitate advanced structures like efficient edge couplers for chip-to-fiber light coupling, with precise layer alignment for high performance. Metallization supports active components such as EO and acousto-optic modulators and thermal phase shifters, using a two-layer metal strategy connected by vias for complex electrical circuitry and efficient RF modulators. Cladding layers protect PICs, enhance waveguide performance, and allow electrical access, supporting hybrid integration and packaging. Our technology enables smooth waveguide patterning, narrow metal

wires for heaters, smooth chip facets, and double-layer edge couplers for fiber coupling, as well as EO modulators for different wavelengths from visible to telecom (Figure 1).

Rigorous inspection and characterization across multiple fabrication runs is maintained to ensure consistent reliability of such PDK components. Our component library, optimized for telecommunications, demonstrates continuous improvement, particularly with high-speed modulators and low loss waveguides. For waveguide propagation loss, our primary light-routing waveguide has seen significant improvement due to enhanced etching processes, with data gathered from multiple samples and wafers per run. We are optimizing the cladding process to consistently achieve losses below 0.5 dB/cm. Our edge couplers are design-tuned for varying spot sizes at chip edges. For EO modulators, recent runs have shown improved efficiencies, reaching around 2 V·cm. Our EO modulator PDK component development focuses on delivering high-bandwidth traveling wave modulators and CMOS-level voltage operation.

While we continue fine-tuning the manufacturing processes, a meticulous approach is required to address the interlinked parameters that influence outcomes. This progress fuels platform standardization and reliability.

In summary, the unique material properties and manufacturing advances in our TFLN PIC platform offer capabilities not easily replicated by other PIC technologies. Our open-access foundry and PDK development process, from design to testing, provide photonic designers worldwide with a dependable set of building blocks. This PDK empowers the development of compact, low-power PICs, paving the way for large-scale, high-performance photonic solutions. CSEM's PIC platform is a key technology in several European projects (ELENA, PATTERN, LOLIPOP, SPRINTER, CLUSTEC, QUANTIFY).

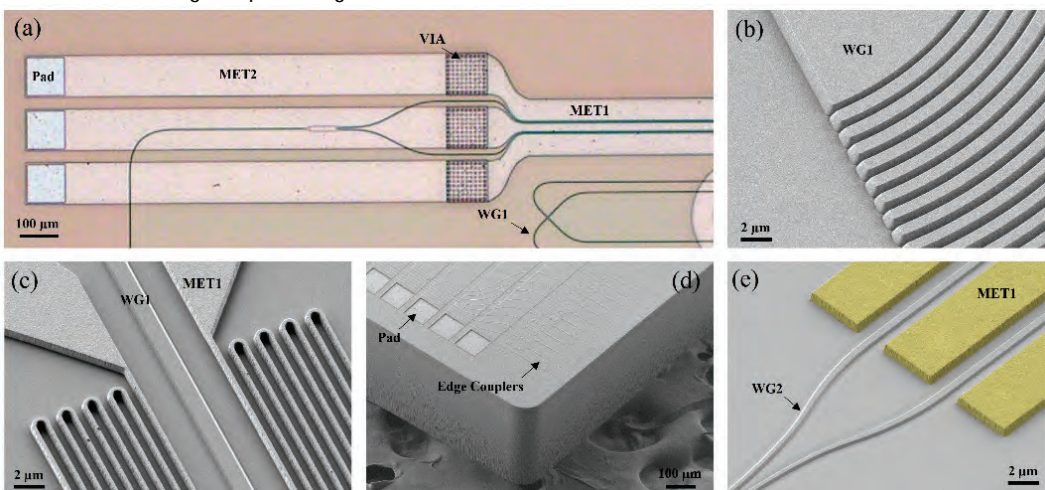


Figure 1: (a) Optical microscope image of a TFLN PIC after the fabrication, (b) SEM image of a grating coupler patterned in WG1 layer, (c) SEM image of a thermo optical phase shifter composed of a heater in MET1 layer and WG1 waveguide layer, (d) SEM image of a TFLN PIC encompassing a series of pads for electrical probing and double-layer edge couplers, and (e) SEM image of an electro optical modulator in WG2 and MET1 layers (MET1 layer false-colored).

Efficient Light Coupling to Thin-film Lithium Niobate on Insulator Photonic Integrated Circuits

F. Dubois, H. Zarebidaki, A. Mettraux, J. Leo, A. Della Torre, I. Prieto, Y. Petremand, O. Dubochet, M. Despont, H. Sattari

CSEM is a pioneer in the development of thin-film lithium niobate on insulator (TFLN) PIC foundry and aim to bring these advances to an industrial scale. This requires reliable fabrication processes and stable performance of the PIC components. Among the set of PIC components, optical couplers must hold a special care in terms of performance and reliability because they enable efficient light coupling between external optical fibers or light sources and on-chip waveguides. We illustrate here the development of an efficient double taper edge coupler designed to couple 5 μm mode field diameter lensed fiber. We experimentally demonstrate a coupling efficiency of less than 2.0 dB losses per facet.

Lithium niobate (LiNbO_3) is an attractive material for photonic applications, offering high Pockel effect for high-speed electro-optic modulation, broadband transparency and high-power handling capabilities. In recent years, thin-film lithium niobate (TFLN) has gained a lot of attention as key material for photonic integrated circuit (PICs), enabling higher integration, low consumption and efficient modulation for data and telecommunication. CSEM has developed and offers an open-access foundry service for TFLN PICs.

In CSEM's TFLN platform, fiber to chip coupling is a challenging topic due to large mode mismatch between the optical fiber and the highly confined TFLN waveguide mode. This is an important challenge for practical applications of the TFLN circuit as many of them requires low loss operation which is typically dominated by the fiber to chip coupling.

To overcome this issue, CSEM has developed and optimized a double taper edge coupler (DTEC) design based on the available layer stack in CSEM platform. The DTEC consists in a bilayer of LN waveguide, depicted in Figure 1a, tapered as depicted in Figure 1b to adiabatically couple the light of a fiber to the TFLN waveguide.

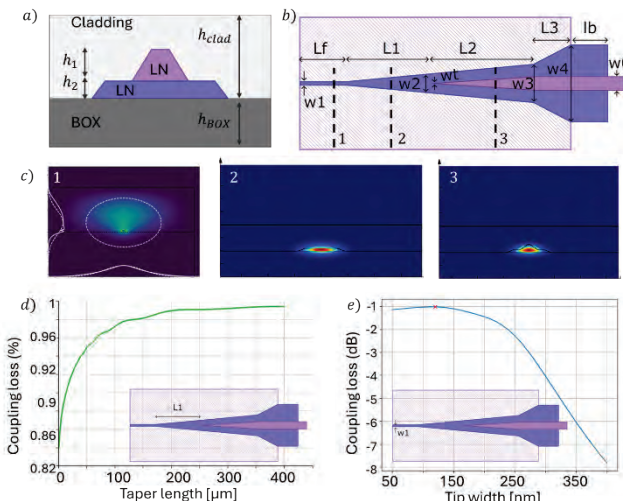


Figure 1: (a)-(b) Cross section and top view of the DTEC. (c) TE0 mode field distribution at the cross-sections depicted in (b). (d)-(e) Simulated coupling efficiency versus taper length and tip width.

The edge coupler has been designed to couple the light from a fiber with a 5 μm mode field diameter. The tip of the edge coupler

has a height of 200 nm and a width of 140 nm which is tapered up to 3 μm at the transition with the second layer over a length of 300 μm . The second layer has a ridge height of 400 nm and a width of 50 nm which is tapered up to a nominal width of 800 nm over a length of 30 μm . According to the simulation, the optimum width for the 5 μm MFD edge coupler is 140 nm as depicted in Figure 1e. The coupling efficiency increases with a longer taper length in the first layer. According to the simulation result depicted in Figure 1d, a length of 300 μm provide a 90% of mode conversion efficiency.

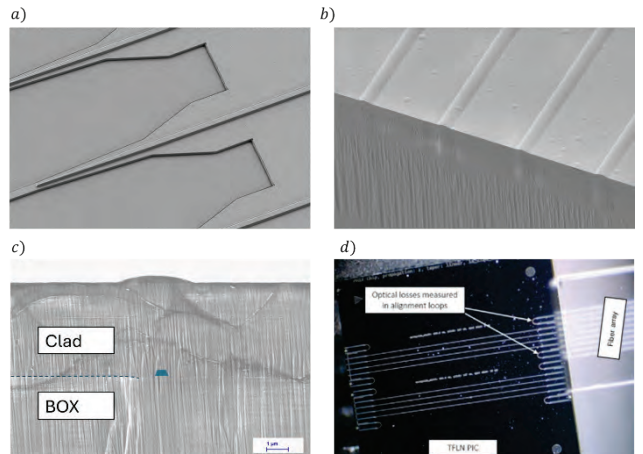


Figure 2: (a)-(c) SEM images of the fabricated chip with (a) top view of the DTEC (b) zoom-in of the tips of the DTEC array and (c) zoom-in on the edge coupling facet of the DTEC. (d) Picture of a TFLN PIC coupled to a fiber array.

The DTEC is fabricated on the TFLN platform developed by CSEM within Pattern project framework^[1]. It consists in a 600 nm thick X-cut LN on 4.7 μm thick BOX from NanoLN, cladded by a 4.7 μm thick silicon oxide. SEM pictures of the singulated chips can be seen in Figure 2a-c. Optical shunts with various lengths have been designed on the chip to enable active alignment of fiber arrays and coupling loss measurements. The micro-assembly of the fiber array and measurements has been carried out by Phix. The coupling efficiency observed is below 2 dB/facet which is a large step toward providing reliable optical interfacing for TFLN PICs and promising achievement for future improvement.

^[1] <https://pattern-project.eu/>

Electro-optical Modulators in a Thin-film Lithium Niobate Foundry Process

A. Della Torre, H. Zarebidaki, F. Dubois, J. Leo, A. Mettraux, A. Manzour, D. Herle, I. Prieto, O. Dubochet, M. Despont, H. Sattari

CSEM is pioneering the development of a thin-film lithium niobate (TFLN) photonic integrated circuits (PICs) foundry to bridge the technological gap between TFLN and other PIC platforms. Among the different photonic building blocks offered by our foundry, electro-optical modulators stand out as a crucial component. This is a brief survey of the performances of CSEM's electro-optical modulators. These components are of high importance for several applications, like telecommunications and quantum computing, that are currently being pursued by different European projects in which CSEM is involved.

Electro-optical (EO) modulators are essential devices in photonics, enabling the control of light signals by modulating properties like intensity and phase through the application of an electric field (Figure 1a). They are widely used in applications such as fiber optic communications and quantum computing. However, traditional EO modulators, often made from bulk lithium niobate, are bulky, power-hungry, and difficult to integrate into compact systems. Photonic integrated circuits (PICs) offer a solution by integrating EO modulators directly into small, scalable platforms, significantly improving performance. PICs enable miniaturization, lower power consumption, and faster modulation speeds, making them ideal for modern telecommunications and data centres. In particular, the use of thin-film lithium niobate (TFLN) EO modulators in PICs allows for precise control at higher speeds and with greater efficiency than traditional designs. Furthermore, fabricating EO modulators within a large-scale foundry process ensures cost-effective mass production, making PICs with integrated modulators a highly attractive option for widespread commercial applications. However, the fabrication technology for TFLN PICs has not yet reached the maturity required to fully meet the demand. CSEM is aiming to fill this gap by providing an open-access TFLN foundry [1], and EO modulators are at the core of this activity. Figure 1b and 1c show Scanning Electron Microscope images of CSEM's platform.

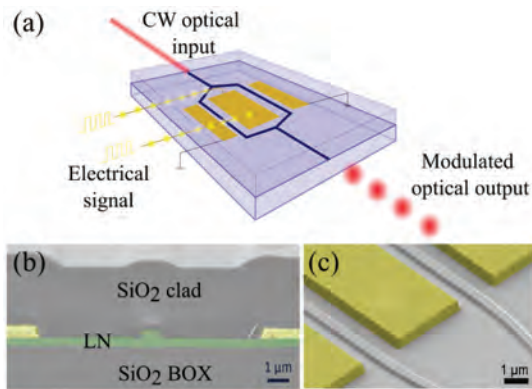


Figure 1: (a) Schematic representation of an integrated EO modulator. (b) Scanning Electron Microscope image of the cross section of our TFLN platform. (c) Close image of the metallization and waveguides.

When evaluating the performance of an EO modulator, two key metrics are often considered: V_{π} and the EO S21 parameter. V_{π} refers to the voltage required to induce a phase shift of π in the optical signal (i.e. switching from on to off state). A lower V_{π} indicates that the device requires less voltage to achieve modulation, making it more energy efficient. The EO S21 parameter represents the frequency response of the modulator, indicating how effectively it can transmit high-speed signals. A

[1] H. Sattari, *et al.*, An Open-Access Platform for Thin-Film Lithium Niobate Photonic Integrated Circuits (TFLN PICs), in CLEO 2024 (Optica Publishing Group, 2024), paper AW3J.6.

common approach to reduce the V_{π} is to increase the modulator's length and fold it so that it occupies a small chip area. By leveraging the two levels of metallization layers of our platform [2], we achieved V_{π} at the 1 V level in a 2.97 cm long modulator that fits in a compact 5mm × 5 mm chip (Figure 2a). This voltage value falls within the CMOS-level-voltage operation that enables to drive the device with fully integrated CMOS electrical circuits. We also measured an EO S21 parameter in a 3 mm long modulator with just 1.2 dB attenuation at 50 GHz (the limit of our testing instrument), suggesting a 3 dB EO bandwidth extending well beyond this frequency (Figure 2b). Moreover, in a foundry setting, achieving consistent V_{π} -length product across fabrication runs is critical for ensuring reliable, predictable modulator performance. Figure 2c shows the consistent V_{π} -length product that we measured in different fabrication runs.

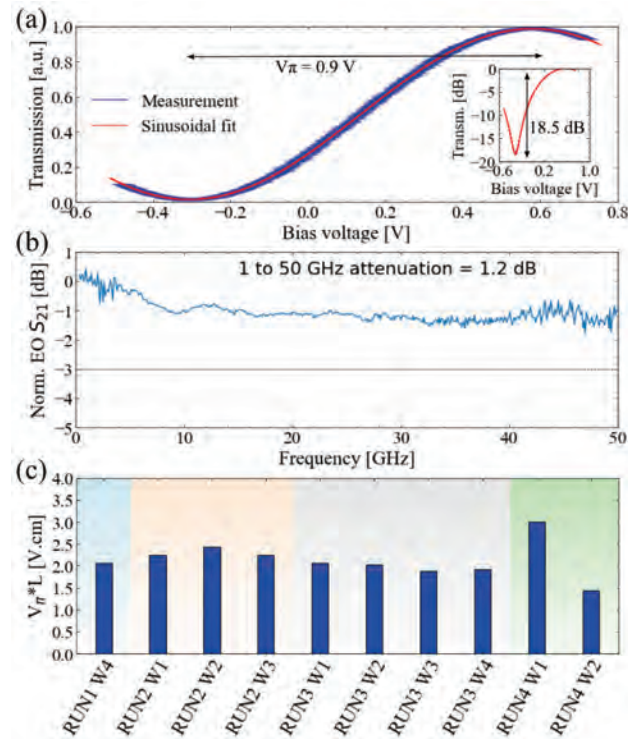


Figure 2: (a) Optical transmission of a folded modulator as a function of the applied electrical bias. (b) Electro-optical S21 parameter of a straight modulator as a function of electrical frequency. (c) Measured $V_{\pi} \cdot L$ in different fabrication runs and wafers.

In conclusion, CSEM is developing a foundry for high-yield fabrication of TFLN PICs, and efficient and fast EO modulators are at the core of this activity. CSEM's PIC platform is a key technology in several European projects (ELENA, PATTERN, LOLIPOP, SPRINTER), and we acknowledge their support.

[2] A. Della Torre, *et al.*, Ultralow Voltage Folded Electro-Optical Modulators in Thin-Film Lithium Niobate Foundry Process, in CLEO 2024 (Optica Publishing Group, 2024), paper AW3J.1.

Surface Acoustic Wave Actuator on Thin-film Lithium Niobate for Acousto-optic Modulator

F. Arefi, M. Despont, H. Sattari, G. Villanueva

Acousto-optic modulator (AOM) is a crucial optical component, functioning as filters, phase and frequency modulators, in a wide range of applications, such as optical networks, internet of things (IOT) and quantum computing system. CSEM, a thin-film lithium niobate on insulator (TFLN) PICs foundry pioneer is heading the development and standardization of various optical building blocks including AOMs.

Recent success in wafer-scale manufacturing of thin-film lithium niobate (TFLN) have introduced significant opportunities to develop novel optical components into photonic integrated circuits (PICs)^[1]. TFLN possesses a unique set of optical and mechanical properties, notably, exhibits exceptionally high piezoelectricity and photoelasticity coefficients, enabling the integration of optical and acoustic functionalities within a single material. AOM is one of the key building blocks in photonics integrated circuits that has different functionalities including frequency modulation, phase modulation and filtering in various applications^[2].

AOM enables precise manipulation of light using sound waves. By applying RF signal to an interdigital transducer (IDT) placed on top of TFLN, surface acoustic waves (SAWs) are generated on the surface of TFLN. This creates periodic variation in the refractive index of a medium as illustrated in Figure 1.

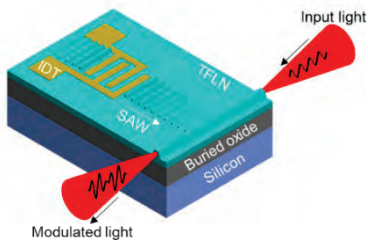


Figure 1: Schematic of acousto-optic modulator (AOM) and its interaction mechanisms.

The introduction of AOM at PIC scale to the commercial domain has been impeded by the absence of a standardized PIC platform. The aim of my thesis at CSEM is to introduce an efficient standardized AOMs as phase modulator and frequency modulator in a standard LNOI PIC platform.

The operation of AOM is driven by two primary multiphysics interactions: the electro-mechanical interaction, responsible for the generation of SAWs, and the photo-elastic and electro-optic interactions, which enable the modulation of light. During last year, we have focused on optimization of SAW devices. We conducted simulations and fabrication experiments to optimize various parameters of AOM to generate efficiently SAW on a X-cut TFLN (Figures 2a and 2c). Z orientation of TFLN is selected as the direction of acoustic propagation due to its high photo-elastic and electro-optic coefficients. Electromechanical coupling (k_{eff}^2) and quality factor (Q) are two key factors in SAW devices that are considered to evaluate the efficiency of SAW devices. The wavelength of SAW, denoted as λ , is equivalent to twice the pitch of IDTs. As λ decreases, the resonance frequency (f) will increase according to the relationship $f = \frac{v_{ph}}{\lambda}$, where v_{ph} represents the phase velocity of acoustic wave. While higher frequencies are desirable for stronger acousto-optic interactions, achieving them poses significant fabrication challenges and

limitations. We have identified several feasible wavelengths for fabrication, specifically at 1 μm , 2 μm , 4 μm , and 8 μm operating within resonance frequency range of 394 MHz to 3.55 GHz. The simulation parameters and results have been validated by actual fabrication outcomes. It was observed that as the wavelength decreases, the electromechanical coupling (k_{eff}^2) increases. However, it is coupled with a corresponding decrease in Q (shown in Figure 2b). Additionally, the effects of using gold and aluminum as electrode materials were tested and analyzed. Gold, with its higher conductivity, reduces parasitic resistance, enhancing device efficiency. However, its greater mass density, lowers the acoustic phase velocity, which in turn reduces the resonance frequency (Figure 2e) and increases wave attenuation and damping. Simulation results reported in Figure 2d show increase in gold thickness to 150 nm will increase k_{eff}^2 and Q. Although, quality factor cannot be estimated accurately using simulation. These effects make gold a preferred electrode material in AOM applications, as it shows higher electromechanical coupling at a thickness of 150 nm and the variability of Q at thickness is low.

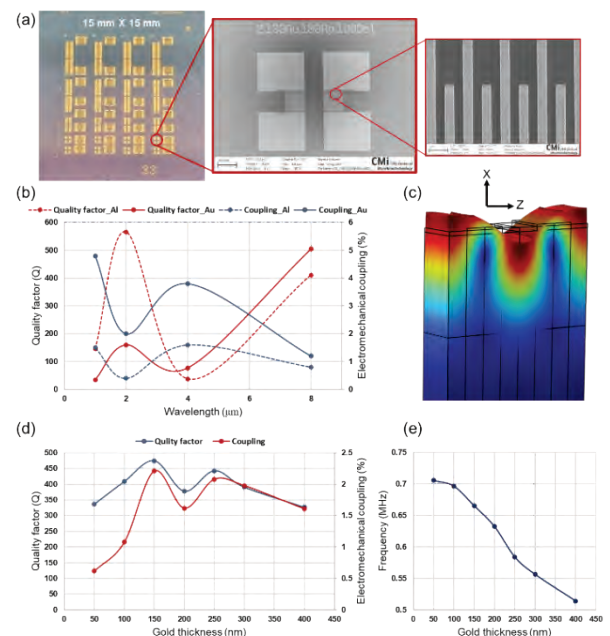


Figure 2: a) SEM image of fabricated IDTs with 1 μm pitch on X-cut TFLN; b) Experimental results of quality factor and electromechanical coupling of gold and aluminum with 100 nm thickness; c) Simulated Rayleigh surface acoustic wave generated on TFLN. Simulation results of effect of various thickness of gold on d) Q and k_{eff}^2 , e) resonance frequency.

As a summary, TFLN has proven that is a promising material for acoustic and AOM applications that can be developed as a standard building block in the TFLN PIC platform at CSEM.

[1] Sattari, Hamed, et al., Standardized TFLN Photonic Integrated Circuits Platform, European Conference on Integrated Optics, Cham: Springer Nature Switzerland, 2024

[2] Shao, Linbo, et al., Microwave-to-optical conversion using lithium niobate thin-film acoustic resonators, *Optica* 6.12 (2019): 1498-1505

Mastering of Advanced-shape Microlens Arrays at Wafer Scale

G. Basset, C. Schneider, F. Zanella

CSEM has been fabricating microlens arrays (MLAs) for decades and keeps improving their manufacturing using wafers-scale and high throughput processes. We previously reported ultra-high aspect ratio microlenses^[1] as well as combined multiple scale MLA – especially well fitting multi-project wafers (MPW) reticles^[2] – and gapless MLA^[3]. In latest developments, very low aspect ratio and asymmetric microlenses have been fabricated at wafer scale, sparking interest for multiple applications.

Microlenses are ubiquitous and enabling our daily digital life but are rarely visible. They are critical for the light coupling in and out of optical fibers, and so a key component in the backbone of internet and telecommunication networks, or in our smartphone sensors. Various manufacturing process allow the manufacturing of microlenses. However, photoresist reflow processes remain by far the most scalable for high quality microlenses at the wafer scale. These processes, while widely known, can still be further improved to reach new unmet specifications.

CSEM developed a photonic driven selective shape modification process allowing to modify each microlens shape individually within a microlens array (MLA), while keeping a wafer scale fully parallel processing^[4]. An example of microlens shape modification is made by creating asymmetric microlenses within a MLA.

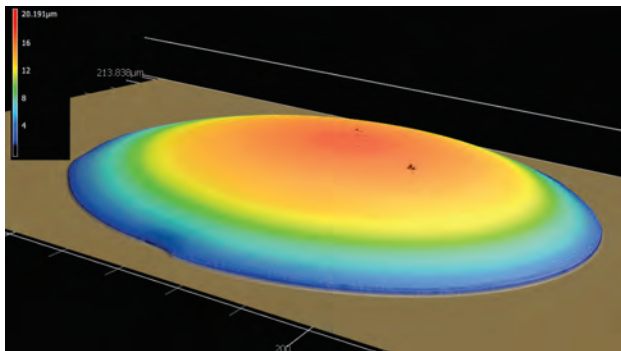


Figure 1: 3D profile of an asymmetric microlens, wafer-scale processed.

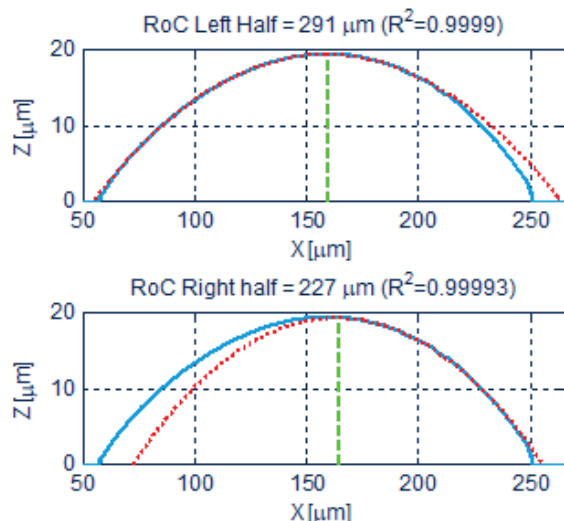


Figure 2: 2D profile cross-section of the above asymmetric microlens fitted on its left half and right half with spherical profiles.

[1] G. Basset, et al., Fabrication of Arrays of Quasi-micro-beads for Parallel Nanojet Super-resolution Imaging, [CSEM Scientific and Technical Report \(2021\)](#), 99

[2] M. K. Lahmar, et al., Mastering of Multi-sag Microlens Arrays at Wafer Scale, [CSEM Scientific and Technical Report \(2023\)](#), 71

The radius of curvature (RoC) of the left and right part of the microlens differs by 28% between the two halves, while keeping the benefit of a photoresist reflow process: ultra-low roughness, sub-micron positioning accuracy of each lens in the MLAs and wafer scale manufacturing.

Such shape customization and asymmetry can be done in a controlled way for each microlens independently in an array and at full wafer scale, enabling high throughput manufacturing.

Similar processes can be used to push the limits of aspect ratio of MLAs towards very low aspect-ratios. This enables manufacturing high quality microlenses with longer focal distances.

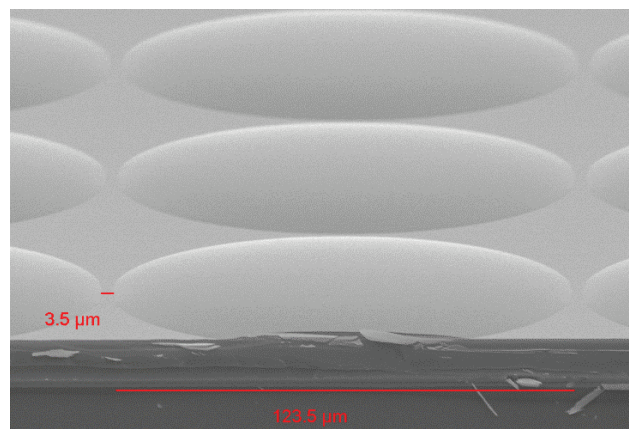


Figure 3: Very low aspect-ratio microlenses in a compact array.

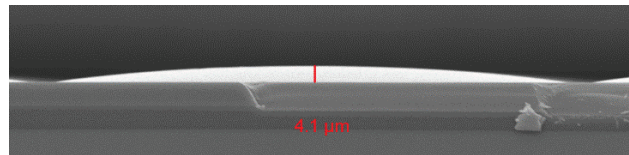


Figure 4: Grazing view of the above very low aspect ratio MLA showing a Sag of 4.1 μm.

Diameter/sag ratios as high as 30 to 40 can be reached while keeping open the possibility to reach densely packed arrays/small inter-lens gaps.

Such developments enable micro-optics suppliers to broaden the range of their products to meet more customer specifications or to replace complex and long post-processing, such as reactive ion etching transfer into substrates by faster processes, increasing the throughput and efficiency of the process and reducing the associated energy consumption.

[3] F. Zanella, et al., Increasing the Quantum Efficiencies of Quantum Devices with Microlens Arrays, [CSEM Scientific and Technical Report \(2022\)](#), 87

[4] <https://www.csem.ch/en/tailored-services/mla-foundry-services/>

MedPhab – Photonics Solutions at Pilot Scale for Accelerated Medical Device Development

R. Krähenbühl, V. Zubkovs, P. Cristofolini, S. Graf, A. Voelker, F. Zanella, G. Bassett, N. Blondiaux, G. Spinola Durante, S. Cattaneo, F. Kurth

In collaboration with other partners of the EU-project MedPhab, CSEM has set up a pioneering Pilot Line dedicated to manufacturing, testing, validating, and upscaling of new photonic technologies for medical applications. Leveraging CSEM's expertise in microelectronics, microfluidics, nanotechnology, and system integration, we support the design, optimization and manufacturing processes of innovative medical devices.

Medical device industry is a rapidly growing market for photonics technologies, with applications ranging from diagnostics to surgical tools and therapeutics. MedPhab's comprehensive approach aims at providing solutions for the main challenges of the photonics industry and RTO community. To establish sustainable operations, three high-level objectives were targeted:

- Set up a reliable open access pilot line for accelerated product development
- Mature technologies further through Use-Cases
- Demonstrate MedPhab operational pilot line model through Demo-Cases

CSEM participates in the pilot line, offering various design, manufacturing and characterization services, such as UV-replicated microlenses, fiber optics design & assembly, thermal management FEM modeling, microfluidics including prototyping and simulation, all printed Pt-MEAs, surface activation, and laser-based hermetic sealing.

Throughout the project, we have matured our technical portfolio regarding medical applications and applied them successfully to several demo cases with different customers as following:

For the startup Maculaser CSEM has contributed to the development of a new therapeutic eye treatment device which can trigger natural healing response of retinal cells by selective local laser heating. Using optical simulations, CSEM has developed and built an integrated infrared illumination module, to illuminate the cornea for real-time eye tracking (Figure 1). Additionally, a low-cost power monitoring system was designed, to measure the effective laser power delivered to the retina. Both contributions were successfully integrated into Maculaser's prototype device.



Figure 1: Integrated illumination system for real-time eye tracking.

For Polar, microlenses were UV-replicated on a photonic integrated circuit (PIC) to collimate the beam emitted by a widely tunable (1495 nm - 1615 nm) III-V-on-Si laser (see Figure 2-left).

With Bialoom, CSEM developed simulation tools (Figure 2-right) to optimize channel geometries and flow conditions on their PICs, tailored to the specific binding and detection chemistry of each case. This approach enabled a 4000-fold increase in detection speed for protein and bacteria in blood.

For the startup SpectraCure, simulations were performed to optimize their new photodynamic cancer treatment. Hereby cancer cells absorb light-sensitive drugs, which are activated by

selective laser irradiation and thus kill the cancer cells. With thermal simulations we could significantly improve the cooling efficiency of the laser modules, reduce the price and assembly costs of the device. Optical simulations were used to analyze stray light in these laser modules. A better optical filtering solution was found, resulting in a 20-fold increase of the signal-to-noise ratio for the laser fluorescence monitoring signal.



Figure 2: (left) SEM image and ray-tracing simulations at 1490 nm and 1610 nm of a microlens on a PIC C-band grating coupler; (right) COMSOL particle concentration simulation in over a PIC integrated in a fluidic cartridge.

With Surfix Diagnostics CSEM further developed their Advanced Drainage System (ADS) cartridge (Figure 3) for scalable production. PIC integration was performed in a clean room using industrial-grade machines, plastic parts were injection molded by Jabil, and high-throughput roll-to-roll tape assembly was demonstrated by VTT. Following technology transfer, Surfix can now produce up to 15,000 cartridges annually on their own.



Figure 3: Disposable microfluidic ADS-cartridge.

With Femtorays, CSEM developed a scalable cartridge concept, produced in small scale, to house their PIC in a PCB with wire bonds and tape protection. This allows Femtorays to validate their PICs and detect specific molecules in saliva.

With SDS Optic, CSEM worked closely with the customer to develop an optoelectronic system including an electronic control unit for a biosensor analyzer used for in vivo diagnostics of HER2-positive breast cancer. CSEM addressed application-specific optics requirements, reduced system costs, and considered regulatory requirements for medical devices commercialization. The device prototypes were validated by the customer.

For the startup Perseus Biomics, CSEM developed a photochemical surface modification process to improve the performance of a microbiome profiling chip. By using vacuum UV photopatterning, wettability patterns were produced to direct the DNA combing process of Perseus and improve its fluorescence optical read-out.

This project has received funding from the European Union's Horizon 2020 research and innovation program under grant agreement No 871345.

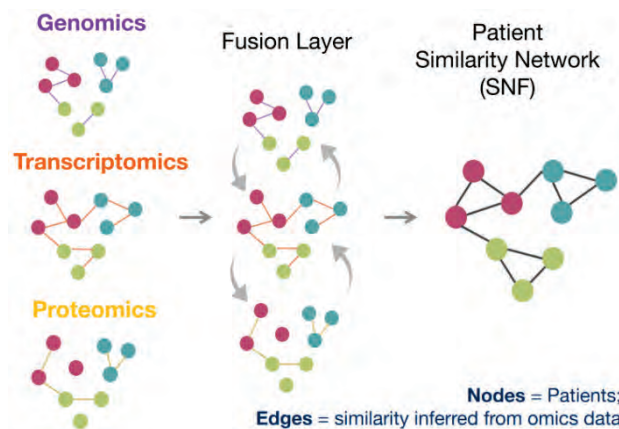
Revolutionizing Precision Health through Multi-modal and Knowledge-driven AI

T. Heinemann, S. Jagtap, J. Meirer, L. D. Wittwer, F. Luongo, M. Lamarine, C. Poussin

Market analyses in the life sciences and pharma sectors underscore the need to make data business-relevant and contextual through integration, modernization, and enhancement, as well as to develop explainable AI. To address these needs, we created PatStrat and DeepBINN, two AI frameworks that are adaptable to various applications across healthcare and therapeutic development, ranging from biomarker discovery and drug candidate selection to personalized medicine.

Precision health is revolutionizing our understanding of human biological variation, driven by breakthroughs in two key areas: the high-throughput measurement of molecular entities across diverse biological scales and the extraordinary advances in AI-driven information integration and predictive analytics. These innovations enable a comprehensive approach to disease management, offering not only personalized diagnoses, treatments, and prognoses but also new strategies for monitoring individual health to detect or even prevent the onset of diseases^[1]. However, the challenge remains in developing frameworks that provide fast and actionable clinical insights while maintaining robustness and compliance within complex international regulatory landscapes, particularly in Europe.

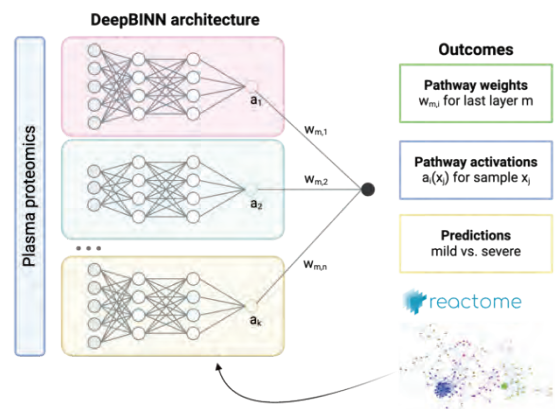
To address this challenge, we have implemented PatStrat, an innovative multimodal network embedding framework that leverages state-of-the-art graph representation learning methods for patient stratification. This framework seamlessly integrates biological a priori knowledge to capture intricate relationships among patients. By combining data from diverse sources — pharmacometrics, genomics, transcriptomics, proteomics, cytokines, and clinical records — PatStrat reveals biologically significant latent patterns that facilitate patient stratification and predict drug responses (Figure 1). Testing PatStrat with hematological data from myeloma patients has shown promising outcomes, including improved patient stratification with better prediction of drug responses, identification of novel biomarkers associated with treatment outcomes, and the development of disease-specific pharmacodynamic biomarkers through the integration of signaling pathways.



Further steps are required before patients can receive tailored therapies based on their personal disease manifestations as

suggested by PatStrat. These include validation in independent cohorts and clinical settings. For commercial use of the platform, another challenge is ensuring the AI model conforms to regulatory requirements, particularly regarding AI in medical devices, data protection, and data enablement. For example, to adhere to the guidelines of the recently formulated EU AI Act, the AI system must be developed to ensure its operations are sufficiently transparent, allowing natural persons to oversee its functioning^[2].

Our further development on biologically informed neural networks demonstrates how this can be achieved. By integrating biological pathway information directly into the neural network architecture, we built an exclusive model called DeepBINN that allows for estimating the significance of each pathway during the training process^[3]. We tested DeepBINN in a preliminary study stratifying patients suffering from different sub-phenotypes of acute kidney injury and showed how to assess pathway importance and how this translates into robust biomarker signatures without resorting to post-hoc explainability methods (Figure 2). Importantly, this gain in interpretability was achieved while maintaining state-of-the-art classification performance.



Moving forward, we are building on these innovative tools providing robust, interpretable insights to enhance decision-making across precision health and biomedical research domains. For instance, we see their application benefiting CDMOs in tasks like stratifying new biologic candidates, optimizing bioreactor conditions, selecting promising drugs, assessing toxicity, and defining optimal cell selections for cell therapies. This versatility highlights their potential to transform healthcare and life sciences, driving the next generation of personalized medicine and therapeutics.

[1] S. S. Lim, *et al.*, Reporting guidelines for precision medicine research of clinical relevance: the BePRECISE checklist, *Nat. Med.* 30 (2024) 1874

[2] J. Schmidt, *et al.*, Mapping the regulatory landscape for artificial intelligence in health within the European Union, *Npj Digit. Med.* 7 (2024) 229

[3] J. Meirer, *et al.*, DeepBINN: A tailored biologically-informed neural network for robust biomarker identification, *IEEE SDS* (2024) 246

Smart Labware for Organoid Positioning

S. Heub, R. Ischer, F. Boudoire, C. Loussert-Fonta, D. Di Stadio, C. Cattin, S. Boder-Pasche, G. Weder

Organoid technologies have transformed biomedical research by providing advanced 3D models that closely replicate human tissues and organs, enabling more accurate studies of disease mechanisms, drug development, and personalized medicine. Despite significant progress, challenges remain in standardizing tools for precise organoid manipulation and positioning, which are critical for improving experimental reproducibility and data quality. To address this, CSEM has developed innovative multi-well plate inserts designed to securely position and immobilize 3D cell models, offering a scalable solution that enhances precision in organoid handling and analysis.

Organoid technologies have advanced significantly, offering powerful models that closely mimic human tissues and organs for research and therapeutic applications. State-of-the-art techniques enable the generation of complex, functional organoids, providing unprecedented opportunities for studying disease mechanisms, drug discovery, and personalized medicine. Multiple platforms are now available for a reproducible and high-throughput production of organoids. However, the availability of standardized, scalable tools and methods for manipulating and positioning organoids is now one of the main challenges towards enhanced precision and reproducibility of experiments and data consistency [1].

CSEM has developed multi-well plate inserts designed to precisely position and secure 3D cell samples on a standard multi-well plate format (Figure 1). When used with the plate, the positioning insert ensures the accurate placement of organoids in a designated area of the well during loading. Additionally, the holding insert applies gentle pressure to keep the sample stationary during fluid movements caused by plate handling or liquid exchanges, ensuring consistent sample analysis. The holding insert combines hard and soft materials with a smart design, unlocked by additive manufacturing technologies. It minimizes sample damage by reducing mechanical stress and preserving structure and functionality during manipulation. A classical lid on top of the inserts ensures sample sterility and suitable gas exchange.

CSEM's smart labware for organoid positioning and immobilization promises optimized analysis for more precise imaging, monitoring, and endpoint assessment.



Figure 1: CSEM multi-well plate labware for organoid positioning and immobilization.

The technology was initially developed and validated with brain organoids ranging from 250 µm to 3 mm in size, facilitating precise electrophysiological analysis on a 24-well multielectrode array custom plate co-developed with 3Brain AG [2][3]. The insert labware immobilizes 3D cell models directly on the electrodes, enabling safe liquid handling and efficient measurement over

time (Figure 2). Results confirmed sample integrity, biocompatibility of the inserts, and the labware's effectiveness in maintaining electrical contact between the organoid and the electrodes for various samples. The inserts are placed into the plate using a customized locking mechanism integrated between the plate wells.



Figure 2: Top view (left) and electrophysiological measurements (right) of brain organoids positioned in the center of a multielectrode array using CSEM's 24-well plate smart labware inserts.

A preliminary assay on a colorectal tumoroid model confirmed a similar potential for the technology for live imaging applications. In this study, non-fluorescent HT-29 spheroids surrounded by a layer of fluorescently labeled HT-29 cells were immobilized at the bottom of a transparent well-plate using the holding insert labware. Microscope imaging confirmed the efficient immobilization of the sample over days and under multiple manual medium exchange and plate-moving operations, while enabling cell migration tracking on the spheroid's surface (Figure 3). In this context, the technology presents a great advantage for orientation-sensitive applications and future correlation of 3D cell models and single-cell data.

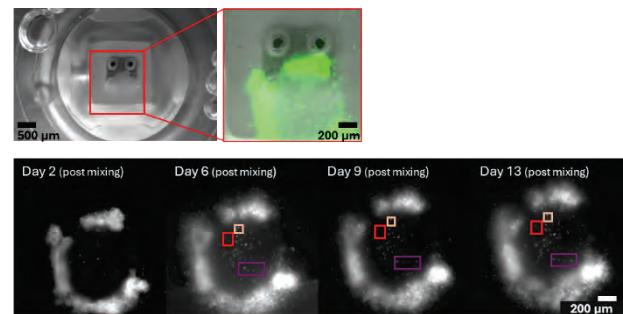


Figure 3: Microscope images of HT-29 spheroids immobilized at the bottom of a transparent well-plate using CSEM's smart labware inserts.

CSEM's next steps in further advancing the technology are the integration of fluidic components for local perfusion, optimization of the z-axis precision and upscaled manufacturing. This future integration promises the best possible features for complex 3D in vitro models, promising significant advancements in the field

[1] Lab Chip, 2022, 22, 4043

[2] www.3brain.com

[3] Innosuisse project 56426.1 IP-ENG

AirLiwell – Organoid Production and Culturing at the Air-Liquid Interface

R. Wimbish, S. Heub, R. Ischer, C. Biffi, L. Jandet, S. Boder-Pasche, G. Weder

Organoids are an attractive model for developing and testing new drugs, but their production is complex and lacks standardization. Many organoid production methods involve their submersion in cell culture medium, which limits oxygen diffusion and leads to cell death due to necrosis in the organoid centers. University of Geneva have developed AirLiwell, a technology for culturing organoids at the air-liquid interface to improve this process. CSEM is developing a platform to increase throughput and standardization of AirLiwell production through semi-automated gel structuring in custom labware.

Organoids are growing in popularity as a drug development model system, largely due to their increased physiological relevance. Development of high-quality organoids for this purpose is hindered by production methodologies, leading to issues in standardization. Current efforts to improve standardization involve growing organoids in structured microwells; however, this strategy requires submerging the microwells in cell culture medium, which hinders oxygen diffusion into organoid centers and impacts health and growth.

Researchers at the University of Geneva developed the innovative AirLiwell technology, in which organoids are cultured in hydrogel microwells at the air-liquid interface to overcome this problem (Patent application EP4029934A1). AirLiwell increases organoid production standardization by growing organoids in hydrogel microwells on porous membranes to allow efficient nutrient and oxygen exchange (Figure 1). Hydrogels are structured using stamps with dense pyramidal microstructures that are used as a mold.

CSEM and the University of Geneva aim to increase scalability and standardization of this process, including the creation of an upscaling platform for producing the AirLiwell technology, and the development of custom multi-well plate labware for culturing organoids at the air-liquid interface [1].

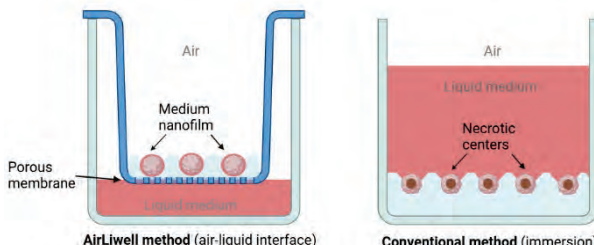


Figure 1: Schematic of AirLiwell vs conventional method for growing organoids in microwells.

Previous to this collaboration, AirLiwell method was implemented by hand, and could be performed in 6- and 24-well plates. CSEM's platform for AirLiwell upscaling was designed to facilitate the process in a high-throughput manner for 96-well plate format, which would be meticulous and time-intensive if done by hand (Figure 2). The platform allows users to transfer melted agarose gel from a heated reservoir with ergonomic pipette access into custom made 96-well inserts using a multichannel pipette and subsequently structure the gel into microwells using structuring stamps.

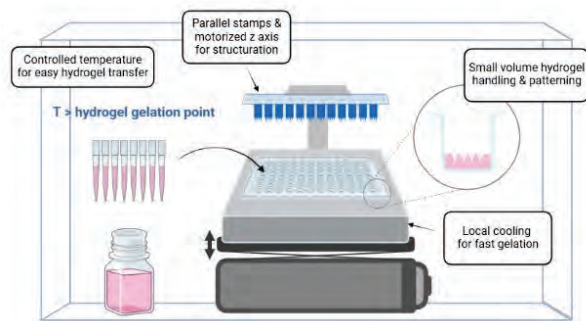


Figure 2: Schematic of the AirLiwell upscaling platform for automated and parallelized structuring of hydrogels in custom labware.

To increase the throughput for organoid production, a custom labware was developed for the AirLiwell upscaling platform. The labware allows for creating AirLiwell technology in 96-well format, increasing the production capacity of this technology. In addition to custom 96-well plates, the labware includes custom-made insert strips which contain individual wells where the gel is structured. The bottom of each well has a porous membrane which allows cell culture medium to form a nanofilm around the organoids, providing continuous nutrients and promoting oxygen diffusion throughout the organoid. As each well of an insert strip contains multiple microwells (each of which will grow a single organoid), the 96-well plate format of the AirLiwell technology allows for the standardized and parallel production of hundreds of organoids per plate with efficient oxygen and nutrient exchange from their environment.

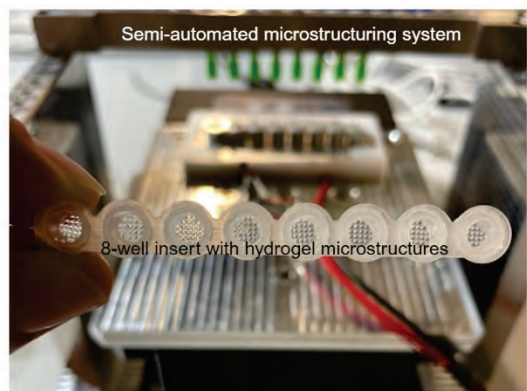


Figure 3: System for hydrogel structuring (background) and 8-well insert strip with structured hydrogel microwells (foreground).

The upscaling allowed by semi-automation and adaptation to 96-well format greatly increases standardization and throughput of producing the AirLiwell technology.

[1] Innosuisse project 107.610 IP-LS

Bioreactors – Inline Sterility Test and Nutrient Multi-sensing Module

M. Dorrestijn, T. Valentin, S. Graf, C. Beyer, M. Fretz, N. Schmid, R. Arnet, C. Biffi, H. Chai-Gao, R. Jose James, R. Limacher, C. Obrist, P. Odermatt, J. Rohrer, J. Zhou, S. Andrieux, C. Fragkos, E. Thelander, S. Cattaneo, F. Kurth, S. Paoletti, V. Revol, L. Tacchetti •, R. Penterman •, H. Bouwers •, J. Ruiter •, H. Boogert •, C. Spruijttenburg •, L. ter Stege •, E. Schreuder ••, R. Dekker ••, A. Boksi ••, M. Super *, J. Scott *, S. Lightbown *

A microfluidic cartridge is being developed for bioreactor process monitoring. It uses photonic sensors to detect microorganisms and nutrients in real-time, reducing costs and improving quality control. This technology is of interest to pharmaceutical companies, CROs and CMOs.

In bioreactors, cell cultures are used to test or produce pharmaceuticals, tissue transplants, or algae-based biofuels, among other applications. These products, however, are often prohibitively expensive. One of the reasons is the occasional loss of cell cultures due to growth of microorganisms or an imbalance of nutrients; so far, however, no solution exists for inline sensing of bioburden and nutrients.

An established technique for capturing microorganisms is to extract them using magnetic nanobeads functionalized with antibodies. However, these antibodies are raised against a single bacterial species only.

As a solution, we are developing a microfluidic cartridge assembly with integrated photonic sensors (PICs) to detect any bacterial species (interferometrically) and all key nutrients (Raman spectroscopy). Figure 1 shows the microfluidic components for up-concentrating and sensing bacteria and nutrient levels. The final cartridge assembly will be inserted into an instrument that automates the movement of reagents and the optical readout of the PICs.

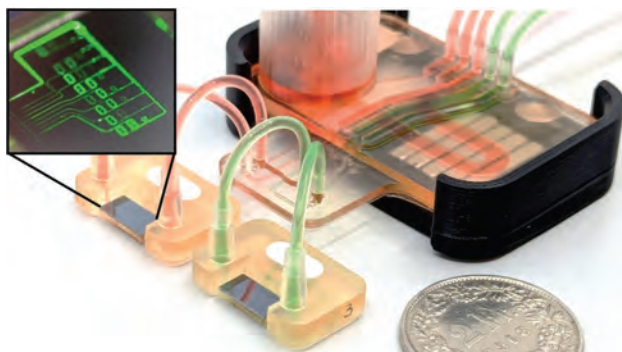


Figure 1: Laboratory prototype with disposable sensing (left) and pretreatment cartridge (right).

To detect any bacterial species and allow for a general alternative sterility test, we use a process involving magnetic nanobeads and a synthetic version of a human innate immune protein called mannose-binding lectin (MBL), which binds to a sugar moiety found on the cell walls of many bacteria [1] (Figure 2a). CSEM tested various bacteria and nanobead types to produce nanobead-bacterium conjugates (Figure 2b).

Preliminary tests demonstrate the ability to up-concentrate magnetic beads as well as to capture nanobead-bacterium complexes onto sensor surfaces (Figure 3).

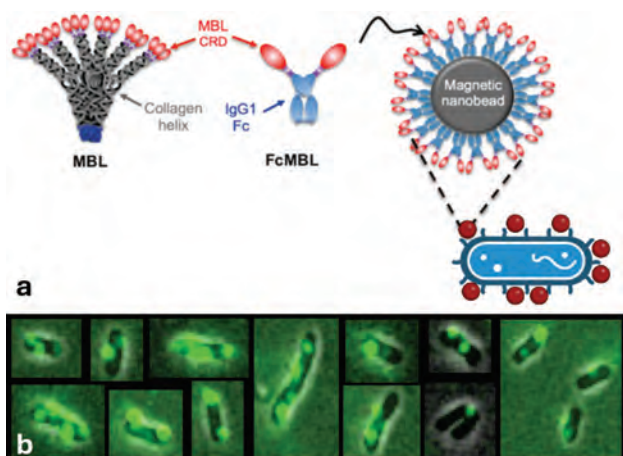


Figure 2: a) Structure of the functional group (FcMBL) on the nanobeads. b) The bacterium *P. protegens* conjugated with green-fluorescent 128-nm magnetic beads.

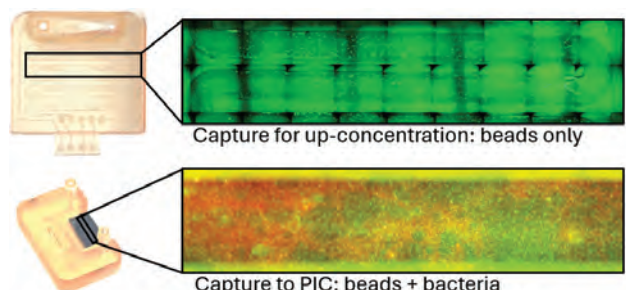


Figure 3: Fluorescence micrographs of magnetically concentrated beads (green) and bacteria (red).

Next steps in the fluidic development include optimization of the bacterial capture efficiency, osmotic up-concentration of nutrients, and design of a user-friendly and scalable cartridge. Once ready, the system will be tested by implementation partners: a manufacturer of bioreactors and an end user.

This work was (partly) funded by SERI through the Horizon Europe program. [2] CSEM gratefully thanks the EC and SERI for their support.

• DEMCON, The Netherlands.
• LioniX International, The Netherlands.
* Wyss Institute at Harvard University, USA

[1] K. A. Kite, et al., FcMBL magnetic bead-based MALDI-TOF MS rapidly identifies paediatric blood stream infections from positive blood cultures, PLoS ONE 17 (2022) e0276777.

[2] HORIZON-CL4-2022 project LIBRA 101093150, www.libraproject.eu.

Optical Sensor System for Monitoring Cardiac Tissue Contractility in a Multi-well Plate

E. Möhr, P. Cristofolini, J. Goldowsky, L. Jandet, Y. Shynkarenko, S. Cattaneo

Cardiovascular diseases are the number one cause of deaths globally. The number of cardiovascular drugs in the research pipeline has declined. The EU project EMAPS-Cardio aims to develop heart-on-a-chip cell cultures for precise *in vitro* cardiac models in both healthy and diseased states. The technology based on electro-mechanoactive polymer-based scaffolds will facilitate the development of physiologically relevant heart-on-chip devices with enhanced sensitivity and accuracy. CSEM has developed and tested an optical sensor system for continuous monitoring of cardiac tissue contractility during its maturation and *in vitro* drug testing.

Cardiovascular diseases (CVD) are responsible for 45% of deaths in Europe and cost the European economy hundreds of billions a year. Despite this, only a few drugs targeting CVDs have been approved in the past decade, primarily due to high failure rate. The European project EMAPS-Cardio, part of Horizon 2020 program, aims to address this challenge by developing heart-on-a-chip cell cultures for accurate *in vitro* cardiac models in healthy and diseased states. To achieve that, electro-mechanoactive polymer-based scaffolds (EMAPS) are being developed and combined with bioactive membranes to optimize the differentiation of the human induced pluripotent stem cell to adult-like cardiomyocytes. The scaffolds will then be placed in a bioreactor to enable continuous monitoring of the cardiac function parameters, such as contractility, action potential, and cardiac bio-markers.

As a part of the EMAPS international team, CSEM has developed an optical sensor for continuous monitoring of cardiac tissue contractility during its maturation and *in vitro* drug testing. The sensor comprises three main components: the imaging system, the readout electronics and the control software. The imaging system uses a multi-lens array to project 10x magnified images of trackable pillar surfaces placed within each well in a 24-well plate onto a full-frame CMOS-camera (Ximea CB200MG-CM). A frame grabber card transfers images to NVIDIA Jetson Orin, a compact and powerful AI edge Linux computer. The in-house developed python-based software controls the camera, a LED illumination PCB-board and performs contractility calculations. For electrical stimulation of the scaffold, CSEM has developed a multi-channel potentiostat, capable of supplying a ± 1.5 V bias voltage across the working and reference electrodes, with the ability to measure current within the range of up to ± 15 mA. During the measurements the EMAPS are maintained under controlled environment (humidity and CO_2) within a customized stage-top incubator.

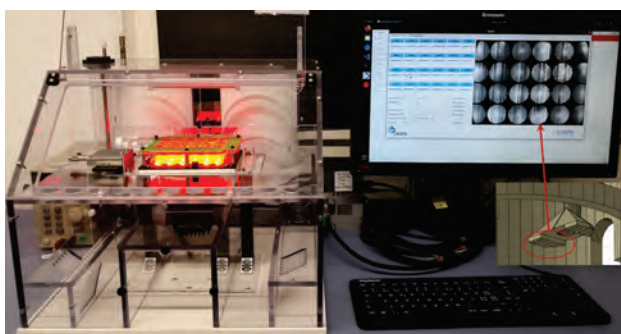


Figure 1: EMAPS tracking sensor in an incubator box; Also shown in the picture is the trackable surface of an insert with a bendable post for scaffold attachment. Each post has a dedicated structured tracking surface, optimized for high contrast features, ensuring that neither the EMAPS scaffold nor the attached cells are influencing the contractility sensors performance. FOV for each well is approx. 500 μm .

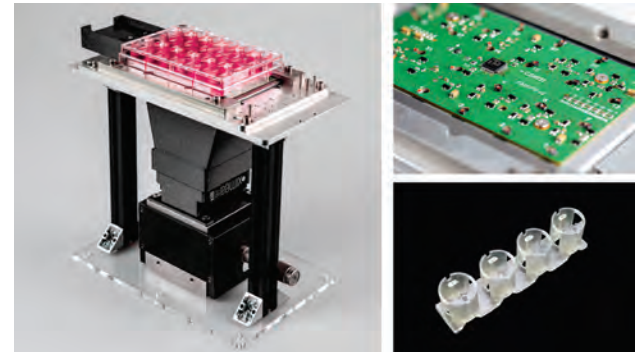


Figure 2: Optical reader module, a LED illumination PCB-board and inserts with trackable pillars.

Various tracking algorithms were tested and optimized to enhance motion-sensitivity and result accuracy. Lab tests with dry wells have confirmed that parallel tracking works reliably for all 24 wells. To simulate equal displacement in all the wells, the entire well plate was periodically moved using a micro-screw. The motion magnitude in all wells is measured with an accuracy of less than $\pm 4\%$ (Figure. 3b). However, the absolute position of the tracked surface drifted slightly over time, particularly in two corner wells shown with bold lines (Figure. 3a). Immersing inserts in RPMI liquid significantly reduces image contrast compared to dry condition, which affects tracking reliability. Despite this, it was still possible to track 20 wells with 6% accuracy. In the first real tests with EMAPS contractions of only a few microns were measured with a 1 μm resolution, meeting all the requirements.

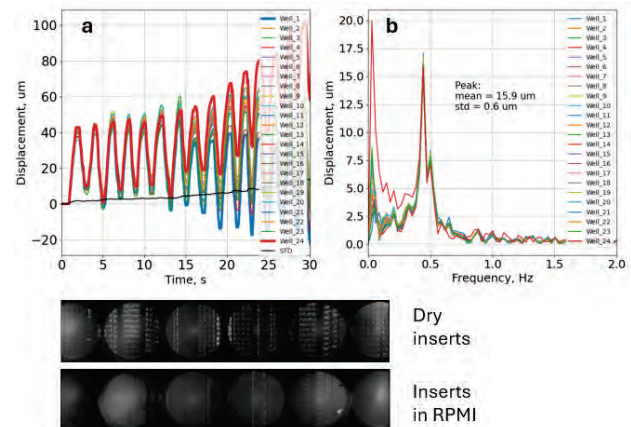


Figure 3: Parallel tracking of periodic motion in all 24 wells with displacement magnitude of $15.9 \pm 0.6 \mu\text{m}$. Absolute position of the tracked surface, drifts slightly with time (STD of displacement increases), especially for two corner wells shown with bold lines.

Tests with cardiac cells are in progress to assess the differentiation of the stem cells into cardiomyocytes.

The EMAPS-Cardio project has received funding from the European Union's Horizon 2020 research and innovation programme under grant agreement No. 953138.

Compact, Safe, and Automated Air Samplers for Collection of Viral Aerosols

R. Limacher, V. Zubkovs, D. Bayat, N. Schmid, D. Schmid, S. Bitterli, K. Krasnopolksi, H. Chai-Gao, F. Boudoire, D. Di Stadio, M. Renggli, C. Beyer, C. Obrist, J. Rohrer, I. Stergiou, S. Paoletti, S. Cattaneo, Jaeyoun Jang •, Artur Summerfield •

Within the projects AirViMo and VirAir, CSEM developed portable, high-efficiency air samplers based on different operating principles to safely collect airborne viruses. These size-selective systems capture pathogens ($1\text{-}10 \mu\text{m}$) at a high flow rate ($0.1 \text{ m}^3/\text{min}$) and can be interfaced with point-of-care diagnostics for rapid virus detection, aiding in future outbreak management.

SARS-CoV-2 has shown how important aerosols are for the global transmission of viruses. Indoors, viruses can spread through the air over long distances and lead to super-spreader events. Monitoring viral load in the air is complex because large volumes of air must be screened, creating a need for new air sampling technologies.

High particle collection efficiency is a crucial parameter for viral aerosol sampling in a possibly contaminated environment with low aerosol concentration. In the Innosuisse project AirViMo, in collaboration with Stat Peel AG and the Federal Institute of Virology and Immunology (IVI), CSEM developed a portable, high-efficiency air sampler prototype for viral load monitoring. The AirViMo sampler (Figure 1) features two particle size separation stages: one to remove particles $>10 \mu\text{m}$ and an impactor stage with a surface-functionalized collection bin for viral particles. Testing showed over 85% efficiency for particles $>1 \mu\text{m}$, with a 50% cutoff at particle size of $0.5 \mu\text{m}$.

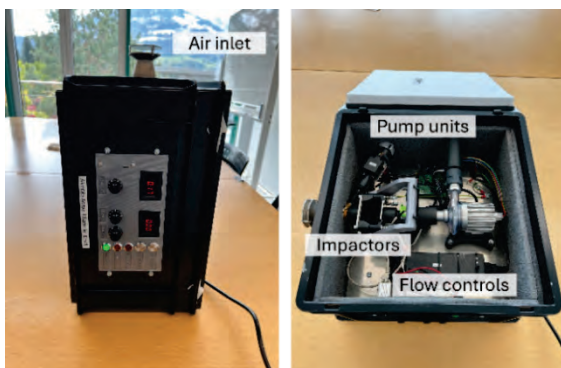


Figure 1: AirViMo sampler with air inlet at top plate (left) and inside view showing impactors, pump units and flow control (right).

In evaluation tests performed at IVI, the AirViMo sampler outperformed a commercial six-stage Andersen Cascade Impactor, showing 2.7 times higher viral RNA recovery (Figure 2). The AirViMo design simplifies RNA extraction and reduces sample preparation steps, enhancing efficiency and reducing costs.

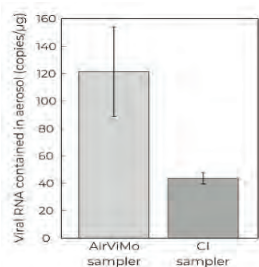


Figure 2: Comparison of viral recovery per aerosol mass from 1 m^3 air sampling for the AirViMo and Andersen Cascade Impactor.

Field tests included monitoring influenza A virus in a containment facility and on a public train. The sampler collected viral RNA in

all positive control samples at relevant particle aerosol concentrations, demonstrating its high performance. The AirViMo sampler is a breakthrough in pathogen sampling in air, offering high efficiency, ease of use, and potential for widespread monitoring in public spaces to improve public health.

In addition to the high collection efficiency, further unmet needs for commercial samplers are automatic sample collection, transfer from the collector to an analyzer and virus detection on-site. To address these challenges, CSEM led the development of a virion collection and elution module for airborne virus sampling and analysis device as part of the VirAir project (Figure 3), in collaboration with the companies GMD Biotech and Volotek.

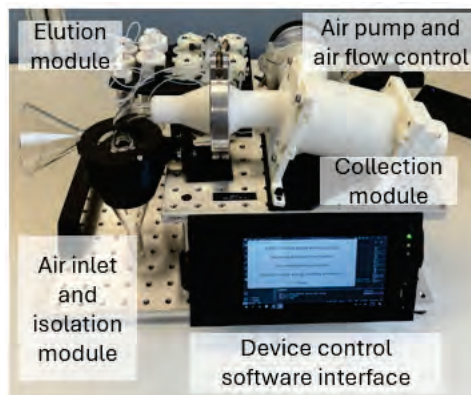


Figure 3: VirAir prototype with virion isolation, collection, and elution modules.

The collection module enables capturing of isolated virions and small particles ($< 5 \mu\text{m}$). The larger size particles are filtered by a cyclone-based sorter, installed before the collector. A high resistance air pump allows operating the device at an air flow of up to 100 L/min . The collection module includes a rotating liquid impactor, consisting of a high-speed rotating cup filled with a sampling liquid that serves as the capturing agent for airborne particles. The captured particles, including virions, are eluted in the liquid through the elution module, allowing for subsequent analysis. An automated control interface for the sampling and elution modules was developed, as well as protocols for sample collection, up-concentration and surface decontamination. The VirAir prototype has been integrated into an airborne virion analysis system for detection of respiratory viruses in the air using nanobiosensors, which is being developed by the project partner GMD Biotech in South Korea.

The AirViMo project has been supported by the Swiss Innovation Agency (Innosuisse) under contract 49735.1 IP-LS. The VirAir project has been financed by the Korea Institute for Advancement of Technology (KIAT) under the project number P00019785.

• Federal Institute of Virology and Immunology (IVI)

Towards Miniaturized, Eco-responsible, and Multi-sensing Platforms for Point-of-care

J. Heidler, G. Bouilly, M. Monroe, A. Zandara, D. Migliorelli, S. Demuru, B. Petkus, C. Seitz, J. Disser, J. Kim, P. Nussbaum, L. Burr, S. Paoletti, F. Kurth

The innovation in point-of-care (POC) products is remarkable and is driving a growing demand for sensors; however, sustainability has not yet become a standard in material selection. This presents a key opportunity to improve ecological footprints, as sensor test strips and cartridges are single use. Transitioning POC devices, that incorporate electronics, such as electrochemical sensors or connectivity components for digital readouts, to sustainable inks and substrates would reduce their environmental impact without incurring additional costs. CSEM's functional electrodes, made from sustainable materials, have shown competitive performance against conventional plastic electrodes for glucose and potassium sensing.

The global POC diagnostics market is expected to grow at a compound annual growth rate of 6% to 10% from 2024 to 2030 [1]. This growth is driven by significant innovation fueled by rapid technological advancements, which render POC devices as increasingly competitive to conventional lab testing, offering advantages such as faster result availability, lower costs, and improved patient outcomes, while enhancing comfort for patients in decentralized settings.

POC devices comprising electrochemical sensors or connectivity components for digital readout would benefit from a technology shift to sustainable inks and substrates. CSEM's printing facilities, offering screen-, inkjet- and aerosol jet printing, work on feasibility projects to down-select the best sustainable candidates, shown in Table 1. Our studies indicate that a combination of promising cellulose-based substrates from the industry and sustainable polymers, such as ethyl cellulose, can effectively replace conventional plastic substrates which are, by design, the largest portion of point of care devices. Examples of screen-printed functionalized electrodes on validated sustainable substrates are shown in Figure 1a and 1b.

Table 1: Successfully down-selected sustainable candidates.

Class	Conventional materials	Sustainable alternatives
Substrate	PET, PI, PC, PCB	Paper, PLA, Ethyl cellulose
Dielectric ink	Acrylates, Urethane, Epoxy	Ethyl cellulose
Conducting ink	Silver	Copper, Carbon

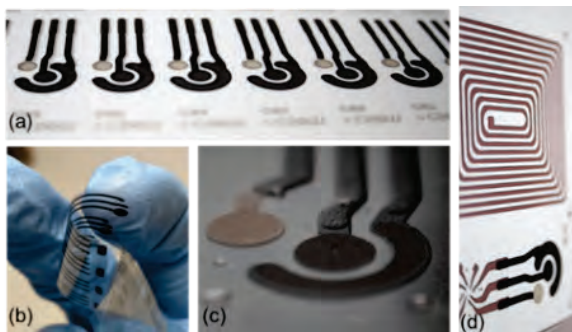


Figure 1: Sustainable substrates are promising candidates for screen printed single-use electrodes [(a) and (b)]. Ethyl cellulose as a dielectric demonstrates high precision in screen printing (c). The successful application of copper ink in a point-of-care device featuring screen-printed electronics highlights its potential for mass production (d).

Moreover, it is already possible to replace conventional dielectric inks deposited via screen printing with more sustainable ethyl cellulose mixtures at high precision (Figure 1c) whilst maintaining

insulating properties. Amongst the conducting materials necessary for signal transmission, the use of copper as a low-cost, high conductivity material for printed electronics is a relatively new approach. Traditionally, silver-based inks have been the go-to material for printed conductors, but they are expensive and environmentally challenging. Copper, on the other hand, is abundant, cheaper, and has better sustainability potential, making it ideal for applications like IoT nodes and disposable electronics. Figure 1d highlights a successful process development to print copper antennas on paper substrates.

Focusing on sustainable substrates, we compared printed electrodes on ethyl cellulose to our benchmark classic printed electrodes on PET: The versions made on sustainable substrates could serve as a base for conventional glucose sensors. As shown in Figure 2a, their performance is comparable to glucose sensors made on PET. Additionally, the sustainable versions demonstrated compatibility for functionalization with polymeric ion-selective membranes, which are necessary for potassium sensing, as illustrated in Figure 2b.

Our feasibility studies highlight that cellulose-based substrates combined with sustainable polymers and conductive inks can effectively replace conventional plastic substrates and environmental critical metals in point-of-care devices.

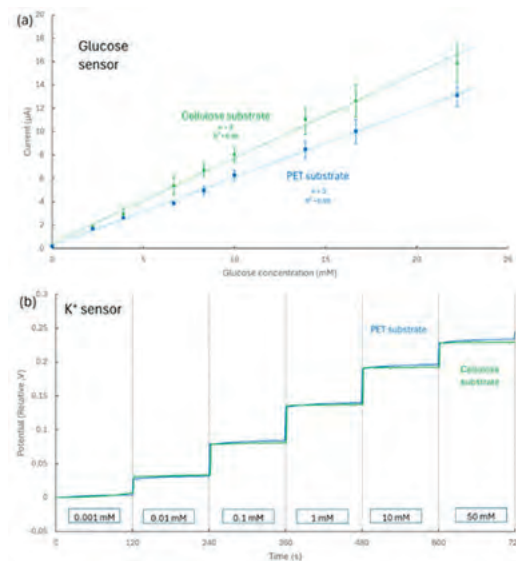


Figure 2: Comparative performances for conventional (PET) and cellulose substrates for 2 different sensor technologies, amperometric glucose sensor (a) and potentiometric potassium ion sensor (b).

This research received funding by the European Union under grant agreement No 101112109 (SUSTRONICS) and No. 101112065 (EECONE).

[1] Horizon Databook. (2023). POC Diagnostics Market Analysis Report 2024 - 2030 (Report ID: 978-1-68038-046-0).

Microfluidic PIC Integration for Aquaculture

S. Graf, M. Fretz, R. Arnet

Aquaculture is crucial for a sustainable path to provide the growing world population with nutritious food. Pathogen outbreaks pose a major risk, making early detection and timely response essential. CSEM and the PhotoSens team have been working on a photonic biosensing platform based on silicon nitride waveguide technology with integrated active components for such applications. Scalable processes for integrating the PIC in a microfluidic cartridge and a prototype desktop readout instrument were developed. DNA biomarkers were identified, primer-probe sets designed, and qPCR assays developed. The hybrid PIC platform successfully demonstrated biosensing. CSEMs role focused on the cartridge and PIC integration.

Biosensors are crucial in medical diagnostics, agriculture, and environmental monitoring, supporting global goals for health, zero hunger, and clean water. A significant challenge is sustainably providing nutritious food for the growing population. Aquaculture, the farming of aquatic species, plays a key role due to its high nutritional value and low carbon footprint. However, disease outbreaks pose significant risks, costing the global aquaculture industry \$6 billion annually.

To address this, biosensors based on Photonic Integrated Circuits (PICs) have been developed. These sensors offer high sensitivity, real-time measurement, and cost-effective production. The integration of PICs in microfluidic cartridges enhances their functionality, allowing for precise control of fluid flow and efficient detection of pathogen-specific biomarkers. This technology enables early detection and monitoring of pathogens in aquaculture facilities, contributing to healthier and more sustainable food production.

While the partners Surfix Diagnostics and Phix focused on the active PIC production, selective coating and biofunctionalization, CSEM focused on cartridge development. In contrast to earlier PIC integration processes, CSEM developed a new method to encapsulate the PIC flush to the cartridge surface with height differences < 12 µm. With this new method (In-PCB method, Figure 1), the PIC footprint can be significantly reduced, and the flow conditions be improved for better detection compared to the standard On-Channel method.

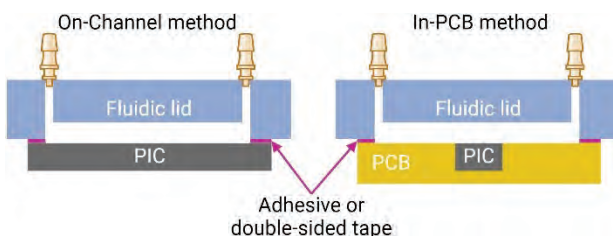


Figure 1: PIC integration methods.

With the PCB as the basis of the cartridge (Figure 2), laser and photo diodes could be wire bonded and this way directly interfaced with pogo pins from the instrument which was developed by LRE medical (Figure 3). Additionally, the PCB has a heating structure incorporated, which allows to pre-heat the liquid to e.g. 37°C for optimal detection or provoking out-gassing and later bubble removal through the degassing membrane in front of the sensor.

The PIC integration process is already performed on industrial grade machines in the clean room. For early prototypes,

cartridges are milled for fast design iteration cycles but already optimized for injection molding (when higher production volume is required). For validation purposes, CSEM offers small scale production from a few to several thousands of cartridges depending on the project status.

When the operator inserts the cartridge into the instrument, the interfaces are automatically air tightly connected and the blisters emptied into the intermediate reservoirs. The operator then inserts the sample with a needle syringe through the septum. The liquids are then pushed with a syringe pump towards the liquid level checks to have a defined start.

In a final step, the PhotoSens project team has been able to successfully perform a first biological detection test on 100 nM *Aeromonas salmonicida* (potential salmon aquaculture pathogen) DNA with a hybrid chip and the presented test setup. The results are published in the open access journal MDPI [1].

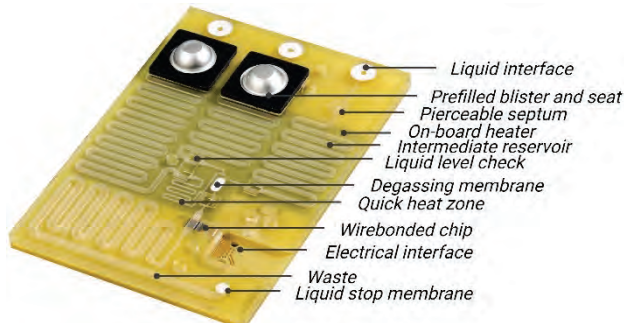


Figure 2: PhotoSens cartridge with highlighted details.

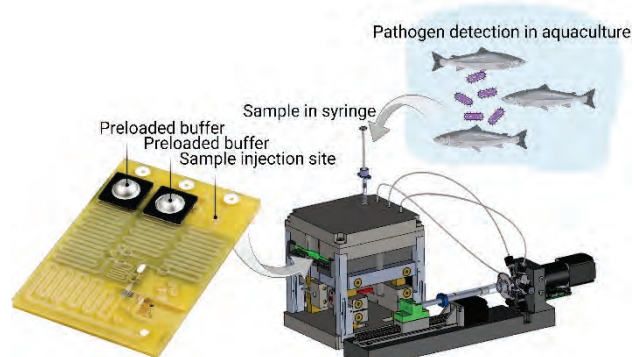


Figure 3: Test set-up with the bread board instrument and cartridge.

This research received funding from the European Union's Horizon 2020 research and innovation programme under grant agreement No. 965643 (PHOTO-SENS). For more information, see <https://www.photo-sens.eu>.

[1] Knoben, W.; Graf, S.; et al., An integrated photonic biosensing platform for pathogen detection in aquaculture, Sensors 2024, 24, 5241.

MIRLA – Mid-infrared Liquids Analytics Platform

C. Beyer, V. Zubkovs, S. Paoletti, S. Cattaneo

In this work we present a QCL-based mid-IR monitoring system for real-time, reagent-free, long-term glucose concentration monitoring of low-volume samples for applications in microfluidics cell-based assays, micro physiological systems (MPSs) and organ-on-a-chip systems.

In-vitro microfluidic platforms with living cells or tissues, such as microphysiological systems (MPSs) and organ-on-a-chip systems, show great promise for disease modelling, drug screening and in-vitro diagnostics. Regenerative therapies based on engineered tissues and organoids have been successful in small-scale studies, but few have reached clinical practice^[1]. This is due to the complexity, high cost, and limited understanding of how the manufacturing conditions of engineered tissues affects their quality. Current manufacturing methods are labour-intensive, non-standardised, time-consuming, lacking suitable monitoring instruments, and having many undefined variables, leading to high production costs and batch-to-batch variation. Automation can reduce operator variability, but controlling biological variability requires specialised sensors for continuous in-process monitoring to ensure consistent quality.

Mid-Infrared (Mid-IR) vibrational spectroscopy is a powerful tool for obtaining specific spectral signatures of functional groups in organic molecules within liquids. However, its industrial application is hindered by the cost, bulkiness and complexity of current Fourier Transform Infrared (FTIR) spectrometers, which are unsuitable for integration in high-throughput in-line applications. Recently, Quantum Cascade Lasers (QCLs) have surpassed traditional light sources in terms of resolution and sensitivity in spectroscopy application. QCLs, with their narrow, tunable emission bands and high output power, combined with nanophotonic structures such as plasmonic antennas, significantly improve the signal-to-noise ratio (SNR) needed to accurately measure low-concentrations of bio-analytes such as glucose. Plasmonic antennas amplify the molecular absorption signal by concentrating electromagnetic fields in sensing hot spots. Machine learning (ML) methods applied to mid-IR spectra allow for improved chemical quantification in complex, multicomponent mixtures.

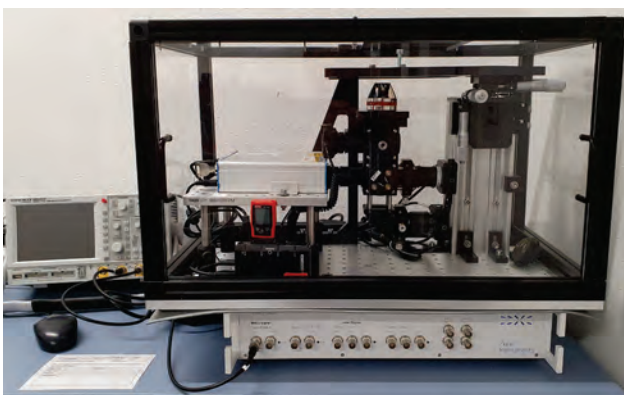


Figure 1: QCL-based measurement setup for analyte monitoring by mid-IR spectroscopy.

[1] F. Schutgens, Frans, H. Clevers, Human organoids: tools for understanding biology and treating diseases, Annual Review of Pathology: Mechanisms of Disease 15 (2020): 211-234.

Building on these advancements, we are developing a contactless, label-free sensing device for real-time monitoring of bio-analytes (Figure 1). The platform comprises a flow cell with integrated plasmonic antennas on a calcium fluoride (CaF_2) substrate, provided by Ivan Sinev from the BIOnanophotonic Systems laboratory (BIOS) at EPFL^[2]. The current setup covers the spectral band from 7.4-10.4 μm ($1335\text{-}960 \text{ cm}^{-1}$) using the QCL LaserTune system from Block Engineering. In a preliminary assessment, the system's capability was demonstrated by measuring glucose concentration in PBS, achieving a detection limit down to 3 g/l, which can be further improved by optimising the setup (Figure 2).

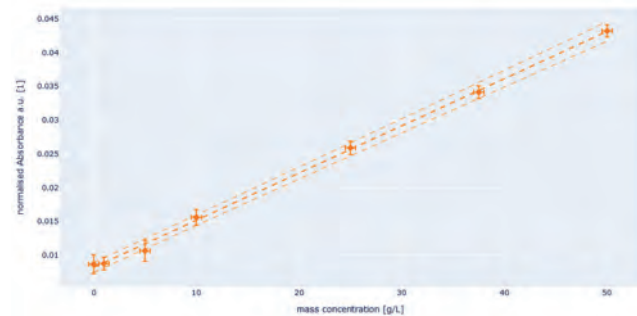


Figure 2: Absorbance signal at various concentration of glucose in PBS.

The modular and versatile configuration of the sensing platform allows extending the detection to other spectral ranges. Furthermore, the inherent stability of the QCL-based system eliminates the need for recalibration, ensuring consistent and reliable measurements over longer periods. Building on this initial concept, within the InnoSuisse project "MIRLA" (121.316 IP-LS) in collaboration with the group of Prof. Altug (BIOS - EPFL), a novel modular sensing platform will be developed targeting continuous monitoring of glucose, lactate, and protein concentrations in cell culture media for up to four weeks. The system will allow reagent-free, real-time bio-analyte monitoring of low-volume engineered tissue cultures (< 5 mL) in a standard 24-well plate placed in an incubator environment. A disposable lid will enable regular, automated sampling of microliter probes without cross-contamination. Additionally, CSEM supports the development of customised multiband QCLs dedicated to glucose concentration assessment, in a cost-efficient system dedicated to upstream process control. The integration of these elements paves the way for the development of compact, sensitive, and selective sensing platforms for real-time bio-analyte monitoring in complex biological media, with the potential to revolutionise how we monitor and control bioprocesses. The technology could greatly enhance the understanding of such processes, improve their control, and ultimately lead to increased product quality and reproducibility of engineered tissues.

[2] John-Herpin, et al., Infrared metasurface augmented by deep learning for monitoring dynamics between all major classes of biomolecules, Advanced Materials 33.14 (2021): 2006054.

Digital Lateral Flow and Electronics

B. Petkus, M. Dorrestijn, J. Heidler, I. Stergiou, M. Renggli, M. Wipf •, C. Wood •, C. Seitz, M. Markocic, N. Schmid, G. Orawez, S. Bitterli, M. Fretz, S. Paoletti

Lateral flow assays (LFAs) are essential in point-of-care diagnostics due to their low cost and rapid results. While traditional LFAs provide only qualitative readouts, quantitative data is increasingly needed for enhanced diagnostic precision. Most digital LFAs use optical line-intensity measurements, which can face challenges with light consistency and smartphone integration. In contrast, MOMM Diagnostics' platform co-developed with CSEM uses enzymatic signal amplification and printed electrodes to digitalize the immunoassay readout electrochemically, allowing simultaneous readings across multiple test lines achieving up to 50-fold greater sensitivity while preserving point-of-care usability for MOMM Diagnostics' rapid pre-eclampsia test.

Lateral flow assays (LFAs) are well-established as rapid, low-cost diagnostic tools in point-of-care and at-home settings, providing an easily interpreted visual indicator. Like any diagnostic test, LFAs contribute to a patient's risk assessment by offering a positive predictive value, thus informing the odds of having a disease when a test is positive. However, as the demand grows for monitoring certain biomarkers over time, the need for quantitative data—rather than just qualitative results—has become increasingly critical. Quantitative biomarker measurement offers a dynamic view of health, enabling individuals and healthcare providers to observe trends, track fluctuations, and adjust treatments based on precise biomarker levels.

To digitalize LFAs, the intuitive approach is to incorporate optical readout methods, given that traditional LFAs are read by visual inspection. However, optical approaches pose challenges: dedicated optical readers depend on specific LFA label designs, such as colorimetric or fluorescent, which may vary significantly between assays. In addition, light conditions can impact results, leading to variability across user settings. Although smartphones are being explored as optical readers, this trend presents its own obstacles, such as regulatory considerations around data management and inconsistencies in raw data access across smartphone models.

To address these limitations, CSEM and MOMM Diagnostics developed LFA-tailored printed electrodes for electrochemical detection, bypassing the need for optical interpretation. A DOE approach was used to optimize the screen-printed inks for compatibility with the lateral flow fluidic membrane materials, while maintaining compatibility with the immunoassay chemistry and measurement method (Figure 1).

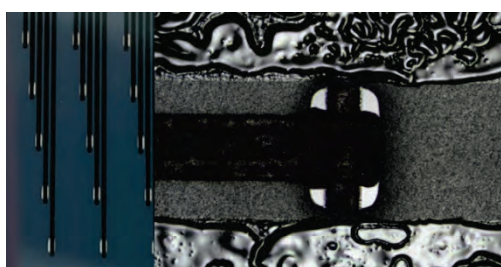


Figure 1: Multi-layer printed electrodes compatible with LFA membranes for electrochemical digitalization of immunoassay sensing approaches.

CSEM's in-house reader is designed to be multiplexed, allowing simultaneous readout of multiple test lines from a single patient sample, enabling the measurement of several biomarkers in parallel—a feature advantageous in comprehensive diagnostics. The reader also offers users several options for potentiometric, amperometric, cyclic voltammetry, and EIS measurement

methods depending on the chemistry of the LFA detection strategy (Figure 2).

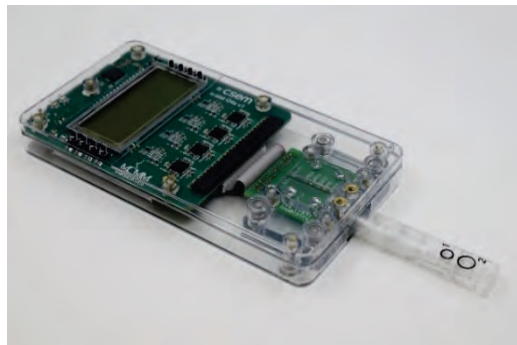


Figure 2: Game boy-sized multi-channel eReader with UI and digital LFA microfluidic cartridge.

An innovative microfluidic cartridge has also been designed specifically for digital LFAs. Some specific LFAs, such as enzyme-linked LFAs, require a developer solution in the assay protocol, but implementation in a user environment leads to variability issues. This cartridge enables users to reliably add the developer reducing variability in the amplified signal.

In summary, this platform allows the point-of-care operation of Enzyme-linked LFAs with a sensitivity level close to that of laboratory-based tests, thus broadening their utility in a range of clinical and at-home applications. Through its novel cartridge design and electrochemical readout, MOMM Diagnostics' and CSEM's technology is poised to meet the increasing demand for sensitive, quantitative biomarker tracking in point-of-care environments, enabling more precise, data-driven healthcare decisions.

With this technology platform, MOMM Diagnostics aims to develop a rapid test for pre-eclampsia, offering unprecedented sensitivity at the point-of-care. Pre-eclampsia is a significant health problem and cost burden (over 2B USD in the US alone). It affects 3-8% of all pregnancies and may lead to severe short- and long-term complications. The test will aim to deliver information on the disease risk during pregnancy check-ups helping doctors to optimize treatment, reduce the stress and anxiety for expectant mothers, save lives and reduce costs.

This work has been carried out within the NewLife project (<https://www.newlife-kdt.eu/>). The project is supported by the Chips Joint Undertaking (Grant Agreement No. 101095792) and its members Finland, Germany, Ireland, the Netherlands, Sweden and Switzerland. This work includes top-up funding from the Swiss State Secretariat for Education, Research and Innovation (SERI).

• MOMM Diagnostics

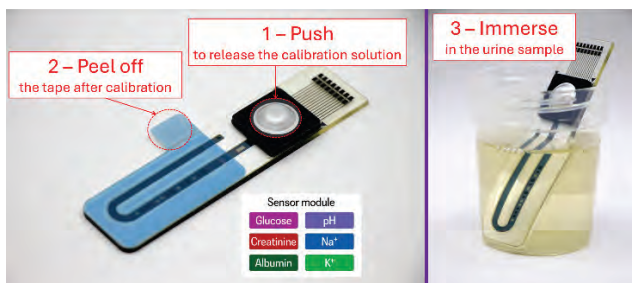
DIGITAL DIPSTICK Revolutionizing Urine Sensing at the Point-of-care

G. Bouilly, J. Disser, J. Kim, F. Geister, M. Dorrestijn, S. Graf, N. Schmid, R. Arnet, J. Zhou, B. Petkus, D. Migliorelli, H. Chai-Gao, R. Junuzovic, C. Berardi, S. Paoletti, L. Burr

The DIGITAL DIPSTICK concept has been designed to address the lack of a multiplexed, fast, simple and quantitative solution for urine analysis in remote healthcare. The concept aims at measuring up to 6 analytes (pH , Na^+ , K^+ , glucose, creatinine and albumin) simultaneously. A calibration solution is embedded directly in the measurement cartridge on a closed fluidic system and is released for use by pressing a unique "push button", significantly reducing manipulation and measurement errors that typically occurs with untrained patients. The CSEM collaborates with clinical partners, like the Swiss Tropical Health Institute (STPH) and the University of Basel hospital (UBS) to validate the digital dipstick as an alternative to conventional urine analysis methods.

Remote healthcare monitoring is emerging as one of the most essential aspects of our society, by allowing an easier medical care for people with chronic disease but also by reducing the burden and the cost for our health system. For this purpose, the analysis of a urine sample can provide essential information that can be correlated to several potential diseases, such as diabetes, kidney failures or high-blood pressure. As a biofluid available in large quantities and without need of an invasive procedure, urine is already widely used for healthcare monitoring but typically require trained practitioner in a clinical environment to perform preparation for sensors, such as regular calibration, to ensure the quality of results.

Our objective is to build a solution mapping several important analytes that can be found in urine and can be linked to some clinical pathologies. The know-how of CSEM in biosensors development and integration lead to build an electrochemical sensor module containing up to 6 indicators (pH , Na^+ , K^+ , glucose, creatinine and albumin) on a flat, flexible, disposable and fully printed substrate. In addition, a flexible microfluidic cartridge is laminated on the top of the sensor module to guide the calibration solution prior to the measurement in urine.



A crucial aspect of remote healthcare is to ensure that the measurement protocol can be performed by anyone, including patient at home, without the support of a trained practitioner. As shown in Figure 1, the digital dipstick was designed to offer a solution where the user is guided through a simple procedure. In the fully integrated cartridge ($98 \times 24 \times 5$ mm, including the blister), a calibration solution is embedded directly into the blister and is ready to be used once activated by the user. Once the calibration of each sensor has been performed, the patient simply removes the protecting tape and immerse the dipstick in urine.

Our first objective was to show that a digital dipstick can simultaneously measure several indicators with an accuracy close to that of other commercially available electrochemical sensors. Figure 2 shows that a short calibration in a solution

allows to obtain a stable signal in urine that can be correlated with the activities of the respective analytes.

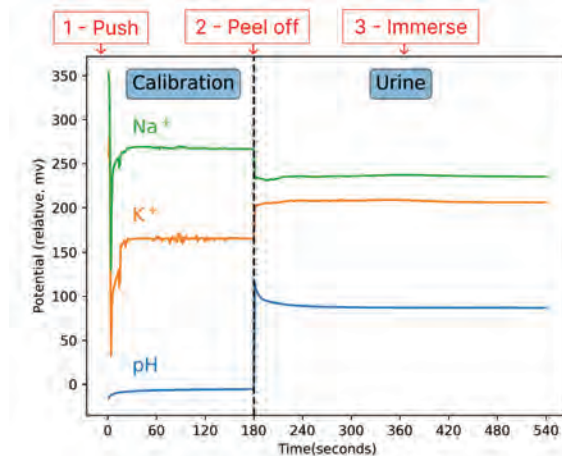


Figure 2: A measurement result in urine for pH/Na/K showing the electrochemical signal shift from the calibration solution to the urine following the protocol of the digital dipstick.

Results obtained have been analyzed to determine the concentration of each analyte in the measured urine. Table 1 shows that the values obtained by potentiometric sensors on the dipstick are very similar to those obtained by commercially available benchmark devices.

Table 1: Comparative results from signals shown in Figure 2 and from commercial ion-selective electrode systems using the same urine test sample.

Analyte	Measured value	Benchmark value*
Na^+	36.9 mM	29 mM
K^+	17.5 mM	18 mM
pH	5.4	5.4

The next stage of the project is to test the digital dipsticks with our clinical partners (STPH and UBS hospital) in real conditions and compared to clinical laboratory benchmark. We are expecting results provided by our solution to be able to detect commonly observed pathologies from urine testing, such as glucosemia or kidney stones. Using the urine of the patient. Due to its intrinsic ease of use, we hope that the dipstick can provide an alternative of the conventional urine test that everyone can do at home, with reliable data directly accessible to the practitioner remotely.

New LiDAR and Oxygen Sensor for Cultural Heritage Site Protection

J.-C. Roulet, X. Bulliard, C. Pache

CSEM is advancing 3D imaging (Flash-LiDAR) and water quality (oxygen sensor) technologies in the TRIQUETRA project to protect Cultural Heritage sites in Europe. These technologies, used in autonomous vehicles and multi-sensor buoys, have many other applications such as underwater infrastructure inspection and drinkable water quality monitoring, enhancing conservation efforts and risk assessment.

CSEM is at the forefront of developing advanced 3D imaging (Flash-LiDAR) and water quality (oxygen sensor concentration) technologies as part of the European project TRIQUETRA. The goal of TRIQUETRA is to create innovative tools to evaluate and mitigate risks that could impact Cultural Heritage (CH) sites across Europe. Additionally, the technologies developed by CSEM have numerous applications, including underwater critical infrastructure inspection (e.g. bridges, dams, etc.) and water quality monitoring (e.g. water treatment plants, etc.).

In this project, an autonomous surface vehicle (USV) is outfitted with a high-precision Global Navigation Satellite System (GNSS) and a watertight container housing a Flash-LiDAR (Figure 1). This setup enables consistent and accurate bathymetric measurements and mapping along predetermined trajectories.

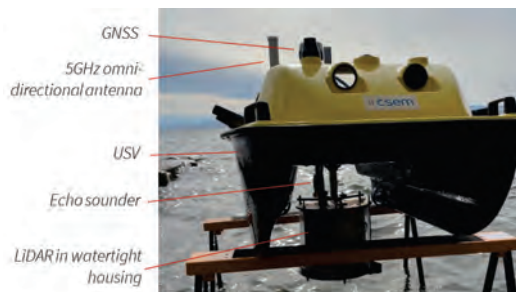


Figure 1: Unmanned surface vehicle (USV) equipped with LiDAR and navigation instruments.

Additionally, water quality is monitored using a multi-sensor buoy (Figure 2) that includes a first-generation sensor designed to measure oxygen concentration in water.

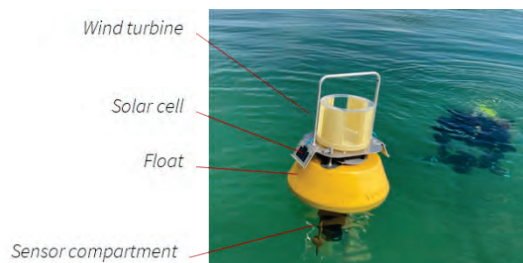


Figure 2: Neroxis buoy on UNESCO site of Les Argilliez (Bevaix, Switzerland) set up by the Archeological Office (OARC) - Neuchâtel.

The TRIQUETRA project will monitor three UNESCO-listed Cultural Heritage (CH) sites between the end of 2024 to mid-2025. These sites include a palafitte settlement in Lake Neuchâtel, dating back to 3871 BC and later 3500 BC, a medieval site in Germany from around 700 AD, and the sunken city of Epidaurus in Greece, dating from the 12th century BC. The primary objective of these investigations is to aid in the protection

and conservation of these sites by monitoring water quality and assessing degradation risks, such as erosion.

The LiDAR system features an array of 2×2 sensors, resulting in a total resolution of 128×128 pixels, initially developed for space applications [1]. Each pixel is equipped with an active gating circuit and comprises several Single-Photon Avalanche Diodes (SPADs) optimized for green light. This makes the LiDAR an ideal tool for underwater 3D imaging, even in conditions of suboptimal water transparency.

The complete LiDAR system, which includes optics, an illumination pulsed laser, and a powerful System on Chip (SoC) for real-time data processing, is compact, with a volume smaller than 20 cm^3 . It has an average power consumption of approximately 25 W, making it suitable for deployment on medium-sized autonomous vehicles, including flying drones.

Figure 3 shows an example of image acquisition with the LiDAR system at Les Argilliez, along a designated test line.

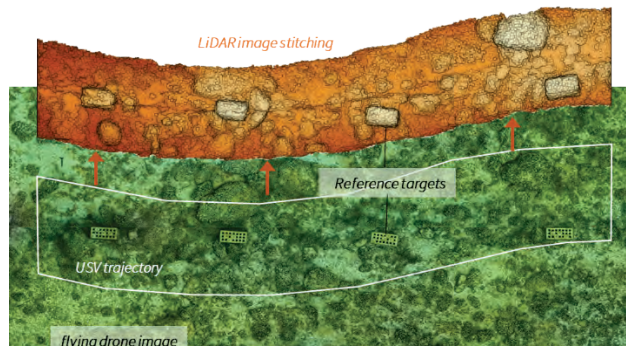


Figure 3: 3D reconstruction of LiDAR acquisition of a test target line (bricks) in Les Argilliez.

Additionally, this project involves the development and laboratory testing of the next generation of sensors. These new sensors will feature doubled lateral resolution, increasing to 256×256 pixels, along with various optimizations to enhance performance and accuracy.

The buoy is powered by a small wind turbine and solar cells. It is equipped with seven sensors: oxygen concentration, pH, turbidity, temperature and a cleaning system for the sensors. Data are sent to a server using 4G cellular network providing nearly real time monitoring of water quality and cross analysis with LiDAR images (e.g. influence of water parameters on water turbidity and hence on image quality). The oxygen sensor in development is a second generation, that includes a patented technology by CSEM for chemical detection. It is based on a mesoporous sensing layer with a hierarchical porosity for enhanced sensitivity.

[1] G. S. Aglietti, et al., The active space debris removal mission removedebris. part 2: In orbit operations, *Acta Astr.*, vol. 168, pp. 310–322, 2020.

Configurable Slit Mask Unit for the MIR MOS Instrument

P. Spanoudakis, M. Gumi, P. Schwab, Y.-J. Regamey, C. Rupf, J. Lahera Perez

First phase: *Development and test in cryogenic conditions of a working prototype of the CSU actuation assembly.*

MIR MOS (Magellan Infrared Multi-Object Spectrograph) is a multi-object and integral field near-infrared spectrograph under development for one of the 6.5 m Magellan Telescopes of the Las-Campanas Observatories (LCO), see Figure 1.



Figure 1: Las-Campanas Observatories (Credit: Yuri Beletsky, courtesy of the Carnegie Institution for Science).

The MIR MOS instrument will integrate a reconfigurable slit mask unit (CSU) which is a mechanism allowing to generate a multi-slit configuration at the focal plane of the telescope. The CSU creates slits on the focal plane by displacing two opposing bars with the space between them creating a slit and allowing light of a selected object to be transmitted to the detector. The CSU (Figure 2) is based on design heritage from the successful MOSFIRE CSU in operation on the Keck Observatory since 2012 and has been adapted for use on the Magellan Telescope featuring a FOV with up to 92 slits.

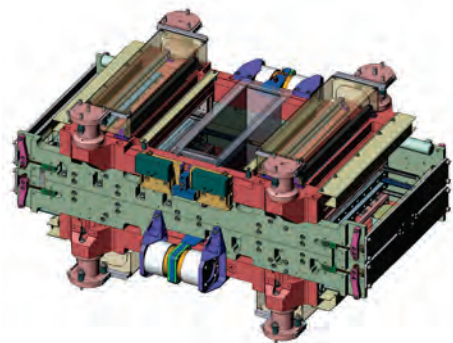


Figure 2: The MIR MOS CSU.

The CSU baseline design (Figure 2) has advanced well and has passed its Preliminary Design Review. Future updates to the CSU as part of the next phase will consist of adapting the interfaces for the cable harness and the Integral Field Unit (IFU) which will sit just above the CSU.

Development prototype

A representative prototype (Figure 3) capable of displacing three masking bars (side-by-side) was manufactured for the test campaign. The electronics to control the mechanism was also developed as was the firmware for communication and error management. The prototype is fully representative of all critical components (ratchet and brake clutches, guide rollers, limit switches, actuators, sensors...) used to displace the masking bars across the instrument field of view.

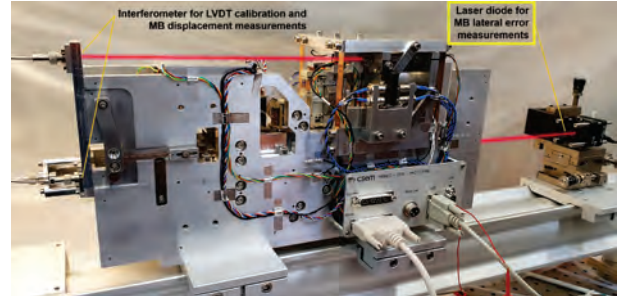


Figure 3: The MIR MOS CSU prototype on test bench.

An extensive tests campaign was carried out to evaluate the effectiveness of positioning the bars in all gravity orientations to be subjected by the CSU. Figure 3 shows the mechanism in a horizontal orientation during the room temperature tests but the worst case will be with the mechanism pointing upward against gravity. The positioning accuracy of the displaced bars in the X-direction has been confirmed at $\pm 7.5 \mu\text{m}$ across the 62 mm field of view. A laser diode together with a four-quadrant photo-detector sensor on the bar tip allowed measurement in the lateral directions (Y & Z).

Electronic racks to control the prototype were developed and are comprised of: Control rack housing the Beckhoff controller and data acquisition models (interferometer and photo-detector sensor), Amplifier rack driving the voice-coil actuator and clutches, Laboratory power supplies (Figure 4).



Figure 4: Electronic racks to drive and control the prototype.

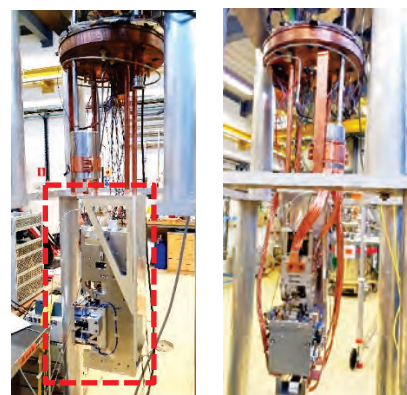


Figure 5: Prototype at CERN cryolab in preparation for cryo tests.

The test campaign at cryogenic temperature (-150°C) was successful and demonstrated the operation of the system in a relevant environment and the ability to position the bars in a vertical, worst-case orientation (Figure 5).

This work was funded by CIS (Carnegie Institute for Science). CSEM thanks them for their support.

TRACTOR – Thruster Pointing Mechanism with Novel Electroactive Polymer Actuator

G. Borque Gallego, J.-L. Helfer, V. Pejchal, F. Beco Albuquerque •, T. Grosgrain ••, E. Omillon

A 3D-printed compliant thruster pointing mechanism with a novel type of actuator for space applications is presented. The novel actuation type of electroactive polymers (EAPs) is of great interest for space due to the large deformations (10% of the total length) that can be achieved when compared to established technologies such as piezoelectric actuators (0.1% of the total length). Due to the reduced actuator stiffness and force output, a dedicated guiding and pivot compliant mechanism with stiffness reduction through pre-stressed lattice flexure blades has been designed and is being currently tested. In parallel, an extensive characterization of the EAP actuators under space conditions (vacuum, thermal and radiation) is being carried out showing a high potential for future space mechanisms.

The continuous increase in performance, precision and efficiency requirements, and the need of reduction of the generated disturbances by actuators in space applications requires the prospection of new technologies that enable quantitative and qualitative improvements in all these domains. Newer materials with novel actuation principles open the opportunity of achieving promising capabilities if used in future space actuators. It is for this reason that smart materials, which exhibit a predictable change in physical properties when subjected to external stimuli, such as temperature, magnetic field, electric field, or radiation, represent a group of materials worthy of further investigation, given the latest advances in their development.

From these newer materials, electroactive polymers (EAP) are promising materials in the field of actuation, which inherently exhibit very low stiffness (0.1 – 2 MPa) and yield very large deformation (> 10%), compared to usual piezoelectric ceramics used in actuators, that typically exhibit maximal strains of 0.1% and significantly higher stiffness (>10 GPa). Electroactive polymers are capacitive actuators which change shape or size when a voltage is applied across the electrodes sandwiching a dielectric layer, thereby converting electrical energy into mechanical energy. EAPs are advantageous owing to their low weight, high energy density, noiseless operation, capability of being miniaturized, as well as their soft and compliant nature, which is not intrinsically present in conventional actuation technologies such as piezoelectric actuators.

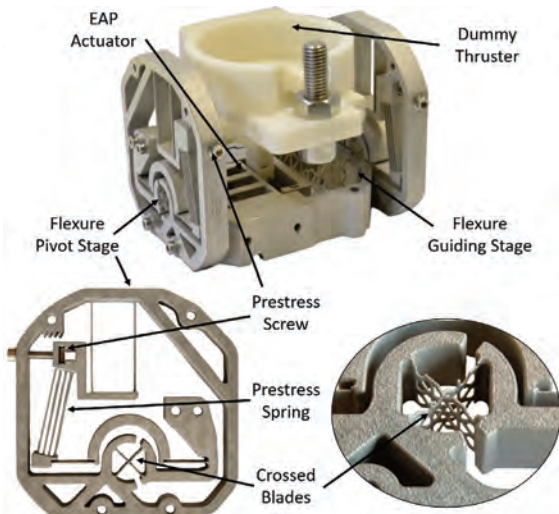


Figure 1: TRACTOR thruster pointing mechanism demonstrator.

In the ESA-funded TRACTOR project, the use of these materials in space applications is further investigated by considering the use case of a simplified (1-DoF) thruster pointing mechanism for which a technology demonstrator, shown in Figure 1, using

flexures and manufactured by additive manufacturing has been developed, manufactured and tested.

In order to achieve very large angles ($\pm 15^\circ$) with such actuators, a special guiding and pivot mechanism with very low stiffness is required. For this, a new concept of prestressed cross blades designed by CSEM has been employed, allowing for a much more constant and lower resistance torque (reduction by x25) even at larger angles, as shown in Figure 2, obtained from the final mechanism manufactured in-house.

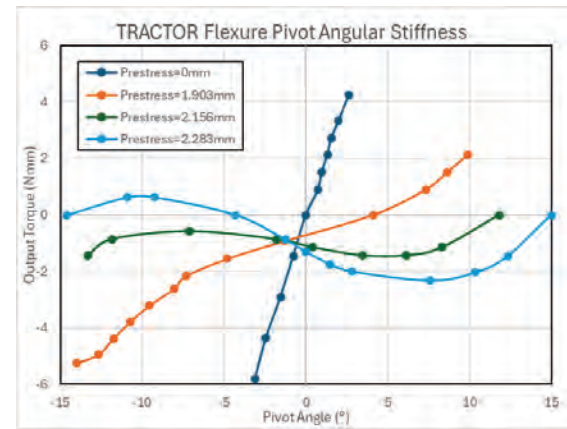


Figure 2: Experimental measurement of the effect of prestress screw displacement (in mm) in flexure torque upon deflection.

In addition to its compatibility with the proposed space mechanism, the primary objective of the TRACTOR project is to evaluate the suitability of the EAPs, designed and manufactured by Dätwyler AG, for use in the space environment. This evaluation will focus on the EAPs' ability to withstand the unique conditions present in space, including temperature, vacuum, and radiation. Furthermore, the project will investigate the EAPs' performance in terms of position accuracy, repeatability, and mechanical limits. The test campaign will be conducted by Almatech SA. The first preliminary results show a very promising outcome in terms of compatibility.

The results obtained throughout the project will allow to better understand this promising type of actuators, enabling new types of space mechanisms not requiring amplification measures typically used with conventional space linear piezoelectric actuators. An on-going ESA-funded project is further developing the integration of EAP actuators into a full tip-tilt (2-DoF) thruster pointing mechanism, targeting to push the technology readiness level (TRL) of both actuator and flexure mechanism, with the intention of being afterwards commercialized by Almatech SA.

The TRACTOR project is funded by the European Space Agency (ESA), and carried out in collaboration between Almatech, Dätwyler, and CSEM.

• Dätwyler

•• Almatech

Next-generation Astrocombs, from Near-infrared to Ultra-violet

E. Obrzud, D. Grassani, J. Holzer, A. Volpini, C. Bonzon, I. Pietro Gonzalez, H. Sattari, M. Despont

The research scope of high-fidelity astronomical spectroscopy ranges over diverse domains of astrophysics from exoplanetology and fundamental physics to cosmology. These research fields require high-fidelity astronomical spectrographs with accurate and precise calibration. Laser frequency combs (astrocombs) are universally recognised as the most suitable calibration source providing a dense grid of equidistantly spaced emission lines over a broad spectral range. Presently, with several tens of high-resolution, extreme precision astronomical spectrographs scattered around the world, scrutinising the sky in the long-wave ultraviolet (UV), visible (VIS) and near infrared (NIR) wavelength ranges, the development of the next generation astrocombs concentrates on improving the spectral coverage, source tunability and operational robustness and stability to enable groundbreaking science in the field of astronomical spectroscopy.

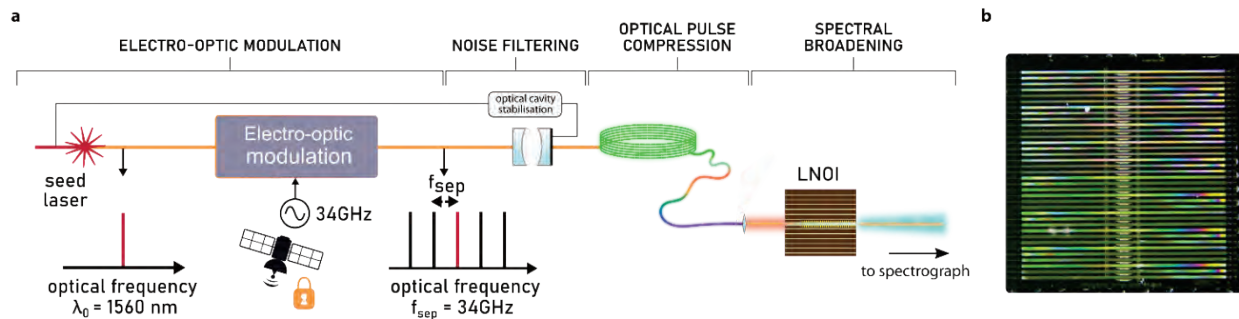


Figure 1: a) Scheme of the prototype astrocomb for the blue/UV to NIR generation; b) Photograph of a lithium niobate on insulator (LNOI) chip.

The research in the field of the high-fidelity astronomical spectroscopy relies on precise measurements of spectral features of various celestial objects, such as stars and distant galaxies - quasars. Observing minute shifts of the absorption lines in a stellar spectrum may reveal existence of a planetary companion and constrain its mass, while quasar spectra host information on the potential variability of the fundamental physical couplings and the expansion rate of the Universe. However, these measurements require exquisite precision and accuracy and one aspect playing an important role in defining the measurement limits is wavelength calibration.

Wavelength calibration of astronomical spectrographs is performed with a light source of known optical spectrum, ideally covering the full operational wavelength range (typically ~370 to 750 nm or 900 to 1800 nm). It has been acknowledged by the astronomical community that laser frequency combs have the highest potential for providing the necessary precision and accuracy to enable groundbreaking astronomical research such as detection of Earth-analogues or a direct measurement of the expansion rate of the Universe.

Since their initial demonstration two decades ago, astrocombs have achieved performance levels that exceed those of competing technologies. They demonstrate exceptional accuracy, achieving $\Delta\lambda/\lambda < 3 \cdot 10^{-11}$ for wavelength markers spaced between 15 and 34 GHz, with linewidths under 10 MHz at a photon flux variation of less than 3 dB.

For astrocombs to become practical tools, they must evolve into commercial products. This requires adopting a turn-key, remotely controllable design, with an operational lifespan of over 10 years and a maximum downtime of 48 hours per year.

The most pressing challenges currently faced by astrocombs are: (1) limited spectral coverage, particularly the lack of operation in the blue/UV wavelength range, (2) insufficient tunability of the optical spectrum, and (3) operational unreliability. The European

Southern Observatory (ESO) has contracted CSEM for the Excalibur project, tasking them with developing a design to address these issues. A conceptual design study has been completed, identifying two high-risk components within the astrocomb. Prototyping has begun as part of de-risking activities.

The project's prototyping activities focus on two key objectives:

- Developing a high-repetition-rate, fiber-based optical pulse generator.
- Designing, fabricating, and optically testing an aperiodically poled thin-film lithium niobate-on-insulator (LNOI) nonlinear integrated waveguide, intended for spectral broadening.

The sketch of the system comprising the two prototypes is shown in Figure 1. The core technology of the first prototype is CSEM-developed electro-optic modulation frequency comb [1], providing tunability, robustness and architectural simplicity. A seed laser at 1560 nm feeds a cascade of 3 electro-optic modulators, operating at 34 GHz, producing an initial 10 nm-bandwidth comb. The RF electronics are disciplined by a 10 MHz reference maser signal. Next, the optical pulses are formed by a dispersion compensation module, amplified, and sent to a chain of carefully tailored optical fibres for further compression of the optical pulses resulting in sub-100 fs optical pulse generation. These optical pulses are then injected into a LNOI-based nonlinear integrated waveguide, where due to strong nonlinear effects the input optical spectrum broadens and subsequently is transferred via harmonic and sum-frequency generation to the UV/VIS wavelength range. A first generation of LNOI waveguides coupons have been tested. Manufacturing parameters have been refined to further improve the performance of the chips in the next fabrication run.

The project provides the necessary input on the feasibility and derisking of critical aspects and provides a basis for the final detailed design of a next generation astrocomb.

[1] E. Obrzud, et al., Broadband near-infrared astronomical spectrometer calibration and on-sky validation with an electro-optic

laser frequency comb, Optics Express Vol. 26, Issue 26, pp. 34830-34841 (2018).

F_{CEO} Detection on GaN PIC Platform

A. Volpini, D. Grassani, I. Rousseau^{*}, C. Bonzon, S. Lecomte

Gallium Nitride (GaN) material is consistently used in microwave applications, and it is qualified as space-graded material. It has large optical nonlinearities and a wide band low absorption transmission region. Such properties make the material suitable for use in Photonic Integrated Circuit (PIC). Here we present a specific application, where a GaN PIC is used for fceo detection of a Mode Locked Laser through f-2f interferometry. This is achieved by simultaneously generating octave spanning supercontinuum and second harmonic within the same waveguide.

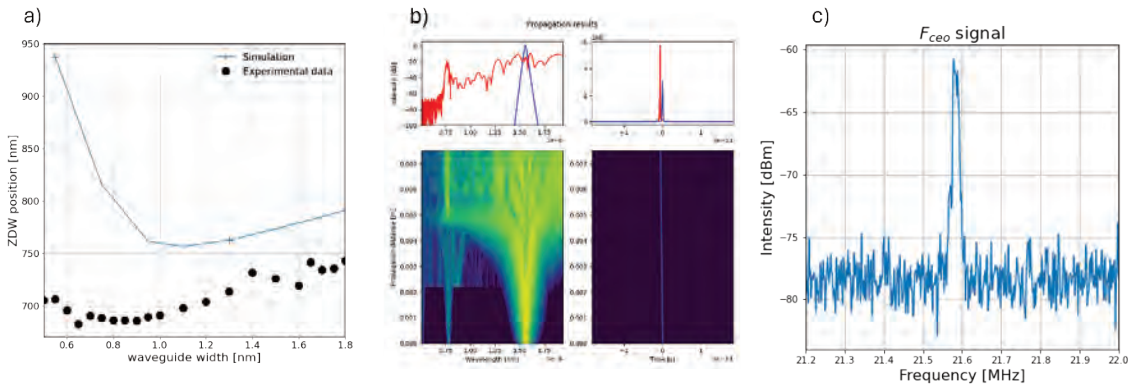


Figure 1: a) Simulation vs experimental data of Dispersive wave location; b) Simulation of supercontinuum generation c. detection of f_{CEO} beat note.

Mode locked lasers deliver trains of pulses in the femtosecond regime. In the frequency domain, the spectra of such pulses generate a frequency comb whose n^{th} line frequency is expressed as: $f_n = n * f_{\text{rep}} + f_{\text{CEO}}$, where f_{rep} is the repetition rate of the laser and f_{CEO} is the carrier-envelope offset frequency. When both f_{rep} and f_{CEO} are known, such combs can be used as an absolute frequency reference for metrology applications. Whereas f_{rep} is readily accessible by beatnote detection of the comb's lines, f_{CEO} requires a different detection scheme, called f to 2f interferometry. The scheme is as follows: the mode lock laser (pump signal) is coupled to a nonlinear crystal where a frequency doubled signal (Second Harmonic, SH) is generated. The SH frequency is $f_{\text{SH}} = 2 * f_{\text{rep}} + 2 * f_{\text{CEO}}$. The SH and pump mode are then spatially and temporally overlapped on a fast photodetector. If the pump signal spans over an octave such that the frequency components $f_n = 2 * f_{\text{rep}} + f_{\text{CEO}}$ exists, a beatnote is detected by the fast photodetector. Such beatnote has an RF frequency $f_{\text{SH}} - f_n = f_{\text{CEO}}$. Often, the octave spanning condition is not satisfied and the pump signal needs to be broadened trough self-phase modulation in an optical fiber with suitable group velocity dispersion (GVD).

Performing f to 2f interferometry on PIC rather than in a bulk crystal and optical fibers offers significant advantages: size and weight are greatly reduced, the pump mode is more confined, implying more efficient nonlinear processes, GVD and phase matching conditions are better controlled, as the waveguide geometry can be tuned with lithographic precision. Nonetheless, not all PIC materials are suitable for this purpose.

In the SuperGaN project, the PIC material used is Gallium Nitride (GaN). It combines strong second (χ^2) and third (χ^3) order nonlinear coefficients of 20 pm/V and $2.2 * 10^{-20}$ m²/V²,

respectively. Such χ^3 value is expected to ease the supercontinuum generation and lower the necessary input power.

Dispersion engineering via extensive numerical simulations (Ansys Lumecrical and Tidy3D softwares) and measurement campaigns are necessary to optimize the design of waveguides (Figure 1a). The Python library PyChi was used to calculate supercontinuum and harmonic generation (Figure 1b). The final goal of this simulation is to ensure the frequency overlap between the dispersive wave (DW) generated through the Supercontinuum and the SH of the signal.

The optimal selected waveguide cross-sections have been fabricated by Hexisense SA. Octave spanning Supercontinuum generation with strong DW has been detected for all waveguides on the chip with estimated pulse coupled energy is < 100 pJ and pulse duration 120 fs. However, compared to what was predicted by simulation, a blue shift in the DW is observed (Figure 1a). The f_{CEO} signal has been detected for many waveguides, with the best SNR of 35 dB (Figure 1c) although with very high-resolution bandwidth (100 Hz).

In conclusion, dispersion engineered waveguides on GaN PICs allows for low-power (sub 100 pJ) octave spanning supercontinuum generation were demonstrated. Such power levels are on par with state-of-the art f-2f scheme in PICs [1] and are five times lower than results reported in GaN [2]. Building on the feedback of this first measurement, further improvements in the design and fabrication are under study. The aim is to refine the numerical model to obtain a fceo with higher SNR by enhancing SH generation while keeping sub-100 pJ level of pulse energy coupled to the waveguide.

The project partner is: HEXISENSE SA. This work was founded by ESA: CSEM thanks it for its support.

^{*} Hexisense SA, Rue de Genève 100, 1004 Lausanne, Switzerland

[1] Yu, et al., Coherent two-octave-spanning supercontinuum generation in lithium-niobate waveguides, Opt. Lett. 44, 1222-1225 (2019).

[2] Fan, et al., Supercontinua from integrated gallium nitride waveguides, Optica 11, 1175-1181 (2024).

DIGITALIZATION TECHNOLOGIES

Alain-Serge Porret

The research priority of **Digital Technologies** is to harness the transformative power of digitalization in order to enhance economic competitiveness and societal well-being in Switzerland. By providing comprehensive support to vertical solutions—from sensing technologies to cloud analytics—the program addresses the critical role of digital innovation in driving growth. CSEM focuses on developing energy-efficient and privacy-preserving solutions, particularly in edge computing and semiconductor technologies, while tackling the rising e-waste crisis through sustainable electronics initiatives.

Additionally, the program both supports advancements in digital health via AI and sophisticated sensors and promotes the adoption of Industry 4.0 technologies to optimize manufacturing processes. This research priority is structured into two strategic initiatives to ensure robust support for the digital transformation of Swiss industries: Transversal enablers and application-specific domains.

TRANSVERSAL ENABLERS

Data & AI focuses on advancing technologies in artificial intelligence and data management. Key advancements include the integration of cutting-edge algorithms tailored to client needs, with an emphasis on environmental sustainability and trustworthiness. Leveraging extensive experience in integrated, constrained devices, CSEM pushes the boundaries of AI in edge computing. Its aim is to simplify AI integration into edge devices while enhancing security, privacy, and anomaly detection. Additionally, it facilitates seamless integration with mainstream cloud platforms. By addressing such challenges and improving tools for data integrity, CSEM strives to streamline AI implementation, reduce development costs, and drive the future of intelligent systems.

ASICs for the Edge focuses on developing application-specific integrated circuits (ASICs) that enable efficient data acquisition, pre-processing, and wireless transmission from end-nodes. This activity emphasizes the design of highly efficient hardware for smart, autonomous sensors, facilitating real-time decision-making with minimal latency, while preserving user privacy thanks to limited data sharing. By integrating sophisticated systems on-chip (SoC), CSEM combines sensor interfaces, analog-to-digital converters, microcontrollers, and machine learning accelerators, resulting in compact, energy-autonomous systems. Overall, CSEM is committed to advancing edge computing capabilities through tailored ASIC solutions that meet the evolving needs of various industries, particularly in IoT and wearable applications.

Quantum Technologies concentrates on the application of fundamental quantum phenomena to enhance the precision of physical measurements and exploit the unique properties of quantum states. Key research areas include quantum sensing, offering unprecedented sensitivity in measuring time, magnetic fields, and gravity, and quantum communication systems based on quantum key distribution.

APPLICATION-SPECIFIC DOMAINS

IoT and Vision is committed to revolutionizing data sensing and processing by enabling seamless, unobtrusive collecting of diverse data types, including images, sounds, and environmental metrics. Central to this initiative is the development of self-governing edge sensors that process data locally, minimizing reliance on centralized systems and enhancing sustainability through local energy harvesting. Additionally, the program addresses challenges such as security and cooperative processing, while focusing on scalable solutions for extensive sensor networks. By integrating automation and digitalization across sectors such as machinery and transportation, it enhances real-time monitoring and data-driven decision-making, ultimately fostering smarter, interconnected manufacturing environments.

The **Industry 4.0** focus area strives to advance digital transformation in manufacturing, particularly for small and medium-sized enterprises. It develops tailored solutions that enhance quality, flexibility, and cost-efficiency. As industries shift towards reshoring, managing small production lots, ensuring traceability, and promoting sustainability throughout the product lifecycle become vital. CSEM addresses these needs in three ways: smart monitoring with multimodal inline measurements to observe and predict, AI-enabled automation to optimize complex processes, and human-centric assistance leveraging AI and data analytics to support operators in decision-making. This comprehensive approach not only boosts production efficiency, but also fosters sustainable practices essential to Switzerland's economic future.

Digital Health is dedicated to advancing telemonitoring, personalized medicine, and AI-assisted systems across medical, wellness, and sports applications. This domain encompasses a range of devices, from wearables to implantables, with a strong emphasis on secure and efficient data management. Key developments include non-invasive wearable technologies for long-term monitoring of vital signs, such as blood pressure and cardiac arrhythmias, utilizing advanced sensors and active dry electrodes. Additionally, Digital Health embraces the Internet of Medical Things (IoMT), integrating advanced sensing and processing technologies to enhance patient care and empower individuals with continuous access to personalized medical services. CSEM is committed to ensuring compliance with regulatory standards while driving innovation in healthcare technology.

Evaluation of Ultra-wideband and Bluetooth® Technologies for Low-power and Precise Localization

V. Kopta, E. Le Roux, A. Dissanayake, K. Manetakis, M. Sénéclauze

Wireless ranging and localization are gaining popularity in recent years, with the adoption of Ultra Wide Band (UWB) - IEEE802.15.4z standard - in smartphones and keyless car access, and the addition of channel sounding in the Bluetooth standard. The trend is expected to continue with the emerging applications such as the indoor asset tracking and real-time localization, and with the two technologies working in complementary fashion, leveraging the low-cost and low-power capabilities of Bluetooth combined with efficient and high-performance ranging of UWB.

With the Bluetooth and UWB devices already providing various localization methods, the indoor asset tracking and real-time localization systems (RTLS) are expected to become a new big market, together with smartphones and secure access applications. Important aspects to consider for indoor localization are the number of anchors needed for localization, their price and complexity. On the other hand, the mobile tags need to be small and low power to be ubiquitous and provide a long battery life. All of these parameters determine the total cost of ownership.

Different RF ranging and localization methods are available, providing different performance (as shown in Figure 1):

- Received signal strength indication (RSSI) uses the signal strength to estimate the distance.
- Channel sounding (CS) is often employed by narrow-band systems. Channel characteristic is measured one frequency at a time over a range of frequencies and subsequently translated into the time domain using IFFT or other methods.
- Angle of arrival/departure (AoA/AoD) is supported by both narrow-band and UWB systems. Angle is calculated by measuring the phase difference between the signal on different antennas, with the angular resolution dependent on the number of antennas
- Time of flight (ToF) is a two-way ranging (TWR), where a round-trip time is measured between two devices. It is sufficient to exchange two packets per measurement (single sided or SS-TWR), but more often three packets are exchanged allowing to compensate for clock offset between the two devices (double sided or DS-TWR)
- Time difference of arrival (TDoA) gives a location estimate based on a difference of arrival to several anchor points. It is an energy efficient method, but requires precise timing synchronization between anchors.

Method	Ranging accuracy	
	LoS	NLoS
BLE RSSI	<5 m	>5 m
CS BLE 2.4 GHz	40 cm	1-2 m
CS BLE 6 GHz	10 cm	60 cm
AoA BLE 2.4	10°-20°	30°
ToF BLE	<4m	-
ToF UWB	<10 cm	60 cm
AoA UWB	20°	-

Figure 1: Typical ranging performance of different methods.

Bluetooth devices use CS for precise ranging. The resolution of the method typically depends on the available bandwidth, which is currently limited to 80 MHz in the 2.4 GHz band. The Bluetooth standard is soon expected to extend to the 6 GHz band where a bandwidth of 500 MHz will be available for communication and ranging. Theoretically, this should allow Bluetooth to achieve comparable ranging performance to that of the UWB, but it remains to be confirmed in practice.

UWB typically uses high-resolution ToF and TDoA, benefiting from 500 MHz signal bandwidth for a resolution of 30 cm. Compared to CS, that requires a large number of measurements to compute the distance, ToF is fast as it works directly in the time domain, and consequently energy efficient.

AoA is supported by both Bluetooth LE and UWB radios. Bluetooth measurements are typically done sequentially, by measuring the carrier tone on different antennas in a sequence, using a single radio. Since there is no equivalent to constant-tone extension in UWB, multiple UWB receivers must operate at the same time, with the number of receivers equal to the number of antennas, which increases the cost of a UWB anchor.

Localization Method	Ranging energy [uJ]	# of events for local.	Loca. energy [uJ]	Local. air time [ms]	# of events for N tags
Infrastructure based localization	RSSI BLE 2.4 GHz	1.8	1	1.79	0.26
	CS BLE 2.4 GHz	47.7	3	143.04	21.73
	CS BLE 6 GHz	309.5	3	928.51	125.05
	AoA BLE 2.4 GHz	8.1	1	8.12	1.02
	ToF BLE 2.4 GHz	6.2	3	18.62	2.50
	SS-TWR UWB	18.8	3	56.26	1.25
	DS-TWR UWB	23.7	3	71.14	1.49
	TDoA UWB	13.8	1	13.79	0.34
Mobile tag based localization	RSSI BLE 2.4 GHz	0.6	3	1.92	0.38
	CS BLE 2.4 GHz	42.8	3	128.45	21.73
	CS BLE 6 GHz	277.8	3	833.28	125.05
	AoA BLE 2.4 GHz	6.1	3	18.31	1.02
	ToF BLE 2.4 GHz	5.4	3	16.32	2.50
	SS-TWR UWB	18.8	3	56.26	1.25
	DS-TWR UWB	30.8	3	92.26	1.49
	TDoA UWB	11.7	3	11.71	0.42
AoA UWB	AoA UWB	13.8	1	13.79	0.34
	RSSI BLE 2.4 GHz	0.6	3	1.92	0.38
	CS BLE 2.4 GHz	42.8	3	128.45	21.73
	CS BLE 6 GHz	277.8	3	833.28	125.05
	AoA BLE 2.4 GHz	6.1	3	18.31	1.02
	ToF BLE 2.4 GHz	5.4	3	16.32	2.50
	SS-TWR UWB	18.8	3	56.26	1.25
	DS-TWR UWB	30.8	3	92.26	1.49

Figure 2: Estimated energy efficiency and scalability of different localization methods.

The comparison of energy efficiency of different methods is given in Figure 2. The assumption for Bluetooth is a consumption of 9 mW in Tx mode and 5 mW in Rx mode, and for UWB 62 mW in Tx mode and 150 mW in Rx mode (with a single Rx). These numbers reflect typical existing state-of-the-art devices, although significantly lower numbers have been demonstrated for UWB in the literature.

One-way ranging methods (TDoA, AoA, RSSI) are typically more energy efficient and convenient as the number of tags increases but, TDoA and AoA require more complexity and increase cost on the infrastructure side (many antennas, synchronization). On the other hand, RSSI is simple, but unreliable as the signal strength is heavily impacted by the environment and not purely by the distance.

In the context of RTLS, Bluetooth can be seen as a low-cost and low-power alternative to UWB, that could cover some of the applications. In the future, UWB and Bluetooth are expected to work as complementary devices, with Bluetooth providing means of efficient and reliable communication, and UWB providing high-precision and energy efficient localization.

A 22 nm, 6-9 GHz ADPLL for UWB Ranging and Communication Applications

V. Kopta, F. Chicco

The demand for Ultra-WideBand (UWB) radio is growing since its inclusion in smartphones and is expected to continue along this path in the future, driven by the demand for precise and secure localization in various applications. One of the most challenging parts of any UWB radio is the frequency synthesizer that covers the needed frequency range in the high UWB band, while minimizing power consumption.

UWB is a proven technology that enables high-precision ranging and localization, in harsh multipath propagation conditions, making it an ideal candidate for indoor asset tracking and real-time localization systems. The centimeter-level precision is achieved using extremely short pulses that minimize interference and maximize temporal resolution. With the growing demand for accurate localization in sectors like smart homes, warehousing, automotive and healthcare, the demand for UWB is expected to grow in the coming years. CSEM has a long experience with the UWB technology through internal development and collaboration with external partners. One of the key parts of a UWB radio is a frequency synthesizer, implemented as a phase locked loop (PLL), that generates the precise internal clocks or the high-frequency carrier signal used for transmission in the Tx mode or downconversion of the received signal in the Rx mode.

The implemented PLL is an all-digital PLL (ADPLL) that uses digital control loop and a time-to-digital (TDC) converter to detect the output frequency and provide phase locking. Compared to the standard analog PLL, the ADPLL is more easily portable to different technology nodes. The digital loop filter typically occupies a significantly smaller area and is configurable, providing the freedom to optimize the phase noise (PN) and dynamic performance in different modes of operation. The TDC is assisted by a digital-to-time converter (DTC) allowing to reduce the range and power consumption of the TDC that operates at the divided Digitally-Controlled Oscillator (DCO) frequency [1]. To cover a broad frequency range the TDC is preceded by a configurable frequency divider that assures that the input frequency falls into the range of the TDC. Each analog block of the PLL is supplied by a separate LDO to isolate different analog blocks from the external supply and minimize coupling between the internal supplies.

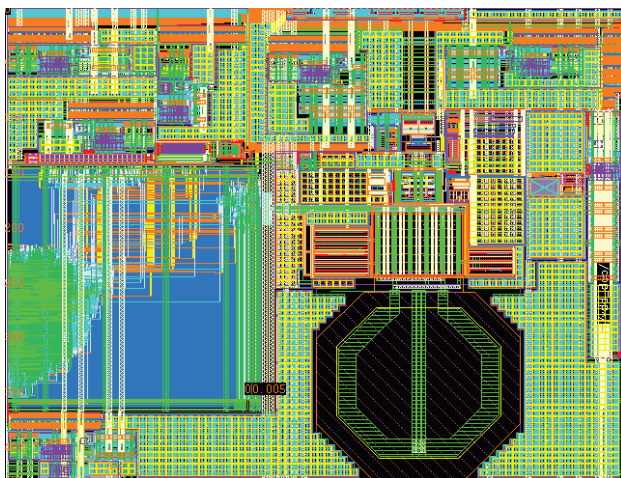


Figure 1: ADPLL layout.

The ADPLL layout is shown in Figure 1, it occupies an area of 0.24 mm² and is implemented in the 22 nm technology node. A significant area is used for the LDOs, as well as the needed decoupling capacitors and the digital controller.

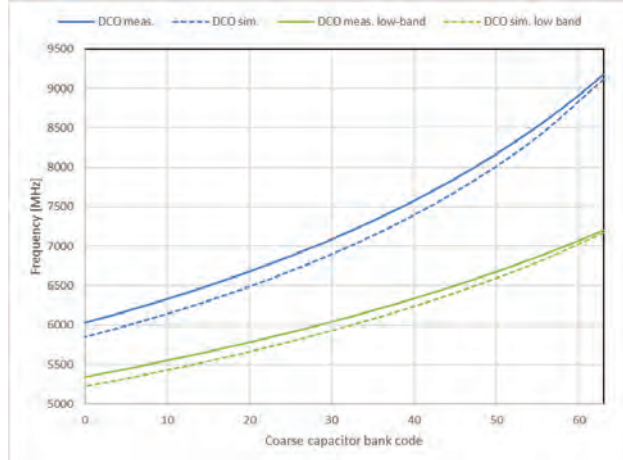


Figure 2: DCO frequency range in the two modes of operation.

The DCO operates at twice the carrier frequency. This is done to reduce coupling to the power amplifier and reduce pulling, and to allow for quadrature signal generation. The DCO is a complementary cross-coupled LC oscillator, that requires a lower current compared to more common NMOS or PMOS-only oscillators. Amplitude feedback is used to guarantee a constant output amplitude over a large frequency range. The DCO frequency range is shown in Figure 2. In the normal mode of operation, the DCO covers the frequencies in the upper UWB band, from 6 GHz to 9 GHz. This range is sufficient to cover the two mandatory channels, channel 5 at 6.489 GHz and channel 9 at 7.987 GHz. The "low-band" option can be used for the narrow-band (NB) radio intended to assist the UWB (NBA-UWB), by extending the link budget and offloading the clock offset estimation and communication to a lower power radio. It operates in the two bands centered at 5.8 GHz and 6.2 GHz, as defined by the UWB standard. In the future these bands are likely to be shared with the Bluetooth extension to 6 GHz, hence expanding the range of possible applications of the PLL. The ADPLL consumes between 10 mA and 14 mA over the wide frequency range of interest. A large portion of the power budget is consumed by the high-speed dividers and buffers that drive the power amplifier and the mixers.

[1] V. K. Chilara, et al., An 860μW 2.1-to-2.7GHz all-digital PLL-based frequency modulator with a DTC-assisted snapshot TDC for WPAN (Bluetooth Smart and ZigBee) applications, ISSCC (2014)

22nm, <10nW, Switched Capacitance or Resistance-based Always-on Circuits for IoT

H. Fattahi, D. Ruffieux, C. A. Salazar Gutierrez

The rapid growth of IoT devices mandates ultra-low-power (ULP) circuits to extend battery life and improve energy efficiency. Such edge nodes are further heavily duty-cycled to lower the average current and thus remain idle most of the time. This project focuses on the design of the few blocks that remains always-on and whose consumption should be further optimized with a sub-10 nW target in 22 nm CMOS, focusing on area-efficient techniques.

The expansion of IoT devices and applications is transforming modern technology, placing new demands on integrated circuit (IC) design. These devices typically operate on limited power sources such as small batteries or energy harvested from the environment. To achieve extended operational lifetime without frequent battery replacements, minimizing energy consumption is essential. Reducing power usage directly enhances battery longevity, which is important for the practicality and scalability of IoT technologies. A primary challenge in designing these devices is the integration of always-on components. These modules must remain active continuously, even when the device enters low-power sleep states, to perform essential functions like timekeeping, environmental sensing, and system wake-up operations. Reliable operation of these always-on blocks requires precise voltage and current references.

Designing such references poses unique challenges. Well-established topologies for Proportional to Absolute Temperature (PTAT) current references and bandgap (BG) voltage references typically rely on large resistors to operate at nanoampere (nA) level currents. Global Foundry's 22 nm FDSOI CMOS (GF22) is a trendy node to implement modern wireless sensors System-on-Chip for IoT at the edge. For always-on blocks, it provides advantages such as reduced leakage currents, minimized parasitics, and a wide body bias range, but it comes with high manufacturing costs making area efficiency critical. Alternative design techniques have thus to be leveraged to implement compact and thus cost-effective high ohmic resistors needed for always-on blocks.

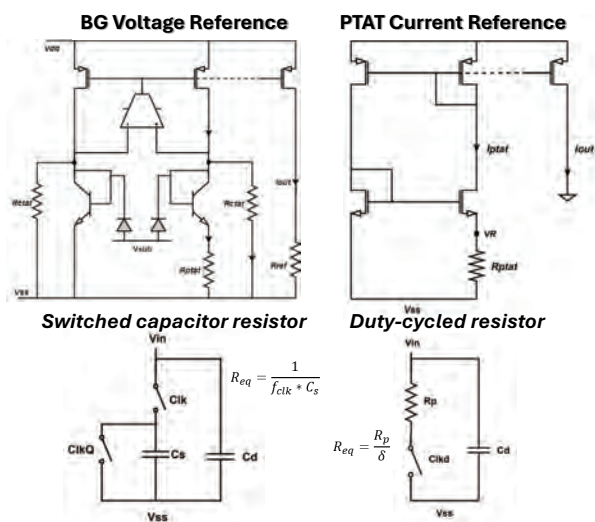


Figure 1: Schematic of the voltage and current reference and details about the switched capacitor or duty cycled resistor to implement compact over 500 MΩ equivalent resistances.

This project addresses these constraints by developing ultra-low power and area-efficient voltage and current references through the substitution of large resistors with switched-capacitor and duty-cycled resistor architectures as pictured in Figure 1. These alternative techniques leverage clock frequency and duty cycle dependencies to achieve the required impedance for generating nW-level references, significantly reducing silicon area usage. By optimizing clock frequency, duty cycle, silicon area, and power consumption trade-offs, the design maintains sub-10 nW power dissipation.

The PTAT current reference, designed using MOSFETs operating in the subthreshold region, achieves less than 4 nW of power consumption and occupies just 0.001 mm² of silicon area. Subthreshold operation allows MOSFETs to efficiently manage extremely low currents while maintaining a high transconductance-to-current ratio.

For the bandgap reference, Bipolar Junction Transistors (BJTs) are utilized to achieve a stable voltage output resilient to process variations and device mismatches. A supply voltage of 900 mV is selected to match the end-of-life voltages of common batteries such as alkaline, silver oxide, and zinc-air, ensuring precise operation throughout the battery lifespan. The reference voltage is set to 800 mV to align with the supply requirements of RF Field-Effect Transistors (FETs) in GF22 and the system core voltage. The reference operates with a nominal power consumption of less than 8 nW, including the ring oscillator, and occupies 0.021 mm² of silicon area with over 2 GΩ of equivalent resistors. It achieves a temperature coefficient (TC) of 60 ppm/°C and a line sensitivity of 0.56%/V. ULP is thus not incompatible with good performances.

Additionally, the bandgap reference serves as a stable voltage reference for a low-dropout (LDO) regulator. The LDO is designed to maintain low noise and high precision, ensuring that its output voltage remains stable despite variations in the supply voltage (ranging from 900 mV to 1.98 V) and low load currents (from 100 nA to 1 μA). By utilizing unity-gain feedback, the LDO eliminates noise multiplication, enhancing the regulator's performance.

In conclusion, this project demonstrates that it is possible to achieve highly efficient, area-conscious sub-10 nW designs for always-on blocks in advanced semiconductor nodes. By carefully sizing the transistors to control leakage currents, utilizing the wide body bias range in FDSOI technology and focusing on innovative design approaches to replace traditional resistor-based techniques, this work lays the foundation for future development of energy-efficient circuits capable of supporting the next generation of IoT devices.

Feasibility Study for a Dense Analog Asynchronous Spiking Neural Network in a 22 nm Process with On-chip Synaptic Time Dependent Plasticity Unsupervised Learning

E. Fragnière •

An analog integrated implementation of a spiking neural network (SNN) in a 22 nm process is proposed and designed at transistor level. Simulation of a behavioral asynchronous VHDL model shows potentially promising dynamics while first layout attempts on successfully simulated transistor-level schematics suggests that dense SNN on a single chip (~10k synapses/mm²) is feasible and could lead to adaptive neural filtering at sensor level.

The human brain consumes an average of around 20 Watts, whereas today's AI system consumes tens of thousands of Watts to perform complex, but highly specific tasks. The *neuromorphic* approach, that takes more precise inspiration from the way the brain works, has occupied researchers for several decades, but interest has waned over the last 20 years. The main reason being the lightning progress made by AI thanks to the exponential growth in the performance of available hardware and the explosion in digitized data collected by companies exploiting it.

To revisit such concepts, an analog integration of a spiking neural network (SNN) in an advanced 22 nm process is investigated. It could ideally complement a companion bio-inspired low-power integrated analog cochlear filter [1] to implement speech recognition or be used for any other time signal preprocessing.

Besides its feasibility, the aim of the project is to explore the applicability of such an SNN for unsupervised learning. A recurrent architecture suited for time series such as speech signal is targeted. The main advantage of inter-neuron communication via asynchronous short logical pulses, the spikes, lies in its much lower power consumption than the one of the classical Artificial Neural Networks (ANN). Storing the synaptic weights of the neurons as analog charges on capacitors is the most challenging aspect of the approach, due to their unavoidable leakage. To alleviate it, each synaptic weight is continuously adapted by a local mechanism called *Synaptic Time Dependent Plasticity (STDP)*, also found in biological neurons. It is expected to perform an unsupervised learning avoiding the need of the biologically unfeasible and very power-hungry back-propagation (BP) algorithm fueling supervised learning in today's ANN.

Figure 1 shows the architecture of an L-layer SNN, each k of them made of N_k fully recurrent neurons. Each neuron j has N_k+N_{k-1} synapses and STDP blocks. A synapse is made of a single MOS transistor working in the weak to moderate inversion regime as a current source, whose value I_{ij}, corresponding to the synaptic weight w_{ij}, is controlled exponentially by the charge stored on its gate capacitor C_w. Each time t_{sp} a spike of duration T_{sp} occurs at input x_i of neuron j, it connects the current source I_{ij} to a common node, the *dendritic tree*, on which weighted spikes q_{ij} = I_{ij}T_{sp} sum spatially. Against a controlled *Leakage* l_{ij}, they also temporally accumulate (*Integrate*) on the neuron's capacitor C_j until its potential p_j reaches a given threshold θ_j at which it resets while the neuron *Fires* a spike on its output y_j (*LIF* neuron model). To each synapse is attached a STDP block, which increases or decreases the charge on synapse w_{ij}'s C_w by sourcing or sinking

a current pulse whose value decreases exponentially with the time interval between spikes occurring on x_i (*pre-synaptic*) and on y_j (*post-synaptic*) whether they are causal or anti-causal.

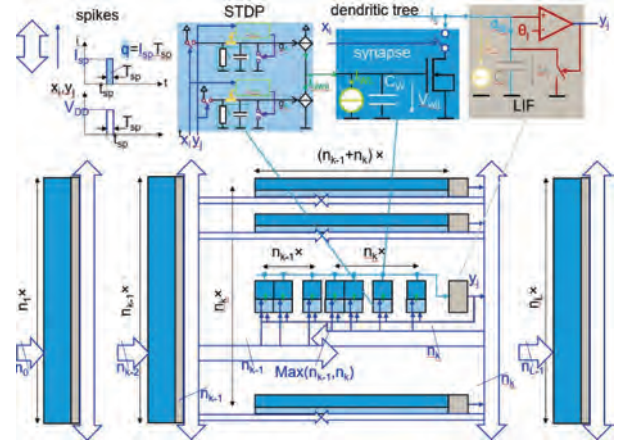


Figure 1: Proposed architecture and blocks of multi-layer recurrent SNN.

Before designing these cells at transistor level, their behavioral and asynchronous VHDL model was developed with which an arbitrary sized SNN can be built and simulated. Figure 2 illustrates the results for a 5-input, 4-layers (5-10-20-4) SNN.

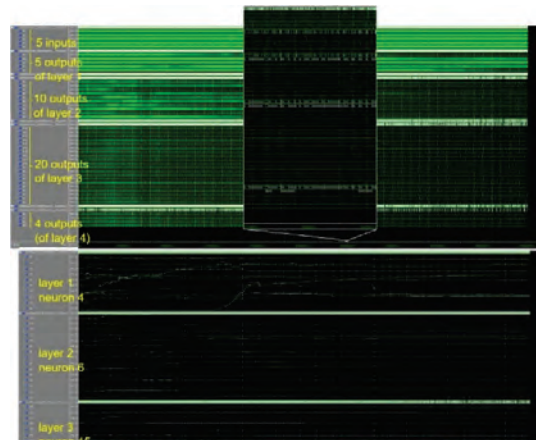


Figure 2: Modelsim simulation result of behavioral VHDL model. Top-plots are spike raster, bottom plots show synaptic weight time evolution.

Transistor-level design in GF22FDX was validated by simulations and a first layout attempt indicates a synapse-STDP block size of about 100 μm², consuming a mere 100 nW of power.

This study was carried out by the author as visiting professor from the University of Applied Science of Fribourg.

• University of Applied Science of Western Switzerland (HES-SO), School of Engineering and Architecture of Fribourg (HEIA-FR)

[1] E. Fragnière, A 100 channel analog CMOS auditory filter bank for speech recognition, ISSCC 2005

High-mmWave FMCW Radar with Antennas-in-package aided by Machine Learning

N. Sahin Solmaz, K. Hafer, F. Chicco, E. Le Roux, K. Manetakis

A low-power radar-based sensor platform employing a G-band (240 GHz) front-end, complemented with the upper layer ML software on a low-power microcontroller has been devised and is currently being designed.

Part of the 6G (sixth generation) wireless systems will operate in the higher millimeter wave (mmWave) spectrum. Applications extend beyond communication and encompass emerging technologies that require highly accurate and robust sensing capabilities. Radar sensors offer important advantages for remote sensing compared to camera-based sensors: privacy, accuracy, low power, penetration, superior operation in harsh environments, and insensitivity to ambient lighting conditions. Range resolution improves at higher frequencies due to increased bandwidth, while embedding the antennas on the same die or package drives the miniaturization of the sensor. The reduced regulation constraints at high mmWave frequencies allows for flexibility in research and development activities. High-mmWave Frequency Modulated Continuous Wave (FMCW) radars will enable higher resolution and precision which align advantageously with the requirements of applications such as presence detection, gesture recognition, vital sign monitoring, material characterization, industrial imaging and inspection. At the same time, the baseband circuitry remains narrowband helping to keep the power dissipation small.

Sub-100GHz radar sensors have enabled gesture recognition, vital sign monitoring, and high precision sensing applications including distance, dimension, wear, and speed measurements, presence/object detection and collision avoidance [1]. Sub-THz frequencies provide valuable supplemental information and reveal additional object properties. At sub-THz frequencies, materials such as paper, clothes, ceramics, plastic and powder exhibit low attenuation, whereas fluids and metals show high attenuation. The absorption spectra of specific chemicals, such as vitamins, sugars and pharmaceuticals, present unique characteristics that could be used as fingerprints for identification. Sub-THz radars have thus high potential for industrial quality control and inspection, as well as in security applications, and can challenge X-ray systems. The high spatial resolution at sub-THz frequencies renders imaging applications an attractive field of investigation [2]. Synthetic Aperture Radar (SAR) systems aided by Machine Learning (ML) models can achieve very high-resolution images.

ML methods have been successfully applied in the radar context to improve target classification in complex environments, automatic target recognition, as well as in cognitive radar systems operating on real time data. Modern ML-based techniques such as Convolutional Neural Networks (CNN) and Temporal Convolutional Networks (TCN) [3] are expected to help not only at the application-level but also to improve the radar signal quality by intelligently removing unwanted disturbances

such as environmental noise, spillover and clutters, as well as to aid in the compensation of system imperfections.

The design of 6G radio hardware in CMOS presents significant challenges. Currently, CMOS high-mmWave radars focus mostly on D-band operation [4]. Work has started on a G-band radar front-end using the Global Foundries 22 nm FDSOI process. The block diagram of the radar front-end (Figure 1) consists of a 60 GHz frequency synthesizer (SYNTH) followed by a frequency multiplier to generate 240 GHz signal for the integrated power amplifier (PA) and down conversion mixer. The received signal at the mixer output is amplified, filtered and digitized by an analog to digital converter (ADC) for the external microcontroller. The operating frequency (240 GHz) is close to the maximum oscillation frequency (f_{max}) of the process and the mmWave models provided by the fab are too restrictive. To address the tradeoff between design freedom and model precision, a combination of parasitic extraction and electromagnetic simulation has been identified as the most suitable methodology. An antenna-in-package (AIP) approach is pursued as embedding the antennas on chip may significantly limit their bandwidth.

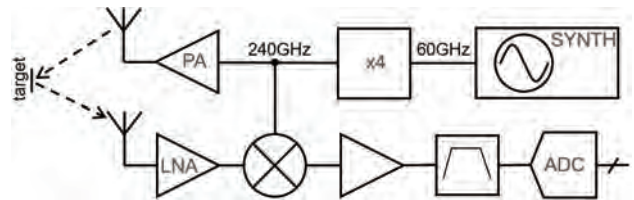


Figure 1: Block diagram of the high-mmWave radar front-end.

The project objective is to realize a low-power radar-based sensor platform employing a G-band front-end, complemented with the upper layer ML software on a low-power microcontroller. The combination of a high-performance radar hardware together with smart ML algorithms on the edge promises to outperform and/or complement current solutions in several applications. ML models will be investigated, and their use will be evaluated in radar-based gesture recognition, vital sign monitoring, industrial inspection, and SAR imaging. The work will benefit from the multidisciplinary expertise of CSEM, that spans from mmWave front-ends to ML models. This project is under the Swisschips thrust "D-band (140 GHz) and G-band (240 GHz) radio frequency circuits and on-chip antennas for radar and precision sensing".

This work has received funding from the Swiss State Secretariat for Education, Research, and Innovation (SERI) - 23.Swisschips.001. The project partner is the Integrated Devices, Electronics, And Systems Group of ETH Zurich.

[1] Wang, Saiwen, et al., Interacting with soli: Exploring fine-grained dynamic gesture recognition in the radio-frequency spectrum, Proceedings of 29th annual symposium on user interface software and technology (2016)

[2] Hillger, Philipp, et al., Terahertz imaging and sensing applications with silicon-based technologies. IEEE Transactions on Terahertz Science and Technology 9.1 (2018): 1-19

[3] Scherer, Moritz, et al., TinyRadarNN: Combining spatial and temporal convolutional neural networks for embedded gesture recognition with short range radar, IEEE Internet of Things Journal 8.13 (2021): 10336-10346

[4] Chou, Ethan, et al. Comparative Performance of 100–200 GHz Wideband Transceivers: CMOS vs Compound Semiconductors. 2023 IEEE BCICTS (2023)

60-GHz FMCW Radar Platform Demonstrator for Presence Detection Applications

F. Chicco, Y. Piguet, S. Cillo, N. Sahin Solmaz, K. Manetakis, E. Le-Roux

This 60-GHz radar platform demonstrator is based on an ultra-low power RF front-end developed in GF 22-nm FDSOI CMOS technology. The system is completed with the baseband processing on FPGA and software to detect targets with a resolution of 1.9 cm up to several meters.

Radio detection and ranging (radar) systems operating in the millimeter wave (mmWave) frequency band have rapidly grown over the past years. Radars based on the frequency-modulated continuous-wave (FMCW) principle benefit from a multi-GHz bandwidth to achieve a range resolution in the order of a few millimeters. The 60-GHz industrial, scientific and medical (ISM) frequency band is one of the most used because of its large available spectrum, namely from 57 to 66 GHz, which corresponds to a nominal range resolution of 17 mm. This band is most suited for short-range devices, including applications such as vital signs monitoring, gesture recognition and smart-home applications [1].

Another important advantage of operating at mmWave is the miniaturization of integrated passive components and off-chip antennas. This aspect is crucial for the integration of several transmitter (Tx) and/or receiver (Rx) chains, allowing to recover the angle of arrival (AoA) and hence to localize the targets. In addition, harnessing the power of the multiple-input multiple-output (MIMO) processing, it is possible to achieve a high angular resolution with a limited number of Tx and Rx elements (denoted as N and M respectively). This is because the number of virtual antennas is equal to $N \times M$, which is very efficient area-wise for large arrays. The arrangement of the antennas can enable angular resolution in azimuth, elevation or both.

This radar platform is based on an ultra-low power 60-GHz 4Tx/4Rx MIMO radar system fabricated in GF 22-nm FDSOI CMOS technology. The integrated circuit (IC) is highly compact thanks to the modular design of Tx and Rx chains with an efficient distribution of the local oscillator, which facilitates the customization of the MIMO array. The total chip surface is $2.5 \text{ mm} \times 1.25 \text{ mm}$, while a Tx-Rx slice occupies $0.4 \text{ mm} \times 1.25 \text{ mm}$. The IC floorplan is designed to maximize the separation of Tx and Rx antennas while maintaining a small-sized PCB, which is crucial to mitigate the direct Tx-Rx coupling.

The key feature of this IC with respect to the other solutions available on the market is its ultra-low power consumption. While operating in the single-input single-output configuration (1Tx/1Rx), the system consumes 40.2 mW in continuous mode, while in the MIMO configuration (4Tx/4Rx), it consumes 101 mW. Thanks to the MIMO processing, the radar IC achieves a record low power consumption of 6.3 mW per virtual channel.

Figure 1 shows the top view of the demonstrator PCB. In the middle there is the IC, on which the whole RF front-end of the system is integrated, including the Tx and Rx chains and the frequency synthesis with FMCW chirp generator and crystal oscillator. Moreover, there are the patch antennas connected to the Tx and Rx I/O, spaced by $3\lambda/2$ on the Tx side and by 2λ on the Rx side. The distance between the virtual antennas is still

$\lambda/2$ to maximize the field of view, while the close-in sidebands are minimized. Most of the baseband (BB) chains, comprising the anti-aliasing band-pass filter with amplification and analog-digital converter (ADC), are designed on the PCB and placed on the back side. The ADC serial outputs are then connected to the I/O of a MicroZed board, which is based on the AMD Xilinx Zynq®-7000 system-on-chip and several peripherals.

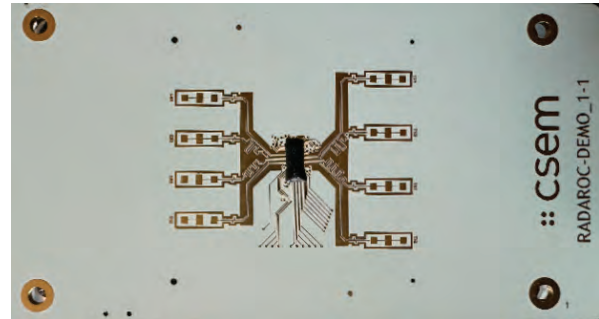


Figure 1: Radar demonstrator PCB.

The preliminary signal processing is carried out on the FPGA. After deserialization, the baseband signal is demodulated with the same codes used to modulate the chirp to separate the contributions coming from the respective Tx. Afterwards, the signals are filtered and decimated to greatly reduce the data rate. The rest of the radar processing is coded on a computer in real-time. Primarily, 3 FFT operations are needed to recover the so-called "radar data cube", i.e. the range-velocity-angle map. The first FFT on the BB signal allows to retrieve the range between the sensor and the targets. Then, a second FFT on the variation of the phase of the first FFT across consecutive chirps provides the radial velocity of the targets. Finally, once the range-Doppler map is available for each virtual antenna in the MIMO array, the third spatial FFT on the phase variations across the channels enables the extraction of the AoA. Figure 2 shows the demonstration of the radar range resolution: the system can distinguish 2 targets separated by 1.9 cm at 1m distance.

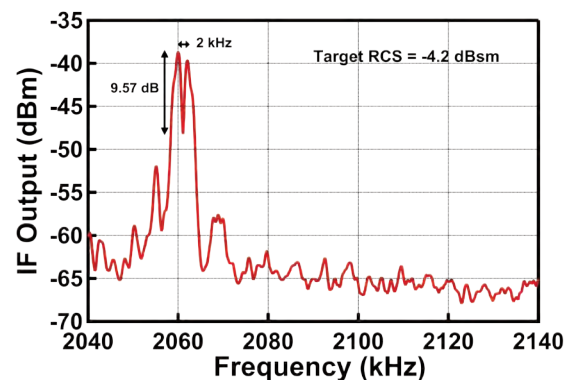


Figure 2: Radar platform range resolution.

[1] S. Cerida Rengifo, et al., An Ultralow Power Short-Range 60-GHz FMCW Radar in 22-nm FDSOI CMOS. IEEE TMTT 72-4 (2024) 2548

Beyond-ML – Accelerating Non-ML Tasks with CSEM EdgeML System-on-Chip

P. Jokic

Machine learning algorithms are compute- and data-intensive, requiring efficient hardware accelerators to deploy them to resource-constrained battery-powered devices. CSEM's edgeML System-on-Chip solutions have demonstrated to enable complex machine learning applications at a mW-range power budget. We show that the embedded hardware accelerators, that enable such efficient processing, can be reused to accelerate other compute-intensive tasks, such as optical flow computations for tracking applications.

The architectures of machine learning (ML) accelerators are optimized for efficiently computing target ML algorithms to accelerate the execution time and improving other performance metrics like power consumption. The Visage ML system-on-chip (SoC) [1] is optimized to run convolutional neural networks (CNNs), which are traditionally used for image processing (e.g. object detection, classification, segmentation). The basic operation of CNNs is a spatial 2D convolution, computing matrix multiplications of a sliding window on the image with a parameter kernel. This is very similar to the block matching algorithm utilized for computing optical flow between subsequent images over time. Our work demonstrates the speed-up for accelerating optical flow computations on CSEM's Visage ML SoC using its integrated CNN accelerator. The same SoC has already demonstrated similar algorithm acceleration capabilities for (non-ML) cryptography algorithms [2].

Optical flow tracks the movement of object points in the image over time. This allows to determine the general movement direction of objects or the movement of the camera itself (e.g. the movement vectors of all pixels have similar values and directions). A block matching algorithm is employed to determine the optical flow. Figure 1 illustrates the concept for a single block, while in practice the entire image would be covered by a grid of such blocks. For each block of the current frame (time t), a defined search space is compared for similarity in the next frame (time t+1). Various similarity metrics, like normalized cross correlation (NCC), exist and each of one can be optimized for the target application. NCC provides robustness towards illumination variation by normalizing the block values but adds a costly division operation on top of a simple convolution (correlation). Comparing to the summation across squared pixel differences, sum-of-squared-differences (SSD) features a significantly lower compute complexity. Since we focus on low power applications, we employ the simpler SSD similarity metric.

To assess the performance gains of accelerating the optical flow computation using a CNN accelerator, the same block matching algorithm is deployed on a) the general-purpose icyflex-V microcontroller (RISC-V core) and b) the CNN accelerator on the same (Visage) ML SoC, both operating at the same frequency (200MHz). While the microcontroller implements 4 nested "for loops" (2 for implementing the sliding window, 2 for the SSD), the accelerator natively supports these loops in its state machine and additionally allows up to 16 arithmetic operations to be parallelized. For a block size of 40 pixels and a search space of 14 pixels in each direction, optimized for a visual odometry application, the CNN accelerator enabled a speed-up of 6.2x relative to the execution time on the microcontroller. This enables similar power savings by duty-cycling the SoC between algorithm executions. The pre-processing of the reference block (e.g. data-

shuffling into a convolution kernel) and the post-processing of the result prevented further performance improvements. One reason for this limitation is that CNNs are normally processed with trained weights, which are stored at a specific location in memory, such that the CNN accelerator only supports constant parameter locations. Since the reference block can be located anywhere in the image this is not the case for block matching, requiring time-consuming data-shuffling (pre-processing) by the microcontroller.

This experiment has demonstrated that optical flow applications can already be accelerated with the CNN accelerator inside the Visage ML SoC but that more flexible input- and parameter-addressing schemes are required to leverage the full potential of the ML engine. Additionally, to support more robust (but compute-intensive) NCC similarity metrics, hardware dividers would be required to achieve low compute latency. These findings have been included in the design of CSEM's next-generation ML SoC, to enable efficient acceleration of compute-intensive algorithms inside the ML accelerators. This opens the door for utilizing ML SoCs in fields beyond the traditional machine learning at the edge, approaching applications like localization, tracking, or odometry.

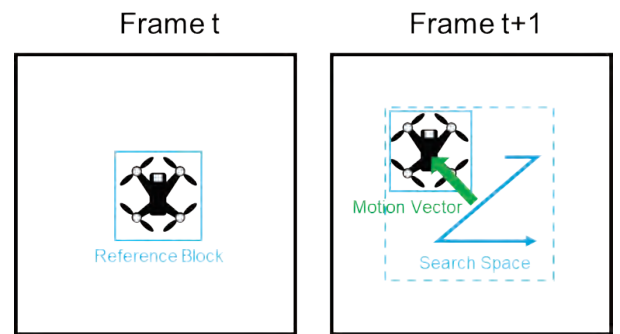


Figure 1: Block matching principle for optical flow computation.

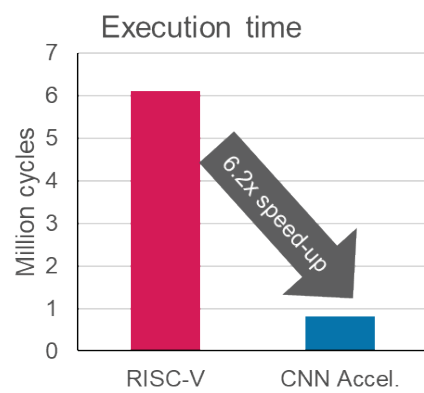


Figure 2: Execution time comparison.

[1] P. Jokic, et al., A ULP 22 nm System-on-Chip with Dual-engine Hardware Acceleration for Edge ML Inference, [CSEM Scientific and Technical Report \(2020\), 106](#).

[2] F. Valencia, P. Jokic, Lattice-based Crypto using Convolutional Neuronal Network Accelerator, [CSEM Scientific and Technical Report \(2022\), 18](#)

Minimizing Power Consumption in Speech Processing using MRAM-based Duty Cycling and Weight Storage

N. Sacchi, E. Azarkhish, R. Catteneoz, F. Caruso, P. Jokic, S. Emery

Speech is now widely used as a human-computer interface for consumer electronic devices. Since speech processing is computationally intensive yet occurs intermittently, implementing duty-cycling in always-on, power-constrained devices can conserve energy whenever feasible. However, loading neural networks from the nonvolatile memory (NVM) to SRAM volatile memory is usually expensive when using off-chip Flash. MRAM allows to replace Flash and use duty cycling effectively. As SRAM leakage is a significant contributor to energy drain in edge processing, it is shown that MRAM is also an option for NN weight storage for small NNs.

Speech is becoming increasingly adopted as a human-computer interface for consumer electronic devices using Keyword Spotting (KWS), such as Amazon Echo, Siri, and language models. Speech processing is possible thanks to Neural Networks (NNs), but they are computation intensive. With available general-purpose SoCs, it is not possible to perform speech processing in an ultra-low-power budget.

On average, a person speaks for 98 minutes over 24 hours. Hence, it is important to deploy compute-intensive NNs only when necessary. However, speech intermittence is not known a priori and is not stationary. It depends on the person and the environment. Doing duty cycling might not be beneficial as loading NNs from NVM to SRAM is energy demanding, such that not doing it in the correct way might lead to undesired energy overhead for booting. At the same time, always-on regime is not desirable as SRAM power leakage is the energy bottleneck of edge System-on-Chips (SoCs). MRAM is a new emergent memory technology which allows on-chip integration of NVMs, reducing by x100 the energy for NN transfer from NVM to SRAM over off-chip FLASH. This overcomes the problem of intermittent speech, as it is shown that it is always beneficial to do adaptive power-cycling rather than staying always on. This is not possible using FLASH^[1].

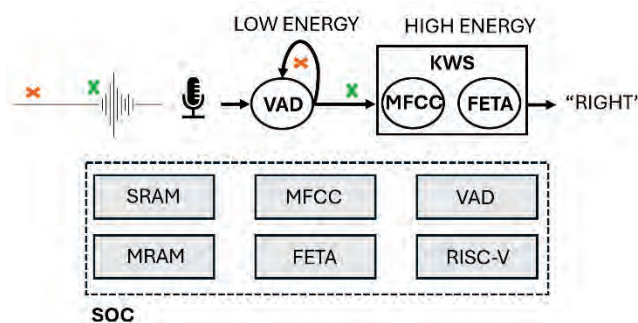


Figure 1: Hierarchical Speech processing with MRAM-accelerated SoC.

In the CSEM SoC, speech processing is performed in the following way: in case there is no speech, CPU and SRAM are off; the neural network for KWS is stored in the on-chip MRAM. Before triggering the NN, a Voice Activity Detection (VAD) recognizes whether someone is talking. If this is the case, it is time to spot the keyword: the neural network configuration is transferred from NVM to SRAM, and a dedicated accelerator extracts the Mel Frequency Cepstrum coefficients (MFCC) which

are passed to a recurrent neural network (RNN) accelerator developed in CSEM, to infer the keyword.

On-chip MRAM allows hierarchical processing thanks to fast low-power boot-up. Indeed RNNs, e.g. LSTM and GRU, require at least 60 kB of memory^[2], and off-chip Flash NVM would require hundreds of milliseconds to transfer the NN parameters from NVM to SRAM for FETA execution. This latency is not acceptable in speech processing as several frames would be lost, dropping KWS accuracy. Moreover, on-chip MRAM is at least x200 more energy efficient than off-chip Flash for booting¹.

To further tackle this issue of SRAM static energy leakage, on-chip MRAM can be used not only for overcoming latency and energy problems given by off-chip Flash, but also as weight storage directly coupled with the RNN accelerator (so NVM-SRAM transfer is avoided). Although MRAM energy access is higher than that of SRAM, eliminating SRAM leakage is beneficial for small NNs, particularly in low-bandwidth applications such as speech processing and energy-constrained devices.

Hence, energy is saved in two ways: first, operations are performed only when necessary, depending on the workload, thanks to MRAM fast boot-up, which allows to use hierarchical processing even for intermittent signal as speech, in which the next event is not known a priori. Then, using MRAM, SRAM leakage energy effect is reduced by coupling the MRAM with the RNN accelerator. This makes the SoC with MRAM suitable for low-power budget applications such as speech processing and time series signals in general.

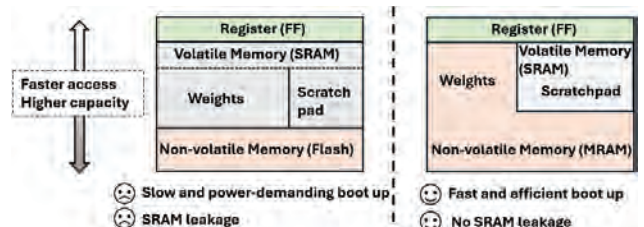


Figure 2: MRAM as changing factor in conventional computing systems memory hierarchy.

This work has received funding from the Swiss State Secretariat for Education, Research, and Innovation (SERI) - 23.Swisschips.001.

^[1] N. Sacchi, E. Azarkhish, F. Caruso, R. Catteneoz, P. Jokic, S. Emery, T. Jang, A Study on MRAM Across Memory Hierarchies for Edge KWS Adaptive Power Cycling, International Conference of Electronics Circuits and Systems (IEEE ICECS) 2024

^[2] Y. Zhang, N. Suda, L. Lai, V. Chandra, Hello Edge: Keyword Spotting on Microcontrollers, arXiv preprint arXiv:1711.07128 (2017)

Monolayer-thick GaN/AlN Quantum Well Anodes and Far-UVC Field Emission Device

D. Boiko, P. Demolon[•], J.-F. Carlin[•], E. Eriksson^{••}, A. Hoogerwerf, K. Bach Gravesen^{*}, A. Brimnes Gardner^{*,**}, M.-A. Dubois, P. Tønning^{*}, E. Zanchetta Ulsig^{****}, M. Marin^{*}, J. Tingsborg[•], N. Volet^{****}, N. Grandjean[•]

We report on unique features of shallow GaN/AlN quantum wells enabled demonstration of field emission device at 226 nm for human-safe disinfection with a record external quantum efficiency of 18% and superior reliability as compared to far-UVC LEDs.

Far-UVC light sources in the spectral range of 200-230 nm effectively kill bacteria and deactivate viruses while being not harmful to health, enabling persistent disinfection of air and surfaces in the presence of humans. So far only excimer lamps have been a unique viable solution in this narrow UV spectral range. Those light sources are commercially available but suffer from EMC compatibility issues and fundamental limitations on size-reduction potential. Far-UVC AlGaN light emitting diodes (LEDs) with wavelengths below 250 nm exhibit exponential collapse of external quantum efficiency (EQE) well below 1% [1]. Only recently, deep-UV LEDs with AlGaN/AlGaN quantum wells (QWs) with an emission at 226 nm were demonstrated with 0.28% EQE and 0.18% wall plug efficiency (WPE), but the device lifetime is limited to ~10 h [2].

In the framework of the SafeUVC project (funded under Eurostars program) we choose a different approach and realized field emission devices (FED) with anodes consisting of a stack of 90 monolayer-width GaN/AlN QWs grown by metal-organics vapor phase epitaxy (MOVPE) deposited on AlN template and emitting at 226 nm (Figure 1). This approach significantly reduces direct Shockley–Read–Hall (SRH) recombination of confined carriers via deep blue-emission traps (DT) in AlN barriers (Figure 2) and allows us to avoid all reliability issues linked with p-doped AlN and contact in UV LEDs [3]. However, like with the UVC LEDs, the emission drops exponentially with shorter wavelengths due to the ease of carrier escape to AlN barriers and their SRH recombination through the DT states.

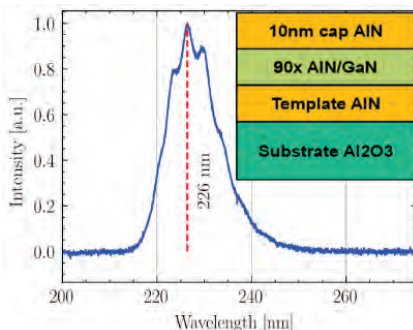


Figure 1: FED emission spectrum and epitaxial composition of its GaN/AlN QW-based anode.

The anodes were integrated into FEDs with nanostructured cold-emission cathodes. The devices demonstrate a record EQE of 18% due to multiple inelastic scattering of high energy electrons in the anode material (Figure 3). However, the WPE is quite low (<0.1%) and is a consequence of high accelerating voltage. Most

importantly, the lifetime of our first FEDs emitting at 226 nm occurs to be well above the tens of hours scale (further studies are needed to define the device lifetime). Eventually, application-field experiments conducted with general hand bacteria (*staphylococcus epidermidis*) validate efficient UVC disinfection features.

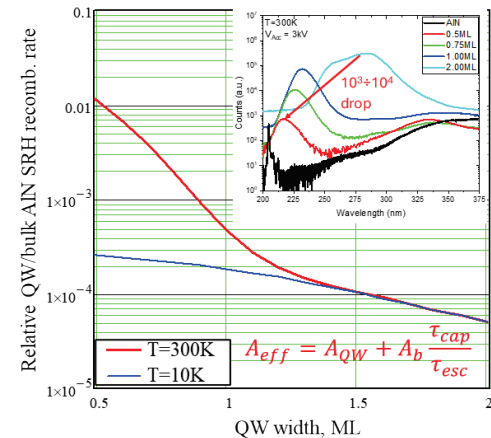


Figure 2: Carrier escape from GaN QW and subsequent nonradiative recombination in the AlN barriers are responsible for the quenching of emission with temperature and photon energy.

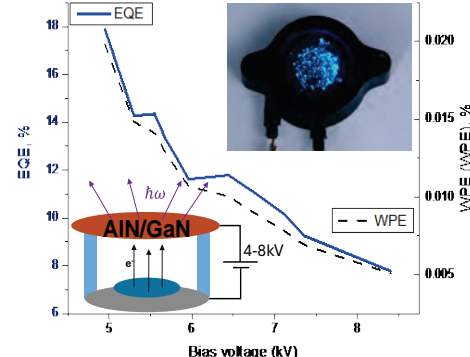


Figure 3: Measured EQE and WPE as a function of applied bias. The photographic image reveals emission from the deep traps in AlN barriers.

In summary, we demonstrate first-generation FEDs emitting at 226 nm with shallow GaN/AlN QW grown by MOVPE. They exhibit 18% EQE and superior reliability as compared to far-UVC LEDs. Next generation anodes will address the light extraction efficiency via surface roughening of the sapphire substrate and the reduction of the template defects via sputter deposition of an additional AlN layer combined with high temperature annealing.

• EPFL, 1015 Lausanne, Switzerland
• PureFize Technologies AB, 754 50 Uppsala, Sweden
* UVL A/S, 8230 Åbyhøj, Denmark
** Aarhus University, 8200 Aarhus N, Denmark

[1] M. Kneissl *et al.*, Nat. Photonics 13, 233 (2019).
[2] T. Kolbe *et al.*, Phys. Status Solidi RRL 18, 2400092 (2024)
[3] N. Roccato *et al.*, IEEE Photonics J. 16, 8200206 (2024)

A Pre-industrial Two Photons High-performance Optical Atomic Clocks

T. Ruelle, E. Batori, S. Kundermann, X. Stehlin, V. Helson, J. Haesler, A. Jallageas •, D. Husmann •, J. Morel •, O. Hog ••, O. Greim ••, S. Lecomte, F. Droz, S. Karlen

A pre-industrial prototype of a two-photon atomic clock currently developed at CSEM in partnership with Rolex is presented. This clock, designed in view of its integration in a 19-inch rack-mount enclosure, is intended for 24/7 operation as Rolex timescales master clock. Its design takes advantage of the high-reliability and high-availability of telecom components. A drift-removed relative frequency stability in the 10^{-15} range at 10^5 s and beyond is achieved.

Thanks to frequencies in the hundreds of THz, optical frequency standards have already outperformed microwave standards as the most stable and accurate clocks. Industrial developments have also been initiated toward compact high-performance clocks based on optical transitions. In this context, the two-photon ^{87}Rb optical clock is a potential candidate for matching or surpassing the performances of active hydrogen masers, the established standard, with improved reliability and lower Size, Weight, Power consumption and Cost (SWaP-C). In this context, our recent advances toward such a device are presented [1].

Our development efforts follow two main axes: the improvement of the frequency stability performance, carried out in a laboratory test setup, and the integration in a compact form factor, realized by assembling a first integrated prototype.

Our systems follow a standard architecture [2]: A frequency doubled telecom laser is used as a local oscillator. A transition at 778 nm in a rubidium vapor contained in a glass-blown vapor cell is interrogated. The laser frequency is then locked using the induced 420 nm fluorescence, detected with a photomultiplier tube. Finally, the frequency stability is converted from the optical to the radiofrequency domain using an optical frequency comb.

When optimized for the short-term, the frequency stability of our laboratory test setup showed a stability at 1 s as low as $3.5 \cdot 10^{-14}$. Thanks to refined regulation loops, performance in a long-term optimized configuration showed drift-removed frequency stability at the level of $5 \cdot 10^{-16}$ for the selected best 5 days (see Figure 1), the drift-included stability being limited by the He permeation of the vapor cell. In this configuration, the short-term frequency stability is limited to $1 \cdot 10^{-13}$ at 1 s integration time. The measured short-term stability is nevertheless still limited by the hydrogen maser reference up to ~ 10 s.

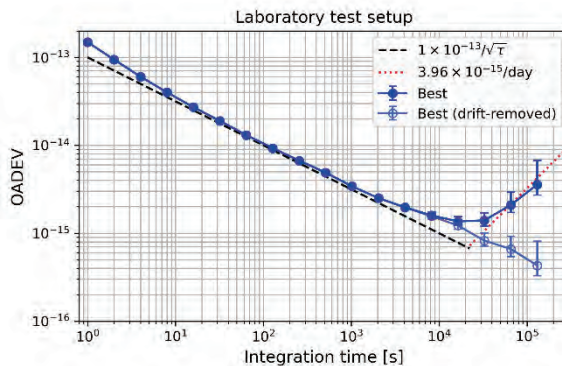


Figure 1: Long-term optimized laboratory test setup stability compared to an active hydrogen maser.

• Federal Institute of Metrology METAS, Bern-Wabern, Switzerland
•• Rolex S.A. Genève, Switzerland

In view of the development of a compact single 3U rack, a first step of integration was realized (see Figure 2). An integrated clock prototype was developed in the form of a bay comprising three 19" 3U racks including (i) a commercial self-standing frequency comb, (ii) an atomic reference composed of the CW laser, the fibred elements, and the atomic reference, and (iii) a control electronic rack.



Figure 2: Integrated optical atomic clock prototype.

This integrated prototype was continuously operated at METAS, the Swiss metrology institute, for more than 4 months before being manually shut down. It was compared against the Universal Time Coordinate (UTC) using the Swiss realization UTC(CH) as pivot.

With typical and best long-term stability below 10^{-15} , our approach compares well to similar state-of-the-art optical frequency standards. Moreover, the continuous operation at METAS for more than 4 months highlights the robustness of the system. The two-photon clock technology is thus considered a valuable candidate for timekeeping applications, such as the Rolex timescale, and for a potential participation to UTC.

[1] T. Ruelle, *et al.*, Development of an Industrial Two-Photon Rb Atomic Clock for Timekeeping Applications, in 2024 European Frequency and Time Forum (EFTF), Neuchâtel, 2024

[2] K. W. Martin, *et al.*, Compact Optical Atomic Clock Based on a Two-Photon Transition in Rubidium, *Phys. Rev. Appl.*, 9(1), 2018

SAND – Stochastic Approach for Feature Selection

P. Pad, M. Dia, H. Hammoud, N. Maamari, L. A. Dunbar

We introduce an ultra-simple layer which automatically selects the k most important features during the training of a neural network, where k is a predefined number. We show that this layer, despite its simplicity in both theory and implementation, provides a one-shot solution to the problem of feature selection with a performance that surpasses or competes effectively with the state-of-the-art methods. In contrast to the conventional approaches that involve two steps of selecting features followed by retraining the neural network on the selected subset, our method simultaneously selects the features and trains the network. Notice that the method requires no alteration of the architecture of the downstream neural network or its loss function.

Feature selection is crucial in machine learning, deep learning, and artificial intelligence because it enhances model performance, reduces computational complexity, and improves interpretability. By selecting the most relevant features and discarding irrelevant or redundant ones, models can learn more efficiently, focusing on the most meaningful data patterns. This reduces the risk of overfitting, where a model learns noise rather than true patterns, leading to better generalization on unseen data. Additionally, fewer features mean lower computational requirements, which is especially beneficial in large-scale data applications. Feature selection also helps provide insights into which factors are most influential in making predictions, supporting better decision-making and model transparency in real-world AI applications.

Feature selection methods can be broadly divided into unsupervised and supervised approaches. Unsupervised methods, such as clustering, matrix factorization, and autoencoders, analyze relationships between input features without needing labeled data, making them useful when labels are scarce. Supervised methods, in contrast, use labeled data to guide selection and are further split into model-independent (filter-based) and model-dependent approaches. Model-independent methods evaluate feature relevance based on statistical tests and information metrics, which are computationally efficient but may miss complex feature interactions. Model-dependent methods, including wrapper and embedded approaches, tailor feature selection to specific models. Wrapper methods evaluate features based on model performance but can be computationally intensive. There is another selection methods category called embedded methods. Embedded methods rank features based on metrics intrinsically learned during model training, seamlessly integrating feature selection into the learning process. Examples include feature importance for tree-based algorithms, Recursive Feature Elimination for Support Vector Machine (RFE-SVM), sparsity-promoting models, and other deep learning techniques. Such methods enable an automatic selection of relevant features during training.

The existing embedded methods typically necessitate alterations to the objective function or significant modifications to the neural network architecture involving the addition of new connections. Consequently, feature selection is often a separate phase followed by a retraining phase on the selected features, or it requires some kind of hyperparameter tuning to control the number of selected features. In this work, we propose a novel, yet exceptionally simple, method for one-shot feature selection. It involves the integration of a simple constrained weighted additive noise layer at the neural network's input. The

constrained stochasticity helps the network generate a polarized input space and effectively select the desired number of features during training. As a result, the network architecture inherently converges to its final form, which can be directly used for inference without necessitating any additional retraining. The constraint on the weights is imposed by construction through a normalization operation and requires no regularization terms in the objective function. The proposed layer imposes negligible computational overhead and can be seamlessly incorporated, akin to the addition of Dropout or Batch Normalization layers. Through this layer, direct control over the number of selected features is enabled without the need for additional grid search or further tuning of regularization term. The method is called SAND [1] which stands for Selection with Additive Noise Distortion.

The simplicity of our method does not compromise the final prediction performance of the neural network. We conduct an extensive benchmarking study against state-of-the-art feature selection methods using common datasets, showcasing our method's effective competition in classification accuracy against existing approaches (Figure 1). We also provide theoretical guarantee on the performance of our method. Moreover, our method needs 33% less number of epochs than other competitors for joint neural network training and feature selection which indicates its higher efficiency.

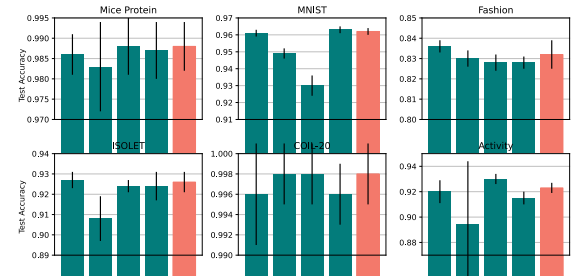


Figure 1: Test accuracies on 6 datasets after selecting features over 10 trials. SA = Sequential Attention, GL = Group LASSO, and SL = Sequential LASSO.

In short, the advantages of the proposed method are as follows:

- On par with the state-of-the-are performance
- Low computational and memory burden
- One-shot feature selection and network training
- Control on the number of selected features
- Considerably faster
- Handy integration of feature selection in neural networks
- Tailored features to the application and the neural network architecture
- Remarkably simple both conceptually and practically.

[1] P. Pad, M. Dia, H. Hammoud, N. Maamari, L. A. Dunbar, SAND: One-Shot Feature Selection with Additive Noise Distortion, under submission

Efficient and Privacy-preserving Smart Edge for Hierarchical Vision Systems

P. Pad, Y. Sepehri, N. Maamari

Edge-cloud systems are increasingly important in today's technology landscape, enabling devices with limited resources, like smartphones and IoT devices, to perform complex AI tasks by offloading some processes to the cloud. These systems allow real-time data processing, reduce latency, and help manage the constraints of memory and computation on edge devices. This work focuses on enhancing deep neural network training on such resource-limited devices by implementing a hierarchical edge-cloud framework that improves efficiency and privacy. A hierarchical training method divides training tasks between edge devices and cloud servers, using early exits to reduce communication and runtime. This approach keeps raw data on the edge device, reducing privacy risks and achieving a 60-80% reduction in training time with minimal impact on accuracy. To further protect sensitive information, adversarial early exits are combined with differential privacy techniques, preventing sensitive content from being inferred from transmitted feature maps while maintaining accuracy within 3%. Together, these methods enable secure and efficient deep learning on edge devices with support from the cloud.

Edge-cloud systems enable efficient processing for deep learning tasks on devices with limited resources by splitting computations between edge devices and cloud servers. This approach helps manage memory and computation constraints, latency, and data privacy. We introduce two key methods that by incorporating early exits, these methods reduce data communication and latency, enhance power efficiency, and safeguard privacy without compromising overall accuracy.

In the first method, an early exit is introduced at the edge device, allowing data to be processed locally without requiring transmitting the gradient from the cloud server to the edge during the backpropagation in the training phase. By reducing the need for data transmission, this approach significantly lowers communication latency and power consumption, making the training phase much more efficient. Since data transfers between edge and cloud consume considerable energy and time, minimizing these transmissions improves the overall training efficiency. Also, the edge in this method only needs to have the transmission capability and does not need to have a receiver which simplifies the edge device architecture. Additionally, only feature maps, rather than raw data, are sent to the cloud, enhancing privacy by reducing direct access to sensitive information. Without needing backpropagation gradients from the cloud, this setup also enables the use of non-differentiable processing techniques—like sophisticated compression algorithms—on the edge, further optimizing data handling and storage. Through extensive experiments, we showed that the proposed method reduces the training time 60%-80% while has a minimal impact on the overall inference accuracy^[1].

The second method expands on privacy protection by implementing an adversarial approach to the early exit at the edge. This method trains the edge device to remove sensitive information, such as personal attributes, from the data before it's sent to the cloud, and retaining only the task-relevant information. During training, the adversarial early exit learns to suppress sensitive content (e.g., a person's gender) while preserving features necessary for the task at hand. For instance, in an application to detect smiling in facial images, the model is trained to eliminate gender information, which cannot be recovered even with advanced processing on the cloud. This method strictly enhances privacy by ensuring that any potentially sensitive

information is filtered out before data leaves the edge, and only essential features for the specific task—such as a smile detection indicator—are transmitted. This setup ensures that data privacy is maintained throughout the training process, as any sensitive details are inaccessible to cloud-side operations.

Figure 1 shows some examples of the performance of the proposed method called PriPHiT against advanced reconstruction methods. We observe that if PRiPHiT is not implemented, the reconstruction attack can very precisely reconstruct the input image from the extracted features of the neural network (e.g. VGG-11, ResNet-18 and MobileViT-xxs). However, by performing the training using the PriPHiT method, the gender of the object is mixed up in the reconstructed image which is even more powerful than preventing the image from being reconstructed^[2].

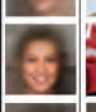
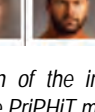
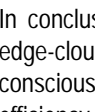
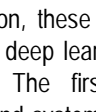
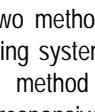
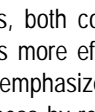
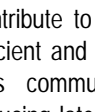
Defined Label Sensitive Label	Input	Deep Reconstruction Attack					
		VGG-11		ResNet-18		MobileViT-xxs	
		PriPHiT	Baseline	PriPHiT	Baseline	PriPHiT	Baseline
Mouth Open With Makeup							
Mouth Closed With Makeup							
Mouth Open No Makeup							
Mouth Closed No Makeup							

Figure 1: Examples of reconstruction of the input image from the features extracted with and without the PriPHiT method.

In conclusion, these two methods, both contribute to making edge-cloud deep learning systems more efficient and privacy-conscious. The first method emphasizes communication efficiency and system responsiveness by reducing latency and energy consumption, while the second ensures strict privacy by eliminating sensitive information at the edge. Together, they provide a robust framework for training deep learning models on edge devices while leveraging cloud capabilities in a secure and efficient manner.

[1] Sepehri, P. Pad, A. C. Yüzügüler, P. Frossard, L. A. Dunbar, Hierarchical Training of Deep Neural Networks Using Early Exiting, IEEE Transactions on Neural Networks and Learning Systems, doi: 10.1109/TNNLS.2024.3396628

[2] Y. Sepehri, P. Pad, P. Frossard, L. A. Dunbar, PriPHiT: Privacy-Preserving Hierarchical Training of Deep Neural Networks, arXiv:2408.05092

Constrained Zero-shot Neural Architecture Search on Small Classification Dataset

R. Vuagniaux, S. Narduzzi, N. Maamari, L. A. Dunbar

CSEM developed an efficient Deep Learning strategy based on Neural Architecture Search (NAS), enhancing the search speed by using proxy functions to estimate the final accuracy, combined with Knowledge Distillation (KD) during the learning process to enrich the performance of the model. Combining these methods achieves improved accuracy with a reduced memory footprint for the models, making them suitable for edge applications.

Deep Learning (DL) has brought significant transformations across scientific domains, marked by the development of increasingly intricate models demanding powerful GPU platforms. However, edge applications like wearables and monitoring systems impose stringent constraints on memory, size, and energy, making device-specific optimization imperative. Machine learning developers frequently use foundation models such as ResNet and MobileNet, simply training them on new data and achieving satisfactory accuracy. However, this practice favors data-agnostic (generalizable) models, whose performance may not be related to the data distribution, potentially leading to overly complex architectures for the task at hand. In particular, for small datasets, the number of parameters might be too high and lead to overfitting. Aligning the architecture with the data's characteristics can lead to better performance, with reduced complexity and fewer parameters, thereby implying a smaller memory footprint and better suitability for edge platforms. Meanwhile, foundation models might simply not fit on the target device. Optimizing DL models to accommodate embedded devices presents challenges due to these platforms' processing and memory limitations. Manually navigating the architectures' space and accounting for hardware constraints is a time-consuming task.

To address these challenges, we have developed an automated NAS approach combining zero-shot estimation and Knowledge Distillation to design and train neural architectures on a small dataset. We demonstrate the effectiveness of our method by classifying 200 different birds (Figure 1) from the small dataset CUB-200-2011 [1] totaling 5994 images (less than 30 images per species). The NAS is based on a genetic (evolutionary) algorithm that identifies the optimal configuration of MobileNetV2 building blocks by tuning their kernel sizes, expansion ratios, and number of blocks. To speed up the search process, we rely on a zero-shot proxy (ZiCo) and its Bias-Corrected version (ZiCo-BC [2]) to estimate the final accuracy of the model from the initial architecture, without having to train it. The ZiCo proxy uses one forward and backward pass on a subset of the data to obtain the gradients and estimate the final accuracy, which guides the genetic algorithm to discover the best architecture. The discovered architecture is then trained using a KD teacher-student approach. We use a large ResNet trained on CUB-200-2011 and transfer its knowledge to smaller MobileNets, which are architecture suitable for edge platforms.

Our results show that, if pre-trained with an external dataset, the networks generally perform better than state-of-the-art architectures pre-trained on ImageNet (Table 1). Adopting a KD approach and receiving guidance from a teacher model for small

dataset classification is beneficial and produces much smaller networks, reaching similar accuracy to a MobileNetV2 architecture with 20% and 40% fewer parameters, respectively. Furthermore, over-parametrized models (such as MobileNetV2) overfit on the dataset without pre-trained weights, reaching 53.4% in test accuracy compared to 67.2% when using pre-trained weights. Architectures smaller than MobileNetV2 (as found by our NAS) reduce overfitting and motivate the design of data-aware architectures. Additionally, the weights of the trained model were quantized to 8 bits, and the model deployed on a Google Coral Edge TPU platform equipped with 8MB of SRAM shared for model parameters and input data. We observed that the latency is not correlated with the number of parameters and FLOPs but is influenced by the topology of the discovered architecture, as certain operations may introduce higher latency if the hardware is not optimized for them (Table 2).



Figure 1: Example of samples from the CUB200-2011.

Table 1: Test performance comparison of the models trained with and without KD on the CUB200-2011 dataset.

Model	Accuracy (w/o KD)	Accuracy (with KD)	Parameters	FLOPs
NTSNet [25] †	96.8 %	-	29.1M	83G
ResNet-101 †	77.9 %	-	42.9M	125G
MobileNet-V2 †	67.2 %	72.9 %	2.5M	612M
MobileNet-V2	53.4 %	69.8 %	2.5M	612M
Zico (2M limit)	55.2 %	69.3 %	1.8M	612M
ZiCo-BC (2M limit)	55.2 %	69.1 %	1.9M	611M
Zico (1.5M limit)	55.5 %	68.5 %	1.5M	550M
ZiCo-BC (1.5M limit)	56.2 %	69.5 %	1.5M	522M

† Pre-trained on ImageNet

Table 2: Performance of the model deployed on CPU and on the Google Coral TPU platform.

Model	Latency (CPU)	Latency (TPU)	Accuracy (float32/int8)	Size (float32/int8)
MobileNetV2	16.3 ms	2.86 ms	69.8 / 69.8 %	9.42 / 2.82 MB
ZiCo (2M limit)	88.8 ms	4.39 ms	69.3 / 69.0 %	7.14 / 2.13 MB
ZiCo-BC (2M limit)	47.5 ms	4.04 ms	69.1 / 68.8 %	7.39 / 2.21 MB
Zico (1.5M limit)	49.8 ms	4.92 ms	68.5 / 68.3 %	5.70 / 1.70 MB
ZiCo-BC (1.5M limit)	35.1 ms	4.29 ms	69.5 / 69.5 %	5.71 / 1.71 MB

By combining a zero-shot NAS approach with knowledge distillation, we have established a pipeline that efficiently generates DL architectures suited for the classification of small datasets. In the future, we will add a latency constraint or employ a multi-objective genetic algorithm during the search process to allow for the simultaneous optimization of architecture design for high accuracy, low latency, and a reduced number of parameters.

[1] C. Wah, S. Branson, P. Welinder, P. Perona, S. Belongie, The Caltech-UCSD birds-200-2011 dataset, 2011

[2] K. Bhardwaj, H. P. Cheng, S. Priyadarshi, Z. Li, ZiCo-BC: A Bias Corrected Zero-Shot NAS for Vision Tasks, 2023

Contactless Water Quality Monitoring for Wastewater Treatment Plants

S. Blanc, Y. Cainaud, M. Dia, L. André, D. Sousa Lemos, Y. Liechti, N. Maamari

This contactless water quality monitoring system for wastewater combines multispectral imaging with edge-based machine learning and application-specific illumination setup to monitor multiple water quality parameters such as turbidity, NH₄, phosphate, etc., in a cost-effective and nearly maintenance-free manner. It includes machine learning models to predict water quality, achieving results that surpass current state-of-the-art methods.

Realtime monitoring of water quality in urban drainage systems and wastewater treatment plants (WWTPs) is crucial for detecting pollutants that may contaminate the environment [1] and for effective operations of the treatment plant. Such monitoring is traditionally conducted through manual sampling campaigns or by using spectrophotometric probes immersed in water [2] or daily/weekly manual sampling. These methods are complex and costly to operate and maintain [3], often leading to delayed responses that can cause harm to the environment and facilities. Periodically and systematically monitoring water pollutant is however essential for optimizing treatment processes at WWTPs.

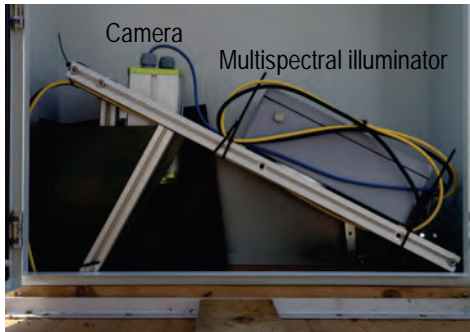


Figure 1: Prototype deployed at Altenrhein.

Water quality is assessed by measuring parameters like turbidity (TUR), NH₄, phosphate (PO₄), and chemical oxygen demand (COD). CSEM developed an industrialisation-ready prototype (Figure 1) for contactless measurement, consisting of multispectral imaging with specific illumination that extracts spectral characteristics and machine learning algorithms that predicts water quality. The system includes a UV-sensitive camera and multispectral illumination with 16 bands (250 nm to 940 nm), operated by an embedded computer that pushes data to the cloud for analysis.

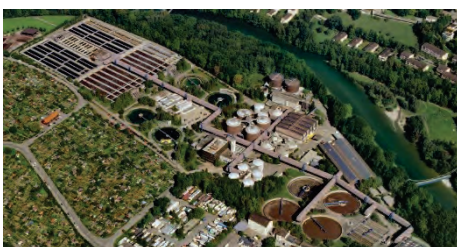


Figure 2: Bird view of Zurich's wastewater treatment plant.

The system deployed at Altenrhein's WWTP (Figure 2) by Photrack AG, with plans for Zurich's WWTP by the end of 2024. Preliminary results illustrated in Figure 3 were obtained by

recording real wastewater at EAWAG's WWTP facility lab. These initial predictions show high correlation for turbidity R²=0.85 (error: 9.7%), and R²=0.66 (error: 21%) for NH₄, and R²=0.73 (error: 39%) for PO₄. WWTPs are enthusiastic about these early results. Improved accuracy is anticipated with the new prototype.

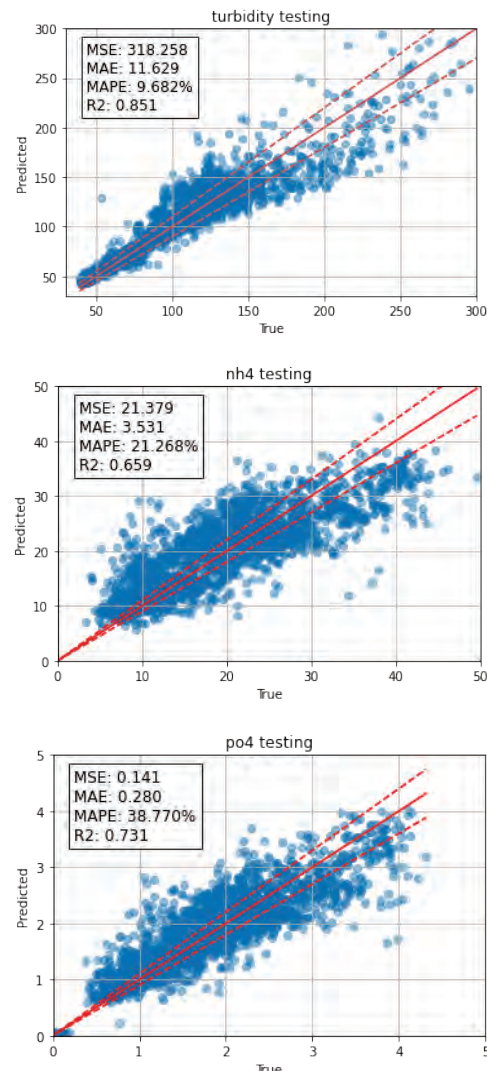


Figure 3: Predictions for turbidity, NH₄ and PO₄.

CSEM's multispectral imaging systems offer tailored solutions optimized for data rate, size, accuracy, and cost. These systems are designed to meet specific application needs, ensuring high performance and reliability while maintaining cost-effectiveness.

[1] Alice Botturi, et. al. (2020), Combined sewer overflows: A critical review on best practice and innovative solutions to mitigate impacts on environment and human health, Critical Reviews in Environmental Science and Technology, 1585-1618 Vol. 51, (2021)

[2] R. Salgado Brito, et. al. (2012), In situ UV-VIS spectroscopy to estimate COD and TSS in wastewater drainage systems Urban Water Journal, 261-273 Vol. 11, (2014)

[3] G. Gruber, et. al. (2006), Practical aspects, experiences and strategies by using UV/VIS sensors for long-term sewer monitoring, Water Practice and Technology, Vol. 1, Issue 1

Advances in Sustainable Electronics: Innovations in Circular Design, Degradable Components, and Eco-efficiency

A. Zandara, L. André, M. Monroe, P. Nussbaum

Rising e-waste concerns have driven European initiatives toward sustainable electronics. This report details CSEM's contributions to European project TESLA. TESLA developed transient, naturally decomposing electronics for agriculture applications. Together with CSEM efforts towards sustainability, this project aimed to create eco-efficient electronics, supporting Europe's vision for a less polluted, zero-waste future.

The global demand for electronic devices has intensified concerns about e-waste and environmental impacts. European initiatives like CHIST-ERA are leading efforts to create sustainable electronics by reducing waste, enhancing recyclability, and promoting a circular economy. CSEM plays a key role in these projects, focusing on sustainable materials, modular design, and energy efficiency across the whole lifecycle.

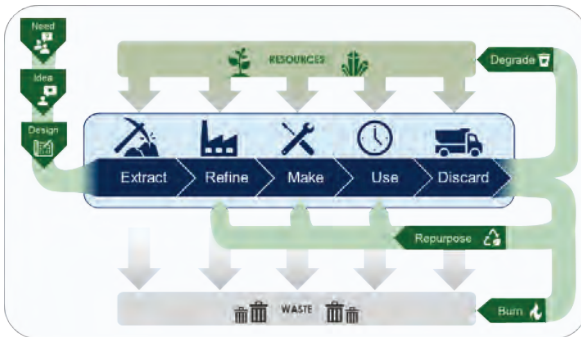


Figure 1: Reference life cycle of sustainable devices developed by CSEM.

TESLA objective: Developing biodegradable on-leaf monitoring patches for sustainable digital agriculture. These sensors are designed to decompose naturally after use, minimizing e-waste and benefiting the soil. By using non-toxic materials, TESLA's solution supports eco-friendly farming by enhancing soil quality while reducing environmental impact.

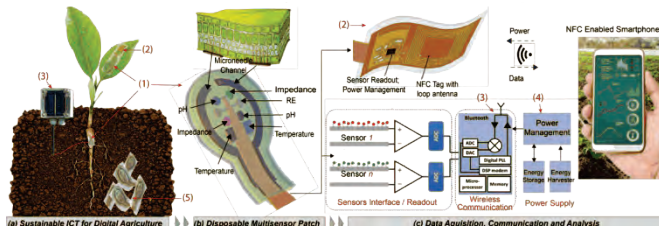


Figure 2: TESLA on-leaf monitoring device.

Biodegradable components: Throughout the project, VTT and TAU respectively developed biodegradable photovoltaic panels and biodegradable supercapacitors. VTT produced 1.3mW, 3.65V 7-cell PV panels. TAU successfully fabricated fully biodegradable 3.6V and 1.1F supercapacitors using K ionic liquid as electrolyte and cellulose diacetate as substrate.

Through a thorough analysis of these power components, CSEM developed an advanced active load system, able to emulate a variety of IoT devices in different scenarios (e.g. transmission, computation, standby) and measure the performance of the harvesting system.

CSEM further implemented MPPT for harvesting, active balancing, and voltage regulation utilizing a COTS tailor-made system. The setup enabled extended performance tests, confirming an IoT node lifetime of more than 15 hours overnight, when PV-harvested energy is not providing support:

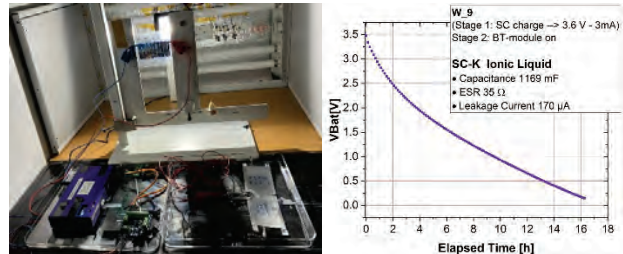


Figure 3: Harvesting system testing setup and discharge results.

Microneedle development: To interface the pH sensors with plants leaves, CSEM developed a microneedle array to interface with the internal fluid of leaves (SAP) by utilizing a sustainable resin (3Dresyns BioDeg Corn). Through multiple design and manufacturing iterations, the final implementation resulted in direct adhesion to the IMIF-manufactured pH sensor surface.

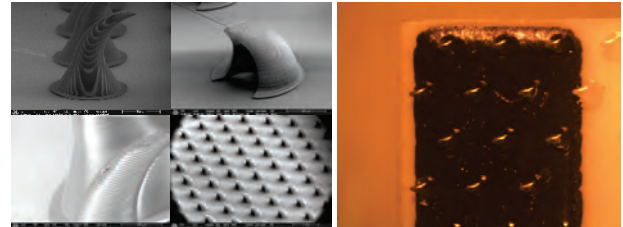


Figure 4: CSEM Microneedles 100nm per layer, 200μm length.

Wireless node: The final integration of all the components developed by the various partner has been executed by CSEM. The wireless system uses a STM32WB with custom BLE stack to communicate with a CSEM-developed android app supporting API 35. The electrochemical sensor is interfaced by the AD5941, with energy harvesting and power management implemented using an AEM10330.

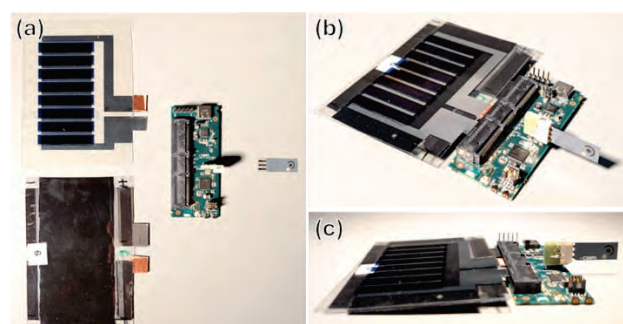


Figure 4: Final implemented demo including (a) disassembled components, and (b), (c) fully assembled device.

We acknowledge the project support from CHIST-ERA and funding support from the Swiss National Science Foundation (SNSF).

Biodegradable Chipless Sensor Tags for Sustainable Smart Packaging in Logistics

O. Vorobyov, C. Beyer, P. Nussbaum, D. Schmid, D. Briand •, G. Nystroem ••

Compostable and biodegradable materials are the pillars of solutions for fighting against electronic waste, CSEM, EMPA and EPFL propose an ultra-low cost, simple, and eco-friendly chipless sensor and identification tags, able of direct biodegradation, disposal, or recycling — eliminating the need for return chain logistics or waste separation.

The combination of chipless RFID tags and a biodegradable substrate offers a cutting-edge solution for sustainable smart packaging. These tags eliminate the need for traditional IC-based technology, reducing costs and environmental impact. Designed for applications like logistics and environmental monitoring, the tags are eco-friendly, ultra-low-cost, and can be biodegraded, disposed of, or recycled without requiring complex waste management systems. This technology provides customers with the ability to monitor and identify items in real-time while supporting global efforts to reduce electronic waste.

Chipless RFID technology enables wireless data transfer without using integrated circuits (ICs), which are commonly found in conventional RFID tags. The tags operate by reflecting RF waves, allowing them to be read remotely. The chipless tag substrate is cellulose-based materials, which are fully biodegradable and free of harmful plastics, ensuring a minimal environmental footprint. Conductive materials such as zinc ink are used for the printed circuitry, which ensures conductivity while maintaining biodegradability.

The chipless tags are designed to function as both identification tools and sensors. For instance, temperature sensors are integrated into the tags by embedding a non-reversible temperature sensing element, such as a mixture of high melting point oils (e.g. coco oil), into the structure. When the temperature exceeds a predefined threshold, the sensor is activated, and the event is recorded^[1]. The prototyped fully biodegradable "GREEN" tag, which functions at short distances (direct contact and up to 3 mm), is shown in Figure 1 and Figure 3.

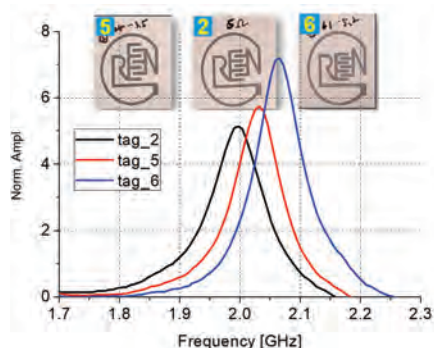


Figure 1: Short-range tags with Zn ink conductive lines: measured performance.

The short range, tag shown in Figure 1, operates over short distances (up to 3 mm). It is completely biodegradable and demonstrates excellent performance in transmitting data for identification and sensing purposes. The use of zinc ink for conductive lines ensures both functionality and environmental friendliness. A longer-range version of the tag, depicted in Figure 2, is capable of operating at distances up to 50 cm, with

current tests achieving a range of 30 cm. These tags can encode data with up to 10-bit resolution (with future potential for 16-bit).

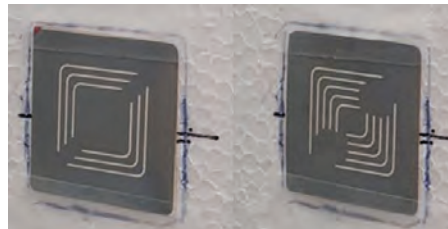


Figure 2: Long-range data tags with Zn ink conductive lines: 3-bit (left) and 10-bit (right).

While biodegradable tags present promising opportunities, they also face challenges. Due to the paper-based substrate and the use of non-toxic metallization like zinc ink, these tags have lower-quality resonators compared to traditional RF tags. Over time, the absorption of humidity by the substrate leads to reduced conductivity, resulting in increased losses and a decrease in operational distance.

The operational system developed at CSEM includes a custom-designed reader and software capable of detecting and classifying chipless RFID tags. It utilizes Principal Component Analysis (PCA) to categorize tags based on their frequency responses. Python-based software supports this process by managing numerical identifiers, such as frequency points and S11 values, which represent the tag's reflection coefficient.



Figure 3: Chipless TAGs (short and long-range) reader developed at CSEM: a portable device for the measured parameter visualization, reader with integrated antenna and short-range chipless tags.

Biodegradable sensors offer minimal environmental impact and a degradation behaviour that can be tuned for applications within zero-waste environmental sensing. Developed tag solutions can be used in smart packaging of perishable goods applications.

The "GREENsPACK – Green Smart Packaging" receives funding from the BRIDGE – DISCOVERY program under grant agreement No. 187223. CSEM thanks them for their support.

• EPFL
•• EMPA

^[1] O. Vorobyov, C. Beyer, P. Nussbaum, Chipless Biodegradable Tags, theoretical performance estimation, IEEE UkrMW (2022)

Functionalization of Helmet with Electromagnetic Stimulation and Near-infrared Spectroscopic Measurement

C. Hennemann, A. Zandara, L. André, D. Lemos, Y. Liechti, P. Nussbaum

CSEM develops an optode that combines controlled electromagnetic fields and infrared spectroscopy into a compact and effective package. Dozens of these optodes are placed on a helmet aiming to enhance brain performance and prevent cognitive decline using electromagnetic stimulation functional Near Infra-Red Spectroscopy (fNIRS) to measure brain activity.

This project aims to establish a proof of concept for a helmet that integrates electromagnetic stimulation into a commercial off-the-shelf (COTS) system designed for cranial Functional Near-Infrared Spectroscopy (fNIRS). Pulsed Electromagnetic Field (pEMF) coils were specifically designed and incorporated into an existing fNIRS system. The overall architecture, illustrated in Figure 1, features a central unit that wirelessly communicates via Bluetooth Low Energy (BLE) with the system configuration mobile app.

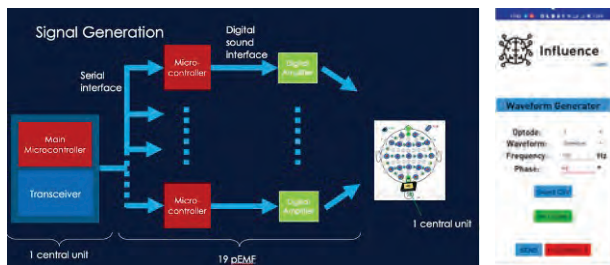


Figure 1: Architecture and mobile app.

This central unit sequentially configures all the optodes (pEMF coils). Each optode is equipped with a low-cost microcontroller to control its respective pEMF coil and embeds an audio amplifier to drive the coil. In addition to the four primary signal types (sine, triangle, square, and sawtooth), the system can also generate an arbitrary waveform shape from the app (download file). These signals' frequency, amplitude, and phase shift are programmable and can be adjusted relative to each other through the app.



Figure 2: Optodes embedding the fNIRS and pEMF coil and drivers.

This integration encompasses the mechanical assembly of the coils within the helmet, as well as the necessary electronics and software controls to enable synchronized operations. The project outlined the complete system architecture and prototyped the mechanical integration of the pEMF coils with the fNIRS photodiodes and emitting units (Figure 2). A phantom head was

designed (Figure 3) to closely replicate the final head environment. This model was used to assess the fields generated at various points within the brain.

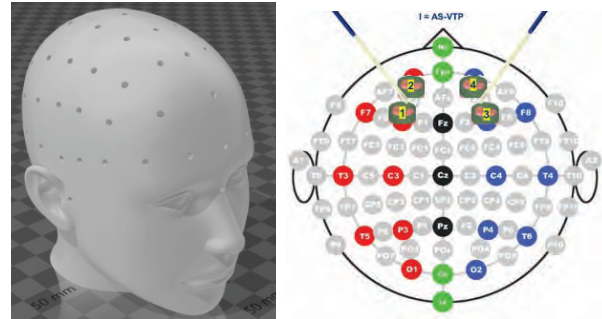


Figure 3: Phantom head used to assess the magnetic field.

The head was constructed to be filled with a liquid, simplifying the complex structure of different layers (skin, fat, muscle, bone, dura, CSF, brain) into a homogeneous model. Two studies [1][2] show that it is possible to replicate a brain with a homogeneous head liquid ($\epsilon_r = 41$, $\sigma = 1.65 \text{ S/m}$). Consequently, worst-case scenarios can be addressed using these homogeneous models. A third paper^[3] outlines the procedure to create a brain-emulating liquid with a permittivity of $\epsilon_r = 40.38$ (Skin Model B).

The optodes were precisely positioned following the 10-20 EEG system reference configuration for accurate placement. Finally, a full helmet was designed (Figure 4) enabling good mechanical stability, optodes placement, and final in-vivo validation.



Figure 4: final helmet for in-vivo validation.

This innovative technology could revolutionize brain health monitoring and improvement, making it easier to maintain optimal brain function.

[1] Meier, K.; Hombach, V.; Kastle, R.; Yew-Slow, T.; Kuster, N., The dependence of electromagnetic energy absorption upon human head modelling at 1800 MHz, IEEE Trans. Microw. Theory Tech. (1997), 45, 2058–2062.

[2] Cooper, J.; Hombach, V., The specific absorption rate in a spherical head model from a dipole with metallic walls nearby, IEEE Trans. Electromagn. Compat. (1998), 40, 377–382.

[3] Siddhant Goswamia, Deepak C kariaa, Tapas Bhuiyab, Vikalp Singh. Design and Analysis of different Phantom Fluids for Implantable and Breast Cancer Detection

Ultra-low-cost Near-field Wireless Power Transfer across Neighborhoods of Tiles

C. Hennemann, O. Vorobyov, J. Soldevila Villarrasa, L. André, D. Lemos, Y. Liechti, S. Sunier, P. Nussbaum

The demand for wireless power transfer (WPT) is rapidly growing, driven by both sustainability and ease of deployment. The developed technology showcases the use of WPT as well as passive energy propagation, across neighboring sensors, forming a 2D sensing array powered by a single feed. The technology is integrated into sensing tiles designed to detect leaks in roof monitoring applications.

The primary goal of this technology is to develop a demonstrator of wireless power transfer with practical applications, paving the way for a wide range of products based on the adjacent distribution of items such as tiles, bricks, and panels. The operational principle involves powering the grid through a master tile or feeding port, which acts as the initial interaction point. This master tile provides power to the first cell via inductive coupling. Subsequently, the power is transferred from the first tile to its neighboring tiles using the same inductive coupling method, pursuing this process until the entire grid is energized. The tiles are arranged in a two-dimensional array (Figure 1). Propagation antennas, printed on a polymer foil that houses the electronics and sensors, are wrapped around each tile. To fit the demonstrator in a standard office, the tile size was reduced to 30 × 30 cm from the commercial 2 × 1 m plates. The coupling between adjacent coils was optimised by using electromagnetic simulations and engineering samples (Figure 1).

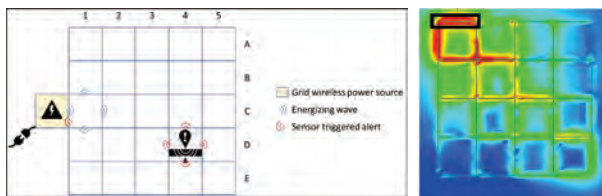


Figure 1: Principle of operation and simulation results.

To drastically decrease the manufacturing costs, the selected manufacturing technique relies on etching of a Copper-PET film substrate covered with photosensitive material, on which the coil pattern is transferred using a screen-printing mask and exposing it to UV light. Finally, the copper layer is removed from the areas of the photosensitive layer which has not been exposed to UV light and exposed again to the copper underneath. Figure 2 presents a complete stripe of film after the etching procedure. The four coils are one next to each other, and the stripe will be wrapped around the square EPS block in such a way that each coil will fit on one of the four sides.

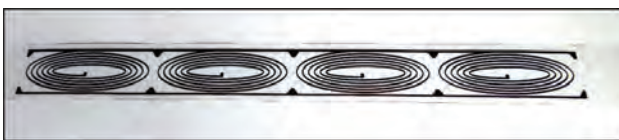


Figure 2: Complete stripe of film after etching procedure.

The tiles can be assembled into a grid by placing them side by side, enabling the grid to report the position of a triggered sensor anywhere within its bounds. The energy harvester converts energy from the RF signal at its input into DC power, which is then supplied to the embedded system. Various RF energy harvesters are commercially available to power a system from a Wireless power (WPT) source. We selected the most efficient circuit, and once sufficient energy is harvested, the system on chip (including the harvester, PMU, microcontroller, and transceiver) boots up and initiates a loop for leakage detection and reporting. If a leak is detected, the system reports it and then returns to hibernate mode. Since the leaking tile consistently transmits BLE advertising packets, identifying the direction of the

highest signal level allows us to pinpoint its location. Our current solution effectively detects leakage using a portable spectrum analyzer and a high-directivity BLE antenna to scan the grid in two orthogonal directions, identifying the source of the strongest Bluetooth packets. The promising results validate the use of our in-house Angle of Arrival (AoA) algorithm for leak detection. All necessary hardware and software can be implemented in the supply port device, which would report the location of the leakage without requiring manual scanning of the grid.



Figure 3: Final tile wrapped around the tile and demonstrator (25 tiles).

Currently, leaks in the building's roof insulation layer are only detected when users notice them, requiring the repair team to search manually for the leak's location. While numerous systems are available, they typically function as standalone units. CSEM offers a novel approach by integrating the detection system directly within the insulation tiles, maintaining competitive costs. Due to the 20-year product lifespan, the use of batteries for the necessary electronics is forbidden. CSEM's innovative solution involves distributing and propagating energy wirelessly between the insulation tiles and employing an alternate RF channel for leak detection and localization.

The CSEM approach introduces significant advancements in:

- Exploitation: Automated, regular leak detection without operator intervention, and simplified localization with user terminals guiding operators directly to leaks.
- Maintenance-free: Ensuring a lifespan of 10-20 years, limited only by the weakest component (capacitors).

In this project, we successfully demonstrated the concept of wireless power transfer using magnetic coupling to energize a 2D array of sensing nodes. This method allows energy to be wirelessly transmitted from tile to tile, eliminating the need for batteries. Each tile can harvest sufficient energy to operate, conduct a humidity measurement, transmit the data via BLE communication, and then return to sleep mode. With a single power supply port, it is possible to transmit and propagate enough power to energize 25 tiles, each measuring 30 × 30 cm, arranged in a 5 × 5 configuration. By extrapolating to commercially available insulating tiles of 1 × 2 m, each supply port could potentially cover an area of 50 m².

A 24-GHz 4-Element Multi-beam Wireless Energy Harvesting Array with Class-F Rectifiers Achieving 51.5 PCE

M. Ghorbanpoor, E. Le Roux, A. M. Ahmadi Najaf Abadi, O. Vorobyov, P. Nussbaum, H. Wang •

This study introduces a compact and efficient Wireless Power Transfer solution for IoT applications, based on a 24GHz 4-element concurrent multi-beam energy harvesting array. Thanks to the utilization of a novel three-line-coupler, the harmonic shaping rectifier achieves the best reported rectifier power conversion efficiency of 51.5%. A 4-port ultra-compact Butler matrix with transformer-based 90° hybrid couplers is utilized for concurrent beamforming.

In the context of the growing Internet of Things (IoT), wireless power transfer (WPT) provides a sustainable alternative to batteries, which are becoming impractical due to their environmental impact and maintenance issues. Most current WPT systems use 2.4/5.8 GHz ISM bands, but these bands have limitations in terms of antenna efficiency, overall Rx size, and reduced system efficiency due to the lack of Tx beamforming. In contrast, millimeter-wave systems offer advantages such as compact antenna sizes and focused beamforming, allowing efficient energy transfer. However, increasing frequency introduces design challenges due to parasitics that degrade the rectifier performance.

The core of the CSEM approach is a cross-coupled Class-F rectifier, which maximizes efficiency by shaping the drain waveform to reduce leakage current. Traditional cross-coupled rectifiers (CCR) suffer from leakage during state transitions, limiting their power conversion efficiency (PCE). By using harmonic termination techniques, the Class-F rectifier achieves a square-shaped drain waveform, minimizing both transition leakage loss by fast transition and conduction loss by limited voltage drop (Figure 1a). The optimal harmonic contents required for Drain and Source terminals are acquired with respect to optimized values in Figure 1b. This rectifier employs a novel three-coupled-line balun design, which achieves wideband operation at both the fundamental frequency (24 GHz) and its third harmonic (72 GHz) (Figure 1c).

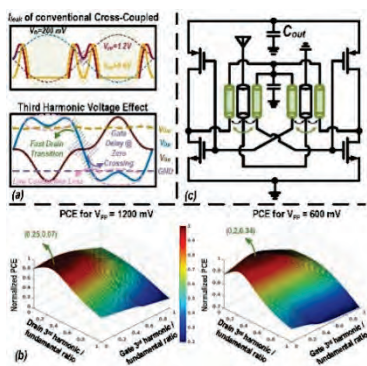


Figure 1: Proposed class-F rectifier. a) 3rd harmonic on S/D signals. b) Optimum PCE point. c) Three-coupled-line class-F rectifier schematic.

A significant novelty in this work is the integration of a 4-port Butler matrix to enable concurrent multi-beam beamforming. This approach is passive, meaning it does not consume additional power, compatible with cold-start, and it allows the system to simultaneously harvest energy from multiple angles, covering the entire field of view (FoV). By performing passive beamforming before rectification, the system enhances the total received power, improving the overall PCE and dynamic range.

In contrast to active beamformers, the passive Butler matrix ensures low-loss and efficient beam steering. This method is

particularly useful for WPT applications where the direction of incoming power is not always known maximizing concurrent reception for 4 different directions (Figure 2).

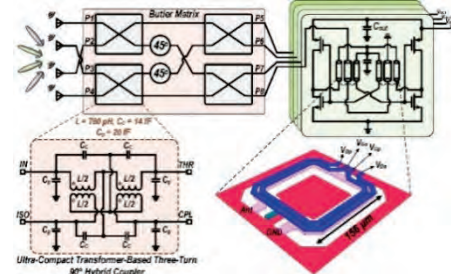


Figure 2: Proposed concurrent multi-beam rectifying array.

The system was fabricated in a 22nm CMOS FD-SOI process with a core area of 0.53 mm². Measurements showed a peak PCE of 51.5% at 22 GHz for a single rectifier, with an optimum DC load of 147Ω. The system achieves a broad 3-dB bandwidth from 17.5 to 28 GHz, maintaining a PCE above 30% across a wide input power range (-5 dBm to 14 dBm).

The Butler matrix demonstrated a low passive loss of 1.21 dB, with a full FoV beam pattern showing a peak-to-null ratio better than 28 dB. The rectifying array's performance showed an output power improvement of 1.49 times compared to non-coherent rectenna arrays, confirming the benefits of the beamforming approach.

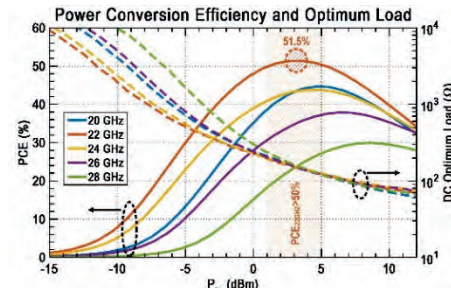


Figure 3: Single rectifier measurement results w/o beamforming.

As shown in Figure 3, this work reports the highest PCE of 51.5% for a millimeter-wave rectifier and demonstrates the effectiveness of combining a Class-F rectifier with a passive beamforming array for efficient wireless power harvesting. The use of a Butler matrix for multi-beam concurrent energy harvesting offers a compact and low-power solution that is particularly well-suited for WPT applications in the IoT era. The system achieves a total efficiency of 30.2% including beamformer, making it a competitive solution for future wireless energy harvesting systems.

This work has received funding from the Swiss State Secretariat for Education, Research, and Innovation (SERI) under the SwissChips initiative.

IoT Fleet Key Management with built-in Post Compromise Recovery

C. Lefevre, D. Vizár

The long lifetime and weak security posture of IoT devices make the loss of cryptographic keys through attacks virtually unavoidable. CSEM formalizes, designs and implements post-compromise security for IoT, enabling resilient IoT fleets with an inherent capacity to recover from such an incident.

The topic of so-called post-compromise security caught the public attention recently, fueled by the revelations about mass surveillance and concerns about privacy. The core objective here is that of restoring end-to-end security (confidentiality, authenticity and integrity) of messaging after an attacker extracts the cryptographic keys of one of the communication partners. Existing research on this topic proposes simple protocols which restore security of messaging by sending more messages (and using sophisticated cryptography underneath); the Signal protocol [1] is one of the most famous examples of such approach, being the baseline of WhatsApp messenger app.

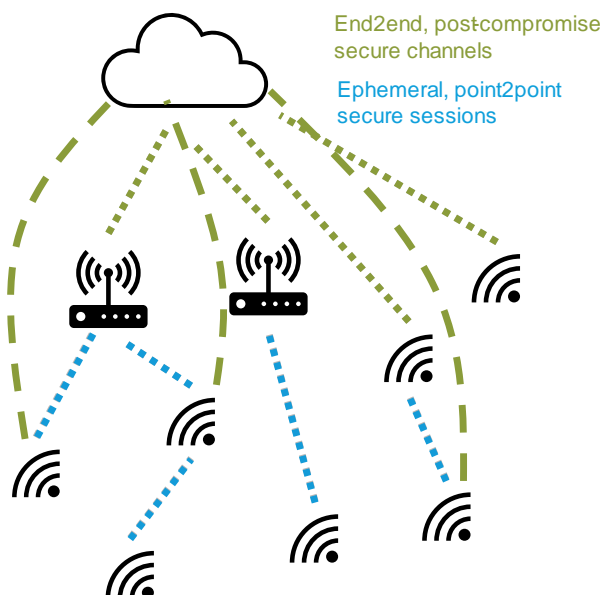


Figure 1: Post-compromise secure key management for IoT fleets.

The problem of post-compromise security is also relevant in the context of Internet of Things (IoT), where connected embedded devices are low-resource, have limited software isolation features, if any, and are often physically located in an uncontrolled environment, potentially accessible by an adversary. Secret keys of such devices are at risk of being extracted, be it through a software exploit or a physical attack. Restoring security from this is non-trivial; manual interventions are incompatible with the IoT business model and traditional key rotation techniques are ineffective against attackers who already possess device keys and are subsequently passive, or perform a short-term man-in-the-middle attacks. This issue will be alleviated by a key management design for IoT device fleet, capable of post-compromise recovery. The intuitive requirement is for a device, whose keys are leaked, to evolve the keys automatically, through normal usage, so that the security is

restored. Translating this intuition of a "post-compromise recovery" to formal requirements requires to define the "security".

To cover this gap, a formal model of post-compromise security has been developed at CSEM. It defines a device fleet key management system with a central (cloud) node, which manages credentials of individual devices. The credentials allow any pair of devices to perform a mutual authenticated key exchange (AKE), to establish a temporary secret key for a point-to-point secure session (Figure 1). This approach covers the need of any communication topology, at any scale, as the size of the devices' long-term secure storage does not grow with the number of sessions established. The post-compromise security is then defined in three formal definitions, which must be met simultaneously: (1) It must be impossible for an attacker who can drop, reorder, or inject messages to bring the system in an unrecoverable state, (2) an attacker who initiates an active man-in-the-middle attack either continues indefinitely, or is detected, and (3) when two devices who were either uncompromised or had a chance to perform the auto-healing protocol exchange a session key, they can be assured of each other's identities and the key is secret.

A construction provably achieving the security goals of the model has been designed. In a nutshell, it combines these ingredients:

- **Signal key exchange.** The communication between each of the devices and the central (cloud) key manager uses Signal. This the so-called ratcheted protocol updates the secret state of each communication participant whenever a message is received or sent, such that exchanging a few messages after a key leakage restores secrecy.
- **Sigma AKE.** Each device has credentials (private key and a "digital certificate") issued by the key manager. With these credentials, any two devices can perform an AKE to establish a session key. The AKE protocol adopted is Sigma [2], a well-tested protocol with low overhead.
- **Certificate management protocol.** The ratcheted channel is used to manage the certificates. A certificate renewal protocol is designed, such that even if the cloud or the device are compromised at its start, the refreshed credentials will still be secure. Two additional protocols allow to assert expiry of certificates in online and offline scenarios

A proof-of-concept implementation in Python has been developed to demonstrate the usage patterns and effects of basic attacks. A resource-optimized embedded C library is being developed, to allow this technology to provide long-term resilience of any IoT platform while simplifying maintenance and reducing the associated costs.

[1] K. Cohn-Gordon, C. Cremers, B. Dowling, L. Garratt, D. Stebila, A formal security analysis of the signal messaging protocol, Journal of Cryptology: 1914-83

[2] H. Krawczyk, SIGMA: The 'SIGn-and-MAC' Approach to Authenticated Diffie-Hellman and Its Use in the IKE-Protocols, CRYPTO (2003)

Extending End-to-end Data Encryption & Sharing Technology with Microledger Audit Trails

C. Bührer, D. Vizár

CSEM's Encryptflow technology extends the end-to-end data encryption and sharing in IoT to generate non-repudiable audit trails for each sharing transaction. This allows traceable resharing and to ensure that the data processors always get the original data, paving the way to a trusted data economy.

The ongoing digitalization together with the expansion of the Internet of Things (IoT) paradigm result in immense quantities of data being collected in virtually all verticals. In most cases, the data collected by a particular organization has a potential value for the ecosystem of the organization that is far greater than the value extracted through the primary processing. Yet, such a secondary data valorization in the ecosystem rarely happens, due to lack of trust. In digital health, patient data collected in diagnostic monitoring are rarely reused at scale to further improve diagnostic, drug development or treatments, due to complex regulation and patients' privacy concerns. Due to fear of uncontrolled data dissemination, data produced by advanced manufacturing machines is rarely reused to increase the power of predictive maintenance models or the efficiency of support from the component suppliers. Similar situation arises in complex logistic ecosystems, for which data could help improve the overall efficiency but instead is remaining siloed.

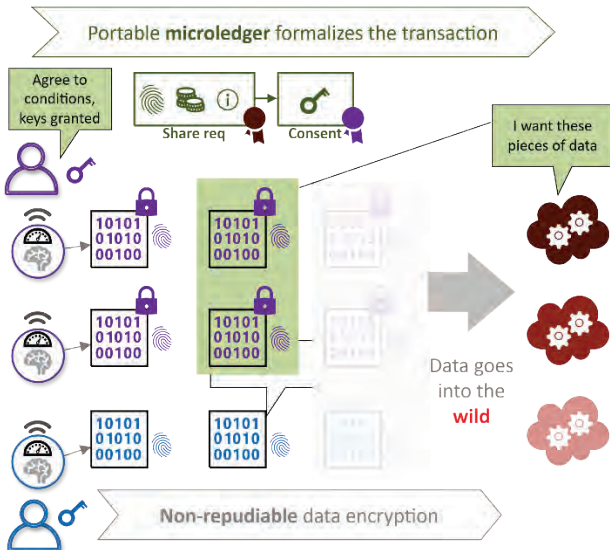


Figure 1: Data protection and controlled sharing with EncryptFlow.

To address these issues, CSEM has previously developed an advanced technology, representing the first step towards advanced data valorization, allowing data to be protected, confidently advertised and then flexibly shared with processors that needn't be identified at the time of encryption. It integrates end-to-end data encryption and transparent data sharing where a data owner retains a fine-grained control over who gets what access, designed and optimized to scale up to IoT proportions^[1]. It encrypts (not only) IoT data directly at source with very low overhead. The data then stay protected until needed for processing, no matter what the underlying transmission and storage infrastructure is. In particular, the decryption keys are not provisioned to any party. Any would-be processor needing

[1] D. Vizár, C. Kassapoglou-Faist, R. Berguerand, User-Centric Key Management for End-to-End IoT Security and Privacy, [CSEM Scientific & Technical Report \(2022\), 20](#)

access can compute a succinct, signed electronic request to access the exactly needed data points (e.g. readings of a sensor from a certain day, week or month), thanks to clever metadata that characterizes keys used to encrypt each data point. Only upon the data owner's consent (explicit or preconfigured) are decryption keys provisioned.

However, fully addressing the issues standing in the way to a data economy requires crucial missing features. On one hand, it is desirable that each data access request granted shall generate an audit trail, i.e., a strong, cryptographically non-repudiable evidence. On the other hand, ensuring that data owners cannot selectively reveal real or dummy, useless data upon key provisioning is needed to extend the trust in the transaction both ways (reassuring data "buyer").

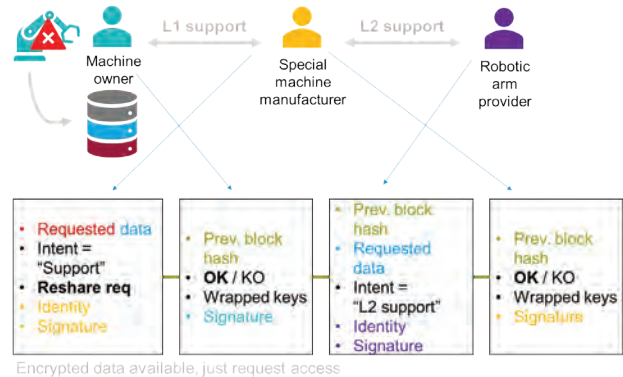


Figure 2: Microledgers allow controlled data forwarding with audit trails.

To address these remaining problems, CSEM has extended the data encryption technology and dubbed it EncryptFlow (Figure 1). The first improvement in EncryptFlow is the use of committing encryption, which protects the data confidentiality but also ensures that, once encrypted data is released, it can only be decrypted to the original plaintext with the original key. The second improvement is that the sharing request and response are now embedded in a microledger, i.e., a hash-chain^[2] with digitally signed blocks. This way, the interaction automatically produces an audit trail available to both parties at the end of the transaction, as the request and response are sequentialized and digital signatures provide non-repudiation. The design of the microledger allows data processors to open any single microledger to a third-party auditor, allowing for an impartial resolution of disputes. A primary sharing microledger can also be extended with a request block made to the primary data processor for resharing (if authorized). This enables flexible, yet transparent data forwarding for level-2 machine support for example, with audit trails for the full path data travels (Figure 2).

[2] D. Horne, Hash Chain, Encyclopedia of Cryptography, Security and Privacy. Springer, https://doi.org/10.1007/978-3-642-27739-9_780-2

Detecting Heap Memory Bugs with Emulation Fuzzing Testbench

R. Müller, D. Vizár

CSEM's initial proof of concept of a fuzzing test bench for embedded firmware has been improved to support more modern ARM-based cores and run more effectively and paired with an address sanitizer for detection of heap memory bugs to help create robust firmware for secure embedded devices.

Fuzzing is a dynamic software testing technique, which helps discover vulnerabilities and bugs by feeding the target with mutating data inputs. Modern fuzzers generate these inputs iteratively, using optimizations and heuristics to optimize the search through the space of possible inputs and speed up the discovery of those that provoke crashes and exhibit potential security flaws. Nowadays, host software fuzzers leverage techniques such as coverage-guided fuzzing, which uses feedback from the software's execution to generate more effective test cases. Tools like AFL (American Fuzzy Lop) and libFuzzer have become industry standards, enabling extensive and efficient vulnerability discovery in complex software systems.

Fuzzing firmware for embedded devices presents unique challenges, however. Due to limited computational resources, it is not possible to run the fuzzer directly on the target. All major approaches run fuzzer on the host and the target software in an emulator and resolve hardware dependencies through **peripheral proxying** (emulator uses attached hardware when needed), **peripheral modelling** (emulator uses software models of the hardware peripherals), or **full-system emulation**: (the full embedded system is emulated, using tools like QEMU, peripherals are mocked Figure 1).

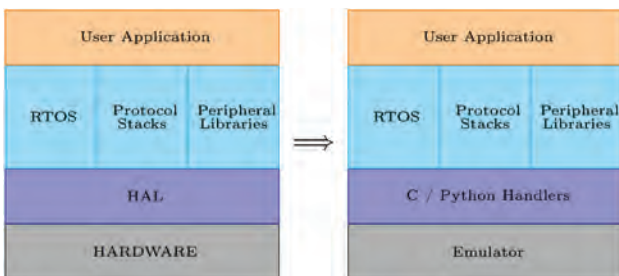


Figure 1: Full-system emulation for embedded fuzzing.

An initial proof-of-concept (PoC) embedded fuzzing test bench has been developed at CSEM, based on full-system emulation [1]. This approach has been estimated as the most scalable for the intended deployment in CI/CD pipelines. The bench is based on the HAL-Fuzz Framework, combining the Unicorn CPU emulator, Avatar2 emulation control framework, and AFL Fuzzer. Emulation of peripherals, such as a UART console, uses Python handlers, enabling the injection of fuzzing inputs and monitoring of the firmware's responses. The bench successfully implemented buffer overflow detection using canaries. However, the emulation speed was limited to ~0.03 fuzzer executions per second, requiring optimizations for higher speed, and the coverage of bugs was limited to buffer overflows in dynamically allocated memory only.

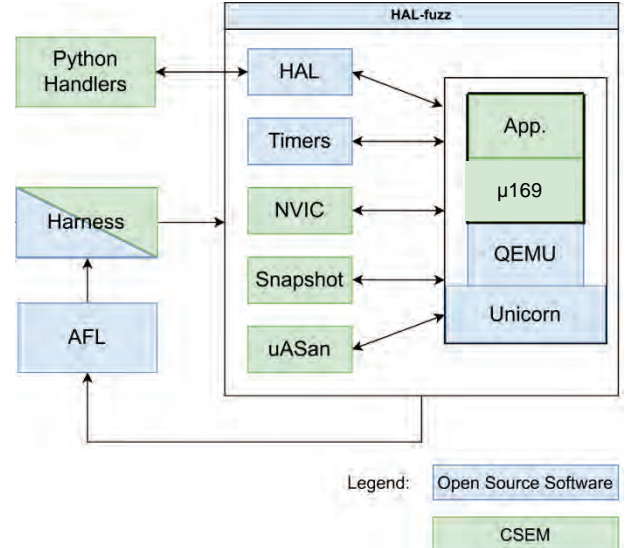


Figure 2: Enhanced fuzzing test bench with uASan for bugs detection in dynamically allocated memory and snapshots for better performance.

The initial PoC has been extended and improved in several ways. By integrating more recent version of the **Unicorn emulation framework**, a wider range of ARM processors, including Cortex-M7, is now supported, enhancing its applicability to modern embedded systems. An enhanced **model of the nested vector interrupt controller (NVIC)** has been implemented for a more realistic exception handling in ARM cores, including floating-point registers and nested interrupts. A custom **address sanitizer uASan** has been developed to use the target operating system's native memory allocator, internally reusing parts of the Address Sanitizer project [2]. The uASan detects bugs in the dynamically allocated memory, such as buffer overflows, underflows, use-after-free, and double-free errors. This is achieved by padding allocated buffers with gaps and by maintaining a shadow memory with distinguished values assigned to addresses corresponding to various types of memory cells, such as red zones in the "gaps", allocated memory, freed memory etc. With these in place, a hook on every memory access instruction allows each access to be checked against the shadow memory to detect access crossing the red zones, double free, etc. Finally, to boost the performance, execution support for execution snapshots has been added. Here, the costly initialization of the firmware can be computed only once, and further iterations only executed from a configured starting point, allowing more inputs to be tested in the same time.

The improved test bench has already helped harden CSEM's embedded operating system μ169. Further improvements include the detection of memory bugs in the stack and its integration into continuous development tools.

[1] D. Vizár, I. Ben Salah, M. Marty, Discovering vulnerabilities in embedded firmware with fuzzing techniques, [CSEM Scientific and Technical Report \(2023\), 32](#)

[2] K. Serebryany, D. Bruening, A. Potapenko, D. Vyukov, AddressSanitizer A fast address sanity checker (USENIX ATC 12)

Low-energy Implementation of ECDSA using Hardware Acceleration

F. Valencia, D. Besse, J.-L. Nagel

Through successful co-optimisation of hardware and software, CSEM designed and implemented high performance ECDSA security algorithms for digital signatures with low footprint and power consumption, suitable for embedded systems.

Security is a required property of all connected systems, although too often neglected on embedded systems due to the high incurred costs. Even if they go unnoticed, embedded systems manage more critical functions, use more sensible data, fulfill higher regulations and are more connected. CSEM implemented a high-performance, low footprint and low power acceleration of ECDSA, a digital signature algorithm based on elliptic curves, using a HW/SW codesign strategy. ECDSA C implementation was mapped to a RISC-V processor and a big-integer Montgomery arithmetic accelerator. The execution time was reduced by a factor of more than 12x while the active power only grows by 1.4x, yielding an energy reduction of 10x.

Elliptic Curve Cryptography (ECC) [1] is a family of Public Key Cryptography (PKE) based on elliptic curves over finite fields. ECC is very suitable for constrained devices because it has the smallest overhead in ciphertext/signature size and computational complexity of existing PKE algorithms. ECC can be used for key agreement, digital signatures, pseudo-random generators, etc. Elliptic curve operations heavily rely on big integer modulo arithmetic.

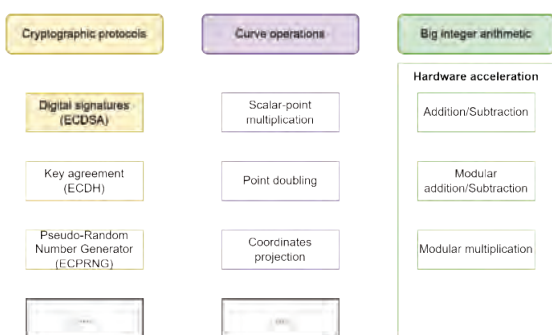


Figure 1: ECC layers.

Figure 1 shows three abstract layers in ECC protocols, where the lowest layer is the big integer arithmetic. This work presents the achieved improvements in ECDSA when big integer arithmetic is accelerated in hardware. The accelerator is integrated with a RISCV processor. The uECC library [2] was used as reference.

Firstly, the uECC code was modified to perform the core operations in the Montgomery domain, which is known to be very efficient in modulo arithmetic. Adding conversions to/from Montgomery domain yields even more Montgomery multiplications as the transformation consists in multiplying by a precalculated constant.

In a second phase, all these multiplications were mapped to an accelerator IP which integrates to the SoC system [3] via the APB

bus, to send commands and configuration, and a small DMA to handle the data directly in the RAM. Not only does the accelerator perform the Montgomery computation faster than the processor, but also less bus transactions to transfer data back-and-forth are required.

For reusability, the accelerator is not specific to curve cryptography but implements generic Montgomery-domain big integer arithmetic. Primarily, it has been optimized for the Montgomery modular multiplication which accounts for the most operations. Nevertheless, the accelerator also supports addition and subtraction with and without modular reduction through reuse of the same hardware. For those operations, the gain in computation time is not as significant but supporting them allows to keep the operands inside the accelerator instead of transferring them to the processor.

A complete system combining CSEM's IcyFlex-V RISC-V processor with a 256-bit wide operands accelerator was simulated in GF22 library with a clock at 25MHz. The operands width is configurable though and clock frequencies up to a few hundreds of MHz were achieved in synthesis with an area of 17kGE for the accelerator.

Table 1 Comparison of ECDSA functions using hardware acceleration.

	SW	SW+acc	Improvement
Time key generation	570 ms	39 ms	14.3x
Time signing	612 ms	41 ms	14.3x
Time verification	696 ms	55 ms	12.5x
Power	273 μ W	385 μ W	0.7x
Energy	512 μ J	52 μ J	10x

The execution time of the three main function of ECDSA (key generation, signing and verification) is reduced by more than 12x. Even if the total power (processor and accelerator) increases by 1.4x, the energy is reduced by one order of magnitude thanks to the shorter execution time.

This work shows how important it is to co-optimize the software and hardware of an SoC to achieve efficient implementations of cryptographic protocols, as energy can be reduced by efficient hardware computation blocks and by minimizing the system load, both processor and bus. Generic accelerators will provide more agility and reuse possibilities when implementing similar approaches for newer cryptographic protocols such as the recently standardized post-quantum algorithms.

[1] Digital Signature Standard (DSS), National Institute of Standards and Technology (2023)

[2] Comparative Study of ECC Libraries for Embedded Devices, Silde, Tjerand (2019)

[3] J.-L. Nagel, Icyflex-V: a new ultra-low power processor based on RISC-V architecture, [CSEM Scientific and Technical Report \(2019\), 116](#)

Multi-sensor Embedded AI Platform for the Acoustic Weather Station Aurora

J. Beysens, J.-M. Koller, D. Lemos, G. Wolfart

The Aurora acoustic weather station now acts as a powerful, yet low power connected sensor hub, to form a solid foundation for a versatile tinyML platform supporting multiple sensors, such as microphone arrays. It contributes to an integrated workflow including data acquisition, remote training and on-board tinyML inference laying the foundations to estimate more challenging weather parameters such as wind direction based on acoustics.

The Aurora Weather station project originally started through the challenge organized by the tiny machine learning (tinyML) foundation in 2022. The challenge consisted of developing a smart weather station without mechanical moving parts, that can estimate the wind and rain conditions using tinyML on a small microcontroller (MCU). After winning the challenge, CSEM coordinated the next edition of the smart weather tinyML challenge in 2023 and 2024, for which the original prototype was improved to enable large-scale data acquisition. Over 200 GB of data were used to train the tinyML models classifying wind speed and rain intensity based on acoustics.

In 2024, we designed a new hardware version of Aurora with the ambition to create a versatile platform capable to 1) support raw data acquisition using the previously developed framework [1] (acquisition mode), and 2) run low power tinyML inference (inference mode). Each operation mode features its dedicated microcontroller (MCU) for maximal efficiency. Figure 1 presents Aurora's operating modes and the MCU interfaces.

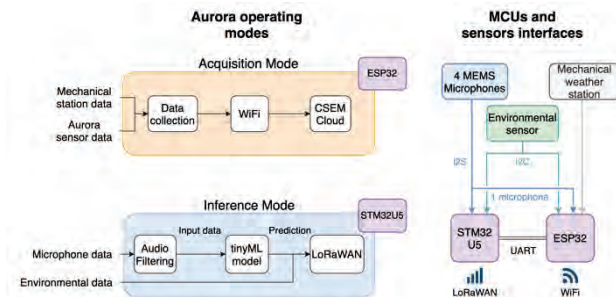


Figure 1: Block diagram of functional diagram of Aurora's operating modes (left), interface between sensors and dual MCU structure (right).

The first MCU, an Espressif ESP32, is used for data acquisition. In this mode, Aurora is connected to a twin mechanical weather station to gather ground truth data on rain and wind conditions (rain intensity and wind speed). Aurora gathers the raw data from all sensors and sends it using MQTT to the CSEM Cloud. This transmission is performed through Wi-Fi to a nearby hotspot, as it requires a large bandwidth to send the audio data (384 Kbit/s per microphone; 16 KHz sample rate at 24 bit per sample). Once the data arrives at the CSEM cloud, it is stored for further processing and performing offline training of the tinyML models. Using this data, both binary (no, yes) and ternary (no, little, heavy) models have been trained to classify wind and rain in coarse intensity zones. The resulting F1-score of the binary model for rain and wind equals 0.97 and 0.85, respectively, while the ternary model yields 0.84 and 0.76, respectively.

The second MCU, a STM32U5 running CSEM's in-house real-time operating system μ169, is responsible for the execution of the embedded AI models at run-time through the TensorFlow Lite

Micro (TFLM) framework, to perform the prediction of the rain and wind conditions based on sound data gathered by the microphones. The trained quantized models are approximately 27 KB in size and thus suitable to be hosted on the STM32U5 for inference. The inference latency using TFLM equals 232 ms. The resulting prediction and environmental data (temperature, pressure, humidity) are sent through low-power and long-range LoRaWAN to The Things Network (TTN) for accessing the live meteorological data.

Figure 2 shows the new hardware, comprising two PCBs. The circular sensor board (Figure 2-left) hosts four microphones spaced at 90 degrees, an environmental sensor (for temperature, pressure, humidity and air quality) and a magnetometer. Extending the single microphone setup from before to multiple microphones paves the way to predict wind direction next to speed in a future iteration. Furthermore, the environmental sensor was updated to include the BME680 gas sensor to measure various air quality indicators.



Figure 2: New custom-designed electronic boards for the Aurora weather station: sensor board (left) and processor board (right).

The square processor board (Figure 2-right) hosts the two different MCUs, the power management system to handle the battery and solar panel for energy harvesting, a LoRaWAN module, and a MicroSD card slot. The ESP32 and the STM32U5 communicate through a serial interface, allowing the ESP32 for transmitting the data sampled from the four microphones by the STM32U5 to the CSEM Cloud for data collection. Additionally, the inter-processor communication will be used to facilitate Firmware Update Over The Air (FUOTA) from the ESP32 to update the tinyML model running on the STM32U5 during the life time of the device deployed in the field.

The next steps include analyzing the tinyML models' robustness (train in one location and test in another) and leveraging the platform to estimate more challenging parameters such as the wind direction.

[1] J. Beysens, M. Haro, R. Berguerand, Data Acquisition Framework for Smart Weather Station Aurora, [CSEM Scientific and Technical Report \(2023\)](#), 20

Time-of-flight Based Gesture Recognition for Touch-free Wearables

J. Beysens, B. Knuchel, J.-M. Koller, P. Liechti, I. Ben Salah, D. Lemos, Y. Piguet

In the rapidly evolving field of wearable technology, touch-free interaction has emerged as a pivotal feature for seamless user experience. This work introduces a low-power time-of-flight (ToF) based gesture recognition system designed specifically for touch-free wearables. Leveraging the precision of ToF sensors to detect and interpret a variety of finger gestures, enables a more intuitive and responsive user interface.

Human computer interaction (HCI) has attracted significant attention in the recent years allowing new forms of touch-free interaction for in-car infotainment and controlling smart home appliances. Traditional human gesture recognition based on cameras involves significant computational power and is energy hungry, while those based on inertial measurement units (IMU) lack the required precision and robustness for those applications.

In this work, we designed a low-power gesture recognition system for touch-free wearables with a Time-of-Flight (ToF) sensor. This sensor captures a depth map in which each pixel represents the distance to a nearby object, measured by the propagation time of infrared light to the object. Using a limited resolution of 4×4 pixels allows to capture data sequences that resemble images with a high accuracy, yet at a minimal latency and energy consumption. Figure 1 depicts the electronic board.



Figure 1: Rendering of designed electronic board for gesture recognition.

Figure 2 shows the architecture. It consists of the ToF sensor, a low-power microcontroller running CSEM's in-house real-time operating system μ 169 and an OLED display for visualization.

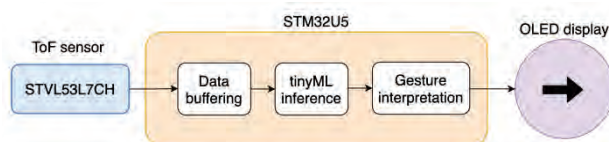


Figure 2: Block diagram of run-time gesture detection setup.

For data acquisition, the ToF sensor is connected to an ESP32, which acts as a bridge to send the pixel distance measurements to an MQTT broker server. A PC then subscribes to the relevant MQTT topic to collect the gesture recordings. Six finger gestures are supported: swipe left (L), swipe right (R), swipe up (U), swipe down (D), turn clockwise (CK), turn counter-clockwise (C-CK). In addition, an "unknown" (X) label is included to cover movements that shall not be detected as any gesture. Figure 3 presents an example, in which a user swipes the finger from left to right, at a distance below 10 cm from the sensor.

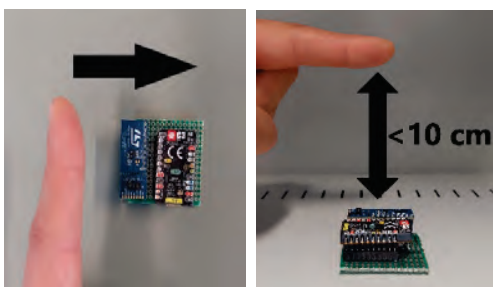


Figure 3: Acquisition setup showing the finger gesture "swipe right".

The dataset contains recordings of finger gestures of 20 participants with 10 repetitions of each gesture. The recording process starts automatically when the sensor detects a movement, specifically when 2 different pixels yield a distance closer than 10 cm. Each recording consists of 30 samples taken at a frequency of 60 Hz, resulting in a 500 ms recording duration. This setup ensures precise and consistent data collection for further analysis and processing. After acquisition, recordings are manually reviewed, and those lacking clarity are discarded. Furthermore, data augmentation is used doubling the dataset size, by flipping the recordings across different axes.

To achieve a robust detection system, sophisticated resource-constrained algorithms are essential. Recurrent Neural Networks (RNNs) and their variants, Long Short-Term Memory (LSTM) networks, are designed to handle sequential data by maintaining a memory of previous inputs. Temporal Convolutional Networks (TCNs) are an alternative to RNNs, using convolutional layers with causal filters to capture temporal dependencies. TCNs require significantly less memory for buffering feature maps compared to RNNs, making them more suitable for low-power embedded systems. Hence, we use a TCN to classify the gestures into the seven identified classes.

After training the TCN model, it is quantized and deployed for inference using TensorFlow Lite Micro on the microcontroller STM32U5. Quantization converts the model's weights from 32-bit floating-point numbers to 8-bit integers, aiming to significantly decreasing the model's size and computational requirements, without substantially compromising the accuracy.

The TCN achieves an overall accuracy of 92.5% on the test set. After quantization, the model size is reduced from 326 KB to 109 KB. This drop in model size comes at a limited cost in accuracy, yielding 92.4%. Figure 4 presents the confusion matrix. We note that most errors occur in the gestures 'CK' and 'C-CK'. This can be due either to insufficient data or to the broad range of possibilities these gestures represent. Indeed, everyone has its own way of turning their finger (at different speed and radius), as well as not always being in front of the sensor, making it challenging for the model to identify consistent patterns.

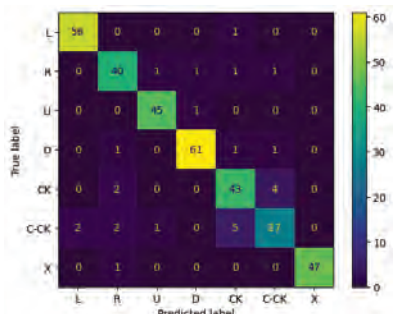


Figure 4: Confusion matrix of quantized model on test set.

The next steps are to make the gesture recognition more robust against false positives, by enriching the dataset with more participants and including a variety of gesture styles.

A Framework for AI-based Side-channel Attacks Featuring a New AI Method

L. D. Meier, C. A. Botocan, D. Vizár, F. Valencia

IoT ecosystems must be secure against adversaries having physical access to them. CSEM python toolbox for Side-Channel Attacks (SCA) allows to understand the leakage of a device and thereby the capabilities of a potential attacker. It provides a novel and efficient method for SCA, advancing the state-of-the-art.

Cryptographic algorithms are designed to ensure that secret input arguments cannot be recovered given the knowledge of public data (e.g. ciphertexts) or even given some inputs considered private (e.g. plaintexts). This is the purview of classical cryptanalysis, where the cryptographic algorithm of interest is treated as a black box. However, in practical implementations on physical devices (software on microcontrollers or hardware accelerators), the execution of these algorithms involves physical processes, which can correlate with input values, making them observable through physical variables. For instance, the power consumption when loading a secret key correlates with its Hamming Weight, leaking key information. Side-Channel Attacks (SCA) exploit such physical channels to recover secret data, even from mathematically secure algorithms. Therefore, real-world security requires cryptographic robustness and secure implementation against SCA, especially in embedded systems that are easily accessible to attackers. Developers must understand the attacker's capabilities in order to design SCA-resistant embedded devices. And the most prevailing ones are AI-based.

To that end, CSEM developed a comprehensive and easily extendable Python package, compiling most of the state-of-the-art preprocessing, Machine Learning (ML) architectures and ML optimizations. This process led to the discovery of a novel ML technique for SCA. This method, dubbed dimension 0, transposes the output of a ML model before the application of the Softmax function. This annihilates class imbalance issues (in the SCA context) and allows a ML model, along with an adaptive optimizer and the correct learning rate weight decay, to target easily recognizable classes more than others. Furthermore, the key derivation algorithm combining the key-byte candidates of each power-consumption trace & plaintext (or ciphertext) pairs, will in turn give more weight to attack traces with an easily recognizable class, as defined during the training phase.

To assess the effectiveness of the aforementioned method, experiments were conducted on the publicly available datasets: ASCAD^[1] (with different desynchronization countermeasures) and AES_HD^[3]. Two different scenarios were tested. The first being unprofiled attacks, where the attacker does not have access to a profiling device to produce a dataset for training the ML model. The second scenario evaluates whether the dimension 0 technique can address the imbalance dataset

problem caused by the Hamming weight labeling function during attacks with a profiling dataset (generated using known keys and plaintext input). For unprofiled attacks on the AES_HD dataset, using dimension 0 allowed the attack to reach the correct key after two guesses (or simply, a Key Rank of 2) in 70% of the cases against only 20% without the technique. Second, during profiled attacks, dimension 0 with the imbalanced HW-labelling, proved to be able to beat, if not match, the state-of-the-art on the ASCAD datasets with fixed key, different levels of desynchronization (a SCA countermeasure) and the easier identity-labelling^[2].

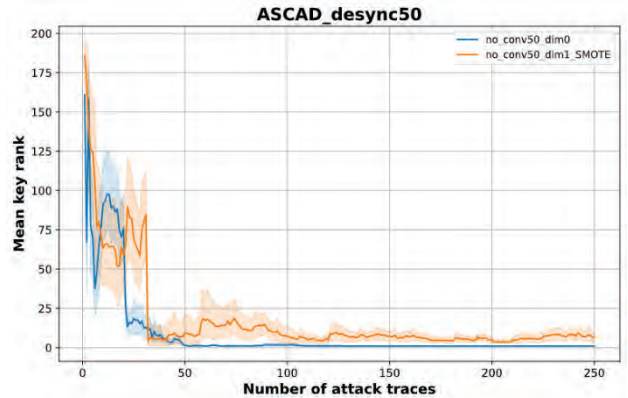


Figure 1: Profiled attack comparing CSEM's dimension 0 technique (blue) against SMOTE (orange) with the imbalanced HW labeled data.

Figure 1 compares the performance of dimension 0 on a HW-imbalanced dataset against the state-of-the-art SMOTE^[3] balancing technique. The plot shows that on the ASCAD dataset with a desynchronization of 50, dimension 0, which integrates seamlessly and with no overhead (in contrast to the SMOTE approach), beats the conventional balancing technique, as an attack is successful with only 50 power-measurement & plaintext input pairs.

The new technique that was explored allows to assess to what extend the leakage of a device can be used for SCA. It takes the state-of-the-art further and is therefore expected to be part of a publication in a conference or a journal, its implementation becoming ultimately open source.

[1] R. Benadjila, E. Prouff, R. Strullu, E. Cagli, C. Dumas, Deep learning for side-channel analysis and introduction to ASCAD database, Journal of Cryptographic Engineering, 10 (2019) 163

[2] L. Wouters, V. Arribas, B. Gierlichs and B. Preneel, Revisiting a methodology for efficient CNN architectures in profiling attacks, IACR 147-168

[3] S. Picek, A. Heuser, A. Jovic, S. Bhasin, F. Regazzoni, The curse of class imbalance and conflicting metrics with machine learning for side-channel evaluations, IACR Transactions on Cryptographic Hardware and Embedded Systems, 2019 (2019) 1

Wireless TDMA-based Protocol for Long-term Periodic Monitoring of Batteries

A. Ferragni, C. Bocquillon, A. Ambühl, S. Scheiben, R. Berguerand

The CSEM ultra-low power Wireless protocol airTDMA offers configurable bandwidth, fault detection and recovery to long term operations to wireless sensor networking, in particular for battery monitoring, where the suppression of wires significantly save weight, simplify manufacturing and maintenance.

Time Division Multiple Access (TDMA) protocols divide time into periodic patterns made of multiple slots, which are allocated to unique transmitters. This scheduling prevents packet collisions as long as the nodes in the network are synchronized. CSEM initially designed the airTDMA, successfully providing low power real-time communication for aeronautical application, supporting periodic transmissions. This protocol proves to perfectly fit the needs of long-term battery monitoring applications, in which sensor nodes are integrated with a Battery Management System (BMS) to monitor battery parameters such as temperature and voltage, and to perform self-healing tasks.

AirTDMA exhibits the following properties:

- Configurable bandwidth: Each node can be configured with different allocated bandwidths, which can be changed in real time depending on the node's requirements. This allows for optimal use of the available bandwidth among all nodes. The configuration also permits control over packet latency.
- Robustness: The protocol includes an acknowledgment mechanism to manage packet delivery. Nodes check if packet were not received and trigger a retransmission of the packet.
- Low-power on the edge: The sensor node keeps its radio off except only when transmitting or synchronizing with the Wireless Data Concentrator (WDC), saving enough energy to allow the system to run on small batteries or through energy harvesting.

As illustrated in Figure 1, AirTDMA consists of cells managed by a Wireless Data Concentrator (WDC), which coordinates communication with multiple Sensor Nodes (SN) that gather data. Both the WDC and SNs interface a nRF52840 processor [1], which contains a 2.4GHz transceiver and run the airTDMA on a Nordic Semiconductor proprietary 1Mbit/s mode.

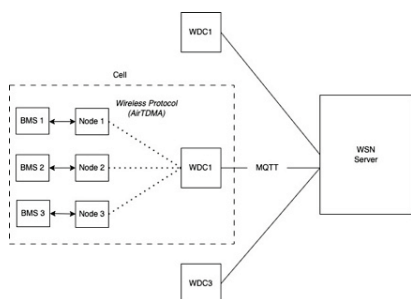


Figure 1: AirTDMA typical network topology.

WDCs are connected to an Ethernet backbone network, interconnecting the Wireless Sensor Network (WSN) server that manages the network. The MQTT publish/subscribe protocol facilitates the integration of multiple cells into the same WSN, enabling the creation of a larger network.

To simplify deployment, the network can be configured using a dedicated file format that includes the network topology, sensor definitions sampling rate for each node. With this file, the WSN Server will automatically associate sensor nodes with their respective WDCs and initiate data acquisition. During data acquisition, the WSN will continuously store incoming data and log, locally for debugging purposes and in a cloud-based InfluxDB for remote analysis.

For detection, the server compares the number of received data packets with the expected number, based on the configured packet rate. If the difference exceeds a certain threshold, an alert is generated to indicate a potential issue in the wireless network, such as a problem with one of the SN or the WDC. Other situations, like unexpected software conditions, can also trigger alerts. These alerts can be notified to the network operator via emails, Microsoft Teams notifications, etc.

Additionally, the WSN server can periodically trigger pre-configured battery self-healing sequences. In the future, these sequences could also be triggered based on the battery condition computed from the received data.

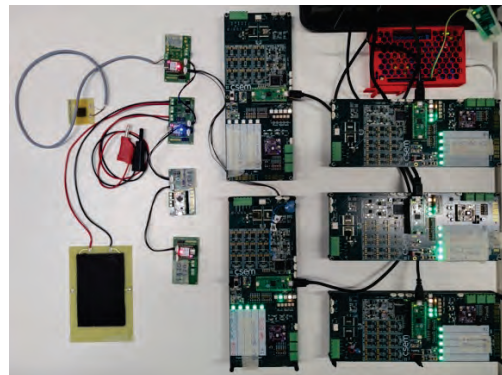


Figure 2: Setup picture.

As illustrated in Figure 2, a long test deployment was conducted with 6 nodes connected to a single WDC. Each node is sending a packet every minute containing a battery status. Additionally, a self-healing command is sent to the node every 1 hours. The packet loss was configured to a 10% loss threshold. During the test, a few alerts were triggered due to node failure but most of them didn't reports any problems.

This technology is currently being developed and tested within the scope of the EU-funded Phoenix [2] project. Future developments will focus on increasing the number of connected nodes and increasing the protocol's bandwidth.

[1] Nordic nRF52840 Processor:
<https://www.nordicsemi.com/Products/nRF52840>

[2] PHOENIX is partially funded by the European Commission under Grant number 101103702; <https://phoenix-smartbatteries.eu>

Showcasing the CSEM Bluetooth Low Energy Stack at UnPlugFest

R. Berguerand

The new CSEM open source BLE stack running on the in-house developed μ169 RTOS successfully drove the IcyTRxDM transceiver at the BT UnPlugfest to connect and interact with numerous marketed devices. This stack has been adapted to fully integrate the transceiver's main functionality to reduce power consumption and improve performance. This new solution is ideal for ASICs and IoT devices targeting low-power application, and its modularity allows for compatibility with various other chipsets.

The CSEM BLE stack is built on a BLE 5.0 open-source stack, which is actively maintained by the community. New features, such as Angle of Departure/Arrival (AoD/AoA), BLE audio, and channel sounding, are currently in development. CSEM has enhanced the existing stack to develop a low-power, high-performance solution, ready for qualification and real product deployment.

As illustrated in Figure 1, the stack includes both the BLE host and controller software, fully integrated into the μ169 OS. The implementation uses generic μ169 kernel primitives, such as timers, semaphores, and queues, which ease deployment on devices supporting the OS. The stack operates through dedicated processes, allowing other applications to run concurrently on the same microprocessor (MCU). The BLE processes are configured with high priority to ensure precise BLE timing.

The HCI interface allows the host to operate independently and can be connected with a third-party software controller or an external controller MCU. Conversely, the BLE controller can be paired with a different host.

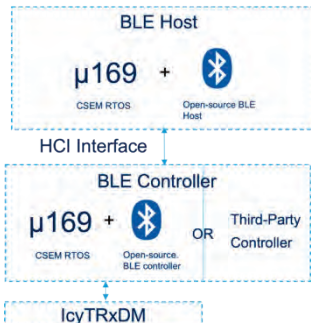


Figure 1: CSEM BLE-stack architecture.

The controller operates the IcyTRx DM transceiver through a dedicated driver, which exploits the various features of the IcyTRx, including a packet handler that enables the MCU to delegate to the transceiver the packet transmission and reception, CRC checking and generation, and the AES encryption/decryption. The IcyTRx also integrates protocol timers that can precisely manage packet transmission and reception timings according to Bluetooth specifications, freeing up the CPU's timers and processing resources.

A dedicated platform was designed to develop and test the stack. As illustrated in Figure 2, it comprises an STM32H7 Nucleo board (light blue) that communicates with an IcyTRx DM test chip (dark blue) via a dedicated interposer PCB (green). The STM32H7 processor runs the stack and interfaces with the IcyTRx DM using the SPI protocol.

The stack implements most of the BLE 5.0 features including legacy features such as peripheral advertising, central scanning and connection. It also supports secure connection with pairing and packet encryption. More recent features such as extended and periodic advertising or 2Mbit/s and coded PHY are also supported. Depending on the memory amount and the application requirements, the stack can be configured to handle up to 5 simultaneous connections. The stacks also implement some simple profiles and services such heart rate or battery service.

With multi-connection and all features enabled, the BLE stack and the μ169 OS require approximately 200KB of ROM and 100KB of RAM. In an optimized, peripheral-only setup, the memory requirement can be reduced to as low as 100KB of ROM and 16KB of RAM on a Cortex-M processor.

Once ported, the stack was tested using the Profile Tuning Suitel^[1] (PTS) software, evaluating the stack's capabilities against a reference implementation and executing BLE use case sequences. The tests target host layers such as GATT, GAP, L2CAP, and the security manager. The Auto-PTS^[2] tools were used to automate the tests as well as to interface the test platform with PTS. A total of 429 tests were passed successfully. Efforts to implement additional test cases are currently in progress.

Subsequently, the stack was tested at the UPF testing event in Bellevue in September 2024. This event brings together industry leaders in Bluetooth devices for cross-testing stack implementations. The CSEM stack brilliantly passed real-world scenarios while the teams consolidated the implementation in real-time all along the discovery of the remaining misbehaviors.

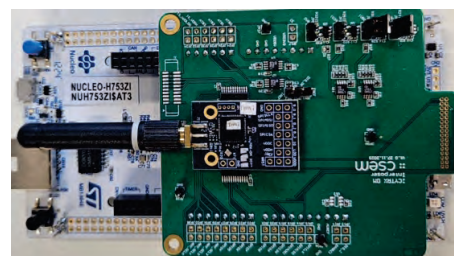


Figure 2: BLE stack test platform.

In the future, the BLE stack will be combined and refined for running on dedicated co-designed SoC or Chiplets, efficiently interfacing with the IcyTRx transceiver. This will allow for taking benefit from additional resources, such as accelerators for encryption and AI, offering opportunities for further reducing the power consumption and footprint.

[1] PTS Tool: <https://www.bluetooth.com/develop-with-bluetooth/qualify/qualification-test-tools/profile-tuning-suite/>

[2] Auto-PTS GitHub: <https://github.com/auto-pts/auto-pts>

μ169 – A Cutting-edge Ultra-low-power OS with Robustness and Security Capabilities

E. Franzi, J.-M. Koller, A. Restrepo, M. Sénéclauze, D. Vizár

The CSEM μ169 Real-Time OS (RTOS) distribution provides an ideal solution for clients adding security, and robustness to customized applications while allowing them to rely on a personalized license.

μ169 is a new Real Time OS, which supports modern MCU features and user needs, with improved system stability and security. Additionally, it allows for the use of high-level languages like Rust, which expands its versatility and robustness. Moreover, the OS can be adapted to client-specific needs as part of projects, with the dedicated IP belonging to the client, like open-source practices.

The CSEM μ169 RTOS offers the same licensing advantages as open-source RTOS, with a flexible license on the base distribution, while giving access to solid technical expertise and know-how through our source library, enabling users to exploit the resource optimized implementations and accelerate their project developments without compromising security or performance. An RTOS has a huge impact on the performance of the entire system, its timeliness, its reliability and, ultimately development and operational costs. While open-source RTOS options, such as FreeRTOS, Azure, etc. are attractive due to their flexibility and illusive zero cost, they present substantial risks to any kinds of projects, in particular, for mission-critical applications. (e.g. those requiring specific security or reliability levels, ultra-low power operations) mainly due to the versatility of the open-source community. In addition, despite their size, they do not always provide solutions to the most complex problems, as experts with in-depth knowledge of these strategic fields often choose to keep their proprietary optimizations confidential to maintain a competitive edge.

A rich and robust implementation

μ169 reuses successful concepts already present in other instances of RTOS developed at CSE which were great commercial and technical success over the past decade and are present in numerous products, such as watches, optical sensors, and battery management systems, often incorporating Artificial Intelligence.

μ169 introduces key features that significantly expand the versatility functionality and stability of the system. The freedom offered by the open nature of μ169 allows for following the rapid evolution of semiconductors and MCU offering new features. Furthermore, μ169 separates user and privileged spaces, isolating critical system operations from user-level applications, thus preventing unauthorized access, unintentional corruptions, interferences and subsequent potential system breaches. Eventually this contributes to the robustness of the system by maintaining a secure and controlled environment for critical operations. To reinforce the product quality, to streamline and to speed up the developments, μ169 now supports a Linux ^[1] -like

^[1] <https://www.kernel.org/doc/html/v6.6/kbuild/kconfig-language.html>

^[2] D. Vizár, I. Ben Salah, M. Fumeaux , Hardening μ111 RTOS with ARM Trustzone-M Technology, [CSEM Scientific and Technical Report \(2022\), 21](#)

predefined configurations to enable quick and safe selection and access to major chip peripherals. Finally, μ169 includes the support for RUST besides μPython and the SysQuake mathematical problem-solving framework, for developing the applications. Rust is a modern, general-purpose programming language designed for performance, safety, and concurrency.

Open to security

Several research and development activities are contributing to the security and hardening of the OS and of the applications using it.

- The implementation of a virtual secure element demonstrates the integration of ARM TrustZoneM into the OS. This represents a low-overhead and vendor independent protection of cryptographic secrets and operations, such as the NIST PQC and LWC standards ^[2].
- To enable trust in the device, the OS also features a secure boot and FUOTA implementation, based on the well-established MCUBoot framework. The design has been verified with a provable analysis approach and an implementation of a full stack FUOTA with AWS is available, for a short time to market ^[3].
- A variety of cryptography and security libraries has been implemented, supporting all the major cryptographic algorithms in SW or configurable to use any onboard HW accelerators. All these are available for reuse.
- A fuzzing test bench for embedded SW is being developed at CSEM. With this approach, the critical components of an embedded firmware (such as communication stack) are stress-tested with mutating inputs to find and fix potentially exploitable SW bugs. This represents a realistic and sensible assessment of the SW robustness before deployment ^[4].

Conclusion

The CSEM RTOS μ169 package now represents a compelling, flexible and efficient alternative to open-source RTOS option for rapidly develop highly demanding, secure products in the fields of Edge AI and IoT. It has been tested and used in this context, in numerous projects. Its ability to integrate Rust will undoubtedly accelerate development while also improving the reliability of applications. Overall, μ169 stands out as a robust solution for a wide range of embedded system needs.

^[3] D. Vizár, M. I. Ben Salah, A. Ferragni, Secure Boot and Firmware Update for μ111 RTOS, [CSEM Scientific and Technical Report \(2021\), 19](#)

^[4] D. Vizár, M. I. Ben Salah, M. Marty, Discovering Vulnerabilities in Embedded Firmware with Fuzzing Techniques, [CSEM Scientific and Technical Report \(2023\), 32](#)

AMC® – Additive Membrane Care

C. Beyer, F. Burri, C. Blum •, A. Fuchs •

The use of membrane filtration in the dairy industry enhances milk value by reducing transport volumes and isolating individual components, but it leads to contamination that requires significant cleaning resources. Halag Chemie AG and CSEM developed a machine-learning-based cleaning optimisation system, which showed potential for resource savings but faced challenges in economic benefits and transferability between plants.

The use of membrane filtration processes in the dairy industry reduces transport volumes and allows separating and concentrating individual milk components used in the production of food and animal feed. These filtration processes inevitably lead to deposits on the filtration membranes, i.e. contamination or fouling, which requires cleaning to maintain the membranes' performance and typically consumes large amounts of chemicals and water. The current cleaning solution for these membranes is based on a rigid schedule using a predetermined volume of chemicals and water, regardless of the amount of contamination. This procedure leads inevitably to a waste of resources and to a downtime of the filtration unit of 15 – 20%.



Figure 1: Photo of a 3-stage membrane filtration plant.

Halag Chemie AG, an innovative, medium-sized Swiss company, has set itself the goal of meeting the demands for increased production safety, more sustainable resource use, reduced environmental impact, and more efficient use of production capacity by establishing a new cleaning procedure, Additive Membrane Care (AMC®).

Halag Chemie AG and CSEM have collaborated in an Innosuisse project (33572.1 IP-ENG) to investigate the feasibility of implementing machine-learning algorithms within a monitoring system designed to automatically and continuously optimise the cleaning processes of membrane filtration plants. Membrane contamination is a complex and still poorly understood phenomenon, with each industrial membrane filtration unit exhibiting a unique contamination profile. This necessitates the development of adaptive, self-learning algorithms capable of responding to these variations.

Two solution approaches were explored by integrating various process parameters, such as conductivity, pressure, and material flow, among others. The first approach focused on the real-time estimation of membrane state through the construction of a cleanliness metric. This metric assumes a clean state prior to filtration and after a traditional cleaning cycle, with cleanliness deteriorating during filtration and recovering during cleaning phases (Figure 2). The approach might allow for the estimation

of the cleaning performance and possible optimisation potential. The second approach involved real-time estimation of membrane resistance, which was then compared to measured values to detect deviations in cleanliness relative to a learned baseline state.

Both approaches were rigorously evaluated and optimised across one laboratory and three industrial plants, collectively processing over 400 hectolitres of raw milk daily. Throughout the project's duration, more than 1400 filtration and cleaning cycles were meticulously documented, providing a robust foundation for analysis. A significant challenge was the absence of ground truth data, as non-destructive assessment of membrane condition is unfeasible and expert knowledge is limited^[1]. Additionally, the industrial plants' process schemes frequently changed due to variations in the feed (milk or whey) and operator inputs.

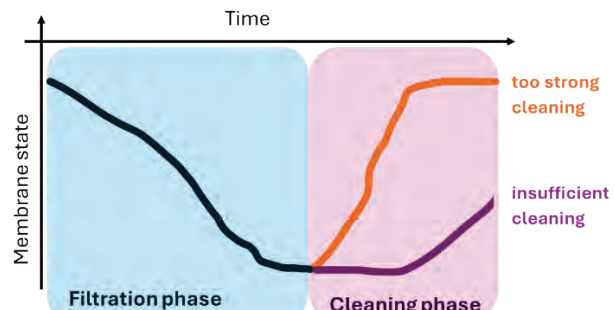


Figure 2: Illustration of real-time estimation of membrane state based on the evaluation of several process parameters, such as conductivity, pressure, and material flow, among others.

In the result, a reliable real-time anomaly detection system was demonstrated, along with a plausible prediction of membrane state using self-learning approaches, typically requiring over 200 filtration and cleaning cycles for training. Although a savings potential for industrial plants was identified, the economic benefits of the AI algorithm were modest compared to the risks associated with inadequate cleaning. Furthermore, the transferability of results between plants was notably low, due to the highly customised process schemes of each plant, further limiting the profitable application of the project's outcomes.

The project offered detailed insights into membrane filtration and cleaning processes at various customer sites, enhancing our understanding of the filtration process and related market success criteria. It also demonstrated the potential and limitations of self-learning AI algorithms in food production. Currently, AI based approaches will not be able to replace personal application consulting for optimised cleaning, as offered by Halag Chemie AG to date.

• Halag Chemie AG, Aadorf - www.halagchemie.ch

[1] Gaudio, Maria Teresa, et al., Application of artificial neural networks for modelling and control of flux decline in cross-flow whey ultrafiltration, *Processes* 11.4 (2023): 1287.

Path Planning Optimization in Deposition-based Additive Manufacturing

I. Sideris, I. Kastanis, F. Crivelli

This article addresses the challenges of inconsistent material properties and residual stresses in deposition-based additive manufacturing caused by inhomogeneous temperature fields. Developing computationally efficient tools using advanced learning models and optimization algorithms enables the design of optimized deposition paths that control the thermal fields, resulting in improved part quality and reduced computational demands.

Deposition-based additive manufacturing is a rapidly developing field characterized by high deposition rates and cost-effective, simple equipment. This approach enhances production efficiency through faster build times, high customization, and reduced expenses compared to traditional machinery. Despite these advantages, the field faces persistent challenges hindering broader adoption.

Foremost among these challenges are the resulting inconsistent material properties, low production repeatability, and residual stresses in the manufactured components. These issues mainly stem from inhomogeneous temperature fields derived from suboptimal material deposition paths that lead to high heat concentration, which affects the microstructures and mechanical properties of the manufactured parts. This issue is especially critical in precision-critical industries like aerospace, automotive, and biomedical engineering.

Controlling these thermal fields is crucial. The most effective strategy involves meticulously designing deposition paths to promote uniform temperature distribution. By carefully planning the deposition sequence and trajectory, thermal gradients can be minimized, residual stresses reduced, and part quality enhanced.

However, designing optimized deposition paths presents significant computational challenges and is performed by trial and error to this day. Predicting process-induced temperatures demands substantial resources due to complex thermal phenomena like transient heat transfer. Accurate modelling requires high-resolution simulations, which are computationally intensive, especially for complex geometries. Moreover, determining the optimal deposition path is an NP-hard problem, meaning computational effort increases exponentially with problem size. Exhaustive search methods are impractical, necessitating efficient strategies to identify near-optimal solutions within reasonable timeframes.

At CSEM, we address these challenges by developing tools to reduce computational demands and address the planning problem efficiently. The first aspect involves reducing computational demand by utilizing advanced learning models and reduced-order modelling techniques. Learning models like machine learning algorithms and neural networks focus on temperature fields within a selected subspace. By concentrating on critical regions impacting material properties and performance, these models reduce the necessary computations without compromising accuracy where it matters. Reduced-order modelling enhances computational efficiency by considering only significant system dynamics. Techniques like proper orthogonal decomposition and dynamic mode decomposition reduce dimensionality, simplifying complex thermal models while

retaining essential characteristics. This reduction enables faster simulations and feasible optimization iterations.

The second aspect optimizes resource allocation by focusing the search for optimal deposition paths among high-performing candidates, excluding underperforming areas. By dynamically constraining the search space, computational efforts concentrate on promising regions, enabling rapid identification of near-optimal solutions. Advanced algorithms like genetic algorithms, particle swarm optimization, or Monte Carlo tree search efficiently navigate possible paths, adapting based on intermediate results to improve efficiency.

The effectiveness of these tools is demonstrated through computational simulations and experimental results. Studies show learning models and reduced-order models accurately predict temperature fields while significantly reducing computation times. Optimizing deposition paths with proposed resource allocation strategies improves thermal management, leading to components with enhanced properties and reduced residual stresses.

Experimental validation provides tangible evidence of improvements. Parts manufactured using optimized deposition paths show greater material consistency, higher repeatability, and improved structural integrity compared to conventional strategies^[1]. Temperature measurements during deposition confirm the models' predicted uniform thermal fields. Mechanical testing validates performance and reliability enhancements.



Figure 1: Optimal path planning offers greater material consistency, higher repeatability, and improved structural integrity compared to conventional strategies.

In conclusion, this article presents solutions to key challenges in deposition-based additive manufacturing. By reducing computational demands and leveraging efficient search algorithms, the developed tools enable the practical design of deposition paths that promote uniform temperature distribution and improve part quality. These contributions advance additive manufacturing and have significant implications for industries adopting this technology.

^[1] Sideris, I., et al., End-to-end path planning for homogeneous temperature fields in additive manufacturing. JMPT, 327:118364, 2024

Optimal Coverage Path Planning in Robotic Wood Floor Grinding

S. Müller, Y. El Goumi, F. Crivelli

Automating wood floor grinding enhances safety and efficiency but demands precise, uniform material removal. This project applied Coverage Path Planning (CPP) to develop optimal sanding paths using simulations in Gazebo. A rotated zig-zag pattern resulted as most effective. A customized mobile robot was used for data collection and testing. These findings are transferable to other mobile robotics applications and offer a rapid development pipeline for multiple use cases.

Wood floor grinding and sanding is an extensive, time-consuming, and repetitive manual task. While equipment such as drum floor sanders and floor buffers facilitate the process, these tools still require human operation. Such manual involvement poses several risks to operators, including respiratory issues caused by dust, noise exposure, and physical injuries such as cuts, abrasions, or clothing entanglement. Automating this equipment would significantly enhance safety and efficiency, particularly in the construction industry.

In a previous project in collaboration with the Swiss companies Enservian AG and Urech Bodendesign AG a mobile robotic platform enabling automated sanding of wood floor was designed and developed (Figure 1). The platform features two lidars for autonomous navigation, 4x actuated mecanum wheels for maximum agility, and it is equipped with a commercially available floor processing machine, mounted on a tailored mechanical system ensuring both stability and quality performance.



Figure 1: Custom designed Paquet Grinding Robot.

Automating a sanding process poses several challenges. Unlike robotic vacuum cleaners and similar, which can operate on random trajectories without much consequence, sanding involves the removal of material, necessitating even and consistent work to avoid surface inhomogeneity and defects. This requires a carefully planned path that ensures uniform sanding across the entire area while accounting for obstacles.

In this project specifically, the Coverage Path Planning (CPP) problem applied to autonomous floor grinding was investigated. CPP is a fundamental problem in robotics, with wide-ranging applications including autonomous lawn mowers, cleaning robots, agricultural machinery, and demining robots. The objective of CPP is to determine an optimal path that ensures complete coverage of a given area or volume of interest, while avoiding obstacles and minimizing operation time. To evaluate the performance of the different CPP algorithms the open-source robotics simulator Gazebo (www.gazebosim.org) was used. The main advantages of relying on a simulation environment were:

- The experiment loop is considerably shorter compared to hardware-in-the-loop experiments, allowing us to explore more possibilities.
- The experiments are repeatable.
- All the tests are end-to-end, where both physics and sensor readings can be simulated.

The main challenge, is identifying a model which is accurate enough to capture the main behaviour of the real process, allowing to bridge the sim-to-reality gap. Modelling the sanding process of a wood floor is a challenging task due to the inherent complexities of wood as an anisotropic material. The physical properties of wood, such as strength and flexibility, vary depending on the direction in which they are measured. Particularly, the wood's properties differ significantly along the grain compared to across the grain.

During this project, a parametric model was developed to capture the main characteristics of the floor sanding process. This model was calibrated with data collected during manual grinding. The experiments have shown that using a rotated boustrophedon (zig-zag) grinding pattern has led to the most robust results. The pattern is rotated after each pass to average out errors.

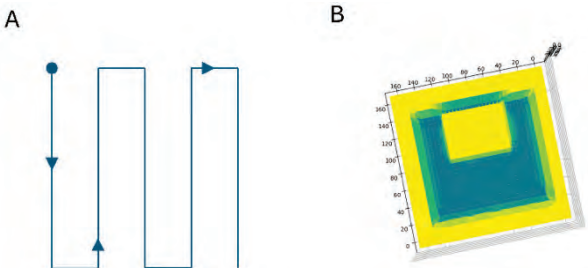


Figure 2: a) Visualization of a boustrophedon grinding pattern, b) Floor profile in mm after the grinding with a rotated boustrophedon pattern with an obstacle in the middle.

In the second phase of the project, the software developed in simulation was transferred to the parquet grinding robot. The whole pipeline, from room mapping to the computation and execution of the optimal coverage path was successfully tested in an apartment-like room with a parquet floor, which reproduces realistic field conditions. More data and experience collected and evaluated on the robot will allow: 1) Improving the model of the grinding process and 2) Exploring alternative path planning trajectories and tuning the parameters. Furthermore, the developed platform will allow encoding and digitalizing such experience. This will grow progressively, allowing more and more to apply data analytics and AI tools, to model, control and optimize the grinding process.

The results from this project are not limited to the task of wood floor sanding but could also be transferred to other grinding process (e.g. concrete floors or walls) and even generalize to other mobile robotics problems (e.g. painting, dispensing).

Instantaneous 360° 3D Scanner of Human Body Parts for Orthopedics Applications

F. Disidoro, M. Russi, M. Höchmer

The Swiss company Swibrace aims to provide 3D printed, patient-specific braces or orthoses. To create the 3D model of the target limb necessary for constructing the brace, CSEM has developed a vision-based system capable of capturing a 360° scan in a single instantaneous shot. This technology eliminates artefacts caused by the natural motion of the limb during the scanning process, which are common with conventional scanning devices.

Braces and orthoses are medical devices designed to support, align, or immobilize body parts, often following injury, surgery, or in cases of chronic conditions. In the current orthopedic routine, braces are made by molding materials such as plaster, fiberglass or thermoplastic to the patient's body part. The procedure can be painful or uncomfortable for the patient, especially when the subject is unable to hold a certain position of the limb throughout the time required for the scanning. Moreover, a trained professional is always required, increasing costs and dependency on the personnel's skills.

The aim of Swibrace is to replace the current procedure with a scanning system able to generate an accurate 360° 3D model of the patient's limb for 3D printing of a custom brace. The advantages of this new system are: the scanning is instantaneous, hence more comfortable for both the patient and the professional; the making of the brace does not require any manual work, and the brace quality does not depend on the skills of the trained personnel; the scanner provides a standard and repeatable procedure for acquiring the full 3D shape of the patient's limb, that allows for follow up comparisons on the same subject based on qualitative assessments.

Swibrace has partnered with CSEM to design and develop a 3D scanning system with the following requirements: the system needs to acquire an instantaneous snapshot of the patient's body part, to avoid artefacts generated by the natural motion of the patient during the scanning; it needs to be portable, easy to mount and to calibrate; it should not cost over 10k CHF; it should provide accuracy better than 1mm.

At first, CSEM analyzed the 3D cameras available in the market. While the Zivid 3D camera offers high accuracy, the price for a single unit is too high for a multi-camera system. On the other hand, off-the-shelf 3D systems such as Nerian, Lidar 1515, Zed2 and Structure, do not meet the required accuracy or do not allow for the required flexibility. For these reasons, custom stereophotogrammetry 3D camera pairs were developed, and a full software pipeline for cameras calibration and 3D reconstruction was implemented.

In the initial phase of the project a half-ring prototype was designed and tested to determine the cameras' specifications (i.e. focal length, aperture) and system's configuration such as baseline distance between the cameras within a stereo pair, distance between cameras and the target, minimum number of cameras needed to maximize the field of view and minimize occlusions. In the second phase of the project a full 360° demo prototype was designed and built specifically for reconstruction of human hands and arms. 16 cameras (MV-CB120-10UM-S, monochrome, 12 MP) assembled in 8 3D stereo pairs, and equipped with 8 mm focal length lenses were placed along a circular support with a diameter of approximately 60 cm. A LED system was included in the ring to guarantee homogenous and

consistent illumination. The 16 cameras are synchronized through a hardware trigger. The software pipeline consists of:

- A multi-camera calibration toolbox^[1] for distortion correction and calculation of the camera intrinsic and extrinsic parameters.
- A software pipeline based on OpenCV python library to generate a 3D point cloud model from the left and right images acquired from each stereophotogrammetry pair.
- A pipeline based on Open3D python library to align together the retrieved 8 point clouds into a common coordinate system, to generate a single 3D mesh and to post-process it.



Figure 1: Full-ring prototype.

A reconstruction accuracy of 0.3 ± 0.3 mm was estimated by comparing the ground truth shape of a mannequin hand acquired with an accurate Artec 3D scanner with the reconstructed shape by our system. However, this estimation is optimistic as a mannequin hand does not present the challenges of a human one, for example body hairs. We observed that the 3D reconstruction quality is significantly worse for surfaces covered by body hairs. Custom algorithms are being tested to digitally remove the hairs and guarantee a smooth output 3D mesh.



Figure 2: Example of reconstructed hand.

[1] <https://github.com/oliver-batchelor/multical>

Self-supervised Numerical Pre-training for Symbolic Regression

F. Morgan, T. Bendinelli

Symbolic regression aims to identify the underlying mathematical expression from a dataset. Unlike black-box methods, symbolic regression produces a human-readable symbolic formula, which is valuable for applications that require full interpretability. Neural Symbolic Regressor methods represent an emerging class of symbolic regression approaches based on pretrained transformers, promising both high accuracy and interpretability. However, these methods suffer from domain shifts. In this research project, we explored whether contrastive learning could help address this issue.

Unlike conventional regression techniques, which rely either on predefined structures or utilized black-box models, Symbolic regression seeks to generate a human readable equation that best describes the data with every possible mathematical operator, allowing for flexibility in capturing complex relationships while preserving interpretability. This unique ability makes it a powerful tool for both scientific discovery and practical applications.

Current state-of-the-art methods for symbolic regression are based on genetic programming algorithms. However, in recent years, a novel and emerging class of algorithms so called Neural SymbolicRegressor (NSR) methods has gained interest.

NSR models are trained by leveraging large synthetic datasets of data-points and symbolic equation pairs. During training, the model is given as data points and learns to predict the corresponding equation. NSR uses an encoder-decoder Transformer architecture: the encoder processes the sampled data points, while the decoder generates the equation that best represents the underlying relationship.

A key challenge faced by NSR models in real-world scenarios is the phenomenon of domain shifts. In practical applications, the distribution of data points encountered during inference can differ significantly from the distribution on which the model was trained. While all data points may fall within the same general range, they might be concentrated in a much narrower subrange or, conversely, span a far wider range than the model's training data. In some cases, data points could even fall completely outside the training range. This variability poses a test for NSR models, as they must generalize effectively across different data distributions to be reliable in diverse settings. Consequently, a significant focus of NSR research is on enhancing model robustness and ensuring it can handle any type of distribution encountered.

The objective of this project was to develop methods that could increase the accuracy and robustness of NSR models, ultimately making them more applicable for complex, real-world data.

We decided to focus our attention on Contrastive Learning, since it has shown impressive results in fields such Computer Vision and NLP. We followed the approach from [1], where contrastive learning is applied jointly with the standard cross-entropy loss during the training of Neural Symbolic Regressor (NSR). The architecture is shown in Figure 1.

In our experimental evaluation, we noticed that a model trained with this additional contrastive learning loss, performs better

outside the training distribution than the baseline, demonstrating the potential of this approach, although only little improvement could be achieved. We also observed a deterioration in performance within the training distribution, indicating a tradeoff.

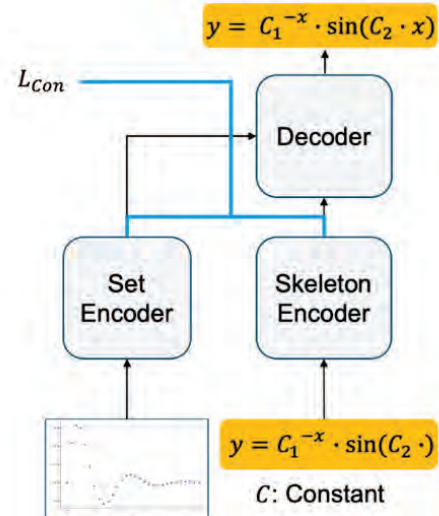


Figure 1: Model Architecture, the contrastive loss (L_{con}) is computed along the standard cross-entropy loss between the target and the input.

In conclusion, this study demonstrates the potential of contrastive learning to improve the robustness of Neural Symbolic Regressor models in the face of domain shifts. However, more work is needed to achieve the level of performance required in real-world scenarios.

This work was part of the Bachelor Thesis of Fabien Morgan (HSLU).

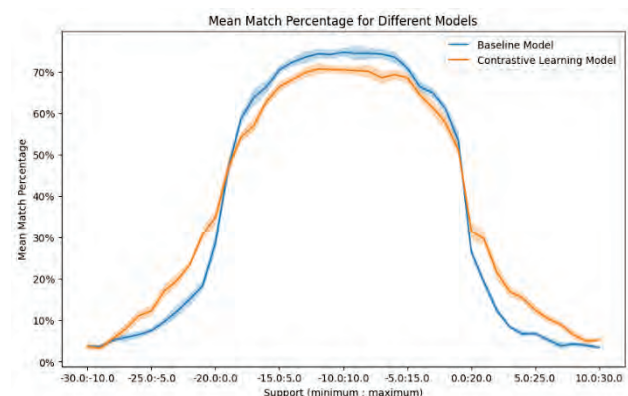


Figure 2: Comparison of prediction accuracy between contrastive learning and non-contrastive learning models across different domains, with the trained range being -10 to 10.

[1] Li, Yanjie, et al., MMSR: Symbolic regression is a multi-modal information fusion task. *Information Fusion* 114 (2025): 102681.

Self-supervised Foundation Models in Holographic Imaging

S. Dietler, T. Bendinelli

Building on previous advances in real-time spore detection with supervised learning, this year's research explores self-supervised foundation models for holographic imaging, specifically through DINOv2. This self-supervised approach allows the model to learn robust, representative features, facilitating adaptation across diverse settings and enabling efficient few-shot learning for new classes. This flexibility is critical for the global scalability of the SwisensPoleno monitoring technology. Current results are promising; however, the challenge ahead is to reduce model size to make deployment even more efficient in varied environments.

Food security is a global challenge and is affected by rapidly compounding effects including climate change, disrupted supply chains and human labor shortages. This is the motivation behind AGRARSENSE, a 3-year Key Digital Technologies Joint Undertaking European consortium project aiming to develop microelectronics, photonics, electronic packaging for agricultural use and forestry.

One of the major objectives of AGRARSENSE is to reduce the use of fungicides while at the same time ensuring crop yield in vineyard by advancing precision viticulture.

Last year's research focused on developing and deploying a convolutional neural network model, EfficientNet^[1], to classify spores using supervised learning. While it demonstrated efficacy in controlled conditions, the supervised approach faces limitations:

- Rigidity: The classifier is restricted to predefined classes, lacking the flexibility to adapt to new species without retraining.
- Scalability: The labour-intensive annotation limits applicability across regions with varied spore profiles.



Figure 1: Two SwisensPoleno Jupiter on the roof of MeteoSwiss in Payerne.

The shift to self-supervised learning (SSL) using DINOv2^[2] addresses these challenges by enabling models to learn from unlabeled data which is collected across the world with the SwisensPoleno^[3] devices. SSL models can capture universal feature representations, which significantly:

- Enhance model adaptability to new classes via few-shot learning

- Allow for on-the-fly addition of new spore types.
- DINOv2 was particularly effective in holographic imaging, showing:
 - Improved classification performance in low-data scenarios, outperforming the EfficientNet baseline when pretrained on domain-specific data.
 - Flexibility in adapting to new classes without the need for retraining, demonstrated by k-nearest neighbours (k-NN) classification.

These findings, detailed in our workshop paper "Evaluating Self-Supervised Foundation Models in Holographic Imaging", were presented at the "Foundation Models in the Wild"^[4] workshop during ICML 2024 in Vienna, underscoring the viability and adaptability of DINOv2 for domain-specific applications.

By leveraging self-supervised learning, SwisensPoleno's deployment can be expanded globally, facilitating real-time spore detection in diverse environments. This approach supports the creation of a vector embedding database, enabling the on-the-fly addition of new particle species and making SwisensPoleno a powerful tool for ecological monitoring and agricultural planning worldwide.

This transition from supervised to self-supervised learning promises a significant evolution in holographic particle detection technology. The potential for reduced fungicide application and improved yield management is vast, with self-supervised models like DINOv2 opening doors for more adaptive, scalable solutions in agriculture.

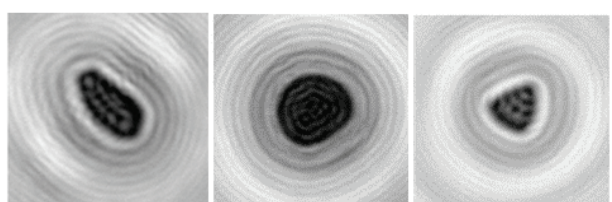


Figure 2: Example of reconstructed holographic images of an aerosol particle collected by the SwisensPoleno which are processed by the EfficientNet.

This research is funded by the Chips Joint Undertaking and supported by the Swiss Confederation under grant agreement no. 101095835.

[1] Mingxing Tan, Q. V. (2019). EfficientNet: Rethinking Model Scaling for Convolutional Neural Networks, <https://arxiv.org/abs/1905.11946>

[2] Oquab, M. (2024). DINOv2: Learning Robust Visual Features without Supervision, <https://arxiv.org/abs/2304.07193>.

[3] <https://www.swisens.ch/swisenspoleno-jupiter>

[4] Dietler S., Bendinelli T. (2024), Evaluating Self-Supervised Foundation Models in Holographic Imaging, in Proceedings ICML 2024 Workshop on Foundation Models in the Wild.

Simplifying Collaborative Robot Programming and Smart Vision Integration for Flexible Lab Automation

B. Platerrier, S. Widmer, F. Crivelli

Although screening test are generally automated, vial handling is still performed by human operators. In this project realized in collaboration with BFH and Aurovis, we design and implement a collaborative robotic cell that demonstrates flexible automation of a vial-handling task, using user-friendly block programming and machine learning for vision.

Lab automation utilizes software to automate equipment and robotic devices with minimal human supervision. This automation enables to reduce errors, increase throughput and lab staff productivity, save costs and space, and improve traceability. Screening tests, and more generally analysis of samples in laboratory, are now automated processing. These processing include complete blood count (CBC), genetic analysis, etc.

However, performing the screening tests entails the manipulation of vials that is today done by hand by a human operator. These tasks may include vial unpacking, identification, inspection, and sorting into different trays for further automatic processing. It is thus of interest to design a flexible robotic system that allows to reduce the human intervention in vial handling while allowing fast and easy reprogramming to adapt to a large variety of tests.

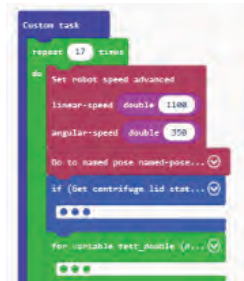


Figure°1: The delivered cobotic cell and the partners of the project.

The delivered demonstrator allows for a safe human interaction with the robotic cell, e.g., to manipulate the vial holders (see Figure 1). The cobot ABB GoFa is equipped with a collaborative parallel gripper from Zimmer. However, the custom-made tips of the gripper do not satisfy the typical safety constraints for collaborative robotics. Hence, radar sensors are installed in each corner of the cell, slowing down the robot when a human enters the vicinity of the cell.

The vial holders can be placed or removed by a human in two zone (Figure 4). The robot can detect vials thanks to its wrist camera and a Deep Learning (DL)-based algorithm based on the YOLO architecture. Once picked, the vials may be sorted based on the barcodes present on their surface. To that end, the barcodes are detected by a Cognex intelligent camera. The vials may then be sent to a mockup centrifugal system or placed into an output vial holder. In the latter case, a DL-based vision algorithm is again used to find vacant slots in the vial holders.

To enable the user to define the sequence of actions required in the process, a block-based programming interface was designed and implemented. The interface makes it possible to use predefined actions, set specific parameters or create custom tasks that combine various pre-implemented features of the cobotic cell (Figure 2)



The robotic cell functioning is orchestrated by CSEM ViSARD (Vision Automation Robotics Designer), our vertical process integration platform. All hardware components, except for the robot low-level control, were integrated into ViSARD and ready to be reused in other applications (Figure 3).



Figure°3: ViSARD is orchestrating the whole robotic cell.

The current system requires the recognition of the vial holder types. Indeed, their characteristics have an impact on the picking and placing heights of the vials. To recognize the vial holders, unique ArUco tags per holder type are employed. This design choice limits the flexibility of the current solution and makes the addition of new labware cumbersome for the end user. Future work will investigate alternative approaches for the picking and placing of vials that would be independent of the characteristics of the vials and holders. One approach would be the estimation of the height of vials based on multiple images taken from a (stereo) wrist camera.



Figure°4: Vial holders in the input and output zones, and their unique ArUco tag type identifier.

Optimizing Bin Picking with 2D Vision – A Cost-effective Approach for Robotic Automation

F. Burri, S. Widmer, B. Platerrier

Bin-picking with robotic arms can significantly enhance industrial automation by eliminating the need for customized storage solutions. However, current methods are often impractical due to high costs and complexity. This study, commissioned by Asyrl SA and developed by CSEM SA and Bern University of Applied Sciences, presents an affordable solution using multiple standard 2D cameras and a deep convolutional neural network (CNN). The system predicts part poses from camera images in less than 100 milliseconds, combining multiple perspectives to enhance accuracy and reliability. Trained on synthetic images with strong domain randomization, the CNN predictions are robust across various environments and lighting conditions. Demonstrators by CSEM and Asyrl SA showcase the technology's effectiveness in real-world applications.

Grasping a part stored in bulk with a robotic arm is called bin-picking. It is of great value for industrial automation facilities, as it allows parts to be stored and further processed directly from any standard box, removing the need for palletizing or mechanical part feeders. Despite its benefits, bin-picking is not yet widely adopted in the industry due to the complexity, high cost, slow speed, low reliability, and geometric limitations of current solutions.

The goal of this work is to develop a solution that relies solely on affordable hardware. Commissioned by Asyrl SA, a leader in part feeding solutions for automation, and developed in collaboration with the research center CSEM SA and the Robotics Lab at Bern University of Applied Sciences, this project introduces a novel approach to address these challenges.

Instead of relying on expensive 3D cameras, this solution utilizes 2 or more standard cameras (Figure 1), mounted around the bin. A deep convolutional neural network (CNN) has been trained to predict the pose of the parts in the scene. The images from all cameras are processed in parallel, allowing for pose predictions in less than 100 milliseconds.



Figure 1: Example image of the bin from one of the cameras.

While a single deep learning prediction cannot achieve 100% accuracy in real-world applications, the multi-camera setup and precise calibration leverage different perspectives from each camera. By comparing and combining predictions from each camera, the system introduces redundancy, thereby significantly reducing the probability of false predictions. This redundancy is key for ensuring high reliability, which is essential for successful implementation in the industry.

To enable the training of the CNN for bin-picking, synthetic images and domain randomization play crucial roles. Synthetic images are artificially generated visuals that simulate real-world bin picking scenarios, allowing the network to learn from a vast array of diverse and controlled environments. In contrast to real

pictures, the exact locations of the parts are known in the synthetic environment and can be used as training data. Domain randomization, on the other hand, involves varying the parameters of these synthetic images—such as lighting, textures, and object positions—to create a wide range of training data. Having more variety in the training data than in the real-world application ensures that the model becomes robust and adaptable, capable of accurately predicting part poses under different real-world conditions. By leveraging these methods and training on hundreds of thousands of synthetic scenes, the CNN can effectively bridge the gap between simulated and real data, leading to reliable performance even with smooth metallic parts, which often pose challenges for 3D camera-based solutions, due to reflections.

CSEM has built a demonstrator to present the technology (Figure 2). Four cameras are mounted around a small bin containing up to 300 fuses, each measuring $10 \times 3 \times 3$ mm. An industrial robot continuously picks fuses from the bin, showcasing the system's efficiency and reliability.

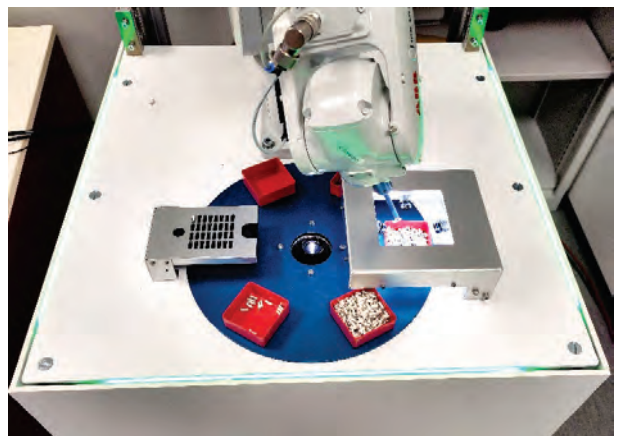


Figure 2: Robot Demonstrator. Four cameras are mounted around the red bin on the right side of the image. The algorithm has determined the 3D position and orientation of the parts. The robot picks one part at a time from the bin.

Visard-HE – Visard for Headless and Embedded Applications

S. Widmer, F. Auf der Maur

The Visard platform is commonly utilized for industrial automation applications where physical space constraints are minimal. However, computational systems used in these applications usually face limitations in real-time control of hardware GPIOs when running on Windows devices. To address this, external IO modules, such as WAGO nodes, are typically integrated. In contrast, tabletop devices used in lab automation often demand compact devices with a smaller footprint and less emphasis on extensive configuration capabilities. To meet these specific requirements, Visard-HE was developed as a streamlined solution. This platform enables Visard to seamlessly interface with generic embedded devices, facilitating efficient manipulation of IOs while running Visard applications. Notably, Visard-HE eliminates the dependency on a display, making it an ideal choice for applications requiring compact, headless operation with robust IO control.

Visard is a software framework developed by CSEM, which serves as a cornerstone in industrial automation, offering robust configurability and advanced features. However, with the growing demand for smaller and more compact setups, especially in the field of laboratory automation, a new set of challenges has emerged. Laboratory automation systems often emphasize efficiency and simplicity over extensive configurability. These systems typically require only a minimal display to show essential information, reducing both hardware requirements and operational complexity.

To address these specific needs, a version of Visard, known as Visard-HE, was developed. This new iteration allows the Visard platform to run applications without the need for a graphical user interface (GUI). By removing the dependency on a screen, Visard-HE reduces hardware overhead and enhances its usability in compact setups, making it ideal for environments where a display is unnecessary or impractical. This design also enables Visard-HE to seamlessly integrate with embedded devices, further streamlining its deployment in constrained or specialized environments.

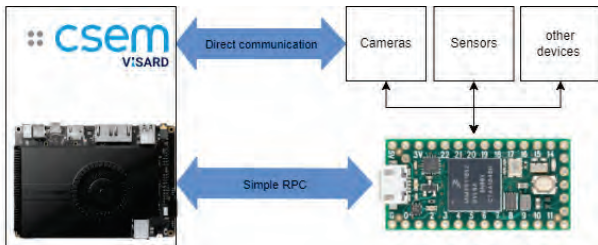


Figure 1: Communication overview. The Visard-HE (simple RPC) connection can be used to communicate with the MCU. The MCU can be used for real-time triggers, while direct communication to the connected devices can be used to extract data from the connected devices.

An additional requirement in laboratory automation is real-time control of GPIOs (General Purpose Input/Output) to interface with switches, sensors, and other critical hardware. Traditional setups often face challenges in achieving precise timing and responsiveness. Visard-HE addresses this with SimpleRPC, an open-source library designed for remote procedure calls to embedded devices. To meet the demanding requirements of real-time control, significant improvements were made to SimpleRPC. These enhancements optimized its communication efficiency and tightly integrated the library with the Visard framework. The result is a highly responsive system capable of controlling GPIOs with precision in the sub-microsecond range. This capability is particularly important for applications requiring tightly synchronized operations, such as triggering image captures and dynamically reacting to their analysis results within precise intervals.

To ensure seamless operation and compatibility with various hardware setups, different embedded platforms were tested. The

LattePanda Sigma was chosen as the primary development platform for its unique combination of an x86-based processor and an integrated Arduino Leonardo microcontroller. This configuration allows for unified control of GPIOs directly from the same board, simplifying hardware integration and improving performance. All in a formfactor of only 146 × 102 × 24 mm. In scenarios where higher processing power is required on the microcontroller side, Teensy 4.1 developer boards are recommended. These boards offer advanced computational capabilities, making them ideal for tasks that require intensive real-time processing.

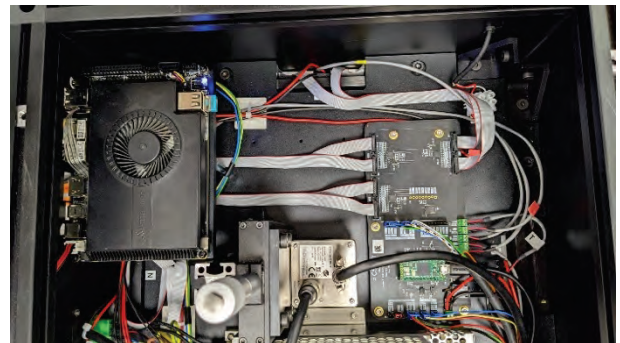


Figure 2: A hardware setup showing the compact solution of Visard-HE in a real-world scenario. The system can precisely control the illumination and camera exposure to improve image capture with this prototype.

Looking ahead, further development efforts are underway to enhance the functionality of Visard-HE. A key focus is on exposing Visard methods and properties to external applications. This would enable seamless interaction with web-based applications, making it easier to monitor and control the system remotely. Such enhancements would significantly broaden the use cases for Visard-HE, particularly in distributed and cloud-connected environments.

The development of Visard-HE marks a significant evolution in the Visard ecosystem. By addressing the specific requirements of compact, screenless setups and providing precise real-time control over GPIOs, it offers a tailored solution for laboratory and industrial automation applications. Its ability to adapt to diverse hardware configurations, coupled with ongoing improvements in connectivity and usability, positions Visard-HE as a versatile and forward-looking platform for automation challenges.

Monaural Electroencephalogram towards Brain-controlled Hearing Aids

G. Yilmaz, J. Lahera, R. Rusconi, M. Frosio, N. Bonzon, M. Waelti •, M. Segesssenmann •, M. Lucchini •, J. Jorge

Reliable long-term electroencephalography (EEG) monitoring in- and around-the-ear could open remarkable new possibilities for medical devices as well as consumer products such as true wireless stereo earphones. Potential applications that can be unlocked with a single-ear wearable device include, yet are not limited to, brain-steered hearing aids, sleep monitoring, auditory attention decoding, temporal lobe epilepsy monitoring, and cognitive load/fatigue monitoring. Preliminary results with our novel single-ear EEG prototype show clear brain responses to auditory stimulation.

Target speaker identification, along with speech enhancement algorithms, improves the performance of hearing aids, in particular for so-called cocktail party scenarios. While hearing aids are optimized to amplify the human speech and suppress background noise, in multi-speaker conditions, further processing to identify the attended speaker and to amplify only their speech is needed. Recently, it has been shown that electroencephalography recordings (EEG) can be analyzed to identify the target speaker.

For hearing aids to benefit from this progress, there is a need for miniaturized EEG solutions which allow reliable, long-term, high-quality recordings without compromising everyday comfort.

To bridge this gap, we developed a new wearable device (ULTEEMear) in a compact form factor compatible with hearing aids and truly wireless stereo (TWS) earphones—wherein a physical connection between the two ears is not needed. The device was developed based on CSEM's proprietary active dry electrode technology,^[1] allowing clinical-grade EEG acquisition and using Daetwyler Switzerland Inc.'s SoftPulse™ flexible dry electrodes; one in-ear and two flat electrodes that sit behind the ear outside hair region. Figure 1 displays the device worn by a subject on the right ear and its key features.



Figure 1: ULTEEMear single-ear single-channel EEG acquisition device in a hearing-aid-compatible form factor. The device is equipped with state-of-the-art connectivity solutions (BLE, USB) and exhibits a clinical-grade EEG recording quality (ISO 80601-2-26 compliant).

For a first evaluation of the functional sensitivity of ULTEEMear, a healthy subject underwent an auditory stimulation protocol while wearing the in-ear device. The EEG was recorded at 256 Hz, with an integrated bandpass filter of 0.5–40 Hz.

The protocol comprised 60 seconds of stimulation followed by silence; the stimulation consisted of repeated 100 ms bursts of white noise alternated with 100 ms of silence, to elicit steady-state evoked potentials (SSEP) in the auditory cortex at a repetition rate of 5 Hz. To avoid any signal contamination, the sound was delivered via audio speakers that were not in

• Daetwyler Switzerland Inc

electrical or physical contact with the subject. Additional variants with different burst/silence duration (e.g., 125 ms) were also tested, to evaluate their impact on the fundamental frequency of the SSEP. After acquisition, the signals were analyzed with wavelet-based time-frequency decomposition and with the Welch method for average spectral estimation.

The time-frequency decomposition showed a clear EEG power peak at the fundamental stimulation frequency, which appeared quickly following the onset of the stimulation period and disappeared with its conclusion; higher frequency activity above 10 Hz was also stronger during the stimulation period (Figure 2a). The average signal spectrum for the 60 s stimulation period displayed the same clear peak at the stimulation frequency, and additionally enabled the distinction of several harmonics (Figure 2b). When computing the signal spectrum on less data (only the first 10 s), to further challenge sensitivity, the estimate showed stronger variability, yet the fundamental frequency and several harmonics (e.g., 15 Hz, 25 Hz) could already be clearly discerned (Figure 2c). Additionally, for protocols employing a different stimulus repetition rate, the fundamental peak moved accordingly to the respective frequency, as expected.

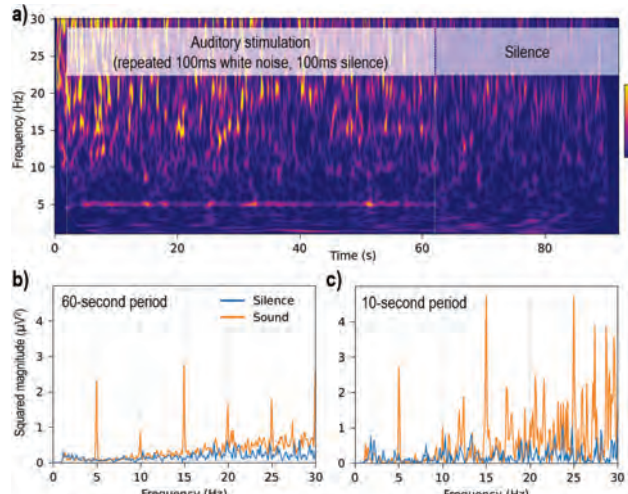


Figure 2: In-ear EEG response to auditory stimulation at 5 Hz repetition rate: (a) time-frequency decomposition, (b) average spectra during full 60-s stimulation period, and (c) first 10 s of stimulation.

In conclusion, this initial development and tests suggest a promising level of functional sensitivity for compact in-ear EEG with dry electrodes. Additionally, a third-party evaluation of our device for focus decoding shows equivalent performance when benchmarked against a commercially available 4-channel EEG headphone.

[1] G. Yilmaz, A. Seiler, O. Chételat, K. A. Schindler, Ultra-Long-Term-EEG Monitoring (ULTEEM) Systems: Towards User-Friendly Out-of-Hospital Recordings of Electrical Brain Signals in Epilepsy, Sensors 24 (2024) 1867.

Dry Electrodes with an Active Guard to Improve Bioimpedance Measurement Accuracy

L. Chabrowski, O. Chételat, A. Moreira de Sousa, J. Rosenthal

Measurements of body tissue impedance can be adversely affected by the skin/electrode impedance, whose value can vary significantly with movement or natural properties of the skin (e.g., dryness, sweat). Bioimpedance measurements can be improved with a tetrapolar configuration, which uses pairs of separate electrodes for current injection and voltage measurement. Based on a simple skin/electrode impedance model, this method succeeds in measuring the internal bioimpedance without being affected by the skin/electrode impedance, however, inaccuracies are observed when applied to more complex, real-world bioimpedance measurement models. To overcome these challenges, we present an electronic innovation using actively guarded dry electrodes that improve bioimpedance measurement accuracy in this more detailed model.

Bioimpedance is a signal $Z(t)$ that is relatively easy to measure using non-invasive skin electrodes at relatively low frequencies (e.g., 50 kHz) with conventional low power electronics. With traditional signal processing techniques, useful information can be extracted from the signal, such as body tissue and body fluid composition, changes of volume, or respiration rate. More complex measurements can be performed by using multiple coordinate bioimpedance channels. One example is electrical impedance tomography (EIT) that provides high temporal resolution and from which relevant signals such as pulmonary artery pressure (PAP) can be computed non-invasively^[1].

For the measured bioimpedance signal to be accurate, the contribution of unwanted impedances, such as the skin/electrode impedance (z_1 and z_2 in Figure 1), should be negligible. The so-called classical tetrapolar method (see Figure 1a) is a well-known solution that allows the measurement of the internal body impedance Z without being influenced by the skin/electrode impedances z_1, z_2 . However, this method is based on a model that assumes a high impedance path between electrodes near the surface of the skin. With a slightly more detailed model that incorporates this impedance (z_3 in Figure 1a), measurement inaccuracies arise. Specifically, if z_3 is not orders of magnitude greater than $z_1 + z_2$, then the measured bioimpedance will not be Z , but $Z + z_1 z_2 / (z_1 + z_2 + z_3)$. This is the case when performing measurements using dry electrodes, where z_3 is the same as for gel electrodes, but $z_1 + z_2$ is much larger.

In this paper we report a new method, called the *guarded tetrapolar method*, which increases the impedance of z_3 by means of actively driven guard electrode^[2]. To experimentally demonstrate this new method, a simple but powerful electronic circuit has been designed (see simplified representation in Figure 1b). While the circuit requires a more complex design with a floating power supply for each electrode (GND1 and GND2 are *not* connected), this degree of freedom allows a simple circuit with the potential to optimize bioimpedance measurements for scientific and medical applications.

The guarded method divides the electrodes of the classical tetrapolar method into three parts (see Figure 1b). The inner disc, which retains the original role of the electrode, is now surrounded by two ring electrodes. The first ring is a guard, i.e., an electrode whose potential is controlled to be equal to that of the inner disc. As a result, the voltage between the guard electrode and the inner disc is zero, preventing any surface current from flowing through z_4 or z_5 . The outer ring is connected to the local ground (GND1 or GND2), allowing any current flowing from the op amp to return to the local power supply (there is no other path). As

GND1 and GND2 are not connected, the current flowing through z_3 is zero (unlike in the classical method). As a result, the guarded tetrapolar method allows accurate measurement of Z for any z_3 independent of the values of z_1 and z_2 .

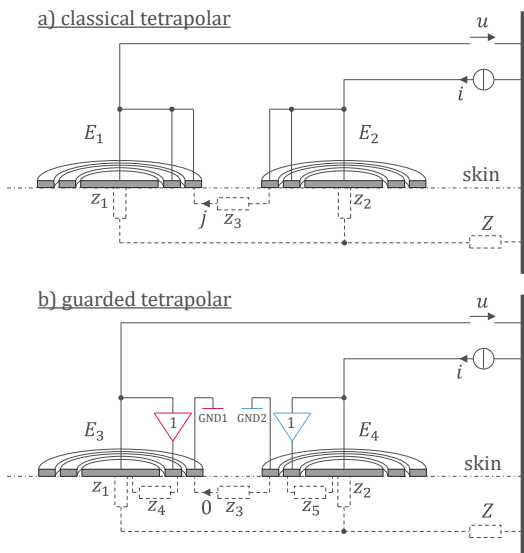


Figure 1: Circuits for a) the classical tetrapolar method; and b) the proposed guarded tetrapolar method. Due to space limitations, only half of the circuit is shown (the other half is identical).

Note that because the guarded method requires two additional rings, the area available for the inner electrode is significantly less than the area available for the classical method. A smaller area is known to be detrimental to measurement quality as it increases the skin/electrode impedance $z_1 + z_2$. For a fair comparison, the total area is kept identical for both methods.

In the context of this project, the electronics include embedded circuitry that allows a double-blind study. At regular intervals (e.g., one minute) known only to the acquisition algorithm, the signals are alternately recorded with a configuration implementing the classical method (Figure 1a) or the new method under tested (Figure 1b). The idea is that during different activities, the subjects are recorded with both methods without knowing when one or the other is used. The engineers/scientists receive two sets of data, each corresponding to a method, but without knowing which one. Only when the analysis is complete does the algorithm reveal which method corresponds to which set. This approach allows unbiased conclusions to be drawn. The method is currently being investigated in measurements on healthy adults.

[1] M. Proenca, et al., Non-invasive pulmonary artery pressure estimation by electrical impedance tomography in a controlled hypoxemia study in healthy subjects, *Scientific reports* 10.1 (2020): 21462.

[2] CSEM's patent EP2727528B1

Electrode Localization through Impedance Measurements

J. Wacker, F. Braun, M. Rapin, J.-A. Porchet, C. Meier, O. Chételat, M. Egger •

Electrocardiographic imaging (ECGI) is a measuring modality which produces maps of the electrical activity of the heart by mathematically back-projecting on the epi- and endocardium the body surface potentials measured by more than 100 electrodes. The accurate localization of the electrodes on the body is important for the algorithms to correctly solve this inverse problem. The state-of-the-art methods for electrode localization, MRI and X-ray CT, are expensive, laborious, logically complex, and potentially harmful. Here, we present a fast and safe localization method through impedance measurements performed via the same electrodes as for ECGI. For sensors measuring biopotentials, the additional hardware requirements for impedance measurement are low and therefore the method results in significant cost reductions.

One difficulty of ECGI is the necessity to precisely know the electrode positions used during the ECG acquisition. Currently, this issue is solved with an MRI or CT-scan that acquires simultaneously the body structures (thorax, heart and lungs) and the electrode positions needed for the ECGI algorithms. This approach has two drawbacks. First, it requires the patient to perform an MRI or CT-scan for every ECGI examination, which is costly, time-consuming and may overexpose the patient to ionizing radiation. Second, the ECGI examination has to be scheduled together with the MRI or CT-scan session, which is an important barrier for acceptance in clinical routine due to logistical difficulties. Methods based on optical imaging of the patient would be possible if the patient torso could be seen all around while lying. For this to be possible, cameras and especially a solution for a transparent bed are required.

The method presented here is based on impedance measurements and requires only some relatively minor modifications in the ECGI electronics. Therefore, no additional special equipment is needed. The method uses an initial recent MRI or CT scan of the patient required for the ECGI algorithm. However, the ECGI electrodes do not need to be affixed on the patient during this scan. Therefore, the ECGI examination is not logically coupled to the MRI or CT scan. Moreover, it is frequent that the same patient requires several ECGI examinations (for example, before and after treatment) and therefore, no additional MRI or CT scans are needed.

In this so-called impedimetric self-localization (ISL) method, safe and imperceptible electrical currents are injected into the body between pairs of electrodes [1]. Simultaneously, the resulting potential is measured by other electrodes on the body. The strength of the potential is a function of space (distance from the current injecting electrodes) and local electrical properties of the body. In summary, the method consists in 1) calculating the potentials on the torso based on a model determined by the initial MRI or CT scan, and 2) identifying the positions matching the measured potentials. The model can be calibrated thanks to the knowledge of a few “landmark” electrode positions on the body. The landmarks are preferably spots which are easily detected by eye/palpation and on MRI/CT scans (e.g. the clavicles, vertebrae).

Using cooperative sensor technology [2], we developed a system with 12 landmark electrodes (injecting currents) and 100

measuring electrodes (recording the resulting potentials) and tested it on a water tank which was filled with saline water and serves as a model for a human torso (see Figure 1). A full recording to localize all sensors takes ~13 seconds.



Figure 1: Cooperative ECGI/ISL sensors mounted on a water tank.

The positions of the sensors were then calculated based on the measured potentials. Since the electrodes are arranged in a regular grid, their actual position is easily defined for comparison with the calculated position. Note that in a study on patients, the position of the electrodes is less regular, and the evaluation of the accuracy of ISL requires comparative imaging (e.g., photography, MRI/CT scans). Overall, we found a localization error of 5.45 ± 5.43 mm (mean \pm standard deviation), and 86% of the electrodes had a localization error < 10 mm which was previously determined by simulations as acceptability threshold. These results therefore stimulated the drafting of a clinical study to verify the performance of the proposed method on a few healthy volunteers.

This study is currently on-going, in cooperation with the Geneva University Hospital (HUG). This project has received funding from Innosuisse (Innovation project 37705.1 IP-ENG). The authors thank Innosuisse for the support.

• EP-Solutions, Yverdon-les-Bains

[1] F. Braun, M. Rapin, J. Wacker, O. Chételat, System and method for automatic localization of the spatial position of electrodes on a conductive body, EP 4 129168A1

[2] O. Chételat, M. Rapin, B. Bonnal, A. Fivaz, J. Wacker, B. Sporrer, Remotely Powered Two-Wire Cooperative Sensors for Biopotential Imaging Wearables, Sensors, 22 (2022) 8219.

SwissFever – Cloud-based Platform Enabling Real-time Fever Alerts for Children Undergoing Chemotherapy

P. Chervet, O. Truffer, Z. Despature, A. Singh, A. Rubio, C. König •, R. Amman •, E. Brack •

Early fever detection in children undergoing therapy for cancer is an important factor in reducing the risk of complications and thus improving the patients' outcome. The SwissFever study aims to continuously monitor the body temperature of children undergoing cancer therapy, and to issue temperature alerts when the body temperature reaches a given threshold. CSEM collaborated with the Inselspital in Bern to develop a platform to support this clinical study conducted by a team from the pediatric oncology department. Using, adapting and further developing the proprietary cloud-based X-Data platform, CSEM shows to be a prime partner for data acquisition, data visualization and data management in clinical trials.

In children and adolescents undergoing chemotherapy for cancer, fever in neutropenia (abnormally low concentration of certain white blood cells) is the most frequent potentially lethal complication. Emergency hospitalization and empirical treatment with broad-spectrum antibiotics have reduced lethality from >50% in certain high-risk situations to <1%. Continuous monitoring of body temperature leads to earlier fever detection compared to the usual discrete body temperature measurements performed only intermittently for clinical reasons. Earlier detection of fever leads to earlier assessment and treatment and thus can reduce the risk of complications. The present study primarily aims to assess the efficacy of automated fever alerts resulting from continuous fever monitoring using wearable devices. A secondary goal is to run an offline exploratory data analysis to assess the possibilities to predict fever or infection events even earlier using physiological data measured by wearable devices.

CSEM contributed to the project with their existing X-Data platform to cover the secure data management needs and tailored it to fulfill all the study's requirements. X-Data is a cloud-based platform to securely collect, store and manage data collected by wearables: either CSEM's proprietary or commercial off-the-shelf devices. To connect the wearable devices to X-Data, a gateway, either in form of dedicated hardware or a smartphone, is used. Once development and testing are finished, X-Data will allow to securely manage and visualize the measured data from the study participants, while offering the real time alerting system needed to send the fever alerts to the patients' caregivers.

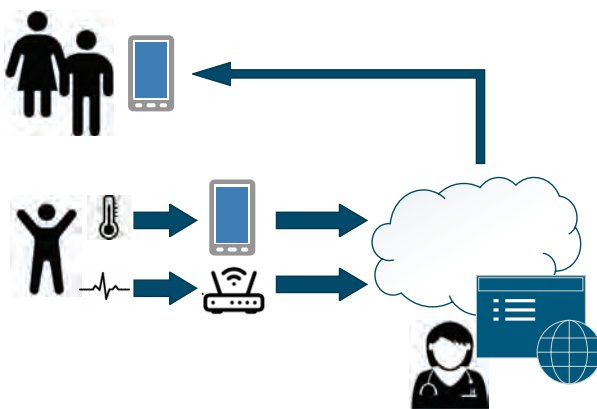


Figure 1: System overview of wearable devices interacting with CSEM's cloud-based X-Data platform.

Figure 1 shows the overview of the system, consisting of the wearable devices, the gateway smartphone application and the X-Data cloud platform.

Two different wearables are used, the commercially available Greentec Core to measure the core body temperature and the Actigraph LEAP (developed in collaboration with CSEM) to measure various other, mainly PPG based vital signs. The latter are to be used in the offline exploratory analysis for the prediction of fever events. The Core is connected via BLE to a smartphone, allowing to send real-time body temperature data to the cloud. The LEAP will once a day be connected via an USB-cable to a dedicated gateway to charge its battery and at the same time transmit the recorded data to the cloud.

On the smartphone, connected to the Core, a gateway Android application is running, which transmits the temperature data to the cloud in real time. The application also shows the current body temperature, together with the battery and connection status of the Core in a simple graphical user interface. The app further allows to securely onboard wearable devices and assign them to the patients, a necessary one-time set-up before the patient receives the wearables and the smartphone.

Already existing features of the platform, such as gateway and user authentication, secure data transfer, secure data storage and secure data access, were used to fulfill the requirements of the study. Additional features were developed, which at the same time extend X-Data's general capabilities to be used in other clinical studies. Those features are easy and secure onboarding of patients or devices, management and monitoring of patients and wearable devices through a web interface and the real-time SMS alerting system. Additionally, the device data visualization and the graphical representation was added to the dashboard. For this study, the system is used to send body temperature SMS alerts to caregivers, however it is extendable to other parameters from the same or other wearables.

The X-Data platform continues growing and it is already requested to be used in other clinical trials. The study described in this article is planned to start in January 2025 with ~10 patients at Inselspital Bern. Upon success, the study will be extended to other cancer centers throughout Switzerland, aiming to include ~250 patients over the next 2-3 years.

This work was partially funded by the Canton of Bern in the scope of the Bern Medtech Collaboration Call 2024. CSEM is thankful for their support.

• Division of Pediatric Oncology, Department of Pediatrics, Inselspital, Bern, Switzerland

Continuous Non-invasive Measurement of Core Vital Signs on the Hospital Ward

G. Bonnier, Y. M. Proust, Y. Degiorgis •, C. Fuligno-Schmidt •, P. Vetter ••, J. Fisher ••, K. Adam, F. Braun, PL. Gaudilliere, M. Gerber, J. N. Pfeuti, M. Proen  , P. Renevey, P. Theurillat, R. Vasireddy, M. Lemay, A. Rubio Anadon, D. Ferrario

VITAL+ aims at combining continuous monitoring of blood oxygen saturation, pulse rate, blood pressure, and respiration rate with a non-invasive upper-arm-worn device on the hospital ward. This automation empowers caregivers to focus on caring for patients, while improving safety and comfort.

Vital signs monitoring in hospital ward is critical to provide valuable information to predict patient deterioration or treatment efficiency. The frequency at which patients' vitals should be assessed is a compromise between insufficient monitoring and work overload. This core hospital process is indeed time-consuming and expensive (>10 million inpatients have their vitals taken 3x/day meaning ~150 million minutes of manual measurement per day), is not frequent enough for robust predictive analytics (measuring 3x/day, but not at night, is not enough to provide reliable early warning of patient changes [1]), and suffers from uneven quality with an error rate up to 19% [2].

The VITAL+ project, in collaboration with the company rheo, aims at providing a photoplethysmography (PPG) based solution for continuous monitoring of oxygen saturation (SpO₂), pulse rate (PR), blood pressure (BP) and respiratory rate (RR) using a unique and non-invasive upper-arm-worn device (Figure 1).

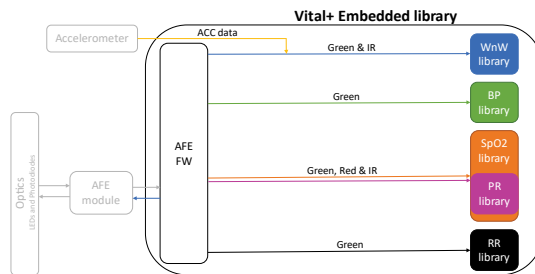


Figure 1 - General architecture of the Vital+ embedded library.

In this collaboration, CSEM developed and evaluated an embedded library, optimized in memory and computational cost for real time processing. This library includes an analog-front-end (AFE) driver controlling the optics for high-quality PPG signal acquisition as well as the following CSEM-proprietary algorithms: (1) a worn-not-worn detector based on accelerometer and PPG signals; (2) a BP algorithm [3], (3) a RR algorithm based on PPG spectral analysis (developed in this project), (4) a PR algorithm based on a detector extracting interbeat intervals, and (5) an SpO₂ algorithm [4]. Multiple PPG channels are acquired and controlled by the AFE driver and fed into the different algorithms (Figure 2).

Optics control by AFE driver was assessed by PPG quality evaluation over 10 recordings of ~1h and compared with specific requirements for accurate vital sign estimation. A dedicated clinical data collection campaign (BASEC 2023-01925), made in

collaboration with the Pourtal  s Hospital (RHNe), has been conducted to pre-validate all algorithms (Table 1). Except for the ongoing BP investigations, all other vital signs were compared against medically validated references.



Figure 2: Pictures of the Vital+ device.

Table 1: Vital signs and their respective protocol and population.

Vital sign	Protocol	Population	Reference
SpO ₂	1h hypoxia 70-100%	N = 10 healthy subjects	Blood sampling
PR	1h hypoxia 70-100%	N = 21 healthy subjects	ECG
RR	1h controlled RR 5-30 cpm	N = 24 healthy subjects	Flow sensor

PPG signal quality evaluation showed quality metrics compliant with requirements. The SpO₂, RR and PR performance (Table 2) meet all medical requirements.

Table 2: Clinical study results per vital sign.

Vital sign	Performance	Acceptance rate [%]	Medical requirements
SpO ₂	1.98 ± 1.08%	94 ± 8	RMSE ≤ 3.5%
RR	0.7 ± 0.5 cpm	38 ± 11	RMSE ≤ 3 cpm
PR	2.08 ± 0.7 bpm	93 ± 9	RMSE ≤ 5 bpm

This study demonstrates the feasibility of CSEM's approach to embed all algorithms into one single non-invasive device. The 3 validated vital signs reach the expected medical requirements. The next steps are (1) to pre-validate BP estimates, (2) increase the acceptance rate of the RR algorithm, and (3) evaluate CSEM's approach in real conditions (rheo's use case).

• D  partement anesth  siologie, RHN, Neuch  tel, Switzerland
•• rheo AG, Z  rich, Switzerland

[1] S. Romero-Brufau, *et al.*, Widely used track and trigger scores: Are they ready for automation in practice?, *Resuscitation*, vol. 85, no. 4, pp. 549–552.

[2] T. Schmidt, U. K. Wil, Identifying patients at risk of deterioration in the Joint Emergency Department, *Cogn. Technol. Work*, vol. 17, no. 4, pp. 529–545, Nov. 2015.

[3] Proen   M, Ambühl J, Bonnier G, Meister TA, Valentin J, Soria R, Ferrario D, Lemay M, Rexhaj E., Method-comparison study between a watch-like sensor and a cuff-based device for 24-h ambulatory blood pressure monitoring, *Sci Rep*. 2023 Apr 15;13(1):6149.

[4] F. Braun, *et al.*, Influence of Measurement Location on Reflectance Pulse Oximetry in Sleep Apnea Patients: Wrist vs. Upper Arm, in *EMBC 2021*, Guadalajara, Mexico: IEEE, Oct. 2021.

Cuffless Blood Pressure Monitoring: Precision is Maintained four Months after Calibration

M. Proen  a, C. Aguet, G. Bonnier, K. Adam, D. Ferrario, M. Lemay

Frequent and accurate blood pressure (BP) monitoring is essential for effective hypertension management. Automated cuff-based devices are poorly suited for frequent and long-term monitoring. Alternatives based on photoplethysmography (PPG) and pulse wave analysis (PWA) offer promising potential, but require calibration. Limiting the number of re-calibrations is crucial for their practical usability. In this study, we tackle this Achilles' heel and demonstrate that CSEM's cuffless BP monitoring algorithm remains within ISO 81060-2 limits over a four-month period after calibration.

Persistently high blood pressure (BP), or hypertension, affecting approximately one third of the adult population, significantly increases the risk of developing cardiovascular diseases. Accurate and frequent BP monitoring is crucial to identify atypical BP fluctuations, especially in treated patients, for effective therapy management and reduction of long-term cardiovascular risk. While automated cuff-based devices are widely used both in clinical and home/ambulatory settings, they suffer from limitations such as discomfort, unsuitability for frequent monitoring, and occasional inaccuracies. These drawbacks contribute to the widespread underdiagnosis of hypertension.

Solutions based on photoplethysmography (PPG) and pulse wave analysis (PWA) offer promising and convenient alternatives, particularly due to their unobtrusive nature. Absolute BP values can be obtained after a calibration with a reference device. However, the need for frequent re-calibrations in case of sensitivity to peripheral effects strongly affects their practical usability, and inevitably raises concerns about long-term trending ability for hypertension management. Leveraging PWA features that reflect central rather than peripheral phenomena can help mitigate the problem. This observation was at the root of the development of CSEM's patented PPG-based PWA algorithm^[1]. We have previously validated its short-term trending ability during general anesthesia induction^[2], and its ability to track circadian fluctuations in 24-h ambulatory BP monitoring settings^[3]. In the present study, our aim was to demonstrate its long-term post-calibration stability, over weeks and months.

To that end, recording sessions were performed on 11 participants (6 female, age: 36.8 ± 10.7 years, body-mass index: 23.0 ± 3.1 kg/m², Fitzpatrick skin type: 2.1 ± 0.5 , treated hypertension: 1, smoker: 1), at irregular intervals of one or several days, depending on their availability, over a period of 123 days, with an average of 30 recording sessions per participant. All subjects provided written informed consent. During each recording session, the subjects were sitting, forearms, elbows and back supported, legs uncrossed and feet flat on the floor and asked to relax and not to talk. PPG sensors were attached at their right upper arm and fingertip, while an oscillometric upper arm BP monitor (Omron M6 Comfort) was installed at their left upper arm. After a resting period of at least 8 minutes, PPG data acquisition was started, and five BP measurements were acquired with the cuff-based monitor. After PPG data processing via CSEM's BP algorithm, five cuff-PPG BP pairs were obtained. As oscillometric cuffs are not accepted BP references, the five cuff measurements were then averaged to produce one single representative cuff BP value, and the same was done for the five PPG BP values. In ~60% of sessions, a BP change was induced after the five measurements through isometric exercise (leg

extension). Two additional cuff-PPG BP pairs (leg extension measurements) were acquired during the exercise. The induced BP change was calculated as the average of the leg extension measurements minus the average of the baseline measurements.

CSEM's PPG-based algorithm calibration procedure – a simple offset correction – can be performed in post-processing. Thus, the one-month stability of the calibration can easily be evaluated by calibrating the PPG-based BP on a given session and evaluating the agreement between the cuff-based and PPG-based BP on a session occurring one month later. It is therefore possible to evaluate the stability of the calibration for various time intervals by combining different pairs of sessions in each subject, depending on the time elapsed between them. All thus-assessed cuff-PPG differences of all subjects were grouped according to their respective time intervals, and the accuracy (bias) and precision (standard deviation (SD)) were assessed for each time interval group for both systolic (SBP) and diastolic BP (DBP).

While evaluating post-calibration stability, it is essential to also verify sensitivity to actual BP changes. We thus pooled all exercise-induced BP changes of all subjects and evaluated their agreement (bias \pm SD) against their corresponding cuff-based changes. The concordance rate (CR) on large changes ($>15/10$ mmHg on SBP/DBP, respectively) was also assessed.

Figure 1 show the post-calibration bias and SD of CSEM's BP. Both SBP and DBP remain within the ISO 81060-2 limits (bias within ± 5 mmHg, SD ≤ 8 mmHg) at all times, for both fingertip and upper arm PPG. No significant correlation (at the 5% level) with time was found, suggesting no deterioration of the stability over time. Regarding BP changes, all agreements were within ISO 81060-2 limits as well, and CR = 100% in all cases.

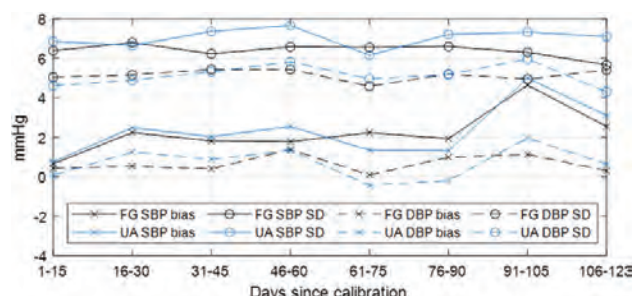


Figure 1: Accuracy (bias) and precision (SD) of CSEM's cuffless systolic (SBP) and diastolic BP (DBP) as a function of the time elapsed since calibration using fingertip (FG) or upper arm (UA) PPG data.

This study demonstrates that CSEM's cuffless BP algorithm is stable for four months after calibration. Clinical studies for further evaluating its long-term stability and trending ability in hypertensive patients are currently ongoing.

[1] M. Proen  a, et al., WO 2016138965 A1, 9th of September 2016

[2] Y. Ghamri, et al., Anesth Analg, 130(5):1222-1233, 2020

[3] M. Proen  a, et al., Sci Rep, 13:6149, 2023

Unobtrusive Long-term Sleep Staging using Photoplethysmography-based Wearables

L. Constantin, J. Van Zaen, A. Lemkaddem, L. Jeanningros, K. De Jaegere •, S. R. Ott ••, A.-K. Brill •, C. M. Horvath •, J.-P. Thiran *, M. Lemay, F. Braun

The diagnosis of sleep disorders is still often based on polysomnography, an in-lab exam allowing experts to perform accurate sleep staging, although this is labor-intensive, expensive, and exposing patients to unusual sleep conditions. Recent work has shown the potential of deep learning models to perform such sleep staging with satisfying accuracy using a simple sensor at the fingertip and the optical technique called photoplethysmography (PPG) commonly used in wearables. In this work, we extended one of these models for the use of PPG data collected from CSEM's wrist-worn wearables in adults and reached encouraging performance (78% accuracy and a Cohen's kappa of 0.68). Even though the model has shown limitations when applied to patients with cardiac arrhythmias (accuracy drop of 10%), it paves the way towards unobtrusive long-term sleep monitoring of patients at home.

Sleep disorders significantly increase the risk of cardiovascular diseases, obesity, diabetes, and depression. Accurate diagnosis requires scoring sleep stages via polysomnography (PSG), the current gold standard for sleep examination, although costly, inconvenient, cumbersome, and poorly scalable. Photoplethysmography (PPG) is a promising alternative, compatible with comfortable, unobtrusive, and continuous monitoring at home. PPG detects blood volume changes through light absorption, which is directly linked to cardiac rhythm and contains respiration and movement artifacts^[1], making it rich for interpretation by a deep learning framework. We adapted and trained SleepPPGNet – a model proposed by Kotzen, *et al.*^[2] – for ambulatory sleep staging, achieving 78% accuracy on wrist PPG, a performance comparable to the inter-rater agreement between clinical experts^[3], and demonstrating remarkable cross-dataset robustness. Additionally, cardiac arrhythmia was identified as a limiting factor in performance.

We used 3 public datasets (accessible via sleepdata.org): 5792 ECG recordings from SHHS Visit 1, 2056 PPG recordings from MESA, and 324 PPG recordings from CFS. Performance was assessed on MESA, CFS, the Wearable Dataset (68 PPG recordings collected on wearable devices^[4]), and the Arrhythmia Dataset (321 PPG recordings) using median accuracy (Ac), Cohen's kappa and confusion matrices as main performance measures. Transfer learning (TL), a short retraining on the target dataset, was performed to mitigate the cross-dataset robustness issue^[2]. All PPG datasets were recorded at the fingertip, except for the Wearable Dataset. All recordings were filtered, standardized per subject, and cropped/padded to 10 hours. Sleep stages from PSG were scored by board certified sleep experts and were used as ground truth for our model.

The model is made of 8 stacked residual convolutional blocks for local feature encoding, followed by 2 stacked temporal convolutional network blocks for long-range context awareness, and a final linear layer as classifier. The exact architecture is described in detail in our previous publication^[4]. ECG data from the SHHS Visit 1 dataset was used for pretraining, and PPG from a subset of the MESA dataset for tuning. Categorical cross entropy was used with Adam optimizer, and balancing weights for output classes. Finally, the model performance was evaluated on the remaining data of the MESA dataset (i.e., test subset) as well as the CFS, Wearable, and Arrhythmia datasets. For the latter three

datasets performance was evaluated twice: 1) once without retraining the model and 2) once with TL, i.e., specifically retraining the model on a subset of the data while evaluating its performance on the remaining data.

Our version of SleepPPGNet achieved 78.5% Ac on the test subset of MESA. Cross-dataset generalization, a major issue in similar contexts, reached 80% Ac on CFS, and 78.1% Ac on wrist PPG (Wearable Dataset). Our model achieved 68.1% Ac on the Arrhythmia Dataset. TL significantly increased results on CFS to 82% Ac. Details on Cohen's kappa and sensitivity can be found in Table 1.

Table 1: Sleep staging performance on all datasets used for testing. Except for MESA, accuracy and Cohen's Kappa are reported once without and once with model retraining, i.e., transfer learning (TL).

	MESA	CFS	Wearable	Arrhythmia
Accuracy (TL)	78.5% -	80% 82%	78.1% 78.3%	68.1% 69.4%
Kappa (TL)	0.67 -	0.71 0.74	0.68 0.68	0.50 0.54
Sensitivity	Wake	90%	91%	82%
	N1/2	63%	66%	68%
	N3	79%	72%	80%
	REM	91%	92%	92%
				79%

Without ever training on those datasets, our model performs exceptionally well on both CFS (fingertip PPG) and the Wearable Dataset (wrist PPG). TL still enhances performance on CFS but yields inconclusive results on the Wearable Dataset due to limited data. Cardiac arrhythmia negatively impacts performance, and TL does not effectively mitigate this loss. Further investigation into the types of arrhythmias involved is necessary. Per-stage sensitivity is consistently balanced; cross-dataset variations partly depend on dataset-specific class distribution.

In terms of future developments, additional experiments were conducted, demonstrating the potential of accelerometry to further improve performance, the possibility of using inter-beat intervals instead of raw PPG through a performance-complexity trade-off, and the promising behavior of our model on 24h recordings (variable-size input and daytime data). The present results pave the way towards long-term sleep monitoring of patients at home using unobtrusive wearables.

* Bern University Hospital, Switzerland

** Bern University Hospital and St. Claraspital Basel, Switzerland

* EPFL, Switzerland

[1] J. Allen and P. Kyriacou (eds.), Academic Press, 2021.

[2] Kotzen, *et al.*, IEEE J Biomed Health Inf, 27:924-932, 2022.

[3] Lee, *et al.*, J Clinical Sleep Med 18:193-202, 2022.

[4] Constantin, *et al.*, IEEE EMBC 2024, 2024.

SUSTAINABLE ENERGY

Christophe Ballif

The Sustainable Energy program focuses on accelerating the transition to renewable energy sources in response to the urgent challenges posed by climate change. It emphasizes the development of clean and efficient manufacturing processes that minimize environmental impact. CSEM aims to enhance technologies in photovoltaics, energy management, and battery innovation.

The program also contributes to the cleantech market by providing advanced deep tech and digital solutions. By fostering collaboration between industries and research entities, CSEM is well positioned to lead in developing sustainable energy technologies. Ultimately, the Sustainable Energy program supports Switzerland's commitment to achieving net-zero emissions by 2050, positioning CSEM as a key player in shaping a sustainable energy future.

To achieve these ambitious goals, the program is structured around four interconnected focus areas and consists of two initiatives each addressing specific technological advancements and industry needs: advanced solutions for photovoltaics, and energy management with a focus on battery storage and digital energy. To support its customers and research, CSEM benefits from a complete infrastructure which allows fully integrated developments, including not only dedicated tools and laboratory scales lines for solar cells and solar module manufacturing, but also encapsulation material extrusion and over 300 m² dedicated to accelerated aging tests. Similarly, over the last three years a full infrastructure for battery manufacturing (coin cells, pouch cells), including a dry room under construction, and an extension for battery systems development and testing, has been parts of CSEM's facilities.

ADVANCED PHOTOVOLTAICS

This initiative is dedicated to advancing solar energy technologies, emphasizing the development and optimization of photovoltaic (PV) cells, modules and systems. This enhances the performance of PV in various applications, from energy scavenging to large PV plant. A large focus is on the use of innovative materials and manufacturing processes. By fostering collaboration with industry partners, CSEM seeks to drive the adoption of novel solar technologies, contributing to the global transition towards renewable energy and a reduced reliance on fossil fuels.

Solar Cells and Modules

This focus area concentrates on advancing PV technology for global deployment of crystalline silicon and next-generation perovskite-on-silicon (PK/Si) tandem cells and modules in different configurations. It encompasses developing materials and processes for solar cells and modules with higher efficiency, extended lifetime and durability, reduced costs, and minimized environmental impact. The research efforts are divided into three main activities: enhancing solar cell efficiency, developing innovative contacting technologies and encapsulation materials, and improving reliability and sustainability.

Integrated and Lightweight Photovoltaics

Creating next-generation PV modules tailored for integration into buildings, vehicles, and other devices or structures is a key objective in this field. It explores two main PV categories: Integrated PV (IPV), using glass-based modules, and Lightweight PV (LPV), employing glass-free designs. Applications range from building-integrated photovoltaics and agricultural settings to electric vehicles, drones, and airplanes. The development of advanced materials, including thin-film solar cells and specialized encapsulants, is crucial to enhancing reliability, aesthetics, and lifespan across diverse environments.

ENERGY MANAGEMENT

Optimizing the storage, generation, distribution, and consumption of energy within integrated systems is the core of this initiative, jointly with all required intelligence for forecasting and usage of energy as well as for supporting the maintenance of energy assets. This ensures that renewable energy sources can be effectively utilized. The application field ranges from IoT to mobility applications (e.g. from new battery chemistry to advanced BMS for batteries), including optimization of energy usage at home or district level, optimized energy usage with CSEM proprietary software, and improved management of district heating or local grid. Taken in its entirety, the approach promotes sustainability and enhances energy efficiency.

Digital Energy

This focus area addresses the digital transformation of energy systems, leveraging connectivity, data analytics, and artificial intelligence to improve resilience, efficiency, and decarbonization. Research efforts include, for instance, developing advanced forecasting models using graph machine learning to predict energy production and consumption patterns. Digital Energy also explores both learning-based control systems to optimize energy conversion and distribution, and asset management solutions for maintaining and optimizing diverse energy resources.

Batteries

Motivated by the growing demand for electrochemical storage solutions, this focus area aims to improve the economic and environmental sustainability of batteries for stationary and automotive applications. The research activities are centered around three areas: battery cell solutions, focusing on next-generation battery technologies, including solid-state batteries with a reduction in critical material or pollution materials; battery system solutions, developing advanced battery models and testing methodologies; and battery manufacturing solutions, demonstrating the application of CSEM-developed technologies in prototypes such as smart battery management systems (BMS) and multi-layer pouch cells. By collaborating with industry stakeholders, CSEM seeks to accelerate the commercialization of next-generation battery technologies.

High-efficiency Perovskite-on-Silicon Tandem Solar Cells Developments

L. Champault, M. De Bastiani, F. Sahli, F. Saenz, A. Theytaz, J.-D. Decoppet, J. Walter, R. Zanotto Razera, A. Paracchino, D. Jacobs, A. Descoedres, V. Gainche, P. Wyss, C. Alleb  , B. Paviet-Salomon, K. Artuk, D. Turkay, M. Othman, C. M. Wolff, Q. Jeangros

Perovskite-on-silicon tandem solar cells have emerged in the last few years as the most promising technology to extend the learning curve of commercial silicon photovoltaic modules. Adding a perovskite thin-film solar cell onto the front side of a conventional silicon solar cell reduces thermalization losses, translating into an improvement in power conversion efficiency by about 20%rel. CSEM is actively engaged in public and industrial projects to bring this tandem technology closer to commercialization. Notable recent results include the demonstration of a certified power conversion efficiency of 28.9% on a device active area of 60 cm².

Integrating a perovskite thin-film solar cell onto the front side of a commercial silicon solar cell enables surpassing the theoretical power conversion efficiency limit of silicon photovoltaics (PV), which is approximately 29.5%. The additional cost of incorporating the perovskite top cell is expected to be offset at the PV system level by balance-of-system components, making this tandem technology commercially viable—unlike other tandem technologies, such as those based on III-V materials. Perovskite-on-silicon tandem modules are anticipated to enter the market soon, with companies like Oxford PV already delivering first-generation products to end-users. However, several critical challenges still need to be addressed to ensure industrial success. First, large-area tandem devices need to achieve higher efficiencies than currently demonstrated. Second, high-throughput and cost-effective perovskite deposition methods must be further developed and made more reproducible. Finally, significant improvements in the service lifetime of the perovskite top cell are required to meet the standards of the PV industry. For reference, product performance warranties of 25 years are now the norm in the silicon PV sector.

CSEM's research and development efforts to advance perovskite-on-silicon tandems are centered on two axes:

- Transferring the high efficiency achieved with small laboratory-scale devices to larger scale industrial devices.
- Enhancing the reliability of perovskite-on-silicon solar cells and modules to ensure a long service lifetime.

Regarding the first point, CSEM, in collaboration with EPFL PV-LAB, demonstrated 60-cm² perovskite-on-silicon tandem solar cells reaching an efficiency of 28.9% certified by Fraunhofer ISE CalLab, which is amongst the best results worldwide for tandems with an active area >50 cm². Internally, on this format of 60 cm², the best tandem reached an efficiency of 30.1%. For reference, best efficiencies achieved in-house with devices of 4 cm² employing the same materials and processes are on the order of 30.5% (Figure 1). Key to these high-efficiency demonstrations was the development of contact materials and passivation interlayers to increase the voltage delivered by these devices.

While a step in the right direction, the device dimensions need to be scaled-up further to >300 cm² to be compatible with today's silicon PV standards. For this purpose, CSEM is focusing on two classes of scalable deposition methods, either single-step solution-based deposition methods or two-step hybrid processes. The latter involves a thermally evaporated inorganic layer capped with a solution-processed organic film and an annealing step to crystallize the perovskite film. Both categories of thin-film deposition methods are being developed in parallel as each processing route has its pros and cons. Perovskite-on-silicon tandems processed via a scalable single-step meniscus coating method are now starting to approach in performance our best

spin-coated tandems, albeit still on small dimensions. Ongoing efforts are now focusing on scaling these results to larger areas.

Research efforts to improve the reliability of perovskite-on-silicon tandem solar cells are now centered on understanding and mitigating degradation pathways occurring during thermal cycling and light soaking tests performed at elevated temperatures. To perform these experiments, an effective packaging strategy relying on a glass/glass encapsulation with an edge sealant was developed to protect the devices against moisture ingress. In summary, accelerated aging tests have highlighted the needs to i) reduce mechanical stress applied on the tandem top electrode to avoid inducing a delamination of the perovskite/C60 interface, and ii) carefully optimize the perovskite absorber to ensure long-term stability under illumination at elevated temperature. The generation and migration of mobile ions in the perovskite absorber is the key challenge that needs to be tackled to make this technology sufficiently reliable for a market introduction.

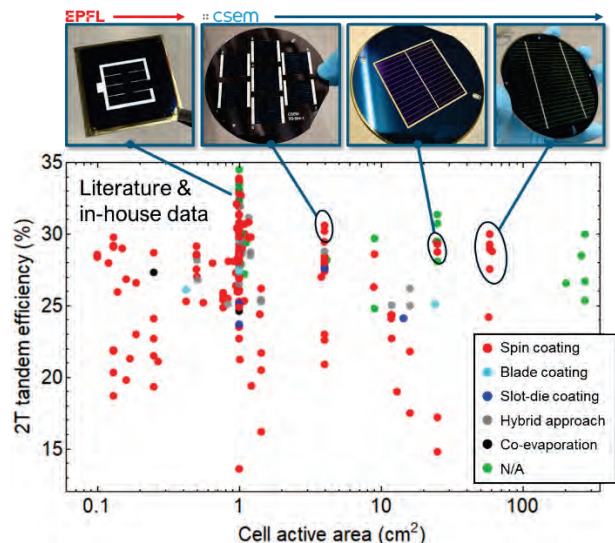


Figure 1: Compilation of literature and in-house efficiency datapoints as a function of the perovskite-on-silicon tandem cell active area. Notable results achieved by EPFL PV-LAB and CSEM are circled. Pictures of the corresponding devices of 1 to 60 cm² made in-house are shown in the top panel. The color code of each datapoint indicates which processing method has been used to make the perovskite absorber.

This work is supported by the Swiss National Science Foundation grant 200021_197006 (PAPEI); the European Union's Horizon 2020 under Grant Agreements No. 861985 (PeroCUBE) and No 101006715 (Viperlab); the Swiss State Secretariat for Education, Research and Innovation (SERI) under contract numbers 22.00413 (PEPPERONI), 22.00369 (VALHALLA), 22.00319 (TRIUMPH). Colleagues from CSEM and EPFL PV-LAB who participated in this research are gratefully acknowledged.

Developing Copper Metallization for Sustainable Production of TOPCon Cells

A. Lachowicz, R. Sakakibara •, C. Allebé, A. Morisset, B. Paviet-Salomon

While transferring a copper plating process for heterojunction cells to the industry, CSEM is developing new processes for TOPCon, the cell technology with currently the highest market share. Within the project COMET, two routes are being investigated: firstly, reinforcement of printed and fired-through lines, chosen for its simplicity; and secondly, a process involving sputtered metal for contact formation on top of a thin poly-Si passivating layer.

The standard metallization of TOPCon cells, using printed and fired-through silver paste, requires approximately 15 mg silver per watt cell power. This remains significantly above the target of 2 mg/W - the maximum consumption postulated for sustainable terawatt-scale production, as it is necessary for the transition to 100% renewable energy until 2050 [1].

With a simple reinforcement of fired-through lines, silver consumption can be significantly reduced (Figure 1). The two primary functions of cell metallization - (i) contact formation and (ii) good line conductivity - are decoupled. Silver paste is used to form solely the contact and serves as seed for electrodeposition, while electrodeposited copper provides excellent line conductivity. This process is being evaluated in collaboration with KalyonPV (Turkey), a cell and module manufacturer with a production capacity of 2 GW.

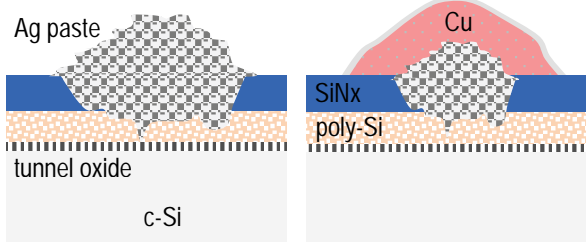


Figure 1: (left) Standard metallization; (right) Reinforcement of fine lines with electrodeposited copper (with tin as capping layer).

Due to the porous nature of the silver paste, a nickel layer is first deposited to prevent any direct contact of copper to silicon. EDX analysis of a line cross section has revealed a potentially concerning feature: copper is present beneath the silver paste, directly on the cell surface (indicated by an arrow in Figure 2, top right). The long-term stability of modules with such plated cells is being evaluated by extended damp-heat and thermocycling tests.

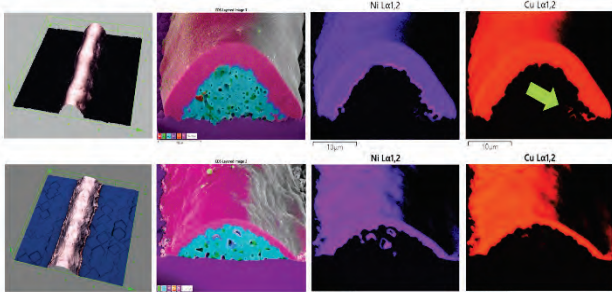


Figure 2: Confocal microscope images and EDX maps of line cross sections. Top row: line on cell front side; Bottom: line on the rear side.

Although line reinforcement reduces silver consumption, still a disadvantage remains: the contact is formed within

• EPFL, Switzerland

[1] Y. Zhang, et al., Design considerations for multi-terawatt scale manufacturing, Energy Environ. Sci., 2021, 14, 5587

the passivating layer, necessitating relatively thick poly-Si layers of about 100 nm. While providing good passivation, the layer is also absorbing: every 10 nm of poly-Si causes a notable loss of photogenerated current in the final device, in the range of 0.5 mA/cm². Therefore, CSEM develops a process with a sputtered metal layer for contact formation only on top of a thin passivating layer.

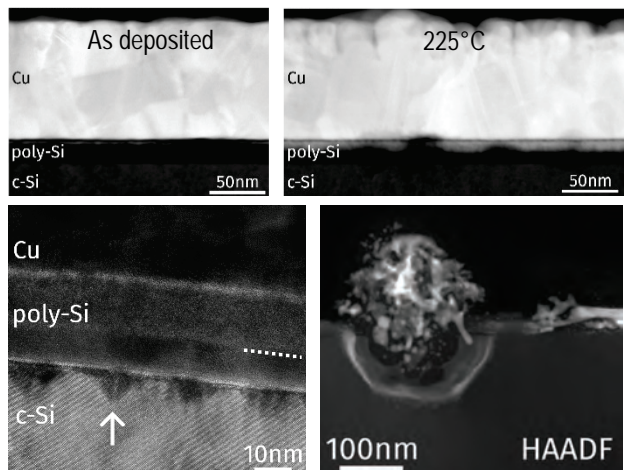


Figure 3: Samples with copper sputtered directly on poly-Si, as deposited and annealed at 225, 250 or 300°C.

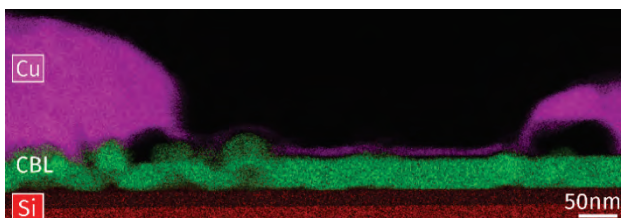


Figure 4: EDX-map of a sample with an additional copper barrier layer ("CBL"), after annealing at 400°C.

Interestingly, in-diffusion and deterioration of photoluminescence intensity of copper sputtered directly on a 20 nm (n-)poly-Si layer have been observed only from 225°C onward. TEM images show spike formations after annealing at 250°C and precipitate formation at 300°C. [2] By inserting a barrier layer the passivation stability is improved to 375°C. After annealing at 400°C, the layers exhibit deformation but remain distinct, with no detected copper diffusion into the silicon (Figure 4). The barrier layer also enhances adhesion and reduces contact resistance to poly-Si. Screen-printing of copper-based pastes is intended as patterning method of the sputtered metal and for subsequent copper plating.

Project COMET is supported under the umbrella of SOLAR-ERA.NET by the Swiss Office of Energy.

[2] R. Sakakibara, et al., Investigating Interfacial Phenomena in Copper-Covered, n-Type Polysilicon-Based Contacts by Electron Microscopy, EU PVSEC, 2024

Perovskite Thin Films for Energy Harvesting and Sensing for IoT

D. Jacobs, Q. Jeangros

Metal halide perovskites are a class of semiconductors with promising properties for photovoltaic and optical sensing applications. In the framework of the Horizon 2020 European project PeroCUBE, CSEM developed a perovskite thin-film device combining both energy harvesting and optical sensing capabilities for IoT and smart electronics applications. The energy-harvesting perovskite solar module ensures energy autonomy or prolongs battery lifetime, while the perovskite optical sensors are used to receive coded information via visible light communication protocols.

Metal halide perovskite materials can be deposited at low temperatures in the form of polycrystalline thin films, while maintaining excellent optical and electrical properties comparable to those of best-in-class monocrystalline III-V and silicon semiconductors. This unique combination of characteristics creates new opportunities in the field of optoelectronic technologies such as thin-film photovoltaic (PV) solar cells, visible light or X-ray detectors, light emitting diodes or displays.

During the Horizon 2020 PeroCUBE (under grant agreement No. 861985, 2020-2024), CSEM has developed a type of device combining energy harvesting and optical sensing capabilities (Figure 1). Using a photodiode layer stack covering a complete substrate (here glass), laser scribing is employed to define small photodetectors in one part of the substrate and a larger area photovoltaic module elsewhere to enable simultaneous visible light communication and energy harvesting.

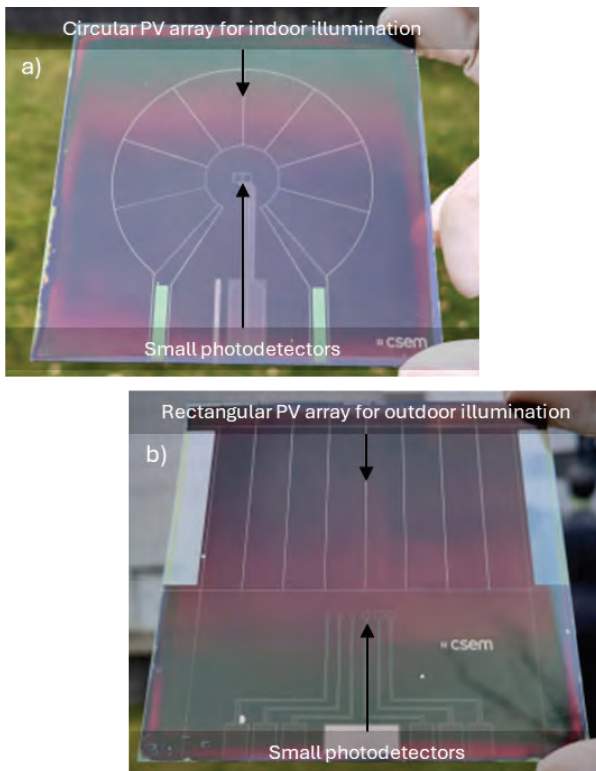


Figure 1: Device combining a photovoltaic module either for outdoor (a) or indoor (b) applications and small photodetectors to which information can be transmitted using visible light communication protocols.

The photodetectors dimensions are kept small to avoid capacitive effects and hence increase the bandwidth of the detector, which enables faster transmission rates. With this approach, free-space optical communication up to a few meters could be demonstrated with these perovskite-based photodetectors.

The flexibility offered by laser scribing enables adapting the dimensions and voltage delivered by the solar module to meet

the demands of a specific application or battery type. Also, the geometry of the solar module array can be adapted for optimum performance in either outdoor or indoor environments (see either circular or rectangular designs shown in Figure 1). For example, circular arrays are more adapted to indoor environments as this design minimizes any mismatch in photocurrent that may arise in the series-connected segments composing the solar module due to a circular illumination beam.

Such a prototype combining energy harvesting and optical sensing can be applied in various IoT and smart device scenarios. For example:

- It can be used in museums to transmit information at specific locations, such as providing audio or text descriptions next to individual artifacts.
- In warehouses, it can enable precise tracking of goods by using multiple lamps to transmit unique IDs across the warehouse space to the optical sensing unit (indoor GPS), while the larger area perovskite module harvests energy to ensure autonomy.
- Additionally, it is well-suited for secure environments such as banks, as the information transfer is inherently safer - light does not pass through walls, making it impossible to intercept the signal without being physically present in the room.
- Energy-autonomous electronic price tags for supermarkets, where the perovskite solar module ensures autonomous operation, while the price information is sent via free-space optical communication protocols.

Finally, encapsulation methods were developed during the project to extend the service lifetime of these energy harvesting and optical sensing devices. For this purpose, CSEM developed a glass-based lamination procedure that ensures long durability when subjecting the devices to the IEC 61215 damp heat test conditions (>5000 hours of stability at 85 °C in 85% relative humidity).

PeroCUBE is a collaboration between CSEM, Alpes Lasers (CH), Optiva Media (ES), Aura Light (IT), Vodafone Innovus, University of Patras, Eulambia, Noesis (GR), CNRS (FR), TU Wien (AT), Fraunhofer FEP (DE), TNO (NL), VTT (FI), and University of Oxford (GB), placed under the coordination of CSEM. The PeroCUBE project has received funding from the European Union's Horizon 2020 research and innovation program under Grant Agreement No. 861985.

PV Modules Reliability Testing Platform

G. Cattaneo, T. Auderset, J. Escarre-Palou, B. Bonnet-Eymard, M. Despeisse

In recent years, the photovoltaic (PV) module reliability testing platform at CSEM has expanded its capacity by increasing the number of tests available for validating internally developed technologies and offering these services to external clients. Established in 2024 within the Solar Module Innovation Hub in Hauteville, the Reliability Testing Laboratory (RTLab) consolidates all the solar module testing equipment of the BU-V.

The reliability of photovoltaic (PV) modules is a critical factor in the widespread adoption of solar energy. As the demand for renewable energy sources grows, ensuring the long-term performance and durability of PV systems becomes increasingly important. Recent advancements in testing standards published by IEC TC82 have introduced more comprehensive methods to assess PV module reliability. These new standards emphasize the importance of sequential and combined accelerated stress tests, which are designed to simulate real-world conditions more accurately than traditional single-factor tests. Moreover, the reliability testing process proposed by the new standards spans from materials to complete modules. This holistic approach ensures that each component, from individual materials to the assembled module, meets stringent reliability criteria.

At CSEM, we conduct comprehensive reliability testing of PV modules and materials, serving both internal development projects and external clients. For internal development, we utilize advanced testing protocols to identify potential failure modes of innovative and improved PV developed by all the groups of the BU-V. For external clients, we offer rigorous testing services for commercial PV modules, providing detailed performance and reliability data that help manufacturers and investors make informed decisions. Particular attention is being given to advancements in new cell technology, polymer materials, and the adaptation to increased module dimensions (up to 2.4 m × 1.3 m).

Since Q1 of 2024, a new Reliability Testing Laboratory (RTLab) has been created at the Solar Module Innovation Hub consolidating all the BU-V reliability testing equipment able to handle a wide range of tests, from material-level assessments to full module evaluations (Figure 1):

- ACS WZH16: 16'000l walk-in climatic chamber performing (24/7) thermal cycling test (-40°C to +85°C) of materials samples and big modules,
- WEISS WK-2500/+20-S: 2'500l climatic chamber performing (24/7) damp heat test (+85°C/85%RH) of materials samples and standard modules and (on demand) potential induced degradation,
- WEISS WK-2500/60-S: 2'500l climatic chamber performing (on demand), humidity freeze test (-40°C to +85°C/85%RH), creepage test (up to 105°C), bypass diode test (1.4Isc and 105°C), light and elevated temperature induced degradation test, cold and dry hot conditioning of standard modules,
- ATLAS SEC 1100: 1'100l environmental chamber for combined accelerated stress tests (temperature, humidity and light) of materials samples and small modules,
- Dr. Hönele steady state solar simulator for UV preconditioning test of material samples and big modules,
- HARREXCO ML 10/11: mechanical load tester (up to +/-8'000 Pa) for standard modules,

- Q-Lab QUV weathering tester for accelerated test of materials with UV light source,
- Q-LAB QSUN: weathering tester for accelerated test of materials with xenon light source.



Figure 1: RLT Lab equipment: (a) ACS WZH16 walk-in chamber; (b) WEISS WK-2500 climatic chambers; (c) ATLAS SEC1100 environmental chamber; (d) Dr. Hönele steady state solar simulator; (e) HARREXCO ML 10/11: mechanical load tester; (f) Q-Lab QUV weathering testers; (g) Q-LAB QSUN: weathering tester.

The RLT Lab's capacity is set to expand significantly in the near future, with the following new equipment already planned for integration:

- Walk-in climatic chambers to perform (24/7) damp heat test of big modules,
- Class A steady state solar simulator for light soaking test of tandem Si/perovskite modules,
- Mechanical load tester for static and dynamic load test of big modules,
- Hail tester to shoot ice bowls with a diameter up to 50 mm.

New Enhancements of CSEM's Internal LCA Tool for Photovoltaic Systems

S. Kandiyoti-Eskanazi, A. Barrou, J. Levrat, G. Cattaneo, M. Despeisse, C. Ballif, B. Paviet-Salomon

CSEM has developed a user-friendly tool to automate Life Cycle Assessment (LCA) for photovoltaic (PV) systems, providing fast and standardized results on the environmental impacts of PV products. The tool's application in European and industrial projects underscored the need for enhanced eco-design strategies and effective communication of environmental impacts. This challenge was addressed by implementing automatic report generation and a comparison interface for different PV module materials. These features facilitate significant eco-design improvements, fostering the development of more sustainable products for CSEM and its partners, while enhancing the transparency of environmental impact reporting.

Life Cycle Assessment (LCA) is a critical methodology for assessing the environmental footprint of energy production devices like photovoltaic (PV) systems. It supports the development of eco-design strategies, such as extending the lifetime of products or optimizing materials to reduce environmental impacts [1]. While LCA offers numerous benefits, the traditional approach remains time-consuming and requires specialized expertise. To overcome this challenge, CSEM developed a user-friendly internal tool connected to its PV module database that automatizes LCA of PV systems and does not require any LCA expertise for the user. Since its creation, the LCA tool has been used as the main resource to treat customers' requests and has recently undergone several improvements.

Automatic LCA report generation

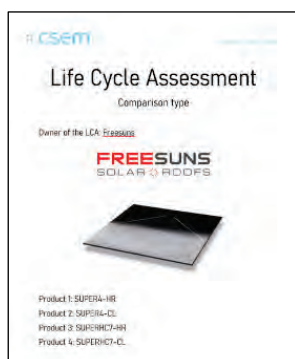


Figure 1: CSEM automatic LCA report illustration (cover page).

An automatic reporting system based on the LCA tool was implemented to provide high-quality and efficient reporting for customers. The report (Figure 1) includes various sections, such as product information (description, datasheet, Bill of Material (BOM), and weight), Life Cycle Assessment hypotheses, and scenarios considered, as well as the results. An accompanying

Excel sheet provides detailed information, allowing for effective communication of the environmental impact of PV products developed by CSEM and its partners.

Enhanced eco-design of PV modules

The eco-design potential of PV modules with the LCA tool has increased with the inclusion of new materials from external sources, such as Environmental Product Declarations (EPDs) [2] or LCAs, combined with a new specific user interface to compare the environmental impacts of raw materials used for PV systems.

Case study: solar tiles vs clay tiles & PV modules

CSEM conducted a comparative LCA study for Freesuns' [3] products using LCA tool recent developments. This study compares 2 different construction scenarios: Freesuns' solar tiles versus conventional roof tiles combined with PV modules. The goal of this study is: i) to compare the environmental impact of 4 Freesuns product and suggest eco-design strategies to reduce those impacts; ii) evaluate the benefits (or burden) of

implementing solar tiles versus constructing a conventional roof with clay tiles, a mounting structure and PV modules.

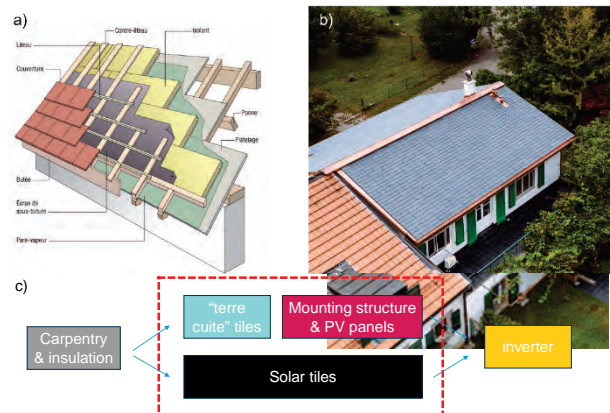


Figure 2: a) Illustration of conventional roof structure; b) Freesuns solar tiles case study (Avully, CH); c) System boundaries for the LCA study.

For this study, the functional unit (FU) is defined as the weather protection of a 130 m² roof, combined with electricity production capacity of 18.23 kWc over a 30-year period in the location of Avully (GE). The study sets specific boundaries from cradle-to-gate (Figure 2), i.e. from raw materials extractions to installation (excluding use phase and end-of-life). Furthermore, carpentry, insulation and inverters are excluded from the analysis, as they are assumed to be the same for both systems.

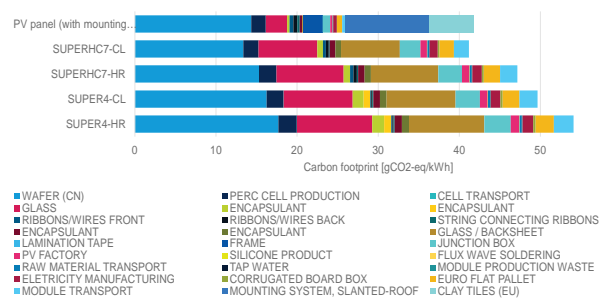


Figure 3: Carbon footprint of solar tiles vs PV module [gCO₂-eq/kWh].

Overall, PV modules combined with mounting structure and clay tiles represent a carbon footprint close to the best Freesuns' solar tile, whose impact is dominated by the glass (Figure 3). In addition, recent Freesuns' solar tiles show better carbon footprint than older tiles mainly due to higher number of cells (with reduced thickness and higher efficiency) present in a tile. Such insights allow to eco-design future products, eventually reducing their environmental impacts. In conclusion, the enhancements to CSEM's internal LCA tool streamline the assessment process for PV systems and provide valuable eco-design insights, supporting CSEM's commitment to sustainable product development in renewable energies.

[1] Muteri, et al., Review on LCA of Solar Photovoltaic Panels (2020).

[2] <https://www.environdec.com/home>

[3] <https://freesuns.com/fr/>

Tunnel IBC HJT Cell Technology Integrated in Modules

J. Champliaud, J. Zhao, H. Li, L. Baume, L. Marthey, N. Badel, L. Perla, O. Arriaga Arruti, T. Auderset, J. Escarré, J. Levrat, M. Roten, S. Pittet, B. Bonnet-Eymard, M. Despeisse, C. Ballif, P. Papet •, R. Grischke •, T. Kössler •, L. Vuithier •, L. Barraud •, D. Baetzner •, W. Frammelsberger •, N. Holm •, C. Carroubi •, R. Kramer •, B. Legradic •, M. Pujol •, D. Lachenal •

The development of "Tunnel IBC HJT" solar cell technology addresses the limitations of standard HJT cells and meets the growing market demands. By combining the benefits of heterojunction (HJT) cells with an interdigitated back contact (IBC) design, this technology achieves superior efficiency, exceeding 25%. This improvement is crucial for making solar cells more competitive and accessible. With reduced manufacturing costs and increased module durability, this technology enables the production of more cost-effective and sustainable solar solutions, serving both current and future market needs.

IBC projects, involving Meyer Burger companies and CSEM, aim to pre-industrialize this new high-efficiency back-contact photovoltaic cell technology (Tunnel IBC HJT) before scaling up to gigawatt production. The back-contacted crystalline silicon solar cell with passivating contacts featuring an interband tunnel junction at its electron-collecting contacts. In this novel architecture, both the hole collector patterning and its alignment to the electron collector are eliminated, thus drastically simplifying the process flow. This technology, already achieving 25.4% efficiency in the lab, boasts a simple 10-step manufacturing process. Protected by multiple patents, IBC projects seek to validate key industrialization elements, from setting up a pilot line to producing and evaluating next-gen modules. The industrialization of this technology was founded by two projects: Sirius, founded by the Swiss Federal Office of Energy and Pilatus, founded by the European Commission within the Horizon program. The goals of these projects are:

- Reducing manufacturing cost (silver down to 3.3 mg/W), making it competitive with dominant technologies (HJT, PERC and TOPCon).
- Establishing a Bill of Materials (BoM) ensuring exceptional reliability beyond 30 years.
- Demonstrating industrial modules with over 400W power.

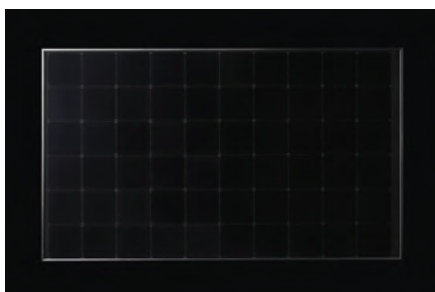


Figure 1: Full size industrial product done with Tunnel IBC HJT cells in the BoM define by CSEM.

The development of IBC technology in photovoltaic modules has seen significant advancements through a close collaboration between CSEM and Meyer Burger. This partnership has focused on both cell and module aspects, leading to the establishment of a manufacturing line for modules utilizing this technology.

This close collaboration has enabled the projects' teams to swiftly address various challenges, achieving high reliability results in climatic chambers. The developments have led to exceptional

results, exceeding requirements and achieving incredible reliability durations, like more than 5 times the requirements.

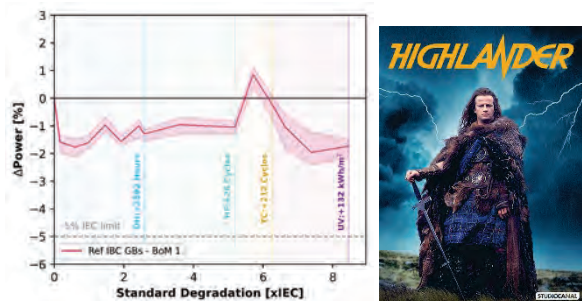


Figure 2: Graph that shown the incredible high reliability of the IBC "Highlander" modules under sequence of several indoor tests.

Furthermore, the production costs associated with these modules were reduced, making this technology competitive with other technologies on the market.

The successful implementation of IBC technology in modules not only demonstrate CSEM's commitment to innovation but also highlights the importance of strategic partnerships in advancing renewable energy solutions. By continuously improving the reliability and efficiency of our products, we are contributing to a more sustainable future while maintaining a competitive edge in the market.

In the IBC projects specialized modules were also developed for building integration and lightweight, modules for electric and solar mobility, expanding the high-performance PV market for specific applications.

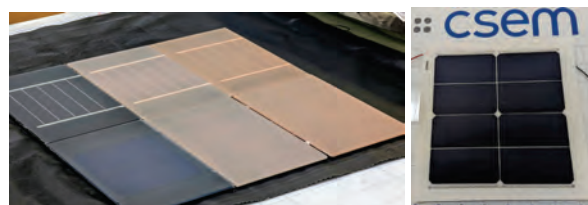


Figure 3: (left) Picture of solar tiles using standard PERC technology compared to Tunnel IBC HJT technology; (right) Picture of lightweight module with IBC cells integrated inside reaching high reliability in extended test.

In conclusion, the collaboration with Meyer Burger has been pivotal in the development and industrialization of IBC technology in photovoltaic modules. Our joint efforts have resulted in high-performance, reliable, and cost-effective solutions that stand out in the competitive landscape of solar technologies.

• Meyer Burger

Solar-powered Balloons: Crossing the Atlantic with the Force of the Winds

P. Duvoisin, H. Li, A. Faes, X. Bulliard, C. Charrière, D. Petri, Olatz Arriaga Arruti, T. Auderset, N. Badel, L. Baume, G. Cattaneo, J. Champliaud, J. Escarré, J. Levrat, L. Marthey, P. Mermet, F. Mujovi, S. Pittet, M. Roten, B. Bonnet-Eymard, M. Despeisse, C. Ballif, J.-M. Nicot •, J.-N. Valdivia •, F. Henault ••, X. Soors •, C.-A. Chevrier •, F. Harmand •, C. Hourtolle •, M. Clavery •, B. Regnier •, N. Bray •, F. Mirc •, S. Louvel •, V. Dubourg •

In collaboration with the French space agency CNES, CSEM has developed a groundbreaking deployable solar charging system. Successfully tested at altitudes up to 40 km, the system powered the first transatlantic flight of a CNES zero pressure balloon in June 2024, significantly enhancing energy autonomy and reducing the need for onboard batteries, thus marking a new milestone in high-altitude scientific missions.

High-altitude balloons are essential for scientific and technological exploration in the stratosphere, but they face significant energy challenges. In collaboration with the French space agency CNES, CSEM has developed a unique solar charging system that integrates robust, high-performing photovoltaic (PV) solar panels into the gondolas of these balloons. This system features also a deployable solar array that allows for reuse across multiple missions. This innovative design of folding the panels into a protective box during take-off and landing ensures their durability and reusability, thereby saving costs.

Developing such a solution required overcoming the harsh conditions of the stratosphere, including high UV radiation and extreme temperature fluctuations, all while maintaining very low weight. To address these challenges, CSEM developed a specialized encapsulating resin on its polymer platform, capable of withstanding these extreme conditions. This resin, combined with carbon fiber structures to reinforce the elements, results in a weight of just 9 grams per watt. This advancement not only enhances the performance and longevity of high-altitude balloon missions but also aligns with sustainability goals by reducing waste and costs.



Figure 1. Extrusion pilot line of CSEM.

The system was successfully tested at altitudes up to 40 km in 2023, as shown in picture 2. In 2024, CNES achieved the first transatlantic flight of a zero-pressure balloon using the 6 m² deployable solar system developed and fabricated at CSEM. This remarkable flight lasted nearly four days. To accomplish its mission, the balloon, with a total mass of 2.9 tonnes and a volume of 800,000 m³, filled with helium, ascended with its gondola to an altitude of about 40 km for the entire duration of the flight. It travelled over Sweden, Norway, Greenland, and Canada.

The flight was organized around the summer solstice at a high latitude, allowing the balloon to benefit from continuous sunlight to maintain a constant altitude. The CSEM deployable solar system successfully powered several measuring instruments, significantly reducing the need for onboard batteries. This innovative system not only proved its ability to support long-duration flights but also showcased its potential to improve the efficiency and sustainability of high-altitude scientific missions. Additionally, it is fully reusable and thus environmentally friendly.



Figure 2: (Top) Picture of a zero-pressure stratospheric balloon from CNES. CNES 2021 (Bottom) Deployment of the Azimuth Deployment and Orientation Mechanism during a flight at 40 km altitude. © CNES 2023.

This flight marks a new milestone for high altitude balloons and enables CNES to envision a new type of service.

Source: Succès du vol du ballon « Transat » opéré par le CNES, <https://cnes.fr/communiques/succes-vol-ballon-transat-opere-cnes>

• CNES

•• ALTEO Industries

SolarTiles to Cover any Surface from Complex to Heritage Protected Roofs

G. Cattaneo, J. Levrat, M. Roten, M. Despeisse, J. Morello •, M. Olesen •, D. Learoyd •

Photovoltaic installations have a key role to play in the energy transition. As part of the Frees'tile project, CSEM and Freesuns have joined forces to develop a new generation of efficient and reliable solar tiles, allowing the complete coverage of roofs, even those of protected buildings. The research activities were conducted at CSEM Solar Module Innovation Hub laboratories.

Photovoltaic panels are typically available as black rectangles of approximately 1-1.3 m by 1.7-2.4 m, which can be affixed to the roof structure of a building or integrated directly as a structural element of the roof (Building Integrated Photovoltaics - BIPV). However, the unit dimensions are sometimes incompatible with buildings with complex shapes, not allowing for complete and uniform coverage of the surface. Various innovative solutions have been developed to make it possible to produce solar modules in various shapes, sizes and colours that can replace standard tiles in a roof leading to the new concept of solar tiles. With the aim of providing a photovoltaic function to the roofs, the company Freesuns created its first solar tile in 2015. Since then, numerous innovation opportunities were shared between this company and the CSEM (Figure 1).



Figure 1: Solar tiles of various terracotta colours, were integrated into the roof of the old Ferlens (left). Collège des Parcs in Neuchâtel, slated for completion in 2025, now featuring a dynamic solar-tiled roof (right).

The project "Frees'tile" – an innovation project supported by Innosuisse from 2022 to 2024 – was carried out with the objective of improving the performance of the solar tiles while maintaining high reliability and great freedom of integration compatibility with roof covering techniques.

In recent years, changes in cell technology in mass production have indeed taken place (Al-BSF first and PERC technologies later), and the next ones are in progress (TOPCon, HJT, or even "back contact" technologies). In addition, the cell format has also been modified to increase the power of the modules and lower the costs per installed W. Thus, after years of producing M2-sized cells (156.75 mm × 156.75 mm), larger solar cells M6 (166 mm × 166 mm) appeared on the market. These cells are now already being phased out in favor of the M10 (182 mm × 182 mm) and G12 (210 mm × 210 mm) cells. The new generation of solar tiles developed within the project is based on seven half-M10 solar cells (Figure 2).

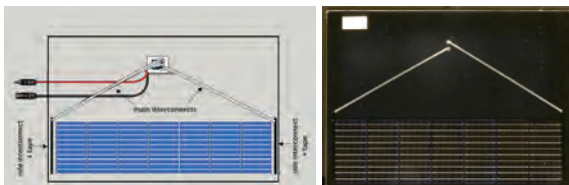


Figure 2: New generation of solar tiles developed within the Frees'tile project based on 7 half-M10 solar cells.

Thanks to this new design, the installed power density of a roof equipped with classic-looking Freesuns solar tiles has increased from 150 W/m² to 172 W/m², which corresponds to a performance gain of 14.6%, with a limited increase in the manufacturing cost per tile. Since these new tiles are slightly higher, this development has made it possible to achieve a reduction of around 15% in the cost per m² of solar tiles.

When changing the design, cell type, interconnection or technology of a photovoltaic module, extensive and iterative work to optimize materials and manufacturing processes is necessary to ensure long-term reliability of the modules and minimal loss of efficiency. This is why CSEM has created the Solar Module Innovation Hub (SMIH) in Neuchâtel for reliability testing and characterization of photovoltaic modules (Figure 3). In SMIH laboratories, the tests required for IEC 61215 and IEC 61730 standards, as well as more intensive, combined and sequential tests can be performed with the aim to accelerate degradation mechanisms and thus detect performance loss phenomena that could be observed in the installation only after decades.



Figure 3: The CSEM PV Module Innovation hub has various test systems, including climatic chambers (left), and facilities for performing mechanical tests (right).

The new Freesuns solar tiles were tested for thousands of hours in damp heat conditions (85°C, with 85% humidity), stressed with hundreds of thermal cycles (from -40°C to +85°C, and even 105°C), and exposed to intense and prolonged UV irradiation (hundreds of kWh/m²) to prove its ability to withstand environmental stress factors. Then, the bypass diodes were stressed with high temperature/high current to analyze the sensitivity of the tiles to hot spot phenomena occurring in the event of partial shading of the installation. In addition, advanced mechanical tests were performed, including static mechanical load tests with applied downward pressure up to 8000 Pa (equipment limit). The solar tile power was measured before and after all the degradation acceleration tests, demonstrating, after the optimizations, a perfect preservation of the performances. Electroluminescence tests also confirmed the absence of internal damage that could subsequently lead to performance degradation, thus validating the high reliability of the tiles developed.

• Freesuns

Solar-powered Van around Switzerland

A. Faes, P. Boilat •, K. Nicolet •, M. Despeisse, B. Bonnet-Eymard, C. Ballif, C. Wutrich ••, T. Wyss *

CSEM has developed, in collaboration with EPFL PV-Lab, glass-free, lightweight and hail resistant photovoltaics (PV) modules to be implemented on an electric-retrofitted van. The expandable and orientable PV structure enables to produce more than 5 kW and enough daily energy to drive up to 185 km. The sandwich structure and fixation point have been tested and simulated by finite element modelling (FEM) to reduce the deflection of the PV module due to wind load during driving or due to snow load. The results of the modelling were implemented in the Soleva solar roof.

The goal from Soleva association is to demonstrate a 100% autonomous solar-powered van as traffic is emitting more than a third of the CO₂ emission in Switzerland (value for 2023). In 2021, Soleva was created and started the electric conversion of a Peugeot J9 diesel van. For the solarization, the team naturally contacted CSEM to get the right photovoltaic (PV) technology implemented on the van roof and in particular for the extendable and tilttable structure to optimize the sunlight capture (Figure 1).



Figure 1: Soleva van with open and tilted photovoltaic assembly.

In collaboration with EPFL PV-lab, CSEM developed and adapted to vehicle integration the crystalline silicon PV modules passing hail test and using a sandwich composite as a rigid backsheet. To design the correct dimension and fixation of the composite PV module, simple 4-bars bending test have been done to extract the mechanical properties (i.e. stiffness) of the sandwich materials (see Figure 2).

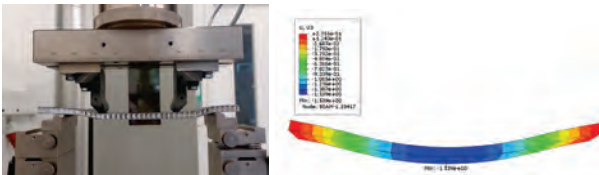


Figure 2: (left) 4-bars bending test on a sandwich composite material and (right) finite element modeling (FEM) of the 4-bars bending test.

Composite nut fixation was glued on the composite backplane and validated during tensile test load as shown in Figure 3. The maximal strength was set to 1000 N per fixation point. The observation of the fracture demonstrated an adhesive failure between the glue and the backside of the PV module (Figure 3).

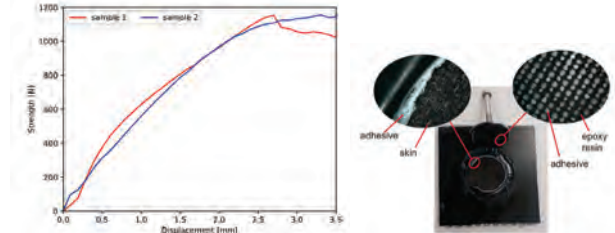


Figure 3: (left) Tensile test measurement graph on a glued fixation on the PV module backside and (right) sample image after the testing.

To optimize the number of fixation points, FEM analyses have been conducted using a 3D model and final positioning are shown in Figure 4.



Figure 4: (left) Modeling of the mechanical load test of the final PV module and (right) location of the fixation point on the final PV module.

Validation of the modeling has been done experimentally as shown in Figure 5. The compression test fit well the model, whereas the traction test deviate from the model as the test bench fixing system in wood was moving (see Figure 5-left).

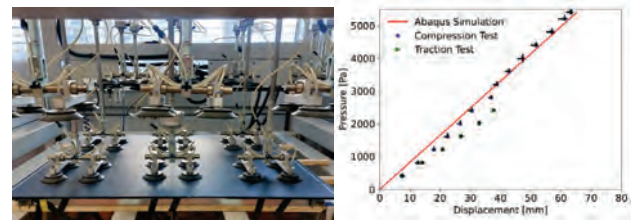


Figure 5: (left) Picture during the mechanical load test of the final PV module and (right) result of the displacement versus applied pressure.

These rigid modules have been implemented on the Soleva van and act as an active and protective layer for the semi-flexible commercial PV modules underneath. When driving the PV system is closed and horizontal, but still producing up to 1'350 W of electricity for the motor. When the van is stopped the 12 extra modules are sliding out and all 16 modules are tilted to convert sunlight into electricity up to 5'100 W.

Last summer, the Soleva team demonstrated that 100% of solar mobility is possible and drove around Switzerland from Lausanne to Sion, Zurich, Davos and Lugano to promote sustainable mobility to a wide audience.

• EPFL

•• Soleva

Vehicle Integrated Photovoltaics (VIPV)

A. Faes, G. Cattaneo, K. Nicolet, J. Levrat, F. Mujovi, B. Bonnet-Eymard, M. Despeisse, C. Ballif, C. Michalowski^{*}, H. Martins^{**}, J. Robin^{*}

As part of the PhotoVoltaic Automotive Body (PVAB) and SFOE SolarBody projects, CSEM, in collaboration with Stellantis, Simoldes, and CEiiA, has developed an innovative lightweight module with a robust, thick polymeric front sheet designed for vehicle integration. Recognizing the significance of aerodynamics for vehicle efficiency and the aesthetic requirements of the automotive industry, CSEM evaluated the feasibility of embedding solar cells within a curved, lightweight, highly durable, and impact-resistant laminate. In the project's final phase, Simoldes integrated this technology into a solar roof for the Citroën AMI and a semi-transparent active rear window for the Peugeot 508, demonstrating the broad applicability of this technology.

Key developments include the successful encapsulation of crystalline silicon back-contacted cells within a robust polymeric laminate that can withstand substantial mechanical stress and impact. The bill-of-materials and the interconnection have been optimized to improve the vehicle integrated photovoltaic (VIPV) element, the (TC) between -40°C to +85°C with minimal degradation, thus meeting over 15-times IEC 61215 standards in term on TC (see Figure 1).

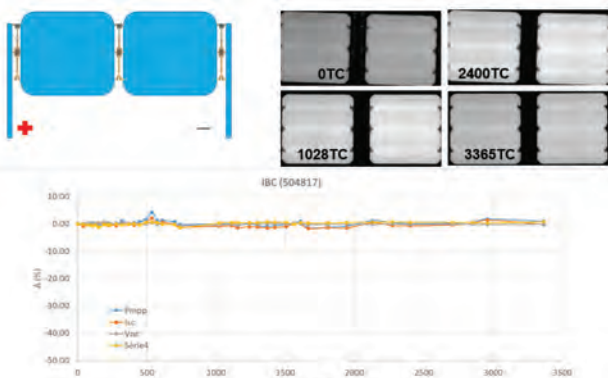


Figure 1: (top left) Scheme of the VIPV mini-module (top right) electroluminescence imaging during the testing (bottom) highly stable electrical parameter during the thermo-cycles.

HETSIM software from CSEM shows that the integration of the 140 W PV roof on the Citroën AMI could extend the driving range by more than 1'800 km annually in Paris and more than 2'700 km in Sevilla, based on the actual car consumption of 8 kWh/100km (see Figure 2).

Glass-free solar roof range extension:
+1'800 km/year in Paris
+2'700 km/year in Sevilla



Figure 2: Glass-free VIPV roof integrated on the Citroën AMI car.

^{*} Stellantis
^{**} CEiiA

Further, a fully polymer-coated exterior on a sedan (see Figure 3) could theoretically support a PV system up to 1.26 kW. Considering a contained vehicle consumption of 14 kWh/100km, it could potentially add over 7'000 km per year in Paris and exceed 10'000 km in Sevilla.



Figure 3: Peugeot 508 fully covered with VIPV element (artist view).

By placing the solar cells in a chessboard-like manner, the transparency is about 50%, comfortable enough to be used as a rear window of a car when properly supplemented by a rear camera. The demonstration of such PV module design has been demonstrated on a Peugeot 508 and is presented in Figure 4.



Figure 4: Semi-transparent rear window made of back-contacted cells arranged in a chessboard design.

In conclusion, this collaboration highlights the feasibility of integrating advanced PV systems into mass-produced vehicles, potentially transforming automotive design and energy efficiency in line with sustainable mobility goals. Future work will include further testing, optimization of the polymer materials, and development of a production line for industrial-scale manufacturing of these novel VIPV systems.

More details on the projects can be found under the link: <https://www.youtube.com/watch?v=az78MDbfXjk>

* Simoldes

Integrating Satellite Imagery and Spatiotemporal Graph Neural Networks for Enhanced Day-ahead Solar Irradiance Forecasting

J. Simeunović, C. Tissier, B. Schubnel, R. Carrillo, P.-J. Alet

Accurate irradiance and solar power forecasting is crucial for integration of renewable energy sources into the power grid. Data-driven solutions that rely solely on data from a network of ground-based sensors have shown state-of-the-art results for intra-day irradiance forecasting. Extending forecasts to day-ahead horizon entails providing additional information on cloud dynamics and a wider spatial context. Thus, CSEM has developed a data-driven model for day-ahead irradiance forecasting that exploits data from both ground-based irradiance sensors and satellite images.

Integrating large amounts of solar power sources into the existing power grid represents a major challenge due to their variability. Solar power depends on local weather conditions and cloud dynamics. CSEM has developed a forecasting solution that only relies on a network of ground-based sensors to forecast irradiance at any location in Switzerland for horizons up to six hours ahead^[1]. However, there are many applications like day-ahead markets, power system operations, or unit commitment that require longer forecasting horizons e.g., 24-72h ahead. To extend the forecasting horizon, a larger spatial context is needed. Thus, mixing the wider spatial context from satellite images and the local information from ground-based stations is a natural extension.

We introduce a data-driven model that leverages both ground-based measured irradiance data and satellite images of clouds for a day-ahead multi-site irradiance forecasting, coined MultiCrossVivit. The developed model extends the work of Boussif *et al.*^[2] for single site irradiance forecasts. MultiCrossVivit model exploits information extracted from satellite data and combines it with information from the time-series data from multiple sites using graph-attention neural networks; see Figure 1. The first part of the MultiCrossVivit model is used to analyze the spatiotemporal context of satellite images. In parallel, the model analyzes the temporal and spatial correlations between different stations, extracting the meaningful relationships between the time-series irradiance data. Finally, the last block uses attention mechanisms to fuse information from the previous blocks and find relations between satellite images and irradiance time series to make irradiance forecasts for up to 24 h ahead with a temporal resolution of 15 minutes.

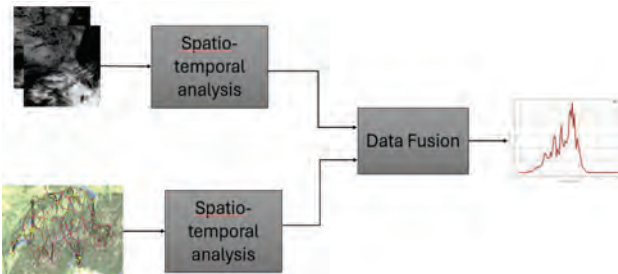


Figure 1: MultiCrossVivit model with spatiotemporal analysis blocks and data fusion of satellite and time-series data.

To test the capabilities of MultiCrossVivit, a model was trained on 3 years of data (2021-2023) and evaluated on a dataset comprising the first seven months of 2024. MultiCrossVivit was

[1] Carrillo, R., Schubnel, B., Langou, R., Alet, P.-J., Dynamic graph machine learning for multi-site solar forecasting, EUPVSEC 2023.

trained on ten stations across Switzerland using that irradiance dataset and on the satellite images dataset. These two datasets have different time resolutions: one hour for the satellite data, and 15 minutes for the irradiance time series.

The results on Figure 2 show the normalized root mean squared error (NRMSE) of the MultiCrossVivit model for 24 hours ahead with a 15-minute resolution. After the first six hours, the error slope goes down and reaches near zero for longer-term forecasts.

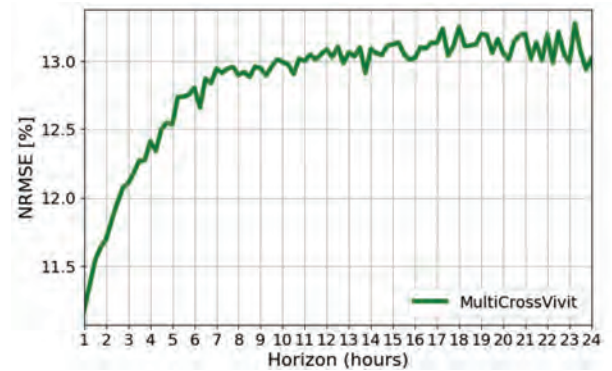


Figure 2: NRMSE of MultiCrossVivit model for a forecasting horizon of 24 hours ahead with a 15-minute resolution.

We analyzed the forecasts made at specific location for the forecasting horizon of 24 hours ahead. The example on Figure 3 shows a variable day with intermittent drops in radiation, which is particularly challenging for forecasting models. MultiCrossVivit captures the overall trend of the ground truth data.

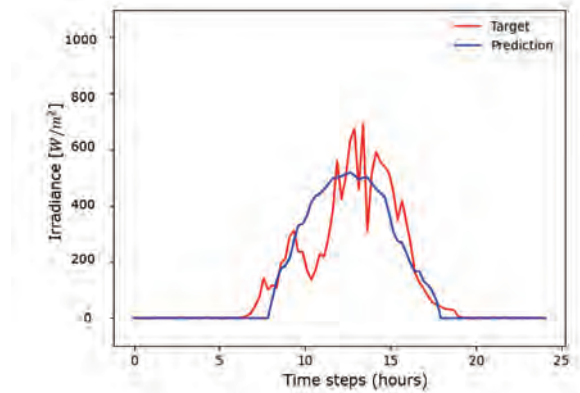


Figure 3: MultiCrossVivit model prediction and ground truth values compared for 24 hours ahead forecasting horizon.

[2] Boussif, O., Boukachab, G., Assouline, D., Massaroli, S., Yuan, T., Benabbou, L., Bengio, Y., Improving* day-ahead Solar Irradiance Time Series Forecasting by Leveraging Spatio-Temporal Context, NIPS 2023.

Unsupervised Anomaly Detection for Commercial Refrigeration Systems using Language Models

B. Schubnel, D. Achi, R. Langou, P.-J. Alet

Refrigeration systems are significant energy consumers that account for 30 to 50% of the total electricity consumption in supermarkets and food stores [1]. This substantial energy usage is due to the continuous operation required to maintain fridge temperatures at the adequate level for the perishable goods. AMICOOL, an Innosuisse project between CSEM and DIGITEL, a Swiss company providing cooling regulation systems for commercial stores and industrial facilities, aims at reducing the total operation costs of commercial refrigeration systems through data-driven monitoring, anomaly detection, recommendations, and optimization of entire refrigeration installations.

The Innosuisse project AMICOOL targets reduction of 20% of electricity consumption from refrigeration systems in commercial stores. This represents significant potential energy and cost savings, as middle-size food stores in Switzerland typically spend around 20 kCHF per year for their electricity bill, the main electricity consumers being refrigeration systems and HVAC systems [1]. We report here on the technical part of the project related to anomaly detection on refrigeration systems.

The anomaly detection tool developed in the project aims to flag anomalous behavior in refrigeration units and at central level (compressors), and to infer potential root cause of the misbehavior. The aim is to report to technical teams (refrigeration specialists) and to food store owners the issues that cause anomalous behavior in the refrigeration system and lead to cooling losses and energy overconsumption. Typical issues encountered in refrigeration units are open doors (doors left open by clients or personnel), blocked or broken fans (including frozen ones), blocked electronic expansion valves, badly tuned PID controllers, air flow obstruction by misplaced goods, ice formation on the evaporator, refrigerant leakage and under sizing of the cooling units (leading to insufficient cooling capacity). At central level (compressors), failures are rare but potentially much more impactful for operation. They include compressor oil issues (leakage, oil degradation), overpressure, mechanical components failures, and control system malfunction.

One challenge encountered in the AMICOOL project was to design an anomaly detection model that can, in a zero-shot setting, adapt to any new installation without retraining. Indeed, every middle-sized food store in Switzerland has around 50 controlled refrigeration units, and it would be unreasonable to create and train single models for each unit. Another major challenge encountered in the project is the absence of labelled anomaly data from standard refrigeration units. Finally, refrigeration units are open systems. Customers and staff constantly interact with them to add, check or pick goods. As a result, refrigeration systems are far from ideal, "isolated" systems for which changes of behavior can only mean degradation or failure.

To solve these challenges, CSEM has implemented a deep-learning solution based on the latest developments in anomaly detection on multivariate timeseries. The algorithm is based on middle size language models, that have proven their ability to be zero or few-shots learners. This learning relies on careful partial fine-tuning of time-series data. The algorithm is capable of:

- reproducing the expected behaviour of the different sensors of refrigeration units and compressors;
- quantifying the uncertainty on this behaviour through confidence intervals;
- adapting directly to any new refrigeration unit and compressor, even if unseen during training. The main ingredient for this adaptation is a very careful normalization of the time series;
- segmenting and classifying the multivariate time series data once labels are provided. The labels can be binary to encode the presence of anomalies, or categorical to describe root causes.

A cloud-based web interface has been implemented by DIGITEL in coordination with CSEM. With this interface, users can follow overconsumption patterns due to anomalous behavior and visualize anomalies. In the first version available to clients, the algorithm only relies on unsupervised anomaly detection, where the criterion for detection is that observed measurements are outside the uncertainty bounds of the model.

Anomaly root cause allocation is currently based on expert knowledge from technicians via decision trees but can be easily switched on to automatic classification by the model once more extensive labels are available.

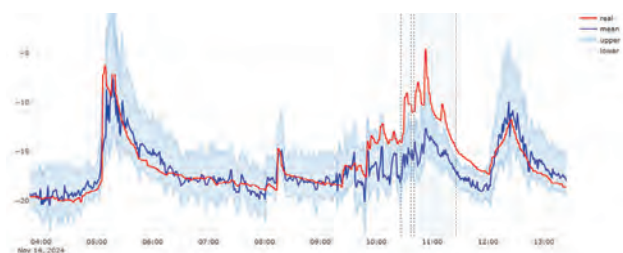


Figure 1: Example of time series reconstruction with uncertainty bounds and anomaly flagging from a cold chamber in a commercial store. The first and last peaks are not flagged as they correspond to programmed defrosting events and are parts of regular operation.

The anomaly detection algorithm has been tuned on artificially generated problems by DIGITEL on untrained stores (data not seen during training) and had a F1-score of 0.9. A higher F1-score is expected when a more supervised approach with (partial) labels become available.

[1] EIA, 2018 CBECS: Principal Building Activities Food Sales, U.S. Energy Information Administration. [Online]. Available: <https://www.eia.gov/consumption/commercial/pba/food-sales.php>

Detection of Crack Patterns to Increase the Yield of Solar Module Production

B. Schubnel, R. Langou, C. Tissier

The PILATUS project aims at advancing the production of highly efficient photovoltaic (PV) technologies within Europe using silicon heterojunction tunnel-interdigitated back-contact (SHJ-IBC) technology. Process issues early in the production chain can cause unnecessary yield loss. To address this issue, CSEM has developed a predictive maintenance solution that detects crack patterns in the module pilot line. The software was installed on one of Meyer Burger's stringers where it has correctly identified most crack patterns and their corresponding root cause.

Photovoltaic (PV) power generation is pivotal in the transition to a clean energy system and the achievement of the zero-emissions target. To help the EU PV manufacturing industry succeed in the competitive global market the PILATUS project was born. With the demonstration of three digitalised pilot lines for the production in Europe of silicon wafers, solar cells, and solar modules, PILATUS aims to contribute to re-building a leading-edge, competitive PV industry with the entire value chain in Europe.

The pilot solar module production operates at a high throughput of 2'500 cells per hour or more. At this scale, handling and interconnecting thin solar cells can lead to cracking and misalignment, which can be incompatible with the target quality levels. To address these risks, a predictive maintenance and process control algorithm is employed to enhance precision and reduce defects at the level of the cell connecting station (CSS) level. The CCS is equipped with a camera that detects cracks and provides their type, location, and dimension. The tools developed by CSEM access the cracks position and classes from this camera. For implementation and offline testing, Meyer Burger extracted camera data from its manufacturing execution system (MES). For production, the developed solution directly accesses the MES database. It can be deployed on any production line with little fine-tuning needs.

The algorithm analyses camera data for systematic patterns in the location and repetition of occurring crack classes. As individual patterns can be linked to specific machine components, the root cause analysis is automated and feedback for predictive maintenance is provided to the operator on a short call. Furthermore, this tool enables one operator to simultaneously monitor multiple machines on their error-free operation, leading to reduced production costs. Malfunctions are detected immediately, product quality is increased, and the amount of scrap modules is drastically reduced.

The logic of the main algorithm is based on features matching and is displayed on Figure 1. After extracting the position, size and shapes of the cracks from the camera outputs, the algorithm constructs a string mask. It then extracts a feature vector from this mask that encodes the position, size, shape and repetition of the cracks. This feature vector is compared to a database of problematic features through a very fast and scalable matching algorithm. The operator is alerted when the current string feature is matched with a feature vector in the database.

Excellent results were obtained in the offline testing. The next step consisted in testing the performance of the method on live data. The PILATUS CCS software has then been installed on one of Meyer Burger's conventional (non-IBC) HJT stringers, which are used for regular module production in an R&D environment. This allowed for long-term evaluation of the software tool as every produced module was analyzed by electroluminescence imaging, thus giving direct feedback on the functionality of the algorithm.

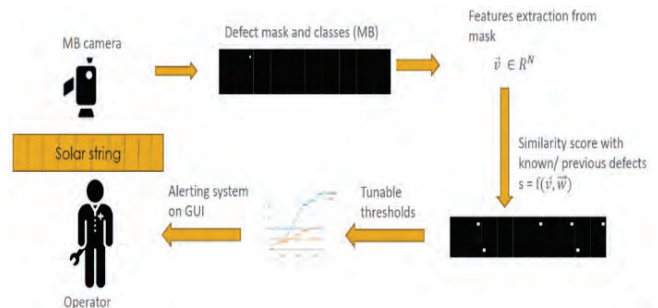


Figure 1: Logic of the Crack Pattern Algorithm.

To create quick feedback on the programmed and observed pattern detection, some machine parts were prepared to generate cell cracks at defined positions. By contaminating the surfaces of different machine parts, for example with a broken silicon part or a tip of a cut wire, crack patterns could be created with known root cause. An example of a crack pattern found on a string during the experience can be seen in Figure 2 with the associated matched pattern obtained by the algorithm in Figure 3. The software sorted all detected cell cracks into patterns, where most crack patterns were identified correctly and assigned the corresponding root cause. On reaching the pre-defined threshold, an alarm was sent to the user with an action recommendation for predictive maintenance.

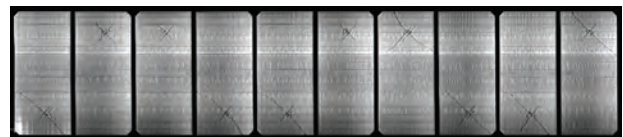


Figure 2: Camera imaging of a crack pattern caused by surface contamination of the robot cell gripper.

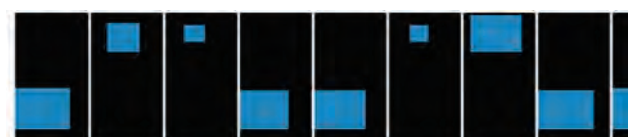


Figure 3: PILATUS CCS software result of the crack pattern caused by the robot cell gripper.

The PILATUS project is funded by the European Union under grant number 101084046. Views and opinions expressed are however those of the author(s) only and do not necessarily reflect those of the European Union. Neither the European Union nor the granting authority can be held responsible for them.

This work has received funding from the Swiss State Secretariat for Education, Research and Innovation (SERI).

Feasibility and Control of Low-temperature District Heating Network with Distributed Sources

M. Boegli, Y. Stauffer

District heating network (DHN) is a key solution for decarbonizing the building sector. While a traditional DHN requires a central heating plant and supplies high-temperature flow, an energy loop consists in a low-temperature thermal network which provides heat to buildings through heat pumps. This structure enables energy savings. Furthermore, single-pipe loops and distributed heat sources along the roads save space and increase pumping efficiency.

District heating networks (DHN) offer an interesting alternative to fossil fuels in the energy mix for heating buildings, by valorizing and optimizing the use of renewable energies. Third and fourth-generation DHN use a heat transfer fluid with a flow temperature between 80°C and 100°C and between 50 and 70°C, respectively. The later uses more climate-friendly heat production technologies, such as renewable energy, heat recovery and wasted energy, also known as anergy. However, these DHN require pre-insulated pipes and a double-pipe network to carry the fluid to the load (at higher temperature) and back (at lower temperature) (Figure 1). This results in energy efficiency losses due to high flow temperatures and heat losses in the ground, as well as a considerable footprint in the subsoil with double insulated pipes.

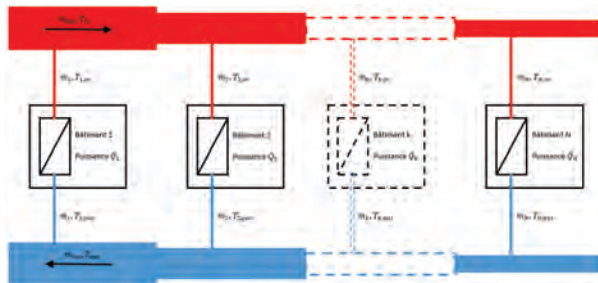


Figure 1: Two-pipes fourth-generation DHN.

In villages or district where there is insufficient space to install large heat production units and pre-insulated pipes in the roads, a fifth-generation DHN, or anergy loop, saves space and energy by using a low-temperature thermal network (between 3 and 15°C) with uninsulated monotubes which feeds buildings in series via a heat pump (HP) (Figure 2). HPs make the most of the anergy, which nonetheless provides a suitable inlet temperature to achieve a seasonal coefficient of performance (SCOP) of 3 to 5. In addition, this solution aims to mitigate the problem of the footprint of the heat source by decentralizing geothermal energy sources along the roads connecting the buildings.

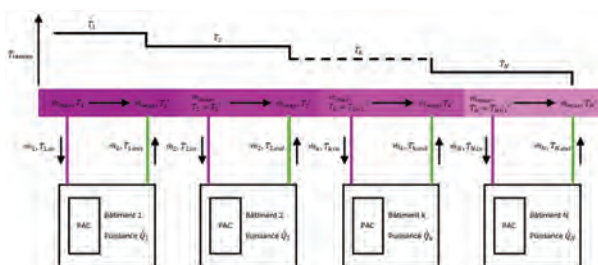


Figure 2: One-pipe 5th-generation DHN.

The ANERGYCAD pilot and demonstration project^[1] studied the feasibility of a fifth-generation monotube network with decentralized main energy sources. This decentralization relates

both to the production of heat by HPs and to the primary supply and storage of energy by geothermal probes, to be distributed between groups of buildings (Figure 3).

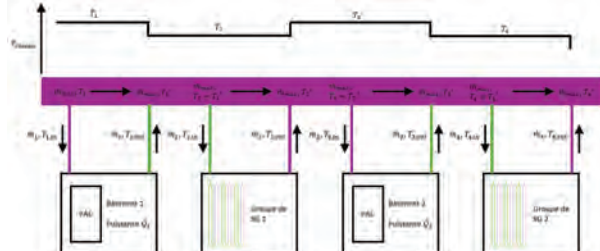


Figure 3: Single-pipe fifth-generation DHN with ground sources.

In addition, the project considered the installation of decentralized energy recovery. This equipment can regenerate the geothermal probes during the warmer months of the year while offering cooling. It can also serve as a back-up during peaks in heat demand in the colder months. Such equipment includes innovative Enerdrapé panels, which can recover heat from wastewater and parking lots, solar thermal systems, and combinations of PV and air/water HPs. This diversity makes it possible to exploit synergies by grouping "prosumers" with different need profiles.

The village of Grandvaux in Lavaux served as a case study. It has 67 buildings, with power requirements per building ranging from 10 kW to 140 kW, and an overall heat requirement of 2'300 MWh/year. The study showed that it is optimal to divide the buildings into groups of six to ten, and to connect them to the anergy loop. Groups of 8 geothermal probes are interspersed between the groups of buildings, resulting in an advantageous ratio of around one probe per building with an average requirement of 35 MWh. The energy dimensioning of the network with an optimal spatial distribution of geothermal probes used the TESSA platform^[2] by the start-up company Planeto. The numerical models developed in the study have enabled us to simulate the network and confirm its viability over 50 years, according to global warming scenarios. The thermodynamic equilibrium within the anergy loop was validated with Modelica, demonstrating the self-regulation of the coefficients of performance, and the stability of the anergy loop temperature.

If each home had its own probes, 33% more probe length would be needed to meet the same needs. A second comparison has shown that, as compared to a traditional centralized DHN, the proposed solution would use 25% fewer probes, 65% less pumping energy and 30% less electrical energy for the same building heating needs.

The project received funding from SFOE.

[1] Ström SA, Réseaux anergie avec sources primaires décentralisées, www.aramis.admin.ch/Texte/?ProjectID=53156

[2] TESSA (Thermal Energy System Simulation Assistant) Toolbox. planeto-energy.ch/solution

Towards PFAS-free Aqueous Production of Cathodes for Greener Li-ion Batteries

A. I Jaffrès, A. Ingenito

CSEM aims at developing an ecofriendly process for lithium-ion electrodes fabrication, based on fluorine-free biopolymers in aqueous systems. Such greener alternatives may allow for a cost reduction by a factor of 2–3 for the polymer and by a factor of about 100 for the processing solvent (NMP vs. water) while reducing environmental impact and facilitating recycling processes. 2 mAh/cm² aqueous-based production of LIBs cathodes realized by CSEM showed equivalent performances to the baseline PVDF/NMP ones (> 80% capacity retention after 1000 cycles of charge/discharge).

Polyvinylidene fluoride (PVDF) is a fluoropolymer commonly used as a binder for electrodes in lithium-ion batteries (LIBs) because of its chemical stability, electrochemical inertness at high voltage, effective binding properties for active materials, mechanical strength and thermal stability up to 400°C. However, as the Registration, Evaluation, Authorization and Restriction of Chemicals (REACH) regulation of the European Union has classified per- and polyfluoroalkyl substances (PFAS) as substances of high concern, the use of PVDF could be subject in the coming years to regulatory considerations from authorities regarding sustainability and environmental responsibility¹. Moreover, PVDF requires to use N-methyl pyrrolidone (NMP) as solvent, which is a highly toxic and high boiling point compound (202°C). Hence, exploring ecofriendly and cost-saving alternatives is critical for preparing cathode slurries without using NMP and PVDF. By doing so, both anode and cathode do not contain fluorine binders anymore and therefore the recycling processes could be facilitated.

Among such greener processes, the combined use of styrene butadiene rubber (SBR) and carboxymethylcellulose (CMC) as binders in water as solvent is the most representative as it has been fully established to produce graphite anodes. However, the pronounced sensitivity of cathode materials towards water leading to lithium leaching, aluminum corrosion and performances degradation has so far hindered the upscaling of aqueous fabrication processes for LIB cathodes². Moreover, the selection of new binders must include their chemical stability towards oxidation. For example, SBR is not sufficiently stable at elevated potentials (> 4.2 V / Li/Li⁺). This highlights the urgent need for new (bio)polymers to be identified to realize mechanically stable and high-mass-loading and high-voltage cathodes for LIBs. CSEM aims to prove the realization of aqueous production of cathodes with equivalent electrochemical behaviour with respect to the state-of-the-art NMP/PVDF processed ones.

For this purpose, CSEM has screened several so-called bio binders in aqueous-based cathodes slurries and evaluated the properties of the obtained electrodes in terms of aspect, homogeneity, adhesion and electrochemical performances. Environmentally friendly bio-based molecules, such as cellulose, alginates, lignin, natural gums produced by either bacteria or plants, offer unique surface functionality with available functional and polar surface groups, such as carboxylic acid and hydroxyl groups (Figure 1). By using the synergy between several bio binders and crosslinkers, 2 mAh/cm² aqueous-processed NMC cathodes could be realized and tested in full cells configuration (Figure 2). The long-term cycling evaluation of such cathodes

show similar or even better performances in the case of Figure 2 to baseline cathodes processed in NMP/PVDF systems (90% of capacity retention for green process versus 78% for baseline process after 1000 cycles). Note that the same setup is used for mixing and coating steps for both processes to allow a fair comparison. The quantity of bio binder(s) used in the ink is also divided by two (2%wt) when comparing to the baseline process (4%wt PVDF) while achieving similar viscosities.

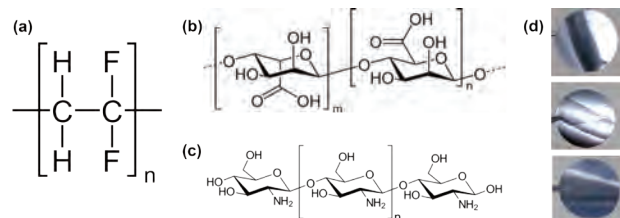


Figure 1: Chemical structure of (a) PVDF fluoropolymer (b) Alginic and (c) Chitosan biopolymers. (d) Electrode bottom view with (top) baseline process, aqueous based (middle) with cracks and (bottom) crack-free.

Nonetheless, the achievement of commercially relevant areal loading electrodes (> 2 mAh/cm²) remains a great challenge in aqueous systems. The high surface tension of water leads to potential cracking and delamination phenomena during the drying stage of the electrodes (Figure 1d). Formulation optimization work is therefore currently underway to produce 3-4 mAh/cm² aqueous-based cathodes.

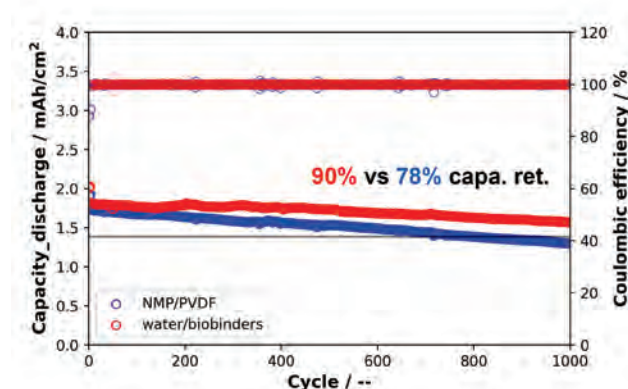


Figure 2: Electrochemical performance of baseline (blue) vs aqueous processed (red) NMC cathodes in coin cells: long-term cycling stability in full cells NMC/graphite at 1C/1C charge/discharge at 20°C.

CSEM has demonstrated the realization of 2 mAh/cm² aqueous-based production of LIBs cathodes with equivalent performances to the baseline PVDF/NMP ones. Work in progress focuses on two areas: the production of 3-4 mAh/cm² cathodes and performance optimization for Ni-rich materials (NMC811, LMNO).

[1] Bresser, et al., Energy & Environmental Science 11, no. 11 (2018): 3096–3127. <https://doi.org/10.1039/C8EE00640G>.

[2] Kukay, et al., Journal of Colloid and Interface Science 581 (2021): 635–43. <https://doi.org/10.1016/j.jcis.2020.07.144>.

Smart Battery Management System with Embedded Electrochemical Impedance Spectroscopy

A. Ambühl, C. Bocquillon

Within the flagship project NEMO, CSEM is using its expertise and know-how with Electrochemical Impedance Spectroscopy (EIS) to develop a Cell Management System (CMS) capable of doing EIS-related diagnostics.

EIS is a non-invasive technique used to measure a battery's impedance across a range of frequencies. By applying a small Alternating Current (AC) signal and analyzing the voltage response, EIS provides detailed insights into the battery's internal processes, such as ion movement, charge transfer, and degradation mechanisms. This allows for precise evaluation of a battery's State of Health (SoH), State of Charge (SoC), and potential issues like aging or defects, making it a powerful tool for optimizing battery performance and lifespan.

Within the NEMO project, several system design requirements were drafted. The EIS-capable CMS must be self-powered by the cell (a 75 Ah NMC cell in this case). The PCB must be space-efficient and well-integrated into the cell and battery pack. In terms of EIS performance, we want to measure the Phase with an accuracy of less than 0.5° , and an amplitude accuracy of less than 1% in comparison to standard reference equipment. From those requirements arose a lot of technical problems that we overcame.

First, the EIS circuitry. As no commercially available chipset is capable of doing such precise measurements, we had to design our own circuitry. For this, we had to design a PCB able to generate an AC current and inject it into the cell, measure the generated AC current along with the cell's voltage response. We achieve this with a specialized acquisition chain that filters the signals without distorting them and removes the DC offset.

Then, the low-power design guided key decisions, with embedded firmware built to minimize consumption by selectively activating CMS components and using specific low-power parts. This ensures accurate EIS results and prevents excessive cell discharge during storage.

Also, the space-saving design turned out to be a challenge. As we are always dissipating energy during an EIS (2.5A @4.2V \approx 10W), we had to perform thermal simulation and validation on the critical components, ensuring the EIS circuit functionality even in the harshest conditions. This required clever component placement and selections.

Finally, to achieve the required high accuracy, careful attention has been given to circuit design and layout, with aspects such as shielding, minimizing noise, and ensuring a stable power supply critically considered. The end results can be seen on Figure 1.

For the results part, when comparing our EIS measured with the NEMO hardware to the reference EIS made using laboratory equipment, we can see in Figure 2 that the results are very similar. The main difference is happening at high frequencies, where we have a smaller inductive tail with our hardware. This is due to the fact that our cables are smaller, and so is the resulting parasitic impedance. The accuracy of our system allows us to correctly monitor the cell's internal temperature, removing the need for costly additional sensors.

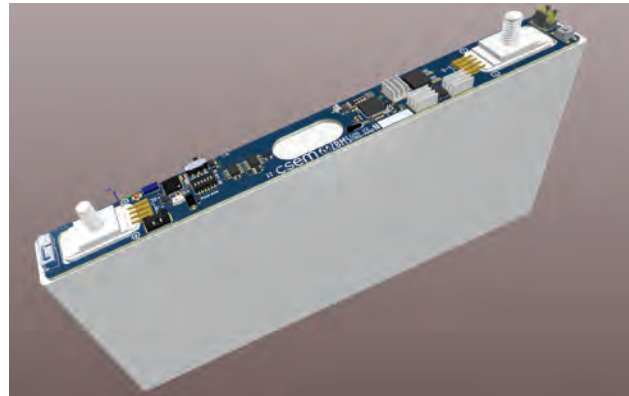


Figure 1: 3D view of the designed EIS-capable CMS.

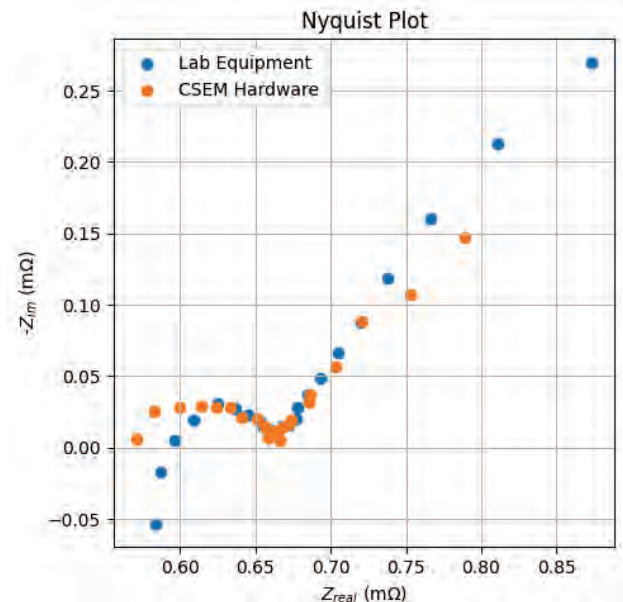


Figure 2: Results of the CMS EIS compared to the reference Laboratory equipment.

This developed CMS has been assembled into a battery pack and tested in real condition in an electric vehicle (Figure 3). It also included CSEM's patented switching concept and the implementation of CSEM's algorithms based on EIS.

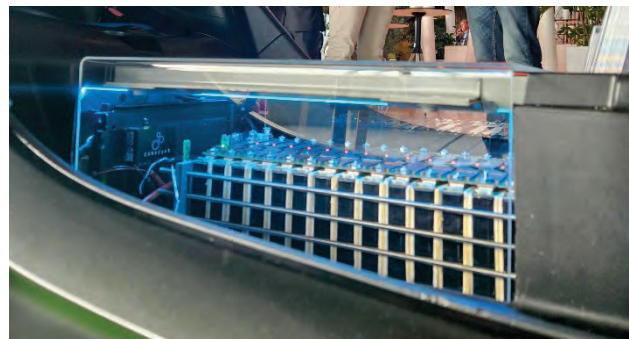


Figure 3: CSEM's Pack into an electric vehicle.

Multi-chemistry Validation of CSEM's 'EIS2MOD' Model for State of Charge Estimation

G. Mourouga, G. Gschwend, A. Hutter

CSEM's Battery Managements Systems (BMS) team developed the Bestimator™ state-of-charge (SoC) estimation algorithm, supported by the EIS2MOD voltage model. The BMS teams plans on expanding these models to other SoTA battery chemistries, including Lithium Nickel Cobalt Oxide (NMC), Lithium Iron Phosphate (LFP) cathode, Silicon-graphite and Li-metal anodes, and Sodium-ion.

Currently, the performance of a battery pack is constrained by the worst-performing cell. Mitigating this involves having high-accuracy SoC algorithms that can be recalibrated as cells age, which will be instrumental in developing SoC-based balancing algorithms, thus allowing to maximize the performance of the battery packs and extend their lifetime. As of today, the SoC is estimated by correlating the measured cell's potential with the open circuit potential curve (OCV), as shown in Figure 1, which is characteristic of each cell chemistry. This involves an uncertainty due to the dependence of the potential on applied current, the cell's state of health and temperature.

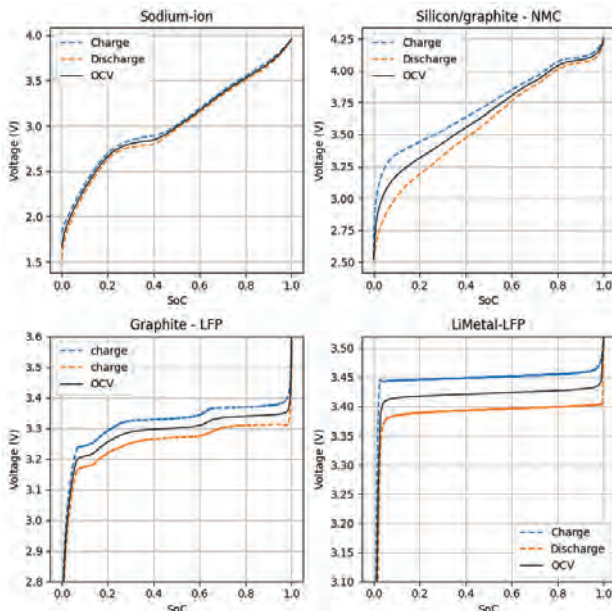


Figure 1: OCV of different chemistries.

CSEM utilizes electrochemical impedance spectroscopy to obtain information on the internal resistance of the battery. This data is then treated with a mathematical transformation called 'Distribution of Relaxation Times' (DRT). The DRT curve is the basis of the EIS2MOD modelling approach (see figure 2).

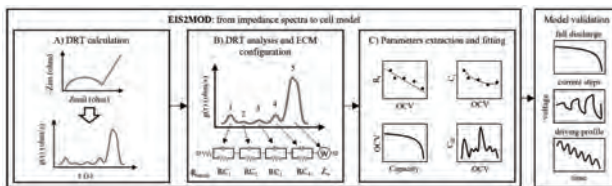


Figure 2: EIS2MOD modelling approach.

The position and area of gaussian peaks on the DRT curve (Figure 3) is used to automatically generate an Equivalent Circuit Model (ECM) which is a series of resistance and capacitance (RC) parallel elements. Together with the OCV (Figure 1), the RC values can be used to model the cell voltage response to a current profile, herein a worldwide harmonized light vehicle test (WLTC).

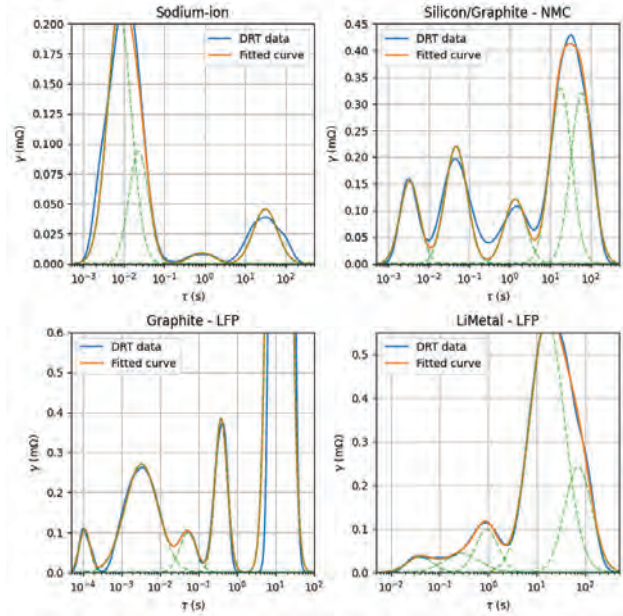


Figure 3: DRT of different chemistries with fitted Gaussian peaks.

In Figure 4 we evaluate the accuracy of the model by calculating the root mean square deviation (RMSE) between the ECM voltage (orange curve) and the measured voltage (blue curve) over 1h of the WLTC profile. The RMSE of the model on the four investigated chemistries was below 10 mV, which is already considered very accurate in the state-of-the-art for a single chemistry.

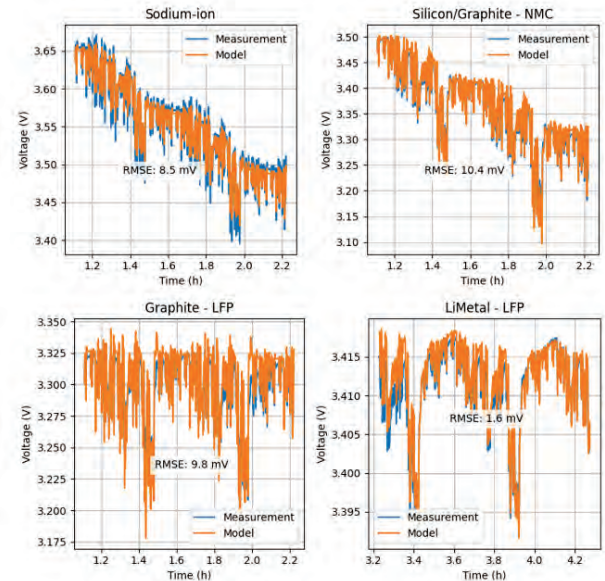


Figure 4: Validation of different chemistries on WLTC profiles.

In conclusion, The EIS2MOD framework was validated across multiple cell chemistries and can be confidently used to develop SoC algorithms that are chemistry-agnostic.

ANNEXES

Publications

- [1] Aeberhard, Jasmin Leonie; Radan, Anda-Petronela; Soltani, Ramin Abolfazl; Strahm, Karin Maya; Schneider, Sophie; Carrié, Adriana; Lemay, Mathieu; Krauss, Jens; Delgado-Gonzalo, Ricard; Surbek, Daniel, Introducing Artificial Intelligence in Interpretation of Foetal Cardiotocography: Medical Dataset Curation and Preliminary Coding—An Interdisciplinary Project, Methods and Protocols, Vol. 7(1), pp. 5, DOI: 10.3390/mps7010005
- [2] Allebe, Christophe; Descoedres, Antoine; Wyss, Patrick; Boillat, Pauline; Pernes, Nicolas; Paviet-Salomon, Bertrand; Ballif, Christophe, Sputtering for the Formation of Si-Based Passivating Contacts, IEEE Journal of Photovoltaics, 14 (1), pp. 35-40, DOI: 10.1109/JPHOTOV.2023.3324998
- [3] Arriaga Arruti, Olatz; Gnocchi, Luca; Jeangros, Quentin; Ballif, Christophe; Virtuani, Alessandro, Potential-induced degradation in bifacial silicon heterojunction solar modules: Insights and mitigation strategies, Progress in Photovoltaics: Research and Applications, 32 (5), pp. 304-316, DOI: 10.1002/pip.3765
- [4] Artuk, Kerem; Turkay, Deniz; Mensi, Mounir D.; Steele, Julian A.; Jacobs, Daniel A.; Othman, Mostafa; Yu Chin, Xin; Moon, Soo-Jin; Tiwari, Ayodhya N.; Hessler-Wyser, Aïcha; Jeangros, Quentin; Ballif, Christophe; Wolff, Christian M., A Universal Perovskite/C60 Interface Modification via Atomic Layer Deposited Aluminum Oxide for Perovskite Solar Cells and Perovskite–Silicon Tandems, Advanced Materials, Vol. 36(21), Art. 2311745, DOI: 10.1002/adma.202311745
- [5] Aydin, Erkan; Allen, Thomas G.; De Bastiani, Michele; Razzaq, Arsalan; Xu, Lujia; Ugur, Esma; Liu, Jiang; De Wolf, Stefaan, Pathways toward commercial perovskite/silicon tandem photovoltaics, Science, 383 (6679), pp. 1-13, DOI: 10.1126/science.adh3849
- [6] Bendinelli T.; Biggio L.; Nyfeler D.; Ghosh A.; Tollan P.; Kirschmann M.A.; Fink O., GEMTELLIGENCE: Accelerating gemstone classification with deep learning, Communications Engineering, Vol. 3 (1), DOI: 10.1038/s44172-024-00252-x
- [7] Bernard G.; Pejchal V.; Sereda O.; Logé R.E., Tensile Properties of Ex-Situ Ti-TiC Metal Matrix Composites Manufactured by Laser Powder Bed Fusion, Materials Vol. 17(22), DOI: 10.3390/ma17225613
- [8] Bernard G.; Pejchal V.; Sereda O.; Logé R.E., In-situ fabrication of Ti-TiCx metal matrix composite by laser powder bed fusion with enhanced elastic modulus and superior ductility, Materials and Design Vol. 248, DOI: 10.1016/j.matdes.2024.113499
- [9] Bhoir, Shubham Sharad; Thenaisie, Guillaume; Brivio, Claudio; Paolone, Mario, Li-ion cells internal temperature estimation using medium-frequency measurements of impedance argument, Journal of Energy Storage, 97, Art. 112754, DOI: 10.1016/j.est.2024.112754
- [10] Blondiaux, Nicolas; Pugin, Raphaël, Conformal surface nanostructuring of microparts based on nanosphere lithography, Colloids and Surfaces A: Physicochemical and Engineering Aspects, 2024, Vol. 694, Art. 133801, DOI: 10.1016/j.colsurfa.2024.133801
- [11] Blum, Roman; Denis, Séverine; Karlen, Lauriane; Kundermann, Stefan; Karlen, Sylvain; Lecomte, Steve, Dual optical frequency transfer through wavelength-division and polarization multiplexing in a 184-meter fiber link, Optics Continuum, Vol. 3 (7), pp. 1038-1050, DOI: 10.1364/OPTCON.516673
- [12] Boder-Pasche, Stéphanie; Demir, Mustafa; Heub, Sarah; Garzuel, Manon; Ischer, Réal; Migliozi, Daniel; Graf, Siegfried; Schmid, Noa; Atakan, H Baris; Gudkova, Daria; Alpern, Daniel; Dainese, Riccardo; Deplancke, Bart; Weder, Gilles, Multi-well plate lid for single-step pooling of 96 samples for high-throughput barcode-based sequencing., Biomedical Microdevices, 26, 18, DOI: 10.1007/s10544-024-00702-5
- [13] Borja Block, Alejandro; Escarre Palou, Jordi; Courtant, Marie; Virtuani, Alessandro; Cattaneo, Gianluca; Roten, Maxime; Li, Heng-Yu; Despeisse, Matthieu; Hessler-Wyser, Aïcha; Desai, Umang; Faes, Antonin; Ballif, Christophe, Colouring solutions for building integrated photovoltaic modules: A review, Energy and Buildings Vol. 314, Art. 114253, DOI: 10.1016/j.enbuild.2024.114253
- [14] Borja Block, Alejandro; Escarre Palou, Jordi; Faes, Antonin; Virtuani, Alessandro; Ballif, Christophe, Accurate color characterization of solar photovoltaic modules for building integration, Solar Energy Vol. 2671 Art. 112227, DOI: 10.1016/j.solener.2023.112227

- [15] Bourely J.; Kim J.; Beyer C.; Vorobyov O.; Aeby X.; Nyström G.; Briand D., Degradable and Printed Microstrip Line for Chipless Temperature and Humidity Sensing, *Advanced Electronic Materials*, Vol. 10 (11), DOI: 10.1002/aelm.202400229
- [16] Cerida Rengifo S.; Chicco F.; Le Roux E.; Enz C., An Ultralow Power Short-Range 60-GHz FMCW Radar in 22-nm FD-SOI CMOS, *IEEE Transactions on Microwave Theory and Techniques* Vol. 72(4), pp. 2548-2559, DOI: 10.1109/TMTT.2023.3348035
- [17] Chételat O.; Rapin M.; Bonnal B.; Fivaz A.; Sporrer B.; Rosenthal J.; Wacker J., Remotely Powered Two-Wire Cooperative Sensors for Bioimpedance Imaging Wearables, *Sensors* Vol. 24 (18), DOI: 10.3390/s24185896
- [18] Chin, Sanghoon; Holzer, Jannis; De Groote, Andreas; Martens, Daan; Naujokaite, Greta; Vizbaras, Augustinas; Vizbaras, Kristijonas; Pache, Christophe, Development of hybrid photonic integrated wavelength-tunable laser at 2 μm and its application to FMCW LiDAR, *Optics Express*, Vol. 32(13), pp. 22470, DOI: 10.1364/OE.522398
- [19] Clément, Pierrick; Schrage, K. Walter; Hoeng, Julia, Recent advances in the development of portable technologies and commercial products to detect Δ9-tetrahydrocannabinol in biofluids: a systematic review, Vol. 6, Art. 9, (2024), DOI: 10.1186/s42238-024-00216-0
- [20] Cole G.D.; Koller S.; Greve C.; Barwood G.P.; Deutsch C.; Gaynor P.; Ghulinyan M.; Gill P.; Hendricks R.; Hill I.; Kundermann S.; Goff R.L.E.; Lecomte S.; Meier C.; Pepponi G.; Schilt S.; Stenzel C.; Sütterlin R.; Voss K.; Zhukov A., Towards space-deployable laser stabilization systems based on vibration-insensitive cubic cavities with crystalline coatings, *Optics Express* Vol. 32(4), pp. 5380-5396, DOI: 10.1364/OE.506833
- [21] Del Giovane, Ste; Neda, Bagheri; Di Pede, A. C.; Chamorro, A.; Ranallo, S.; Migliorelli, D., Challenges and perspectives of CRISPR-based technology for diagnostic applications, *TrAC Trends in Analytical Chemistry*, Vol. 172(2024), Art. 117594, DOI: <https://doi.org/10.1016/j.trac.2024.117594>
- [22] Desai, Umang; Nicolet, Kléber; Prabhudesai, Sukanya; Cattaneo, Gianluca; Robin, Julien; Cunha, Cristiano; Silva, José; Jacques, Louis; Mujovi, Fahradin; Levrat, Jacques; Despeisse, Matthieu; Hessler-Wyser, Aïcha; Faes, Antonin; Ballif, Christophe, Stress tolerance of lightweight glass-free PV modules for vehicle integration, *EPJ Photovoltaics*, Vol.15, Art. 10, DOI: 10.1051/epjp/2024003
- [23] El Zein Y.; Lemay M.; Huguenin K., PrivaTree: Collaborative Privacy-Preserving Training of Decision Trees on Biomedical Data, *IEEE/ACM Transactions on Computational Biology and Bioinformatics* Vol. 21(1), pp. 1-13, DOI: 10.1109/TCBB.2023.3286274
- [24] Gnocchi, Luca; Arruti, Olatz Arriaga; Ballif, Christophe; Virtuani, Alessandro, A comprehensive physical model for the sensitivity of silicon heterojunction photovoltaic modules to water ingress, *Cell Reports Physical Science*, 5 (1), Art. 101751, DOI: 10.1016/j.xcrp.2023.101751
- [25] Golobostanfar M.R.; Othman M.; Turkay D.; Artuk K.; Chin X.Y.; Mensi M.D.; Jacobs D.A.; Jeangros Q.; Wolff C.M.; Hessler-Wyser A.; Ballif C., Bifacial perovskite/silicon heterojunction tandem solar cells based on FAPbI₃-based perovskite via hybrid evaporation-spin coating, *Nano Energy*, Vol. 131, DOI: 10.1016/j.nanoen.2024.110269
- [26] Guesnay Q.; Sahli F.; Artuk K.; Turkay D.; Kuba A.G.; Mrkyvkova N.; Vegso K.; Siffalovic P.; Schreiber F.; Lai H.; Fu F.; Ledinský M.; Fürst N.; Schafflützel A.; Bucher C.; Jeangros Q.; Ballif C.; Wolff C.M., Pizza Oven Processing of Organohalide Perovskites (POPOP): A Simple, Versatile and Efficient Vapor Deposition Method, *Advanced Energy Materials* Vol. 14(10), DOI: 10.1002/aenm.202303423
- [27] Heymann, F.; Quest, H.; Lopez Garcia, T.; Ballif, C.; Galus, M., Reviewing 40 years of artificial intelligence applied to power systems – A taxonomic perspective, *Energy and AI*, 15, Art. 100322, DOI: 10.1016/j.egyai.2023.100322
- [28] Ioannidis, Charalabos; Verykokou, Styliani; Soile, Sofia; Istrati, Denis; Spyros, Constantine; Sarris, Apostolos; Akritidis, Dimitris; Feidas, Haralambos; Georgoulias, Aristeidis K.; Tringa, Efstathia; Zanis, Prodromos; Georgiadis, Charalampos; Martino, Salvatore; Feliziani, Federico; Marmoni, Gian Marco; Cerra, Daniele; Ottinger, Marco; Bichofer, Felix; Anastasiou, Anastasia; Charalampopoulou, Vasiliki (Betty); Krebs, Patrick; Mizaikoff, Boris; Roulet, Jean-Christophe; Bulliard, Xavier; Dudnik, Gabriela; Anyfantis, George C., Safeguarding Our Heritage—The TRIQUETRA Project Approach, *Heritage*, Vol. 7 (2), pp. 758-793, DOI: 10.3390/heritage7020037
- [29] Jaffrès, Anaël; Othman, Mostafa; Saenz, Felipe; Hessler-Wyser, Aïcha; Jeangros, Quentin; Ballif, Christophe; Wolff, Christian M., Blade-Coating of High Crystallinity Cesium-Formamidinium Perovskite Formulations, *ACS Applied Materials and Interfaces*, 16 (28), pp. 36557-36566, DOI: 10.1021/acsami.4c04706

- [30] Jeanningros, Loïc; Bloa, Mathieu Le; Teres, Cheryl; Siklody, Claudia Herrera; Porretta, Alessandra; Pascale, Patrizio; Luca, Adrian; Muñoz, Jorge Solana; Domenichini, Giulia; Meister, Théo A.; Maldonado, Rodrigo Soria; Tanner, Hildegard; Vesin, Jean-Marc; Thiran, Jean-Philippe; Lemay, Mathieu; Rexhaj, Emrush; Pruvot, Etienne; Braun, Fabian, The influence of cardiac arrhythmias on the detection of heartbeats in the photoplethysmogram: benchmarking open-source algorithms, *Physiological Measurement*, Vol. 45 (2), pp. 025005, DOI: 10.1088/1361-6579/ad2216
- [31] Jung, Dongju; Park, Jeong Woo; Min, Sejong; Lee, Hak June; Park, Jin Su; Kim, Gui-Min; Bulliard, Xavier; Pugin, Raphaël; Shin, Doyoon; Im, Seongbin; Lim, Jaemin; Kim, Ka Hyung; Chae, Jong Ah; Lee, Doh C; Hwang, Euyheon; Park, Ji Sang; Park, Young Shin; Bae, Wan ki, Strain-graded quantum dots with spectrally pure, stable and polarized emission, *Nature Communications* (2024) 15:5561, DOI: 10.1038/s41467-024-49791-z
- [32] Kikelj, M.; Senaud, L.-L.; Geissbühler, J.; Sahli, F.; Lachenal, D.; Baetzner, D; Lipovšek, B.; Topič, M.; Ballif, C.; Jeangros, Q.; Paviet-Salomon, B., Do all good things really come in threes? The true potential of 3-terminal perovskite-silicon tandem solar cell strings, *Joule*, Vol. 8(3), pp. 852-871, DOI: 10.1016/j.joule.2024.01.009
- [33] Knoben, Wout; Graf, Siegfried; Borutta, Florian; Tegegne, Zerihun; Ningler, Michael; Blom, Arthur; Dam, Henk; Evers, Kevin; Schonenberg, Rens; Schütz-Trilling, Anke; Veerbeek, Janneke; Arnet, Roman; Fretz, Mark; Revol, Vincent; Valentin, Thomas; Bridges, Christopher; Schulz, Stephan; van Kerkhof, Joost; Leenstra, Anne; Orujov, Farid; van Middendorp, Henk, An Integrated Photonic Biosensing Platform for Pathogen Detection in Aquaculture, *Sensors* 2024, 24(16), 5241, DOI: <https://doi.org/10.3390/s24165241>
- [34] Kothandaraman R.K.; Siegrist S.; Dussouillez M.; Krause M.; Lai H.; Pious J.K.; Nishiwaki S.; Gilshtein E.; Müller A.; Cabas Vidani A.; Jenatsch S.; Ruhstaller B.; Jeangros Q.; Carron R.; Tiwari A.N.; Fu F., Sputtered NiO Interlayer for Improved Self-Assembled Monolayer Coverage and Pin-Hole Free Perovskite Coating for Scalable Near-Infrared-Transparent Perovskite and 4-Terminal All-Thin-Film Tandem Modules, *Solar RRL*, Vol. 8 (21), DOI: 10.1002/solr.202400176
- [35] Koyaz Y.; Lafforgue C.; Zarebidaki H.; Hefti O.; Grassani D.; Sattari H.; Brès C.-S., Ultrabroadband tunable difference frequency generation in a standardized thin-film lithium niobate platform, *Optics Express*, Vol. 32(26), pp. 46776-46787, DOI: 10.1364/OE.540893
- [36] Lachowicz, Agata; Badel, Nicolas; Barrou, Alexis; Barth, Vincent; Harrison, Samuel; Frasson, Nicola; Galiazzo, Marco; Cohen, Natali; Cohen, Eyal; Zhao, Jun; Paviet-Salomon, Bertrand; Ballif, Christophe, Aging tests of mini-modules with copper-plated heterojunction solar cells and pattern-transfer-printing of copper paste, *EPJ Photovoltaics*, 15, Art. 11, DOI: 10.1051/epjp/2024008
- [37] Lang G.; Rouvinet J., Fast mobility analysis for generative design applications through a real vector space representation of mobilities, *Mechanism and Machine Theory* Vol. 203, DOI: 10.1016/j.mechmachtheory.2024.105790
- [38] Larocque H.; Vitullo D.L.P.; Sludds A.; Sattari H.; Christen I.; Choong G.; Prieto I.; Leo J.; Zarebidaki H.; Lohani S.; Kirby B.T.; Soylak O.; Soltani M.; Ghadimi A.H.; Englund D.R.; Heuck M., Photonic Crystal Cavity IQ Modulators in Thin-Film Lithium Niobate, *ACS Photonics*, Vol. 11(9), pp. 3860-3869, DOI: 10.1021/acspophotonics.4c01138
- [39] Libraro S.; Bannenberg L.J.; Famprakis T.; Reyes D.; Hurni J.; Genc E.; Ballif C.; Hessler-Wyser A.; Haug F.-J.; Morisset A., Development and Characterization of N₂O-Plasma Oxide Layers for High-Temperature p-Type Passivating Contacts in Silicon Solar Cells, *ACS Applied Materials and Interfaces*, Vol. 16 (36), pp. 47931-47943, DOI: 10.1021/acsami.4c10612
- [40] Ludwig, Markus; Ayhan, Furkan; Schmidt, Tobias M; Wildi, Thibault; Voumard, Thibault; Blum, Roman; Ye, Zhichao; Lei, Fuchuan; Wildi, François; Pepe, Francesco; Gaafar, Mahmoud A.; Obrzud, Ewelina; Grassani, Davide; Hefti, Olivia; Karlen, Sylvain; Lecomte, Steve; Moreau, François; Chazelas, Bruno; Sottile, Rico; Torres-Company, Victor; Brasch, Victor; Villanueva, Luis G; Bouchy, François; Herr, Tobias, Ultraviolet astronomical spectrograph calibration with laser frequency combs from nanophotonic lithium niobate waveguides, *Nature Communications*, 15 (1), 7614, DOI: 10.1038/s41467-024-51560-x
- [41] Maradesa, A.; Py, B.; Huang, J.; Lu, Yang; Iurilli, Pietro; Mrozinski, Aleksander; Law, Ho Mei; Wang, Yuhao; Wang, Zilong; Li, Jingwei; Xu, Shengjun; Meyer, Quentin; Liu, Jiapeng; Brivio, Claudio; *et al.*, Advancing electrochemical impedance analysis through innovations in the distribution of relaxation times method, *Joule*, 8 (7), p 1958-1981, DOI: 10.1016/j.joule.2024.05.008

- [42] Nasim S.; Bichsel C.; Pinto A.; Alexandrescu S.; Kozakewich H.; Bischoff J., Similarities and differences between brain and skin GNAQ p.R183Q driven capillary malformations, *Angiogenesis*, Vol. 27 (4), pp. 931-941, DOI: 10.1007/s10456-024-09950-8
- [43] Nasim S.; Bichsel C.; Dayneka S.; Mannix R.; Holm A.; Vivero M.; Alexandrescu S.; Pinto A.; Greene A.K.; Ingber D.E.; Bischoff J., MRC1 and LYVE1 expressing macrophages in vascular beds of GNAQ p.R183Q driven capillary malformations in Sturge Weber syndrome, *Acta Neuropathologica Communications*, Vol. 12 (1), DOI: 10.1186/s40478-024-01757-4
- [44] Othman, Mostafa; Jeangros, Quentin; Jacobs, Daniel A.; Futscher, Moritz H.; Zeiske, Stefan; Armin, Ardalan; Jaffrès, Anaël; Kuba, Austin G.; Chernyshov, Dmitry; Jenatsch, Sandra; Züfle, Simon; Ruhstaller, Beat; Tabean, Saba; Wirtz, Tom; Eswara, Santhana; Zhao, Jiashang; Savenije, Tom J.; Ballif, Christophe; Wolff, Christian M.; Hessler-Wyser, Aïcha, Alleviating nanostructural phase impurities enhances the optoelectronic properties, device performance and stability of cesium-formamidinium metal-halide perovskites, *Energy and Environmental Science*, 17 (11), pp. 3832-3847, DOI: 10.1039/d4ee00901k
- [45] Othman M.; Jeangros Q.; Rothmann M.U.; Jiang Y.; Ballif C.; Hessler-Wyser A.; Wolff C.M., Linking Nanoscopic Insights to Millimetric-Devices in Formamidinium-Rich Perovskite Photovoltaics, *Advanced Materials* 2024, 2409742, DOI: 10.1002/adma.202409742
- [46] Özkalay, Ebrar; Valoti, Flavio; Caccivio, Mauro; Virtuani, Alessandro; Friesen, Gabi; Ballif, Christophe, The effect of partial shading on the reliability of photovoltaic modules in the built-environment, *EPJ Photovoltaics*, Vol. 15, Art. 7, DOI: 10.1051/epjpv/2024001
- [47] Özkalay, Ebrar; Virtuani, Alessandro; Eder, Gabriele; Voronko, Yuliya; Bonomo, Pierluigi; Caccivio, Mauro; Ballif, Christophe; Friesen, Gabi, Correlating long-term performance and aging behaviour of building integrated PV modules, *Energy and Buildings*, 316, Art. 114252, DOI: 10.1016/j.enbuild.2024.114252
- [48] Pievani M.; Ribaldi F.; Toussas K.; Da Costa S.; Jorge J.; Reynaud O.; Chicherio C.; Blouin J.L.; Scheffler M.; Garibotto V.; Jovicich J.; Jelescu I.O.; Frisoni G.B., Resting-state functional connectivity abnormalities in subjective cognitive decline: A 7T MRI study, *Neurobiology of Aging*, Vol. 144, pp. 104-113, DOI: 10.1016/j.neurobiolaging.2024.09.007
- [49] Quest, Hugo; Virtuani, Alessandro; Ballif, Christophe, Intrinsic performance loss rate: Decoupling reversible and irreversible losses for an improved assessment of photovoltaic system performance, *Progress in Photovoltaics: Research and Applications*, Vol. 32(11), pp. 774-789, DOI: 10.1002/pip.3829
- [50] Quest H.; Ballif C.; Virtuani A., Multi-Annual Year-on-Year: Minimising the Uncertainty in Photovoltaic System Performance Loss Rates, *Progress in Photovoltaics: Research and Applications*, DOI: 10.1002/pip.3855
- [51] Raghavan H.; Tayler M.C.D.; Mouloudakis K.; Rae R.; Lähteenmäki S.; Zetter R.; Laine P.; Haesler J.; Balet L.; Overstolz T.; Karlen S.; Mitchell M.W., Functionalized millimeter-scale vapor cells for alkali-metal spectroscopy and magnetometry, *Physical Review Applied*, Vol. 22 (4), DOI: 10.1103/PhysRevApplied.22.044011
- [52] Rospars N.; Trout M.; Fu C.; Mourouga G.; Mensi M.; Ingenito A., High performance ultra-thin lithium metal anode enabled by vacuum thermal evaporation, *Communications Materials*, Vol. 5 (1), DOI: 10.1038/s43246-024-00619-9
- [53] Ruedi, Pierre-François; Quaglia, Riccardo; Graf, Hans-Rudolf, A 90 µW at 1 fps and 1.33 mW at 30 fps 120-dB Intrascene Dynamic Range 640 × 480 Stacked Image Sensor for Autonomous Vision Systems, *IEEE Solid State Circuit Letters*, Vol. 7, pp. 106-109, DOI: 10.1109/LSSC.2024.3370797
- [54] Sampaio da Silva C.; Boos J.A.; Goldowsky J.; Blache M.; Schmid N.; Heinemann T.; Netsch C.; Luongo F.; Boder-Pasche S.; Weder G.; Pueyo Moliner A.; Samsom R.-A.; Marsee A.; Schneeberger K.; Mirsaidi A.; Spee B.; Valentini T.; Hierlemann A.; Revol V., High-throughput platform for label-free sorting of 3D spheroids using deep learning, *Frontiers in Bioengineering and Biotechnology*, Vol. 12, DOI: 10.3389/fbioe.2024.1432737
- [55] Scharnhorst P.; Schubnel B.; Carrillo R. E.; Alet P.-J.; Jones C. N., Risk-aware scheduling and dispatch of flexibility events in buildings, *Sustainable Energy, Grids and Networks* Vol. 39, DOI: 10.1016/j.segan.2024.101512
- [56] Sepehri, Yamin; Pad, Pedram; Yüzüğüler, Ahmet Caner; Frossard, Pascal; Dunbar, L. Andrea, Hierarchical Training of Deep Neural Networks Using Early Exiting, *IEEE Transactions on Neural Networks and Learning Systems*, DOI: 10.1109/TNNLS.2024.3396628

- [57] Shi Y.; Ruster T.; Ho M.; Karlen S.; Haesler J.; Treutlein P., Broad Instantaneous Bandwidth Microwave Spectrum Analyzer with a Microfabricated Atomic Vapor Cell, *Physical Review X*, Vol. 14(4), DOI: 10.1103/PhysRevX.14.041043
- [58] Sideris, Iason; Duncan, Stephen; Fabbri, Maicol; Crivelli, Francesco; Afrasiabi, Mohamadreza; Bambach, Markus, End-to-end path planning for homogeneous temperature fields in additive manufacturing, *Journal of Materials Processing Technology*, Vol. 327, 118364, DOI: 10.1016/j.jmatprotec.2024.118364
- [59] Sideris I.; Petrik J.; Bambach M., Too hot to print, too slow to handle; finding optimal path characteristics for WAAM, *Manufacturing Letters*, Vol. 41, pp. 879-890, DOI: 10.1016/j.mfglet.2024.09.108
- [60] Thenaisie G.; Brivio C., Hystimator: DRT-based hysteresis modelling for accurate SoC estimation in LFP battery cells, *IET Renewable Power Generation* Vol. 18(S1), pp. 4387-4398, DOI: 10.1049/rpg.2.13130
- [61] Turkay, Deniz; Artuk, Kerem; Chin, Xin-Yu; Jacobs, Daniel A; Moon, Soo-Jin; Walter, Arnaud; Mensi, Mounir; Andreatta, Gaëlle; Blondiaux, Nicolas; Lai, Hua gui; Fu, Fan; Boccard, Mathieu; Jeangros, Quentin; Wolff, Christian M.; Ballif, Christophe, Synergetic substrate and additive engineering for over 30% efficient perovskite Si tandem solar cells, *Joule*, Vol. 8 (6), pp. 1735-1753, DOI: 10.1016/j.joule.2024.04.015
- [62] Yilmaz, Gürkan; Seiler, Andrea; Chételat, Olivier; Schindler, Kaspar A., Ultra-Long-Term-EEG Monitoring (ULTEEM) Systems: Towards User-Friendly Out-of-Hospital Recordings of Electrical Brain Signals in Epilepsy, *Sensors*, Vol. 24 (6), pp. 1867, DOI: 10.3390/s24061867
- [63] Zabihzadeh S.; Ionescu C.; Biselli S.; Blanchard A.; Sereda O., Importance of the drying method in crystalline phase formation and metallic elements distribution of glycine complexes, *Results in Chemistry* Vol. 7, DOI: 10.1016/j.rechem.2024.101457
- [64] Zhang, Chun-Min; Quaglia, Riccardo; Shulga, Artem; Goossens, Vincent; Blanca Cruz, Paula; Rüedi, Pierre-François, A Quantum-Dot-Coated Image Sensor with a Wide-Spectral Sensitivity From X-rays to SWIR Photons, *IEEE Sensors Letters*, Vol. 8(8), August 2024
- [65] Zwingelstein, Thibault; Figarol, Agathe; Luzet, Vincent; Crenna, Maude; Bulliard, Xavier; Finelli, Alba; Gay, Julien; Lefèvre, Xavier; Pugin, Raphaël; Laithier, Jean-François; Chérioux, Frédéric; Humblot, Vincent, A Kinetic Approach to Synergize Bactericidal Efficacy and Biocompatibility in Silver-Based Sol-Gel Coatings, *ACS Omega* 2024, 9, 24574-24583
- [66] Lang G.; Perruchoud G.; Novo D.; Brun S., Uncoupling Development Time from the Size of a Library of AM Parts Through Complexity Reduction and Modeling of Topology Optimization Results, *Springer Tracts in Additive Manufacturing*, Part F3256, pp. 130-144, DOI: 10.1007/978-3-031-42983-5_9
- [67] Roulet J.-C.; Nguyen D.; Meier C.; Ummel A.; Gasparini L.; Pache C., New Space Compact Flash Lidar, *Springer Aerospace Technology*, Part F2592, pp. 139-149, DOI: 10.1007/978-3-031-53618-2_13.
- [68] Voroshazi E.; Beaucarne G.; Lossen J.; Faes A., Summary of the 11th Workshop on Metallization and Interconnection for Crystalline Silicon Solar Cells, *Solar Energy Materials and Solar Cells* 2024, Vol. 269, DOI: 10.1016/j.solmat.2024.112772

Proceedings

- [1] Ahmadi Najafabadi, Amir Mohsen; Ramirez, German A.; Ghorbanpoor, Mohsen; Vorobyov, Alexander; Nussbaum, Pascal; Skrivervik, Anja, Plug-in Plug-Out Multibeam Dielectric Rod Antenna for Target Dedicated mm-Wave RF-WPT Applications, 2024 18th European Conference on Antennas and Propagation (EuCAP), Glasgow, United Kingdom, 2024, pp. 1-5., DOI: 10.23919/EuCAP60739.2024.10501365
- [2] P. Asthana, *et al.*, A Power Simulation Tool for The Optimization of Wireless Sensor Nodes, 2024 IEEE 23rd International Conference on Micro and Miniature Power Systems, Self-Powered Sensors and Energy Autonomous Devices (PowerMEMS), Tønsberg, Norway, 2024, pp. 61-64, DOI: 10.1109/PowerMEMS63147.2024.10814224

- [3] Balet, Laurent; Christoph, Hofer; Giriens, Laurent; Chin, Sanghoon; Van Zaen, Jérôme; Muntané Calvo, Enric; Denis, Séverine; Lecomte, Steve, Design and Realization of a Broadband Optical Sensor for Air Pollution Monitoring, Optica Sensing Congress 2024 (AIS, LACSEA, Sensors, QSM), Technical Digest Series (Optica Publishing Group, 2024), paper LTu1F.4., DOI: 10.1364/LACSEA.2024.LTu1F.4
- [4] C. Barretta, *et al.*, Guidelines for Selection of Encapsulant Materials for Modules Using Perovskite/Si Tandem Cells, 2024 IEEE 52nd Photovoltaic Specialist Conference (PVSC), Seattle, WA, USA, 2024, pp. 0486-0488, DOI: 10.1109/PVSC57443.2024.10749124
- [5] Basset, Guillaume; Krähenbühl, Roger; Renggli, Martina; Mohrdiek, Stephan, Scalable and versatile chip to fiber optical interconnects, Proc. SPIE PC12892, Optical Interconnects XXIV, PC1289206 (12 March 2024), DOI: 10.1117/12.3003107
- [6] Bhati A.S.; Andreeva E.; Vizár D., OAE-RUP: A Strong Online AEAD Security Notion and Its Application to SAEF, Lecture Notes in Computer Science (including subseries Lecture Notes in Artificial Intelligence and Lecture Notes in Bioinformatics), Vol. 14974 LNCS, pp. 117-139, DOI: 10.1007/978-3-031-71073-5_6
- [7] Bigdely S.A; Lin G.; Dunbar L.A.; Portenier T.; Zwicker M., Learning Generative Models Using Denoising Density Estimators, in IEEE Transactions on Neural Networks and Learning Systems, Vol. 35, no. 12, pp. 17730-17741, Dec. 2024, DOI: 10.1109/TNNLS.2023.3308191
- [8] Blanc, Sébastien; Pad, Pedram; Türetken, Engin; Cantale, Nicolas; Dia, Mohamad; Honzatko, David; Kündig, Clément; Dunbar, Andrea; Feldhaus, Stephan; Hauenstein, Gian; Meier, Marcel; Meier, Thomas; Mendler, Tomaso; Michelon, Giovanni, VIVALDI: Steel Billet Tracking with Advanced Computer Vision, Proc. SPIE PC12903, AI and Optical Data Sciences V, PC1290308 (13 March 2024), DOI: 10.1117/12.3001270
- [9] Blum R.; Kundermann S.; Ruelle T.; Lecomte S.; Karlen S., Light shift mitigation for the 5S-5D two-photon transition in rubidium, Proceedings of SPIE - The International Society for Optical Engineering, Vol. 12993, DOI: 10.1117/12.3027257
- [10] Mathieu Boccard; Jun Zhao, Heterojunction Silicon Solar Cells: Recent Developments, in Photovoltaic Solar Energy: From Fundamentals to Applications, Vol. 2, IEEE, 2024, pp.71-80, DOI: 10.1002/9781119578826.ch7
- [11] Boiko D.L.; Torcheboeuf N.; Mitev V.; Balet L.; Grandjean N.; Resneau P.; Garcia M.; Gerard B.; Krakowski M., Two faces of superradiance in tandem-cavity ridge waveguide heterostructures, Proceedings of SPIE - The International Society for Optical Engineering, Vol. 12895, DOI: 10.1117/12.3002224
- [12] D. Cerra, *et al.*, Assessing the Spread of Invasive Mussels in Lake Neuchâtel as a Potential Threat to the Les Argilliez Heritage Site with Sentinel-2, IGARSS 2024 - 2024 IEEE International Geoscience and Remote Sensing Symposium, Athens, Greece, 2024, pp. 3376-3379, DOI: 10.1109/IGARSS53475.2024.10640529
- [13] Chin, Sanghoon, Optical Frequency-Domain Reflectometry for Distributed Thermal Monitoring inside Lithium-Ion Pouch Cell, Optica Sensing Congress 2024 (AIS, LACSEA, Sensors, QSM), Technical Digest Series (Optica Publishing Group, 2024), paper SF4C.6., DOI: 10.1364/SENSORS.2024.SF4C.6
- [14] Chin, Sanghoon; Obrzud, Ewelina, THz wave generation using hybrid electro-optic modulators: simulations and experimental results, 2024 International Topical Meeting on Microwave Photonics, MWP 2024, DOI: 10.1109/MWP62612.2024.10736315
- [15] Chin, Sanghoon; Soto, Marcelo A., Dynamic Brillouin Sensor in Optical Fibres Using Fast Fourier Analysis and Low-Bandwidth Acquisition, Optica Sensing Congress 2024 (AIS, LACSEA, Sensors, QSM), Technical Digest Series (Optica Publishing Group, 2024), paper SW3C.3., DOI: 10.1364/SENSORS.2024.SW3C.3
- [16] Chin, Sanghoon; Van Zaen, Jerome; Muntane, Enric; Denis, Severine; Lecomte, Steve; Balet, Laurent, Deep Learning Algorithms for Chemometric Analysis in MIR Gas Spectroscopy, Optica Sensing Congress 2024 (AIS, LACSEA, Sensors, QSM), Technical Digest Series (Optica Publishing Group, 2024), paper LTu1F.3, DOI: 10.1364/LACSEA.2024.LTu1F.3
- [17] Cygan A.; Bielska K.; Charczun D.; Kowzan G.; Nishiyama A.; Wcislo P.; Wójtewicz S.; Zaborowski M.; Maslowski P.; Lisak D.; Ciuryło R.; Fleisher A.J.; Gillis K.A.; Hodges J.T.; Voumard T.; Wilidi T.; Herr T.; Brasch V., Pure frequency-based dispersive spectroscopy, Journal of Physics: Conference Series Vol. 2889(1), DOI: 10.1088/1742-6596/2889/1/012061

- [18] Della Torre A.; Zarebidaki H.; Leo J.; Mettraux A.; Choong G.; Orvietani M.; Petremand Y.; Prieto I.; Dubochet O.; Despont M.; Sattari H., Electro-Optic Modulator in Thin-Film Lithium Niobate Foundry Process, Springer Proceedings in Physics Vol. 402, pp. 530-535, DOI: 10.1007/978-3-031-63378-2_87
- [19] Della Torre A.; Zarebidaki H.; Leo J.; Mettraux A.; Volpini A.; Grassani D.; Prieto I.; Dubochet O.; Despont M.; Sattari H., Ultralow Voltage Folded Electro-Optical Modulators in Thin-Film Lithium Niobate Foundry Process, 2024 Conference on Lasers and Electro-Optics (CLEO), Charlotte, NC, USA, 2024, pp. 1-2
- [20] Demolon P.; Carlin J.-F.; Dubois M.-A.; Hoogerwerf A.; Grandjean N.; Boiko D. L., AlN-based anodes for far-UVC field emission device at 225 nm, Proceedings of SPIE - The International Society for Optical Engineering Vol. 12906, DOI: 10.1117/12.3002650
- [21] Demuru, Silvia; Chai-Gao, Hui; Shynkarenko, Yevhen; Hermann, Nicola; Boia, Patricia; Cristofolini, Peter; Petkus, Bradley; Generelli, Silvia; Paoletti, Samantha; Cattaneo, Stefano; Burr, Loic, Point-of-Care Fluorescence Biosensing System for Rapid Multi-Allergen Screening, Sensors 2024, 24, 3280., DOI: <https://doi.org/10.3390/s24113280>
- [22] U. Desai, *et al.*, Novel Lightweight PV Modules Based on Polymeric Honeycomb for Building Integration, 2024 IEEE 52nd Photovoltaic Specialist Conference (PVSC), Seattle, WA, USA, 2024, pp. 0089-0091, DOI: 10.1109/PVSC57443.2024.10749199
- [23] Dietler, Silas; Zeder, Yanick; Graf, Elias; Koch, Kilian; Schwendimann, Andreas; Bendinelli, Tommaso, Evaluating Self-Supervised Foundation Models in Holographic Imaging, ICML 2024 Workshop on Foundation Models in the Wild, Vienna, Austria, July 2024, <https://openreview.net/forum?id=BrDboZXCD>
- [24] El Zein Y., Niksirat K.S.; Zufferey N.; Humbert M.; Huguenin K., Shadow Health-Related Data: Definition, Categorization, and User Perspectives, ACM International Conference Proceeding Series, pp. 58-76, DOI: 10.1145/3688459.3688462
- [25] Finelli, Alba; Clément, Pierrick; Beard, Alexandra; Lefèvre, Xavier, Towards Metal-Organic Framework based Optical Sensors for Pesticides Detection, AMA association for sensors and measurements, DOI: 10.5162/EUROSENSORSXXXVI/PT5.185
- [26] Gasparin, Enrico; Hoogerwerf, Arno; Bayat, Dara; Spinola Durante, Guido; Petremand, Yves; Tormen, Maurizio; Despont, Michel; Close, An Integrated MEMS Magnetic Gradiometer Rejecting Vibrations and Stray Fields, European Solid-State Circuits Conference ESSERC 2024, Bruges, Belgium 9-12, pp. 532-535, DOI: 10.1109/ESSERC62670.2024.10719515
- [27] Ghorbanpoor M.; Roux E.L.; Najafabadi A.M.A.; Vorobyov O.; Nussbaum P.; Wang H., A 24-GHz 4-Element Multi-Beam Wireless Energy Harvesting Array with Class-F Rectifiers Achieving 51.5% PCE, IEEE MTT-S International Microwave Symposium Digest, pp. 2-5, DOI: 10.1109/IMS40175.2024.10600372
- [28] Graf S.; Fretz M.; Arnet R., Challenges and Solutions of Photonic Chip Integrations into Micro-Fluidic Cartridges, Proceedings of SPIE - The International Society for Optical Engineering Vol. 12999, DOI: 10.1117/12.3016715
- [29] Grivon, Daniel; Gumy, Mathias; Onillon, Emmanuel; Pache, Christophe, Custom Voice Coil Actuator for flexure-based electromechanical RF switch, ACTUATOR24, International Conference and Exhibition on New Actuator Systems and Applications, Wiesbaden, Germany, 2024, pp. 223-224
- [30] Haesler J.; Bischof L.; Bennes J.; Balet L.; Greim O.; Hog O.; Jallageas A.; Husmann D.; Morel J.; Droz F.; Karlen S., Development of a High-Performance and Swiss Based Rolex Timescale System Including a Unique Optical Atomic Clock, 2024 European Frequency and Time Forum (EFTF), Neuchâtel, Switzerland, 2024, pp. 49-50, DOI: 10.1109/EFTF61992.2024.10722272
- [31] Hefti, Olivia; Tremblay, Jean-Etienne; Volpini, Andrea; Zarebidaki, Homa; Prieto, Ivan; Dubochet, Olivier; Despont, Michel; Lecomte, Steve; Brès, Camille-Sophie; Sattari, Hamed; Grassani, Davide, Symmetry breaking of the $\chi(2)$ polarization in poled thin-film lithium niobate waveguides enabling phase matching, CLEO 2024, Technical Digest Series (Optica Publishing Group, 2024), paper STu3E.4., DOI: 10.1364/CLEO_SI.2024.STu3E.4
- [32] Kirsch, Nicolas; Salizzoni, Giulio; Gorecki, Tomasz T.; Kamgarpour, Maryam, A Distributed Game Theoretic Approach for Optimal Battery Use in an Energy Community, ACM SIGENERGY Energy Informatics Review, Volume 4 Issue 4, October 2024

- [33] Koyaz Y.; Lafforgue C.; Balakleyskiy N.; Hefti O.; Zarebidaki H.; Sattari H.; Grassani D.; Brès C.-S., Design rules for frequency conversion in periodically poled thin-film lithium niobate waveguides, Proceedings of SPIE - The International Society for Optical Engineering Vol. 12889, DOI: 10.1117/12.3002631
- [34] Larocque H.; Vitullo D.L.P.; Buyukkaya M. A.; Sludds A.; Errando-Herranz C.; Papon C.; Harper S.; Tao M.; Carolan J.; Sattari H.; Christen I.; Choong G.; Prieto I.; Leo J.; Lee C.-M.; Zarebidaki H.; Lohani S.; Kirby B.T.; Soykal Ö.O.; Richardson C.J.K.; Leake G.L.; Coleman D.J.; Soltani M.; Ghadimi A.H.; Heuck M.; Fanto M.L.; Waks E.; Englund D., Tunable quantum emitters and coherent modulation on foundry integrated photonics, Proceedings of SPIE - The International Society for Optical Engineering Vol. 13028, DOI: 10.1117/12.3021136
- [35] Lefèvre, Xavier; Beard, Alexandra; Finelli, Alba; Clement, Pierrick; Pugin, Raphaël, MIP-based sensors for fast nicotine monitoring in aerosol, Eurosensors 2024, Debrecen, Hungary, 2-4 September 2024, DOI: 10.5162/EUROSENSORSXXXVI/OT6.196
- [36] Meirer J.; Wittwer L.D.; Revol V.; Heinemann T., DeepBINN: A tailored biologically informed neural network for robust biomarker identification, Proceedings - Swiss Conference on Data Science, SDS Vol. (2024), pp. 246-249, DOI: 10.1109/SDS60720.2024.00044
- [37] Mylonakis M.; Pekridis G.; Nikas T.; Morales C.; Martinez-Sarriegui I.; Jeangros Q.; Chin X.; Syvridis D., Novel Li-Fi Transceiver design based on Perovskite Photodiode Devices (PeLiFi), Proceedings of SPIE - The International Society for Optical Engineering Vol. 12894, DOI: 10.1117/12.3003326
- [38] Najafabadi A.M.A.; Ramírez G.A.; Ghorbanpoor M.; Vorobyov A.; Nussbaum P.; Skrivervik A., Plug-in Plug-Out Multibeam Dielectric Rod Antenna for Target Dedicated mm-Wave RF-WPT Applications, 18th European Conference on Antennas and Propagation, EuCAP 2024, DOI: 10.23919/EuCAP60739.2024.10501365
- [39] Ntavelis E., Shahbazi M., Kastanis I., Danelljan M., Van Gool L., StyleGenes: Discrete and Efficient Latent Distributions for GANs, 2024 IEEE/CVF Winter Conference on Applications of Computer Vision (WACV), Waikoloa, HI, USA, 2024, pp. 4065-4074, DOI: 10.1109/WACV57701.2024.00403
- [40] Pepe, Francesco; Bugatti, M.; Baur, A.; Berney, Jean; Bozzo, Enrico; Broeg, C.; Carzzolara, B.; Deep, A.; Droz, Fabien; Figueiredo, J.; Haile, H.; Jolissaint, A.; Lecomte, Steve; Moerschell, Joseph; Mordasini, C.; Obrzud, Ewelina; Praplan, C.; Sarjilic, M.; Soja, B.; Van den Broeck, M., vAncestor: an artificial satellite-borne star for accurate frequency calibration of ground-based EPRV spectrographs, Proceedings Vol. 13100, Advances in Optical and Mechanical Technologies for Telescopes and Instrumentation VI; 131005W (2024) <https://doi.org/10.1117/12.3016547> Event: SPIE Astronomical Telescopes + Instrumentation, 2024, Yokohama, Japan, DOI: <https://doi.org/10.1117/12.3016547>
- [41] Pierrick, Clément; Alba, Finelli; Xavier, Lefèvre; Saleem, Kahn; Alexandra, Beard; Raphaël, Pugin, Aptamer-based Electrochemical Sensor for the Monitoring of Carbamazepine in Freshwater Systems, EUROSENSORS XXXVI, September 1-4, 2024, DOI: 10.5162/EUROSENSORSXXXVI/OT6.195
- [42] Reyes S. M., Fong C., Rosenthal J. D., Reynolds M. S., ZeroScatter BLE: All-Digital, Fully Synthesizable Bluetooth Low Energy (BLE) Backscatter Communication in Verilog RTL for FPGA-Based Devices, 2024 IEEE International Conference on RFID (RFID), Cambridge, MA, USA, 2024, pp. 7-10, DOI: 10.1109/RFID62091.2024.10582510
- [43] Roa M.A.; Nottensteiner K.; Rodriguez I.; Bachmann T.; Lutze J.-P.; Letier P.; Ummel A.; Rouvinet J.; Cosandier F.; Nguyen D.; Schaffter V.; Trinh S.; Bissonnette V.; Germa T., Autonomous Precise Assembly of Segmented Mirror Tiles for a Space Telescope, IEEE Aerospace Conference Proceedings, DOI: 10.1109/AERO58975.2024.10521382
- [44] Rosenthal J. D., Reynolds M. S., Wideband OFDM Backscatter with Limited-Bandwidth Antennas for WiFi-6 and Future High-Data-Rate Backscatter Systems, 2024 9th International Conference on Smart and Sustainable Technologies (SpliTech), Bol and Split, Croatia, 2024, pp. 1-6, DOI: 10.23919/SpliTech61897.2024.10612616
- [45] Ruelle T.; Batori E.; Kundermann S.; Stehlin X.; Helson V.; Haesler J.; Lecomte S.; Droz F.; Karlen S., Development of an Industrial Two-Photon Rb Atomic Clock for Timekeeping Applications, EFTF 2024 - 37th Edition of the European Frequency and Time Forum, pp. 1-2, DOI: 10.1109/EFTF61992.2024.10722354

- [46] Sattari, Hamed; Despont, Michel; Prieto, Ivan; Dubois, Florian; Zarebidaki, Homa; Jacopo, Leo; Choong, G; Arefi, F; Orvietani, M; Della Torre, A; Mettraux, A; Herle, D; Petremand, Y; Palmieri, M; Dubochet, O, Thin-film lithium niobate PICs: advancements and potential applications in telecom and beyond, Proceedings SPIE, Vol. 13012, Integrated Photonics Platforms III, 130120H (2024), DOI: 10.1117/12.3026042
- [47] Sattari, Hamed; Prieto, Ivan; Zarebidaki,, Homa; Jacopo, Leo; Choong, Gregory; Arefi, Fatemeh; Orvietani, Mattia; Della Torre, Alberto; Petremand, Yves; Palmieri, Michele; Dubochet, Olivier; Despont, Michel, An Open-Access Platform for Thin-Film Lithium Niobate Photonic Integrated Circuits (TFLN PICs), 2024 Conference on Lasers and Electro-Optics (CLEO), Charlotte, NC, USA, May 2024, pp. 1-2
- [48] Sattari H.; Prieto I.; Zarebidaki H.; Leo J.; Choong G.; Arefi F.; Orvietani M.; Della Torre A.; Mettraux A.; Dubois F.; Herle D.; Petremand Y.; Palmieri M.; Dubochet O.; Despont M., Thin-film lithium niobate PICs: advancements and potential applications in telecom and beyond, Proceedings of SPIE - The International Society for Optical Engineering Vol. 13012, DOI: 10.1117/12.3026042
- [49] Sattari H.; Prieto I.; Zarebidaki H.; Leo J.; Choong G.; Arefi F.; Orvietani M.; Della Torre A.; Petremand Y.; Palmieri M.; Dubochet O.; Despont M., An Open-Access Platform for Thin-Film Lithium Niobate Photonic Integrated Circuits (TFLN PICs), 2024 Conference on Lasers and Electro-Optics (CLEO) 2024, pp. 1-2
- [50] Sattari H.; Prieto I.; Zarebidaki H.; Leo J.; Choong G.; Orvietani M.; Arefi F.; Torre A.D.; Petremand Y.; Palmieri M.; Dubochet O.; Despont M., Standardized TFLN Photonic Integrated Circuits Platform, Springer Proceedings in Physics Vol. 402, pp. 85-89, DOI: 10.1007/978-3-031-63378-2_15
- [51] Scolari, Nicola; Pengg, Franz Xavier; Manetakis, Konstantinos; Salazar, Camilo Andrés; Vouilloz, Alexandre; Pérez Serna, Ernesto; Dissanayake, Anjana; Persechini, Pascal; Kopta, Vladimir; Le Roux, Erwan; Chicco, Francesco; Cillo, Stefano; Gerber, Nicola; Berbelenet, Cédric; Epifano, Fabio; Dal Fabbro, Paulo Augusto; Raemy, Nicolas, A 1mm² Software-Defined Dual Mode Bluetooth Transceiver With 10dBm Maximum TX Power and -98.2dBm Sensitivity 2.96mW RX Power at 1Mb/s, 2024 IEEE International Solid-State Circuits Conference (ISSCC), San Francisco, CA, USA, 2024, pp. 402-404, DOI: 0.1109/ISSCC49657.2024.10454304
- [52] Vitullo D.L.P.; Lohani S.; Larocque H.; Sludds A.; Sattari H.; Christen I.; Choong G.; Prieto I.; Leo J.; Zarebidaki H.; Soltani M.; Searles T. A.; Ghadimi A. H.; Kirby B. T.; Heuck M.; Englund D. R., Optimized Encoding for Coherent Communication using Photonic Crystal Cavity IQ Modulators in Thin-Film Lithium Niobate, Proceedings of SPIE - The International Society for Optical Engineering Vol. 12871, DOI: 10.1117/12.3011172
- [53] Vuagniaux, Rémy; Narduzzi, Simon; Maamari, Nadim; Dunbar, L. Andrea, Constrained Zero-Shot Neural Architecture Search on Small Classification Dataset, 11th IEEE Swiss Conference on Data Science (SDS), Zurich, Switzerland, 2024, pp. 146-150, DOI: 10.1109/SDS60720.2024.00028
- [54] Wacker, Josias; Djordjevic, Srdjan; Trotošek, Blaž; Krašna, Simon; Žumer, Jan; Haenni, Etienne; Banderet, Grégoire; Richard, Patrick; Yilmaz, Gürkan, Non-invasive Continuous Measurement of the Intra- Abdominal Pressure, In: Jarm, T., Šmerc, R., Mahnič-Kalamiza, S. (eds) 9th European Medical and Biological Engineering Conference (EMBEC 2024), IFMBE Proceedings, Vol. 113. Springer, Cham, DOI: 10.1007/978-3-031-61628-0_18
- [55] Zanella, Frédéric; Lahmar, Mohamed K.; Schneider, Christian; Ceric, Luka; Basset, Guillaume, Advanced microlens origination by thermal reflow, Proc. SPIE PC12898, Advanced Fabrication Technologies for Micro/Nano Optics and Photonics XVII, PC1289805 (15 April 2024), DOI: 10.1117/12.3003227
- [56] Zhang, Chun-Min; Quaglia, Riccardo; Shulga, Artem; Goossens, Vincent; Hussain, Adib Al-Haj; Stadlinger, Bernd; Rüedi, Pierre-François, Dental Imaging with a Quantum-dot-based Direct Conversion X-ray Image Sensor, 2024 IEEE Nuclear Science Symposium (NSS), Medical Imaging Conference (MIC) and Room Temperature Semiconductor Detector Conference (RTSD), October 2024, Tampa, USA, DOI: 10.1109/NSS/MIC/RTSD57108.2024.10654883
- [57] Zhang, L., et al., A-102-dBm Sensitivity Multichannel Heterodyne Wake-Up Receiver with Integrated ADPLL, in IEEE Open Journal of the Solid-State Circuits Society, Vol. 4, pp. 43-56, 2024, DOI: 10.1109/OJSSCS.2024.3387388

Conferences and Workshops

Ayenew, Getachew T.; Haas, Gunther; Hauptmann, Jacqueline; Mendizabal, Laurent; Schnieper, Marc; Siitonens, Samuli; Offermans, Ton, Enhancing OLED Micro-display Performance Using Microlens Arrays, EuroDisplay 2024, Genoble (FR)

Bosch, Eleonoor; Holzer, Jannis; Nguyen, David; Ummel, Antoine; Roulet, Jean-Christophe; Meier, Christophe; Gasparini, Leonardo; Pache, Christophe, Flash LiDAR for Bathymetry Using a 2D SPAD Array, ISSW 2024 - The International SPAD Sensor Workshop & the SPAD SENSOR SCHOOL, Trento (Italy), June 4-5, 2024

Dietler, Silas; *et al.*, Spores Detection with Deep Learning, 9. F&E-Konferenz zu Industrie 4.0, Industrie 2025, Januray 2024

Disidoro, Fabio; Schmidt, Verena; Mehmedovic, Adi; Schöpe, Till; Netsch, Christoph, Ladle Slide Gate Health Monitoring for Steel Industry: Overcoming the Industrialization Challenges of Data-Driven Diagnostics in Steel Plants, 11th European Continuous Casting Conference, Philharmonie Essen Conference Center, Germany, October 7-11, 2024

Disidoro, Fabio, Health status monitoring of ladle gates in steel plants., F&E-Konferenz zu Industrie 4.0, Industrie 2025, January 2024

Jeanningros, Loïc; Meister, Théo A.; Soria, Rodrigo; Tanner, Hildegard; Vesin, Jean-Marc; Thiran, Jean-Philippe; Lemay, Mathieu; Braun, Fabian; Rexhaj, Emrush, Heartbeat Detection in Photoplethysmography Signals for the Monitoring of Cardiac Arrhythmias, Annual Meeting of the Cardiovascular Research Cluster Bern (CVRC), Switzerland, January 24, 2024

Kiener, Lionel, Advanced Manufacturing Technologies for Compliant Mechanisms, ESA Mechanisms Final Presentation Days, Noordwijk (NL), March 13, 2024

Krauss, Jens, Digital Health Tools as Driver of the Digital Transformation in Healthcare, Life Span, Health Span, Wealth Span, Zürich (CH), March 19, 2024

Lefèvre, Xavier; Beard, Alexandra; Finelli, Alba; Clement, Pierrick; Bulliard, Xavier; Crenna, Maude; Gay, Julien, Porous layers for environmental (electrochemical) sensors, IEEE Sensors France Chapter Workshop, Grenoble, France, 13-14 June 2024

Lemay, Mathieu, Continuous Monitoring of Physiology and Vital Signs with Photoplethysmography, ActiGraph Digital Data Summit 2024 (ADDS2024), Pensacola Beach, FL (USA), February 28, 2024.

Russi, Mario, Introduction to AI for Agriculture, Student Talk @ BFH-HAFL, March 21, 2024

Russi, Mario, AI for Industry, Diplomfeier HSLU, Mrach 22, 2024

Russi, Mario, Künstliche Intelligenz zwischen Hype und realer Anwendung, Fachtagung KMU goes digital: Im Spannungsfeld zwischen Mensch und Technik, April 10, 2024

Russi, Mario, KI – Chancen in der Instandhaltung? fmpro Symposium - Fachtagung, June 27, 2024

Russi, Mario; Steinecker, Alexander, AI in der produzierenden Industrie: Sprint oder Hindernisparkours? C-Level «AI» Strategie-Forum: Beyond the Hype, Pfäffikon SZ, June 20, 2024

Sacchi, Nazareno; Azarkhish, Erfan; Cattenoz, Régis; Caruso, Francesco; Jokic, Petar; Emery, Stéphane; Jang, Taekwang, A study on MRAM Across Memory Hierarchies for Edge KWS Adaptive Power Cycling, IEEE ICECS24, November 18-20, 2024, paper 4104

Schmid, Philipp A. E., Digitalisierung in der Firma, FRITZ Führungskreise - Plattform Softwareentwicklung, February 15, 2025

Schmid, Philipp A. E., Implementation Insight: KI produktiv zum Laufen gebracht, The Swiss AI Conference 2024, March 5, 2024

Schmid, Philipp A. E., AI for Industry - Reindustrialization & Automation, The Singularity Group Applied Innovation Days, March 8, 2024

Schmid, Philipp A. E., AI for Industry - How production in Switzerland is still possible?, Crypto Mountain Davos 2024, March 12, 2024

Schmid, Philipp A. E.; Rüdlinger, Stephan; Linnenbach, Frank, Deep Learning im Wald, Impulsveranstaltung: Künstliche Intelligenz in der Holzwirtschaft, May 7, 2024

Schmid, David; Demuru, Silvia; Mutton, Renato, Optoelectronics and biosensors against increasing endemic diseases, CSEMnext: Frühling, Pollen und Allergien - Prävention dank Technologie, Landquart (CH), March 2024

Steinecker, Alexander, AI in Industry for Higher Efficiency, IVAM Hightech Summit 2024, Frankfurt (Main), May 7-8, 2024

Wacker, Josias, Shaping the healthcare of tomorrow through patient-centered digital technologies, EMBEC 2024, June 9-13, 2024, Portorož, Slovenia

Research Projects

ANERGYCAD

Anergy grid in Bourg en Lavaux

AOP-PLUGNPLAY

Implementation of adverse outcome pathway in a “plug & play” microfluidics system. Liver fibrosis as a proof of principle

APNEASENSE	PPG-based apnea monitoring and detection tools
ARCTIC	Development of a 10-GHz ultralow noise photonics-based microwave generator that is turn-key and based on a homemade diode-pumped mode-locked solid-state laser
ASSURED-PV	Assessing uncertainties and risks in photovoltaic plant performance and operation
BEAT-IT	Breakthrough multi-purpose electrodes for activity tracking for interoperative patients and elite sport athletes
BESTOBOT	Approaches for highly efficient & scalable solar cells with reduced carbon footprint
BLUVES	Development of nanophotonics based structures to generate blue and UV frequency comb for the calibration of spectrographs used in exoplanet search
COMET	Developement of copper metallization processes for current p-type and future n-type solar cells and modules
COPRESS	Cooperation platform for renewable energy storage systems
COVENT	Improve ventilation safety by means of intra-tracheal pressure monitoring – a short-term and a long-term solution
DARE	Development of AI-supported remote patient monitoring solution
DECIDER	Development of dry electrodes for solid state batteries
EMBODISENSE	Embodiment of sensors to improve real-life gait
EMIL	Emotion in the loop: a step towards a comprehensive closed-loop deep brain stimulation in Parkinson disease
ENABLE	Standardized integrated photonic nonlinear building blocks for lithium niobate on insulator
ENHEART	Exploring full content of optical signals to enhance cardiac arrhythmia screening
ENSQSENS	Novel, ensemble-based quantum sensors
FHE-CLOUD	Fully homomorphic encryption (FHE) based cloud service for healthcare
FITSILVER	Fitness and calorie tracking for the silver generation
GREENSPACK	Green smart packaging for perishable goods
HYPER	Hybrid approach for perovskite-silicon tandem-solar cells
IEA-TASK13-2022	Performance, operation & reliability of photovoltaic systems – Swiss Consortium
IMPULSE	Closed-loop control of blood pressure for people with spinal cord injury
IPRECISE	Industrial passivating contacts approaches for high efficiency c-Si Solar cells
LAMBADA	Lightweight battery pack made by additive manufacturing
LANTERN	Living Labs interface for the energy transition
LINIOS	Gas spectrometer based on lithium niobate on insulator photonics integrated circuit
META-DISPLAYS	Design and fabrication of metasurfaces for rollable displays
MICROAC2	Acoustofluidic platform for 3D positioning of microtissues for efficient microhistology
OPERA	Utilisation optimale de l'énergie renouvelable avec PAC pour les immeubles collectifs en rénovation
OPOSSUM	Ultra-sensitive photonics accelerometers for next generation seismic sensor networks
PAPET	Protective, passivating, and selective transport layers in perovskite/c-Si tandem solar cells
PEDALO	Positive energy district algorithms for load forecasting and optimal dispatch

PHASE-LOGIC	Phase logic networks for optimized computation
PROOFED	Piezoelectric motors for extreme conditions
PUZZLE	Bridging gaps in the neuroimaging puzzle: advanced techniques for comprehensive mapping of brain anatomy and multi-scale network activity
QSBI (MagScopy)	Quantum sensors for brain imaging
RADICALS	Rationally designed thin contact layers enabling large-scale perovskite-on-silicon tandem photovoltaics
RAMSES	High power femtosecond laser system based on ytterbium doped sesquioxide crystals
SAFEUVC	Field-emission 210 nm light source for disinfection
SELFHEALTECH	Technologies for non-invasive diagnostics and self healing
SHAMAN	Shadow mask localization of thin films for back-contacted crystalline silicon solar cells and energy harvesters
SIRIUS	Development of next generation IBC-HJT modules for mass production
SOLARBODY-OFEN	Integration of photovoltaic element for automotive applications
SQ-NET	Scalable high bandwidth quantum network
SWISSCHIPS	Swiss chip-design initiative
TESLA	Transient, electronics for sustainable digital agriculture
UTP4Q	A versatile quantum photonic IC platform through micro-transfer printing
VIPS	Ultra-low power visual perception system

Innosuisse – Swiss Innovation Agency

47005.1 IP-ICT	ADAPTIVESTORM	An ultra-energy-efficient AI chip for next-gen ICT applications
48036.1 IP-ICT	ADRIO-S-LIDAR	Real-time autonomous navigation system for on-orbit servicing
115.669 IP-ENG	AHESS4HD	Active hybrid energy storage system for heavy-duty applications
71400.1 INNO-ICT	AI Layout Study	Configurator tool for coating machinery
107.610.1 IP-LS	AirLiWell	Microstructured membrane for organoid production and culture at air-liquid interface
49735.1 IP-LS	AIRVIMO	Airborne virus monitoring
33572.1 IP-ENG	AMC	Process optimization for additive membrane care
106.920.1 IP-EE	AMICOOL2023	Artificial intelligence for maintenance and improved control of commercial refrigeration systems
55307.1 IP-EE	ATLAS	Development of new generation agrivoltaic translucent module architecture based on silicon
104.300.1 IP-EE	BeePV	Building integrated lightweight PV
73105.1 INNO-ENG	BEER	Heterogeneous compete platform for image processing
70596.1 INNO-LS	Beyond Fertility	Telomerase analysis for fertility assessment
72349.1 INNO-ENG	BILADI	IMU-based power consumption optimization wellness algorithms (steps, fall, ...)

55450.1 IP-EE	BIO-NO2	Reducing agricultural emissions with a new manure treatment technology
70203.1 INNO-LS	BONMORG-Prep	Scale up for in-vitro bioprinted bone tissues
70340.1 INNO-ENG	CAJON	Lightweight bio-based PV module for highway and railway infrastructures
65645.1 INNO-LS	CALFVIEW	Try and adapt cooperative sensors (ECG) and Icarus (Stethoscope) for calf monitoring around neck (collar) or thorax
68886.1 INNO-EE	Carport-Solar	Testing of new design solution for lightweight PV module and mounting structure
35221.1 IP-LS	CEREBRO	ASIC-enabled depth electrodes for neural recording and ablation
114.193.1 IP-LS	CERES 2 (HORM-EC2)	Subcutaneous medical implant providing women with a safer and more effective artificial reproductive treatment
57757.1 IP-ENG	CHAMLED	Development of high-power rod-type femtosecond laser for micro-LED display production
69369.1 INNO-ENG	Check-My-Screw	Quality control of small screws
115.052.1 IP-LS	ChronoType	Functional profiling of cellular aging for personalized immune health
FLAGSHIP PFFS-21-20	CIRCUBAT	Swiss circular economy model for automotive lithium batteries
73319.1 INNO-ENG	Circuit-Eye	AI companion to support manual inspection for small batch sizes
102.375 IP-EE	COLORPOWER	New generation colored encapsulant foil solution for the manufacturing of next-generation-colored photovoltaic modules for building integration
69572.1 INNO-EE	COLORSTILE	Development of new design of solar tile
74242.1 INNO-LS	CORTI-SALIVA	Novel cortisol monitoring sensor
114.917 IP-ICT	CTRL-AM	Closed-loop layer-to-layer control of laser powder bed fusion additive manufacturing
70033.1 INNO-LS	CytoXpress	CytoExpress
107.254.1 IP-LS	DropTCR	TCR cross-reactivity screening. In-droplet screening of reporter ACDC cells expressing genetically encoded peptide libraries against a TCR of interest
102.648.1 IP-LS	DURAPATCH	Implantable patch for dura sealing
105.699 IP-LS	EARONCHIP	Human blood-labyrinth barrier (BLB) organ on a chip platform
103.963 IP-ENG	Easy	Easy assessment of solubility with high efficiency second harmonic light scattering
51474.1 IP-ICT	EBRAIN	Smart robust wireless control and management of heavy machines
68582.1 INNO-LS	eLFA	At-home blood test optimization
68721.1 INNO-ENG	ELOISE	AM-based compliant gimbal for electrical thruster gimbal
103.713 IP-LS	EXTRACE	Enabling single cell resolution analysis of cancer cells extracted from blood
104.350.1 IP-ENG	FEMTOALIGN	Femtolaser-based alignment of atomic clock
71179.1 INNO-LS	FluoDX	Fluorescence neutrophils DX for bacteria diagnostics

101.441 IP-EE	FREESTILE	Development of new generation of photovoltaic tiles demonstrating cost effective manufacturing and high reliability
118.401 IP-LS	FRESH	Novel dental clear aligner with integrated microfluidic channels for precise, high-efficiency antibacterial and fluoride delivery
101.599 IP-ENG	FUTURE-LC	Design, fabrication tolerancing and prototyping of future light carpets
73507.1 INNO-EE	GETPV	Graphene paste for silicon/tandem PV
73434.1 INNO-ENG	HAIRLESS	Human appendage image restoration: lessening excessive strands
106.492.1 IP-LS	Hedgehog	Non-invasive microneedle patch for glucose monitoring of interstitial fluid
100.379 IP-LS	HYGIE	Detection of respiratory infections in indoor spaces
56499.1 IP-LS	Impulse NEON	Neonate monitoring - Add SpO2, BP and oHRM features to OxyPRem NIRS medical system
56426.1 IP-ENG	IMPULSECOREPLATE	Development of a multiwell plate system for accurate 2D and 3D cell-based assays
58669.1 IP-LS	INSPIRING	Development of a device for in-mouth lactate monitoring for sports applications
107.482.1 IP-ENG	ION-POWER	Green and stable high-yield ion fuel development for microfluidics fuel cells applications
103.882.1 IP-ENG	JETOPTICS	Fabrication of microwedges and semi-transparent coatings for pressure/temperature sensing on aircraft engines
74289.1 INNO-LS	LACTATE-DISP	Precision dispensing of different solutions on needles for lactate monitoring
56816.1 IP-LS	LarvaeSorter	Development of a novel device capable of handling zebrafish larvae for high throughput
100.554 IP-EE	LEARN-CEM	Self-learning energy manager
43059.1 IP-ENG	LIFELUB	Development and implementation of a new lubrication technology
103.631.1 IP-ENG	LIGHTMASTER	Développement des cadrants photovoltaïques pour la prochaine génération de montres connectées. Technologie IBC tunnel
71441.1 INNO-ENG	LOPERES	Low perturbation double oscillator in resonance
61056.1 IP-LS	LOPLUS	Machine learning powered light obscuration technology for improved robustness and particle classification
109.391 INT-ENG	LOTIS	Lidar for detailed inspection of underwater structures
70844.1 INNO-LS	LungAIDX	Integrating nasal fluid biomarkers and patient history with multiomics precision
101.321.1 IP-ENG	MARIE	Automatized and electro mechanized syringe for animal health
115.570 IP-LS	MATCHME	Automated microfluidics cancer drug screening using novel liquid handling strategies
116.366 IP-ENG	MATPATCH	Molecular maternity management
61801.1 IP-ENG	M-CUBE	Development of a high-resolution magnetic field gradiometer
71243.1 INNO-LS	MEDULLA	Monitoring of strain on the implant during and after insertion with simplified and less invasive surgery

105.241.1 IP-ENG	METEORE	Developing the mechanical watches of tomorrow
69745.1 INNO-EE	MEZENC	New generation innovative lightweight PV systems
102.837.1 IP-LS	MICE	Multispectral imaging for intra-operative cancer delineation
102.485.1 IP-ICT	MIEWA	Multispectral imaging for examination of works of art
107.611.1 IP-LS	MISO	Automated mitochondria isolation
106.780.1 IP-ENG	MODEN	Design of a moisture and density sensor dedicated to grain and flour flow monitoring during grinding operations
115.293 IP-ENG	MONA	Additive manufacturing of high precision smart medical instruments
73126.1 INNO-LS	Musclespan-IC	Measuring age-related muscle loss using advanced technologies
107.108.1 IP-LS	Neophytes	Efficient, aerial based detection solution for the most significant neophytes in Switzerland
108.672 IP-LS	OPAFA	Redefining standard fatigue assessments with digital biomarkers
113.699.1 IP-EE	OPTIKOAT	Multi-functional optical coatings developments for PV
105.335.1 IP-LS	OrganoCell	Standardized individualized organoid dissociation for single cell downstream analysis
70692.1 INNO-LS	OrganoSpace	Concept development for automated and parallel organoid culture in space
75202.1 INNO-LS	OrgoPrep	BufferPrep organic mixing module (OMM)
60042.1 IP-LS	ORTHO	Closing the gap in digital orthopedics
105.402.1 IP-ICT	Panama	Customer specific, multi-modal solution for automatic characterization of thermoanalytical measurements
61071.1 IP-LS	PERFORM	Biomimetic 3D tumor microenvironment on-chip for preclinical testing of cancer immunotherapies
106.177.1 IP-ENG	PLEASURE	Photoplethysmography simulator for blood pressure
103.067.1 IP-EE	PollutionKeeper2	Water flow and quality monitoring
68993.1 INNO-ICT	ProfileCheck-Study	ProfileCheck-study
104.797.1 IP-ICT	PUMPSTATEDETECTION	Method for detecting the health state of a pump based on both external and embedded sensor systems
67673.1 INNO-ENG	QReam	Quality control and process automation for reaming parts
116.090.1 IP-EE	Quattro	Development of simplified, bifacial, hot-spot resilient tunnel-IBC devices and 4TT devices based thereon
56972.1 IP-ENG	REACT	Development and implementation of a full pipeline for process optimization (offline, refinement & online) for generating gear grinding machines
70175.1 INNO-ENG	SABRA	Feasibility study for an autonomous safety bracelet
69866.1 INNO-ENG	SATISFIED	Sachets and sticks film sealing device
72130.1 INNO-ICT	SCARABEUS	Develop and enhance security of the platform, which is focused on supply chain B2B, logistics and data market
115.570.1 IP-LS	ScreenMe	Automated microfluidics cancer drug screening using novel liquid handling strategies

73444.1 INNO-LS	SECREAC	Magnetic mitohormesis bioreactor for secretome production
102.006 IP-EE	SELMA	Development of Li-metal composite anodes for Li-metal batteries
65610.1 INNO-LS	SINIVALI	Feasibility study on monitoring and assessing risks of preeclampsia
57886.1 IP-ICT	SMARTLADLEGATE	Additive, real-time monitoring system to increase safety and efficiency for steel casting
100.583 IP-ICT	SMARTRAIL	Maintenance, asset management and health indicator of rolling stock materials
43816.1 IP-ENG	SMARTSPRING	Intelligent spring that reduces machine downtime, prevents failures and helps to design the optimum spring
53212.1 IP-ICT	SmartWaste	Plug & play smart waste management
58504.1 IP-ENG	SPADLENS	Reliable development and characterization of SPAD sensors enhanced with thin and gap-less microlenses
53012.1 IP-ICT	SPG-ROBOT	Development of a tool to automate floor processing tasks
72002.1 INNO-SBM	SteelPro	Steel production monitoring with remote sensing for trend generation
101.260.1 IP-ENG	TID	Integrated tourbillon with detent for watch movement
117.762 IP-LS	U-ADD	Digital dipstick for urine analysis
70138.1 INNO-ENG	VIBRATO	Industrial wireless vibration sensing
105.500.1 IP-ICT	Vital-Plus	Continuous non-invasive measurement of core vital signs on the hospital ward

European Commission Projects

HORIZON-KDT-JU-2022-1-IA	14AMI	14-angstrom module integration to advance semiconductor technologies
HORIZON – KDT-JU-2021-1-IA	AGRARSENSE	Smart, digitalized components and systems for data-based agriculture and forestry
H2020 – ATTRACT	AHEAD	Advanced heat exchange device
H2020 – INFRAINNOV-2019-2020	AIDAINNOVA	Advancement and innovation for detectors at accelerators
H2020 – ECSEL-2019-2-RIA	ANDANTE	Ai for new devices and technologies at the edge
HORIZON-KDT-JU-2023-2-RIA-Topic-1	ARCTIC	Advanced cryogenic technologies for innovative computing
HORIZON – CL5-2022-D2-01	BATMAX	Battery management by multi-domain digital twins
HORIZON – CL5-2023-D2-01-04	BATTERY2LIFE	Battery management system and system design for stationary energy storage with 2nd life batteries
H2020 – LC-SC3-RES-6-2018	BESMART	Innovative building envelope for sustainable, modular, aesthetic, reliable and efficient construction
HORIZON-CL6-2023-ZEROPOLLUTION-01	BIOSENSEI	Biosensor-based diagnostic platform enabling real-time monitoring of existing and emerging pollutants
HORIZON-CL5-2023-D3-03	BLAZETEC	High-efficiency, ultra-high-temperature batteries for a green transition
H2020 – FETOPEN	CFLOW	Coherent ultra-fast long wave infrared communications
H2020 – ECSEL-2019-1-IA	CHARM	Challenging environments tolerant smart systems for IoT and AI

HORIZON – CL4-2021	CLUSTEC	Scalable continuous variable cluster state quantum technologies
HORIZON – CL4-2022-HUMAN-02	dAIEDGE	A network of technology enablers for the research and delivery of secure, efficient and scalable AI at the edge & deep edge
H2020 – LC-SC3-EE-2019	DOMOS	Operating system for smart services in buildings
HORIZON – EIC-2021	ECLIPSE	ECL-based infectious pathogen (bio)sensor
HORIZON – KDT-JU-2022-2-RIA	EECONE	European ecosystem for green electronics
H2020 – ICT-2020	ELENA	European electro-optic and nonlinear PIC platform based on lithium niobate
H2020 – NMBP-23-2020	EMAPS	Electro-mechano-active polymer-based scaffolds for heart-on-chip
HORIZON-CL5-2024-D3-01-01	EMPOWER	Alternative advanced manufacturing PV equipment
H2020 – ECSEL-2020-1-IA-two-stage	ENERGY ECS	Smart and secure energy solutions for future mobility
HORIZON – CL4-2022-SPACE-01-11	EROSS-IOD	European robotic orbital support services in-orbit demonstration
HORIZON-CL5-2022-D3-03	EVERPV	Highly efficient delamination technologies to recover and reuse metals, glass, polymers from end-of-life photovoltaic panels
H2020 – FETPROACT-2020-2	EXPERIENCE	The “Extended-Personal Reality”: augmented recording and transmission of virtual senses through artificial-intelligence
HORIZON – CL4-2021 TWIN- TRANSITION-01-02	FLASH-COMP	Flawless and sustainable production of composite parts through a human centred digital approach
HORIZON-CL3-2023-DRS-01	FORESIGHT	Improving last-kilometer navigation & transportation of emergency personnel, equipment and relief items in hazardous and challenging environments
HORIZON – CL5-2021	GENEX	New end-to-end digital framework for optimized manufacturing and maintenance of next generation aircraft composite structures
HORIZON – CL5-2022-D3-01	GLOCALFLEX	A global as well as local flexibility marketplace to demonstrate grid balancing mechanisms through cross-sectoral interconnected and integrated energy ecosystems enabling automatic flexibility trading
H2020 – SC1-2019 Single-Stage-RTD	HEDIMED	Linking immune-mediated diseases to early exposures for innovative solutions
HORIZON-JU-Clean-Aviation-2023-01	HERFUSE	Hybrid-electric regional fuselage & empennages
HORIZON – KDT-JU-2021-1-IA	HICONNECTS	Heterogeneous Integration for connectivity and sustainability
H2020 – LC-BAT-14-2020	HIDDEN	Next-generation lithium-metal batteries with improved quality, reliability, and life (QRL)
H2020 – LC-SC3-RES-15-2019	HIGHLITE	High-performance low-cost modules with excellent environmental profiles for a competitive EU PV manufacturing industry
HORIZON – CL4-2023-DIGITAL-EMERGING-01-53	HIGHLIGHT	Highly integrated versatile laser source enabling two-photon excitation in digital diagnostics and biomedical research
H2020 – LC-SC3-RES-15-2019	HIPERION	Hybrid photovoltaics for efficiency record using integrated optical technology

HORIZON-CL4-2023-DATA-01	HYPER-AI	Hyper-distributed artificial intelligence platform for network resources automation and management towards more efficient data processing applications
HORIZON – CL4-2022-RESILIENCE-01	I-EDGE	Nanomechanical hardware platforms for edge computing
HORIZON – HLTH-2021-ENVHLTH-02	INCHILDHEALTH	Identifying determinants for indoor air quality and their health impact in environments for children: measures to improve indoor air quality and reduce disease burdens
HORIZON – CL5-2023-D3-01	INCREASE	Integrated PV solutions, effective advancements towards uptake of PV integrated in buildings & infrastructure
HORIZON-CL5-2023-D3-02	LAPERITIVO	Large-area perovskite solar module manufacturing with high efficiency, long-term stability and low environmental impact
HORIZON – CL4-2022-DIGITAL-EMERGING-01	LIBRA	Light-based multi-sensing system for screening of pathogens and nutrients in bioreactors
HORIZON – KDT-JU-2022-2-RIA	LOLIPOP-IOT	Long life power IoT solutions for predictive maintenance
HORIZON – CL4-2021	LOLLIPOP	Lithium niobate empowered silicon nitride platform for fragmentation free operation in the visible and the NIR
H2020 – FETFLAG-2018-2020	MACQSIMAL	Miniature atomic vapor-cells quantum devices for sensing and metrology applications
HORIZON – CL4-2022-RESILIENCE-01	MADE-3D	Multi-material design using 3D printing
H2020 – NMBP-FOF-2018	MANUELA	Additive manufacturing using metal pilot line
H2020-ICT-2018-2019	MEDPHAB	Photonics solutions at pilot scale for accelerated medical device development
H2020-ICT-2017-1	MOLOKO	Multiplex photonic sensor for plasmonic-based online detection of contaminants in milk
H2020 – ECSEL-2019-1-IA	MOORE4MEDICA	Open technology platforms for medical devices
HORIZON – MSCA-2021 SE-01	NANOIMMUNOERA	Nanotechnology-enabled detection of clinically relevant antibodies for early cancer Diagnosis and immunotherapy monitoring
H2020 – BG-2020-1	NAUTILOS	New approach to underwater technologies for innovative, low-cost ocean observation
HORIZON – CL5-2022-D2-01	NEMO	Next-generation models for advanced battery electronics
H2020 – LC-SC3-EE-2020-2	NEON	Next-generation integrated energy services for citizen energy communities
HORIZON – CL4-2022-RESILIENCE-01	NETHELIX	Intelligent digital toolbox towards more sustainable and safer extraction of mineral resources
HORIZON – KDT-JU-2021-1-IA	NEWLIFE	New remote non-invasive monitoring solutions for ensuring the health of mothers and babies before and after birth
HORIZON – CL5-2022-D2-01	NEXTBAT	Next generation technologies for battery systems in transport electrification based on novel design approach to increase performance and reduce carbon footprint
H2020 – SFS-2018	NUTRISHIELD	Fact-based personalized nutrition for the young

H2020 – EIC-FTI-2018-2020	OFFSHOREMUSTER	An integrated emergency response decision support system for enhancing workers' safety in offshore oil & gas operations
H2020 – NMBP-FOF-2018	OLED SOLAR	Innovative manufacturing processes and in-line monitoring techniques for the OLED and thin film and organic photovoltaic industries (CIGS and OPV)
HORIZON – CL4-2021	PATTERN	Next generation ultra-high-speed microwave photonic integrated circuits using advanced hybrid integration
HORIZON – CL5-2021	PEPPERONI	Pilot line for European production of perovskite-silicon tandem modules on industrial scale
H2020 – NMBP-TR-IND - 2018-2020	PEROCUBE	High-performance large area organic perovskite devices for lighting, energy and pervasive communications
H2020 – ICT-2019-2	PHABULOUS	Pilot-line providing highly advanced & robust manufacturing technology for optical free-form micro-structures
H2020-DT-2018-2020	PHACTORY	One-stop-shop open access to photonics innovation support for a Digital Europe
HORIZON – CL5-2022-D2-01	PHOENIX	Building more reliable and performant batteries by embedding sensors and self-healing functionalities to detect degradation and repair damage via advanced battery management system
H2020 – FETFLAG-2018-2020	PHOG	Sub-poissonian photon gun by coherent diffusive photonics
HORIZON – CL4-2022-DIGITAL-EMERGING-01-03	PHOREVER	Photonic integrated OCT-enhanced flow cytometry for cancer and cardiovascular diagnostics enabled by extracellular vesicles discrimination
H2020 – DT-2020-1	PHOTONHUB	One-stop-shop open access to photonics innovation support for a Digital Europe
HORIZON-KDT-JU-2023-2-RIA	PHOTONMED	Pilot line for photonics-based medical devices
H2020 – EIC-FTI-2018-2020	PHOTONSENS	A plug-and-play photonics-based biosensing platform for salmon pathogen detection
HORIZON – CL5-2021-D3-03	PILATUS	Digitalised pilot lines for silicon heterojunction tunnel interdigitated back contact solar cells and modules
HORIZON-CL4-2023-DIGITAL-EMERGING-01-CNECT	QUANTIFY	Quantum enhanced photonic integrated sensors for metrology
HORIZON-CL4-2023-TWIN-TRANSITION-01	R3-MYDAS	Remanufacturing, repurposing and recycling energy goods through advanced mechatronic and digital technologies
HORIZON – KDT-JU-2021-2-RIA	REBECCA	Reconfigurable heterogeneous highly parallel processing platform for safe and secure AI
HORIZON – CL5-2022-D2-01	RECIRCULATE	Reuse of batteries through characterization, smart logistics, automated pack and module dismantling and repackaging and a blockchain enabled marketplace
H2020 – LC-SC3-2018-2019-2020	RE-COGNITION	Renewable cogeneration and storage technologies integration for energy autonomous buildings
HORIZON – CL4-2021-RESILIENCE-01	RESILEX	Resilient enhancement for the silicon industry leveraging the European matrix

HORIZON – KDT-JU-2022-2-RIA	RESILIENT-TRUST	Trusted SMEs for sustainable growth of Europe's economical backbone to strengthen the digital sovereignty
H2020 – ICT-2018-20	SARMENTI	Smart multi-sensor embedded and secure system for soil nutrient and gaseous emission monitoring
HORIZON – CL5-2022-D3-01	SEAMLESS-PV	Development of advanced manufacturing equipment and processes aimed at the seamless integration of multifunctional PV solutions, enabling the deployment of IPV sectors
H2020 – SPACE-2018-2020	SELECTOR	SMT compatible electromechanical relay for compact redundancy ring
HORIZON – CL5-2021	SIC4GRID	Next-generation modular SiC-based advanced power electronics converters for enhanced renewables integration into the grid
H2020 – BHC-2018-2020	SIM4BDR	Smart bone regeneration
HORIZON – CL5-2021-D2-01	SOLID	Sustainable manufacturing and optimized materials and interfaces for lithium metal batteries with digital quality control
H2020 – LC-BAT-2020-3	SPARTACUS	Spatially resolved acoustic, mechanical, and ultrasonic sensing for smart batteries
HORIZON – CL5-2023-D3-01	SPHINX	Sustainable photovoltaics Integration in buildings and Infrastructure for multiple applications
HORIZON – CL4-2021	SPRINTER	Low-cost and energy-efficient hybrid photonic integrated circuits for fiber-optic, free-space optical and mm-wave communication systems supporting time critical networking in industrial environments
H2020 – ECSEL-2020-1-IA two-stage	STORAGE	Embedded storage elements on next MCU generation ready for AI on the edge
HORIZON-CL5-2023-D3-02	SUPERNOVA	Tools and solutions for self-governed solar data fusion and insight explosion for management and maintenance of pv plants
H2020 – SPACE-2018-2020	SURPRISE	Super-resolved compressive instrument in the visible and medium infrared for Earth observation applications
HORIZON – KDT-JU-2022-2-RIA	SUSTRONICS	Sustainable electronics for circular economy and eco-design
HORIZON – CL5-2022-D6-02	TRACE	Integration and harmonization of logistics operations
H2020 – ICT-2020-2	TRIAGE	Development of a smart, compact and cost-effective optical air quality sensor network for the hyperspectral detection of all relevant atmospheric pollution gases
HORIZON – CL2-2022-HERITAGE-01	TRIQUETRA	Toolbox for assessing and mitigating climate change risks and natural hazards threatening cultural heritage
HORIZON – CL5-2021-D3-02	TRIUMPH	Triple junction solar modules based on perovskites and silicon for high performance, low-cost and small environmental footprint
HORIZON-CL6-2023-ZEROPOLLUTION-01	UNIVERSWATER	Universal interoperative sustainable agri-water management platform
HORIZON-KDT-JU-2023-1-IA	UNLOOC	Unlocking data content of Organ-On-Chips
HORIZON – CL5-2021-D3-03	VALHALLA	Perovskite solar cells with enhanced stability and applicability
H2020 – INFRAIA-2020-1	VIPERLAB	Fully connected virtual and physical perovskite photovoltaics lab
H2020 – ICT-2018-2	WELMO	Wearable electronics for effective lung monitoring
H2020 – ICT-2019-2	ZEROAMP	Nanomechanical switch-based logic and non-volatile memory for robust ultra-low power circuits

European Space Agency, Swiss Space Office, and Swiss Space Center Projects

ESA Projects

AEOLUS-BSM	Beam steering mechanism
AMARETTO	Optically pumped magnetometers for Earth observation
AMICA	Flexure pivot for SPICA SAFARI in additive manufacturing
ANGELE	Motion transformation compliant mechanism based on additive manufacturing
ASTROBOX	Laser frequency comb for the NIRPS astronomical spectrograph
ATOM	Additive manufacturing of metal matrix composites for space application
BATMAM	Additive manufacturing for multifunctional battery packaging
CAMPING	Innovative compliant structures enabling damped precision motion guiding
CASSANDRA	Composite autonomous sensing and repair
CCM_MTG	Development and manufacture of corner cube mechanisms for MTG satellite
CRUSSADER	Capture system for servicing and debris removal
DESCARTES	Embedded thrust vector tilting technology based on smart devices
ELISAMET	Laser metrology for the LISA mission
EXCALIBUR	Exoplanet search calibration uniter
FIFREDO	Fibered frequency doubler at 1560 nm
GC-Connect	Development of fluidic connections and packaging for gas chromatography chips
GLOOM	Design for additive manufacturing of spaceborne compliant mechanisms
HEROIC	High-power fibre-coupled optical switch for space applications
IMPROVE	Microvibration simulation and analysis tools
INWAVE	Developement and validation of three breadboards of fully integrated passive feed chains (including diplexers, OMTs, filters) at Q, V and W-band respectively
ISOL	Development of a high performance microvibration isolation system
LARSEN	Laser stabilisation unit EQM for NGGM
LESS	Microchip laser specification and test
LICORIS	Development of a compact LiDAR for futur new space mision
LINES	Lidar for infrastructure, natural risks, and environmental survey: space technology transfer programifac
LINGO	Flexible hinge design and analysis for the LISA optical assembly tracking mechanism development
LISA_mvib	Actuator modelling and testing in micro-vibration (exported forces)
LPC	Low-power cathodes: development of field emitting cathodes arrays for space neutralisers
LPcsRO	Low-power chip-scale rubidium oscillator
MACADAM	Magnetically levitated pump for space applications: requirements definition and commercial evaluation
MBRW_DR2	Magnetic bearing-based reaction wheel
MCC-X	Development of a miniaturized motor controller for space exploration
NUANCESTOR	Frequency anchor for cross-calibration of extreme precision astronomical spectrographs
OSIP-2PH	Light-shift reduction of two-photon rubidium atomic clock
OSIP-VIB	Adaptive regulation for micro-vibration active-passive isolation systems
OSRC	Digital stabilisation electronics for lasers
PHOTAC_DERISK	Future on-board atomic clock critical items de-risking
POWERSAIL	Disruptive PV power array technology to enable economic viability of SPS

QMPARE	Quantum compact reference
RESHAPE	Reusable shape memory shock absorption elements for future landing systems using additive manufacturing (OSIP)
R-MTS	Development and fabrication of robust miniature timing source (R-mTS) engineering models (EMs). These R-mTS EMs are double-resonance miniature atomic clocks
SLOTT	Straylight lidar OGSE verification tool
SPARCOM	Ruggedized hermetically sealed optical cavity for high repetition rate ultrafast lasers
STAMP	Laser detector and laser retro reflector array unit tester development
SUPERGAN	Supercontinuum generation in a nitride semiconductor photonic integrated circuit
TEM-BULB	Follow-up project for the finished AGAL project
TRACTOR	Smart materials for space actuators
TRUMET-PDIODE	Characterization of photodiodes for the ESA's TRUTHS mission
WALLIE	Development new time-of-flight detector
WAVEGUIDE	Development of waveguide switches based on friction-free mechanisms

The Carnegie Institution for Science – Observatories

MIRMOS PHASE-B+ Assessment of pre-production electronic rack

Industrial Property

Patent portfolio

In 2024, CSEM filed on its name 21 patent applications related to new inventions (first filings). All of these filings were regular applications (no provisional filings).

The patent portfolio was further enhanced by the extension to different countries of 7 patent applications based on previously filed inventions.

9 additional patents were filed in the name of CSEM partners as a first filing for an invention developed in cooperation with CSEM inventors.

Collaboration with Research Institutes and Universities

University	Institute	Professor	Field of collaboration
Aarhus University	Department of Biomedicine	K. Eyer	Single cell technologies
Agroscope	Animal Production Systems and Animal Health	C. Ollagnier	Vital sign monitoring in livestock (pigs)
Alpen-Adria-Universität Klagenfurt, Austria	Digital Age Research Center	E. Oswald	Cryptography & security
AO Research Institute Davos	Regenerative Orthopaedics	S. Grad, M. Stoddart	Biosensing
BFH	Inst. Human Centered Engineering (HuCE)	T. Niederhausen, G. Kuert	Packaging & bonding
Carolina Center for Neurostimulation	Department of Psychiatry, UNC School of Medicine, Chapel Hill, NC	F. Frohlich, A. Seiler	Effects of transcranial alternating current stimulation (tACS) on memory recall and sleep-EEG in healthy elderly participants
CHUV Lausanne	Head and Neck Surgery	S. Christian	Multispectral endoscopy for real time delineation in surgery
CHUV Lausanne	Department of Nephrology and Hypertension	M. Pruijm	Continuous blood pressure monitoring in dialyzed patients

University	Institute	Professor	Field of collaboration
CHUV Lausanne	Department of Cardiology	E. Pruvot	Classification of cardiac arrhythmias
CHUV Lausanne	Department of Nephrology and Hypertension	G. Wuerzner	Long-term blood pressure monitoring in patients with chronic hypertension
EMPA	Cellulose & Wood Materials	G. Nyström	Sustainable electronics
ENISE Lyon	Laboratoire de Tribologie et Dynamique des Systèmes	E. Cabrol	Powder spheroidisation
EPF Lausanne	Institute of Bioengineering / Bionanophotonic Systems Laboratory	H. Altug	Optical biosensors
EPF Lausanne	PVLab	C. Ballif	PV modules and cells
EPF Lausanne	Laboratory of Nanobiotechnology	A. Boghossian	Optical biosensors
EPF Lausanne	TCL Telecommunications Circuits Laboratory	A. P. Burg	Ultra-low power design, bias control
EPF Lausanne	EPFL STI IEM SCI-STI-SC	S. Carrara	Biosensing
EPF Lausanne	Laboratoire d'architecture quantique (STI IMT AQUA)	E. Charbon, C. Bruschini	Color filter arrays and on-chip microlens arrays for photodetectors (SPAD)
EPF Lausanne	Mixed-Signal Integrated Circuits Lab	K. Choo	RF transceiver
EPF Lausanne	Laboratory of Systems Biology and Genetics	B. Deplancke	Genomics
EPF Lausanne	LTS4 Signal processing laboratory	P. Frossard	Privacy preserving machine learning and hierarchical computing
EPF Lausanne	Computer Vision Laboratory	P. Fua	Reduced labelling machine learning
EPF Lausanne	Laboratoire de physique des hautes énergies OS (SB IPHYS LPHE-OS)	G. Haefeli	On-chip microlens arrays for photodetectors (SiPM)
EPF Lausanne	EPFL-ECAL Lab	N. Henchoz	Digital experience – Meditation study in collaboration with Ming Shan (Bullet's Taoist center)
EPF Lausanne	LAP Processor Architecture Laboratory	P. lenne	Embedded systems
EPF Lausanne	Thermomechanical Metallurgy Laboratory	R. Logé	Additive manufacturing of shape memory lattice structures
EPF Lausanne	Laboratory for Biomedical Microfluidics	C. Merten	Microfluidics
EPF Lausanne	Distributed Electrical Systems Laboratory (DESL)	M. Paolone	Predictive maintenance for batteries
EPF Lausanne	Integrated Neurotechnologies Laboratory	M. Shoaran	Biomedical circuits
EPF Lausanne	STI IEM SCI-STI-AS	A. Skrivervic	Wireless power transfer
EPF Lausanne	School of Engineering, Institute of Bioengineering	D. Van De Ville	Cuffless blood pressure estimation using raw photoplethysmography signal & wearable heart rate measurement during daily life and sport

<i>University</i>	<i>Institute</i>	<i>Professor</i>	<i>Field of collaboration</i>
EPF Lausanne	School of Computer and Communication Sciences	S. Vaudenay	Security
EPF Lausanne	Advanced NEMS Laboratory	G. Villanueva	PhD Thesis Advisor on MEMS and RF IC integration for IoT (SwissChips)
ETH Zurich	Integrated Systems Laboratory	L. Benini	RISC-V; Neural network
ETH Zurich	Computer Science	S. Capkun	System security group
ETH Zurich	Computational Mechanics Lab	L. De Lorenzis	Mechanical engineering
ETH Zurich	Department of Biosystems Science and Engineering	P. Dittrich	Sample preparation for diagnostics
ETH Zurich	Neurotechnology Group	M. F. Yanik	Neurotechnologie
ETH Zurich	Department of Biosystems Science and Engineering	A. Hierlemann	Organoid sorting
ETH Zurich	Intelligent Interactive Systems	C. Holz	Machine learning
ETH Zurich	Energy-Efficient Circuits and IoT Systems	T. Jang	Analog-to-digital converters
ETH Zurich	Computer Vision Laboratory	E. Konukoglu	Machine learning
ETH Zurich	Department of Biosystems Science and Engineering	S. Panke	Enzyme development, droplet microfluidics
ETH Zurich	Macromolecular Engineering Laboratory	M. Tibbitts	Acoustofluidics
ETH Zurich	Dept. of Information Technology and Electrical Engineering	H. Wang	Wireless power transfer; PhD Thesis Advisor on G-Band Radar-on-Chip (Swisschips)
FHNW, University of Applied Sciences and Arts Northwestern Switzerland	Institute for Pharma Technology	M. Kuentz	Analytical tools for pharmaceuticals
FHNW, University of Applied Sciences and Arts Northwestern Switzerland	Institute for Chemistry and Bioanalytics	D. Meinel	Biosensing
FHNW, University of Applied Sciences and Arts Northwestern Switzerland	Institute of Chemistry and Bioanalytics	L. Suter-Dick	Biosensing and 3D in-vitro models
Haute Ecole d'Ingénierie et de Gestion du Canton de Vaud (HEIG-VD)	Institut de recherche appliquée et développement	E. Messerli	FPGA programming and embedded processing
HE-ARC La-Chaux-de-Fonds	Engineering – Medical Devices	A. Kaempfer-Homsy	Biosensing

<i>University</i>	<i>Institute</i>	<i>Professor</i>	<i>Field of collaboration</i>
HEIA-FR, Fribourg	Génie électrique	E. Fragnière	Expert bachelor projects; Supervision internship 60GHz radar EVK development; sabbatical semester on analog IC design for machine learning at CSEM
HEIG-VD, Yverdon-les-Bains	Information and Communication Technologies	A. Duc	Security
HES HE-Arc, Neuchâtel	Material Science	J. Charmet	Sustainable electronics
HES HE-Arc, Neuchâtel	Computer Science	S. Monnerat	Embedded software
HES HE-Arc, Neuchâtel	Institut d'ingénierie	N. Pasoz Escudero	Embedded & edge AI, sustainable electronics
Idiap Research Institute	Speech and Audio Processing	M. Magimai Doss	Detection of QRS landmark in ECG signals
Inselspital, Universitätsspital Bern	Chirurgie viscérale	Y. Borbély	Oesophageal reflux detection/monitoring
Inselspital, Universitätsspital Bern	Universitätsklinik für Pneumologie	S. Guler	Electrical impedance tomography for the functional assessment of patients with interstitial lung disease and/or pulmonary hypertension
Inselspital, Universitätsspital Bern	Universitätsklinik für Pneumologie	C. Horvath	Detection of atrial fibrillation and other cardiac arrhythmic events during sleep polysomnography
Inselspital, Universitätsspital Bern	Universitätsklinik für Intensivmedizin	C. A. Pfortmüller	Non-invasive measurements of changes in pulmonary artery pressure in intensive care unit patients using electrical impedance tomography
Inselspital, Universitätsspital Bern	Universitätsklinik für Frauenheilkunde	A. Radan, D. Surbek	AI-based decision support system for delivery & fetal monitoring by transabdominal electrocardiogram recording
Inselspital, Universitätsspital Bern	Department of Cardiology and Clinical Research	E. Rexhaj	Post-partum blood pressure monitoring in pregnant preeclamptic patients
Inselspital, Universitätsspital Bern	Department of Cardiology and Clinical Research	E. Rexhaj, R. Bulgheroni Luigi	Long-term blood pressure monitoring in patients with chronic hypertension
Inselspital, Universitätsspital Bern	Universitätsklinik für Neurologie, Leitender Arzt, Geschäftsführender Direktor Schlaf-Wach-Epilepsie-Zentrum (SWEZ)	K. Schindler	Epilepsy detection and prediction
Inselspital, Universitätsspital Bern	Universitätsklinik für Kardiologie	B. Schnegg	Pilot study on non-invasive blood pressure monitoring in patients with a left ventricular assist device
Inselspital, Universitätsspital Bern	Department of Diabetes, Endocrinology, Nutritional Medicine and Clinical Nutrition (UDEM)	C. Stettler	Vocal biomarkers for the detection and prevention of hypoglycaemia (HypoVoice)

University	Institute	Professor	Field of collaboration
Inselspital, Universitätsspital Bern	Department of Diabetes, Endocrinology, Nutritional Medicine and Clinical Nutrition (JDEM)	C. Stettler, V. Lehmann	Non-invasive glucose measurement using impedance tomography (GLEAM)
Inselspital, Universitätsspital Bern	Universitätskliniken für Neurologie und Neurochirurgie	W. Z'Graggen	Blood pressure monitoring in patients with autonomic neuropathy
IOB - Institute of Molecular and Clinical Ophthalmology Basel	Human Organoid Platform	M. Renner	Retina organoid sorting
Kantonsspital St. Gallen	Klinik für Pneumologie und Schlafmedizin	M. H. Brutsche	Unobtrusive long-term monitoring of sleep apnea using photoplethysmography
KNF-Laboratori Oy (Finland)	Sleep Lab	J. Heiskala	Technical feasibility study on screening sleep related breathing disturbances and sleep apnoea with wearable sensors (SCREENBEAT)
Ł-IMiF Sieć Badawcza Łukasiewicz - Poland	Instytut Mikroelektroniki i Fotoniki	B. Synkiewicz-Musialski	Sustainable electronics
Radboud University, Nijmegen, Netherlands	Institute for Computing and Information Sciences	B. Mennink	Security
Réseau Hospitalier Neuchâtelois (RHNe)	Department of Anaesthesiology	Y. Degiorgis	VITAL+, continuous non-invasive measurement of core vital signs on the hospital ward
Réseau Hospitalier Neuchâtelois (RHNe)	Department of Cardiology	C. Pellaton	Comparison of cardiac activity information contained in 1-lead ECG and multi-lead ECG signals (SCREENBEAT)
RhySearch	Ultra-Precision Manufacturing Lab	R. Catrin	Microfluidic chip manufacturing
Robert-Bosch-Hospital	Clinical of Geriatric Rehabilitation	C. Becker	Fall prediction and detection
Swedish University of Agricultural Sciences	Biosystems and Technology	A. Herlin	Vital sign monitoring in livestock (pigs) in the framework of IoF2020
Swiss TPH	Department of Medicine	D. Paris	Diagnostics
The Open University	Faculty of Science, Technology, Engineering & Mathematics	S. Psoma	Biosensing
Tor Vergata (Rome -IT)	Dipartimento di Scienze e Tecnologie Chimiche	A. Porchetta	CRISPR-Cas biosensing
TU Delft, Netherlands	Electronic Instrumentation Laboratory	K. Makinwa	Always-on circuits for IoT
TU Delft, Netherlands	Faculty of Electrical Engineering, Mathematics, and Computer Science	Q. Wang	Embedded & edge AI
Università della Svizzera italiana	Istituto ricerche solari Aldo e Cele Daccò (IRSOL)	R. Ramelli, D. Gisler	Optical systems for CCD cameras
Université de Sherbrooke	Neonatology	E. Fortin-Pelerin	Evaluation of PAP measurement accuracy in sheep and neonatal human patients

<i>University</i>	<i>Institute</i>	<i>Professor</i>	<i>Field of collaboration</i>
University Hospital Basel	D&ICT / Internal Medicine	J. Eckstein	Multifunctional, calibration-free & integrated wearable for non-invasive blood pressure monitoring
University Hospital Basel	Research Center for Clinical Neuroimmunology and Neuroscience	J. Lorscheider	improving monitoring solutions for multiple sclerosis patients
University Hospital Inselspital Bern	Lung Cancer Center	G. Kocher	Machine learning for efficient surgery
University of Athens, Greece	Dept. of Informatics & Telecommunications	S. Hadjilefthymiades	Internet of things, location-based services, mobile and vehicular applications
University of Basel	Biomedicine	V. Petkovic	Inner EarResearch
University of Bern – ARTORG	Organs-on-Chip Technologies	O. Guenat	Organ-on-chip, AI for multi-omics
University of Geneva	Faculty of Science	E. Bakker	Biosensing
University of Geneva	Department of Medicine	O. Preynat-Seauve, K. H. Krause	Organoid production
University of Glasgow, UK	James Watt School of Engineering	J. Kettle	Sustainable electronics
University of Lausanne (NTIL)	Department of Information Systems	K. Huguenin	Privacy and security in healthcare IoT systems
University of Modena Reggio-Emilia, Italy	Dipartimento di Scienze Fisiche, Informatiche e Matematiche	P. Burgio	
University of Tempere, Finland	Faculty of Information Technology and Communication Sciences	M. Mäntysalo	Sustainable electronics
University of Zurich	Institute of Neuroinformatics	T. Delbrück	On-chip convolutional neural network for visual scene processing
University of Zurich	Sensors Group at Institut für Neuroinformatik,	S.-C. Liu	Neuroinformatics
Vrije Universiteit Brussel	ETRO – Engineering ICT & Electronics	M. Kuijk	On-chip microlens arrays for photodetectors (SPAD)
ZHAW, Zurich University of Applied Sciences	School of Engineering, Winterthur	A. Drewek, R. Locher	Joint Innosuisse with Mettler-Toledo: Automatic evaluation of thermoanalytical curves (35056.1 IP-ENG)
ZHAW, Zurich University of Applied Sciences	School of Life Sciences and Facility Management, Wädenswil	M. Rimann	Organoid automation
ZHAW, Zurich University of Applied Sciences	High Performance Embedded Platforms	M. Rosenthal	Embedded & edge AI

Teaching

	<i>Title of lecture</i>	<i>Context</i>	<i>Location</i>
G. Basset	Industrial Applications of Micro & Nano Optics	Collaboration on the teaching unit "Technologies Optiques – TNOP"	Université de technologie de Troyes

	<i>Title of lecture</i>	<i>Context</i>	<i>Location</i>
G. Basset	Micro-Nano Optics: Principle, Fabrication Methods and Industrial Applications	Erasmus Mundus Joint Master Degree Photonics For Security Reliability And Safety Course	University of Saint Etienne
O. Chételat	Sensors in Medical Instrumentation	EPFL Course EE-511	EPFL Campus
A. Corbaz	Operating System	Bachelor course	HEIG-VD
A. Corbaz	Real-Time Computing	Bachelor course	HEIG-VD
M. Despont	Packaging and Hybridization, the Valorization of MEMS Technologies	Micro- 534 Advanced MEMS 2022 (D. Briand)	EPF Lausanne
L. A. Dunbar	Digital Transformation	EMBA	EPF Lausanne
L. A. Dunbar	Professor of Practice	College of management	EPF Lausanne
L. A. Dunbar	Digital Transformation	EMBA	Imperial College Business School London
R. Krähenbühl, etc.	Nanotechnology and Industrialization at CSEM	Information lecture & excursion/visit of CSEM Basel	Uni Basel, SNI
F. Kurth	Microfluidics in Life Sciences: translating ideas to industrial solutions	Forschungsseminar FHNW	FHNW, Muttenz
M. Lemay, P. Renevey, J. Jorge, M. Proença, G. Bonnier, C. Moufawad El Achkar, C. Aguet, K. Adam	Applied Biomedical Signal Processing	EPFL Course EE-512	EPFL Campus
S. Morisod, S. Blanc, B. Roustom	Tendances transformationnelles	CAS en management du changement	University of Lausanne
D. Ruffieux	Radio Frequency Circuits Design Techniques	Master course	EPF Lausanne

Theses

PhD Degrees Awarded in 2024

<i>Name</i>	<i>University</i>	<i>Title</i>
Ahmadi Najafabadi, Amir Mohsen	EPF Lausanne	Target-oriented mm-wave wireless power transfer for IoT applications
Sainz Martinez, Cristina	University of Lausanne	Novel approaches for human brain monitoring with electroencephalography and magnetic resonance imaging at 7 Tesla
Sepehri, Yamin	EPF Lausanne	Smart edge for hierarchical vision systems
Sideris, Iason	ETH Zurich	Path planning optimization in deposition-based additive manufacturing

CSEM Employees carrying out a PhD & PhD Funded by CSEM

Name	Professor / University	Theme / CSEM Unit	Start year
Arefi, Fatemeh	G. Villanueva / EPF Lausanne	Acousto-optic modulators with LNOI technology / Micro & Nano Systems	2023
Bhoir, Shubham Sharad	M. Paolone / EPF Lausanne	Exploitation of electrochemical impedance spectroscopy for predictive maintenance for batteries / Sustainable Energy	2021
Blache, Manon	K. Eyer and J.C. Leroux / ETH Zurich and Aarhus University	Highly selective continuous flow isolation of circulating rare cells from whole blood and retrieval for droplet microfluidic single cell analysis / Industry 4.0 and Life Sciences	2023
Blum, Roman	G. Miletti / University of Neuchâtel	Long-term frequency stability improvement of a 2-photon Rubidium clock / Instrumentation	2021
Brero, Giorgio	P. Dittrich / ETH Zurich	Extracellular vesicle isolation from whole blood and labeling for flow cytometry / Industry 4.0 and Life Sciences	2023
Brock, Lukas	L. De Lorenzis / ETH Zurich	Process agnostic modelling and optimization / Industry 4.0 and Life Sciences	2024
Chen, Xi	T. Jang / ETH Zurich	Area-efficient neural recording frontend / Integrated and Wireless Systems	2024
De Sousa, Leticia	G. Villanueva / EPF Lausanne	<i>not defined yet</i> / Integrated and Wireless Systems	2024
Diez Clos, Arnau	M. Shoaran / EPF Lausanne	CMOS-based low-power Closed-loop biomedical interfaces / Integrated and Wireless Systems	2024
Ebrahimi Argi, Farnaz	A. Eichler / ETH Zurich	Ultra-sensitive photonics accelerometers for next generation seismic sensor networks / Micro & Nano Systems	2023
Fattah, Hasti	F. Yanik / ETH Zurich	Wireless power transfer for implantable devices / Integrated and Wireless Systems	2024
Ghorbanpoor, Mohsen	H. Wang / ETH Zurich	Receiver SoC for long range mm-wave wireless power transfer with focus on IoT applications / Integrated and Wireless Systems	2022
Hafer, Kilian	H. Wang / ETH Zurich	High-millimeter-wave radar integrated circuits for 6G applications / Integrated and Wireless Systems	2024
Hefti, Olivia	C. Brès / EPF Lausanne	Periodic poling of lithium niobate on insulator photonics waveguide and its application / Instrumentation	2022
Keller Martinez, Daniel	L. Benini / ETH Zurich	Area-efficient neural recording frontend / Integrated and Wireless Systems	2024
Klauser, Elias	A. Karimi / EPF Lausanne	Control for hybrid micro-disturbance isolation systems / Instrumentation	2020
Knuchel, Benoît	E. Oswald / AAU Klagenfurt	Embedded intrusion detection for the IoT / Integrated and Wireless Systems	2022
Lang, Guilain	M. Meboldt / ETH Zurich	Automatic generation of compliant mechanism designs / Instrumentation	2021
Luongo, Francesca	E. Konukoglu / ETH Zurich	Generative methods for organoid data augmentation and generation / Industry 4.0 and Life Sciences	2022
Miotello, Enrico	T. Jang / ETH Zurich	Advanced ADC design / Integrated and Wireless Systems	2022

Name	Professor / University	Theme / CSEM Unit	Start year
Narduzzi, Simon	S.-C. Liu / ETH Zurich	Ultra-low power resource algorithms for neuromorphic hardware / Integrated and Wireless Systems	2020
Rospars, Nicolas	ETH Zurich	<i>not defined yet</i> / Sustainable Energy	2023
Sacchi, Nazareno	T. Jang / ETH Zurich	Compression-aware hardware architectures for edge AI / Integrated and Wireless Systems	2022
Snoeijns, Jan	L. Benini / ETH Zurich	<i>not defined yet</i> / Integrated and Wireless Systems	2024
Urhan, Özcan	H. Wang / ETH Zurich	<i>not defined yet</i> / Integrated and Wireless Systems	2024
Vuille-dit-Bille, Emilie	S. Sakar / EPFL Lausanne	Acoustic manipulation of organoids / Industry 4.0 and Life Sciences	2021
Xu, Shijie	A. Burg / EPFL Lausanne	<i>not defined yet</i> / Integrated and Wireless Systems	2024

Commissions and Committees

P.-J. Alet	Committee, Co-leader of the Digital PV & Grid Working Group European Technology and Innovation Platform – Photovoltaics (ETIP-PV): Member of the Steering Top Jury, EM-Power Award Top Jury, Intersolar Award
G. Basset	Bern Medtech Collaboration Calls (BMCC)
C. Beyer	Member of the board of Sensors.ch association
L. Burr	Expert for bachelor and master theses program at HE-ARC PhD Thesis Co-Director at EPFL
S. Cattaneo	Expert for MSE Master Theses at OST Eastern Switzerland University of Applied Sciences Expert for W.A. de Vigier Foundation Innovation Coach for INOS Innovationsnetzwerk Ostschweiz
P. Dallemande	Member of EpoSS Edge AI working Group Swiss representative of Technical Committee 5 "Information Technology Applications", International Federation for Information Processing (IFIP)
M. Despeisse	Committee of nPV workshop and of IPV workshop, scientific committee of EUPVSEC conference
M. Despont	Chairman of the Swiss-MNT network Swiss Representative of the iMNEs (international Micro and Nano Engineering society)
L. A. Dunbar	Academic co-Lead of Machine Learning Clinic in the Swiss Alliance for Data-Intensive Services Jury member of the BCN innovation prize TinyML Swiss Committee
S. Emery	Member of the Technical Committee of the IEEE SOI-3D-Subthreshold (S3S) Conference
A. Faes	Chair or the PVinMotion Conference 2024, Co-organizer of Metallization & Interconnection for Crystalline Silicon Solar Cells Workshop (MIW2024 & MIW2025), IEA PVPS-Task 17 about PV and Transportation Swiss Representative Member, Solar Swiss Connect Committee Member, scientific committee of EUPVSEC conference, ASOM Member, ETIPV Intergated PV Member, Expert ANR
B. Gallinet	Advisory Board Member, Erasmus Mundus Joint Master Intelligent Photonics for Security, Reliability, Sustainability and Safety Jury Member for DayOne Tech start-up accelerator

E. Györvary	<p>Core group member and CSEM representative of EARTO Working Group on Emerging Technologies for Healthcare</p> <p>Member and CSEM representative of EPOSS Association; Chair of WG Green ECS</p> <p>Member of Finnish Chamber of Commerce in Switzerland</p> <p>Member of the Board of European Organ-on-Chip Society (EUROoC)</p> <p>Member of the Organizing Committee and session chair of EUROoCS Annual event 2024</p> <p>Member of the Scientific & Organizing Committee of "Next Gen Organ-on-Chip & Organoids" event</p> <p>Member of the Steering Board of Innovation Group Digitalization at Swiss Food Research</p> <p>President (2024) of the Heterogeneous Technology Alliance and member of the Extended Board (alliance federating the Fraunhofer (microelectronics), VTT, CEA-Tech, and CSEM)</p>
H. Heinzelmann	<p>Expert, Austrian Research Promotion Agency FFG</p> <p>Expert, German Federal Ministry of Education and Research BMBF</p> <p>Member of the Board of the Heterogeneous Technology Alliance (HTA)</p> <p>Member of the Board, Advanced Manufacturing Technology Transfer Centers (AM-TTC)</p> <p>Member of the Executive Board, EARTO</p> <p>Member of the Foundation Board, Switzerland Innovation</p> <p>Member of the Strategic Advisory Board "Produktion der Zukunft", Austrian Federal Ministry for Climate Action, Environment, Energy, Mobility, Innovation and Technology (BMK)</p> <p>Membre du Conseil d'Administration de Centredoc</p>
A. Hutter	<p>BEPA – Batteries Europe integrated working group member to WG5 Mobility Applications and Integration</p> <p>Federal Office of Transport (FOT), Energy Strategy for Public Transport 2050 (ESPT 2050) programme, expert</p> <p>Innosuisse expert</p> <p>President iBAT Association (www.ibat.swiss)</p>
A. Ingenito	BEPA – Batteries Europe integrated working group member to WG3 Advanced Materials and WG4 Cell Design and Manufacturing
H. F. Knapp	<p>Board of Directors member for cluster initiative Toolpoint for Lab Science</p> <p>Jury member for the Innovationspreis of the Industrie- & Handelskammer Zentralschweiz</p> <p>Jury member for Zinno Ideenscheck</p> <p>Pre-jury member for Swiss Technology Award</p>
J. Krauss	<p>Board member of the Deep Tech Switzerland Foundation</p> <p>Member of Program Committee of the Swiss Medtech Day (SMD)</p> <p>Member of the Innovation Committe of the Swiss Medtech Association</p>
F. Kurth	<p>Academic supervisor and external expert for PhD program at D-BSSE, ETHZ Basel & at D-CHAB, ETHZ Zurich</p> <p>Advisory Board Next-Gen Single Cell Omics Workshop</p> <p>Bioincubate startup track advisor</p> <p>Coach and jury member BioIncubate, ETH Zürich, Zurich</p> <p>Expert for bachelor and master theses program at FHNW Muttenz</p> <p>Member of the E&S committee, International Conference on Miniaturized Systems for Chemistry and Life Sciences (mTAS)</p> <p>Organizing committee member and executive program committee member Swiss e-Print</p>
M. Lemay	Board Member, Swiss Society for Biomedical Engineering
S. Paoletti	<p>Biointerfaces Scientific Committee</p> <p>Chair of the Swiss Symposium in Point of care diagnostics</p> <p>Digital Health Innovation Booster Steering Committee</p> <p>Executive Board member of biotechnet, Switzerland and co-lead of the IVD platform</p> <p>Member of the Bridge proposal evaluation panel</p> <p>Tech4Eva Mentor</p>

A. Pauchard	Membre du Comité de pilotage CSEM-Inselspital-Universität Bern Membre du Conseil d'administration d'EARTO Membre du Conseil de fondation de Switzerland Innovation
V. Pejchal	Member Additive Manufacturing Expert Group SATW Member Steering Committee SATW Advanced Manufacturing Research Alliance
D. Petri	Member of the Scientific Committee for the AgriVoltaics World Conference
A.-S. Porret	Full Member of the Swiss Academy of Engineering Sciences SATW
V. Revol	Board Member, Health Tech Cluster Switzerland Co-Founder and deputy head of the Digital Innovation Hub LifeHub.Swiss (www.lifehub.swiss) InnoSuisse expert
D. Ruffieux	Chair of the RF and mm-Wave Circuits Track of the International Technical Program Committee of the European Solid State Circuit Conference (ESSCIRC)
D. Schmid	Co-initiator Diversity-gr platform for diversity in leadership & tech Expert for bachelor and master theses program at HSLU Jury member for Tech Startup Award Südostschweiz Point of entry INOS Innovationsnetzwerk Ostschweiz President of the Board KinderLab Landquart, Switzerland
P. Steiert	Advisory Board Member for Institute für Chemistry and Biological Chemistry at the ZHAW Advisory Council for cluster initiative Toolpoint for Lab Science Member of the Executive Board for Verein Nachhaltigkeitsnetzwerk Zentralschweiz Member of the Executive Board for Verein Startup Pilatus
A. Steinecker	Cluster manager "Production & Systems" at Technologie Forum Zug Coach for RIS Zentralschweiz CSEM contact for Smart Card Forum (René Meier, HSLU) CSEM Representative EPoSS and Member of Working Group Robotics CSEM Representative IVAM
T. Valentin	Bioincubate startup track advisor

Prizes and Awards

April 2024	Olatz Arriaga Arruti won the best poster award at the SiliconPV 2024 with her poster named "Are All Bifacial High-Efficiency c-Si Technologies Equally Sensitive to Potential-Induced Degradation?".
June 2024	Paul Scharnhorst won the IEEE CSS Swiss Chapter Young Author Best Journal Paper Award 2024 for his work on "Robust Uncertainty Bounds in Reproducing Kernel Hilbert Spaces: A Convex Optimization Approach".
June 2024	Roman Blum was awarded the Best Poster Award at the 2024 EFTF for his innovative work on a rubidium two-photon optical atomic clock. His work addresses long-term frequency stability using two lasers to mitigate the light shift.
September 2024	Jean-Paul Calin won the best poster award at the Solar&Storage Live Zürich with his poster named "Modeling of Partial Shadows on Photovoltaic Modules" based on his master thesis at CSEM.
October 2024	Nicolas Kirsch received the Hans-Jürgen Appelrath Best Paper Award at the 2024 Dach+ Energy Informatics conference for the paper "A Distributed Game Theoretic Approach for Optimal Battery Use in an Energy Community" based on his master thesis at CSEM.
November 2024	Pietro Iurilli awarded the Battery Young Researcher Award for groundbreaking work on lithium-ion battery aging and management systems at the Battery Innovation Days 2024.

ALLSCHWIL
Hegenheimermattweg 167A
CH-4123 Allschwil

ALPNACH
Untere Gründlistrasse 1
CH-6055 Alpnach

BERN
Weyermannstrasse 36
CH-3008 Bern

LANDQUART
Bahnhofstrasse 1
CH-7302 Landquart

NEUCHÂTEL
Jaquet-Droz 1
CH-2002 Neuchâtel

ZURICH
Technoparkstrasse 1
CH-8005 Zürich

www.csem.ch
info@csem.ch

